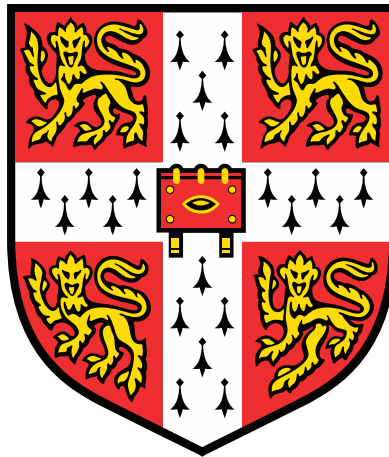


Improving the mechanical properties of Y-Ba-Cu-O single grain bulk superconductors



Jasmin Vivien Joan Congreve

Christ's College

University of Cambridge

This dissertation is submitted for the degree of
Doctor of Philosophy

February 2019

Declaration

This dissertation is the result of my own work and includes nothing which is the outcome of work done in collaboration except as declared in the Preface and specified in the text.

It is not substantially the same as any that I have submitted, or, is being concurrently submitted for a degree or diploma or other qualification at the University of Cambridge or any other University or similar institution except as declared in the Preface and specified in the text. I further state that no substantial part of my dissertation has already been submitted, or, is being concurrently submitted for any such degree, diploma or other qualification at the University of Cambridge or any other University or similar institution except as declared in the Preface and specified in the text.

This dissertation contains less than 65,000 words including appendices, bibliography, footnotes, tables and equations and has fewer than 150 figures.

Jasmin Congreve

February 2019

Acknowledgements

I would first like to thank my supervisor, Prof. David Cardwell, he has been a great mentor, encouraged me and provided great advice.

I am extremely grateful to Dr Yunhua Shi for her continued support and guidance throughout my research. Dr Shi has patiently provided extensive and invaluable help and guidance. Alongside this she has been an inspiration, both in terms of her work and her work ethic. I am very pleased to have been able to work with her guidance and support.

I would like to thank Mr Anthony Dennis for his kind assistance with my experiments. He has always been eager to offer assistance whenever I have encountered any problems with lab equipment.

I am grateful to Dr John Durrell for his assistance, guidance and support throughout the PhD.

I would also like to extend my thanks to all the members of the Bulk Superconductivity Group. Their kind words, support and assistance have made it a pleasure to work in the group.

I would like to acknowledge the Engineering and Physical Sciences Research Council (EPSRC) for financial support. In addition I would like to thank both Christ's College and the Department of Engineering for financial assistance which made it possible to attend and present at a number of conferences.

I would like to thank all my friends and family for their continued support and encouragement. I would especially like to thank Peter Wilkinson for his support. I would also like to thank my housemate, Josh Hodgson, for cheering me up at difficult times and providing encouragement. In addition I would like to thank Ian and Jenny Wilkinson for their help and support. Finally, I would like to thank Khojasta Talash for her constant positivity and support throughout.

Finally, I would like to thank my mum for all her support and love during my younger years.

List of Publications

J. V. J. Congreve, Y. H. Shi, K. Y. Huang, A. R. Dennis, J. H. Durrell, and D. A. Cardwell, "Improving mechanical strength of YBCO bulk superconductors by addition of Ag," *IEEE Transactions on Applied Superconductivity*, vol. **29**, p. 5, Aug 2019.

J. V. J. Congreve, Y. H. Shi, A. R. Dennis, J. H. Durrell, and D. A. Cardwell, " Comparison of the superconducting properties of Y-Ba-Cu-O and Y-Ba-Cu-O-Ag bulk superconductors," *IOP Conference Series: Materials Science and Engineering*, vol. **502**, p. 012181, April 2019

J. V. J. Congreve, Y. H. Shi, A. R. Dennis, J. H. Durrell, and D. A. Cardwell, "The successful incorporation of Ag into single grain, Y–Ba–Cu–O bulk superconductors," *Superconductor Science & Technology*, vol. **31**, 035008, Jan 2018.

J. V. J. Congreve, Y. H. Shi, A. R. Dennis, J. H. Durrell, and D. A. Cardwell, "Growth rate of YBCO-Ag superconducting single grains," *IOP Conf. Ser.: Mater. Sci. Eng.* **279** 012027, 2017.

J. V. J. Congreve, Y. H. Shi, A. R. Dennis, J. H. Durrell, and D. A. Cardwell, "Improvements in the processing of large grain, bulk Y-Ba-Cu-O superconductors via the use of additional liquid phase," *Superconductor Science & Technology*, vol. **30**, p. 11, Jan 2017.

J. V. J. Congreve, Y. H. Shi, A. R. Dennis, J. H. Durrell, and D. A. Cardwell, "Microstructure and Composition of Primary and Recycled Single Grains of YBCO, GdBCO-Ag, and SmBCO-Ag Bulk Superconductors," *J. Am. Ceram. Soc.*, **99**: 3111-3119, 2016.

Abstract

The overall aim of this work was to improve the mechanical properties of single grain YBCO bulk superconductors without causing significant detrimental effects to the superconducting properties of the material. It is widely acknowledged that large single grains of GdBCO and SmBCO with silver can be batch processed successfully with superior mechanical properties compared to silver-free GdBCO or SmBCO, grown by standard top seeded melt growth (TSMG). However, the successful, reliable growth of large single grains of YBCO-Ag by TSMG is significantly more difficult and has not previously been documented. The ability to alloy the YBCO system is desirable, since this base material has better inherent mechanical properties than GdBCO or SmBCO. This work approached the successful and reliable single grain growth of YBCO-Ag via a number of incremental stages.

The first stage investigated the provision of additional liquid-phase to the recycling of multi-grain samples of YBCO, GdBCO-Ag and SmBCO-Ag. The provision of sufficient additional liquid-phase improved both the reliability and uniformity of growth of large single grains. The additional liquid enabled the growth of single grains even when large silver or cerium-rich agglomerates were present in the melt. The provision of additional liquid-phase was then trialled in the primary growth of YBCO by TSMG. This addition resulted in a higher reliability of growth of large single grains. In addition, these single grains had superconducting properties of magnitude comparable to, or higher than, those of YBCO grown by standard TSMG with a greater uniformity. The increase in reliability and in the tolerance to silver-rich agglomerates provided by the provision of additional liquid-phase suggested that this technique may enable the successful growth of single grains of YBCO-Ag. Initially the growth rate of YBCO-Ag was investigated. Large single grains of YBCO-Ag were then successfully and reliably grown by TSMG using heating profiles derived from the growth rate models. A large number of large single grains were grown reliably and their superconducting properties were tested. In addition, this development enabled the mechanical properties of YBCO-Ag to be analysed in detail for the first time.

Contents

Declaration	ii
Acknowledgements	iv
List of Publications	vi
Abstract	viii
Contents	x
List of figures	xiv
List of tables.....	xxvi
List of abbreviations	xxviii
List of symbols.....	xxx
1 Introduction	1
1.1 Superconductors	1
1.1.1 Bulk high temperature superconductors for applications	1
1.1.2 Fabrication and superconducting properties of (RE)BCO	2
1.2 Crystal growth of single grain bulk (RE)BCO	3
1.3 Improvement of mechanical properties	6
1.4 Models related to the growth of (RE)BCO single grains	12
1.4.1 Push-trap theory	13
1.4.2 Diffusion theory	14
1.4.3 Ostwald ripening	14
1.4.4 Secondary nucleation	15
1.5 Superconductivity theory	16
1.5.1 Fundamental characteristics of superconductivity	16
1.5.2 Types of superconductors	17

1.5.3	<i>M-H</i> curves.....	18
1.5.4	Magnetisation.....	20
1.5.5	Transition temperature and critical current density	20
1.5.6	The Bean Model.....	21
1.5.7	The effect of pinning centres	21
1.5.8	Superconducting properties of (RE)BCO	23
1.6	A review of the developments in processing of (RE)BCO	23
1.7	An outline of the work	26
2	Experimental methods	28
2.1	Top seeded melt growth	28
2.2	Trapped field measurement.....	35
2.3	Superconducting quantum interference device measurements	36
2.4	Microscopy.....	39
2.5	Energy dispersive X-ray spectroscopy.....	40
2.6	Threshold analysis.....	42
3	The provision of additional liquid-phase in the recycling of YBCO, GdBCO-Ag and SmBCO-Ag bulk superconductors	44
3.1	The growth process	45
3.2	Superconducting properties.....	47
3.2.1	Trapped field.....	48
3.2.2	Transition temperature and critical current density	49
3.3	Microstructure	52
3.4	Composition	59
3.5	Conclusions	63
4	The provision of additional liquid-phase to enhance the growth of YBCO single grains by TSMG	65

4.1	Powder preparation and analysis.....	66
4.2	Incremental optimisation of sample growth.....	69
4.3	Superconducting properties.....	74
4.3.1	Trapped field.....	75
4.3.2	Transition temperature.....	81
4.3.3	Critical current density.....	82
4.4	Density and Porosity.....	83
4.5	Microstructure.....	84
4.6	Composition.....	92
4.7	Comparison of superconducting properties, microstructure and composition.....	94
4.8	Conclusions.....	96
5	Optimisation of growth rate for fabrication of large single grains of YBCO-Ag.....	98
5.1	The growth process.....	104
5.2	Microstructure prior to oxygenation.....	117
5.3	Microstructure of the oxygenated samples.....	122
5.4	Composition.....	125
5.5	Conclusions.....	128
6	Comparison of the superconducting properties of YBCO and YBCO-Ag single grains....	129
6.1	The growth process.....	131
6.2	Superconducting properties.....	134
6.2.1	Trapped field.....	134
6.2.2	Transition temperature and critical current density.....	136
6.3	Microstructure.....	139
6.4	Porosity and Silver distribution.....	145
6.5	Relation between microstructure, composition and superconducting properties.....	145

6.6	Conclusions	149
7	Small scale tests of the mechanical strength of YBCO-Ag.....	151
7.1	The growth process	151
7.2	Mechanical properties	154
7.3	Microstructure	159
7.4	Composition	162
7.5	Relation between microstructure, composition and mechanical properties.....	163
7.6	Conclusions	166
8	Conclusions	168
9	Future work.....	173
	References.....	175
10	Appendix 1: Chapter 3.....	182
11	Appendix 2: Chapter 4.....	190
12	Appendix 3: Chapter 6.....	194
13	Appendix 3: Chapter 7.....	201

List of figures

Figure 1.1: The structure of YBCO: a) non-superconducting tetragonal phase and b) superconducting orthorhombic phase, with the atoms in colours: Blue=Y, Yellow=Ba, Red=Cu and Grey=O [13].	3
Figure 1.2: The phase diagram for the YBCO system [14].	4
Figure 1.3: A plot of the flexural stress against displacement for YBCO alloyed with: 1) 0 %, 2) 50 %, 3) 67 % and 4) 92 % by volume Ag [25].	11
Figure 1.4: A schematic illustration of the forces acting on a particle in front of the solid/liquid interface; F_D is the drag force due to viscous flow around the particle and F_I is the force due to interfacial energy.	14
Figure 1.5: An M-H curve for a typical ideal superconductor showing: (black) an ideal Type I superconductor, (red) an ideal Type II superconductor.	19
Figure 1.6: An M-H loop for practical superconducting Type II materials showing loops predicted using the Bean model and the Kim model (including the dependence of J_c on B, the magnetic flux density) [51].	19
Figure 2.1: The assembly used for: a) conventional TSMG, and b) the recycling process, c) LR YBCO, d) YBCO-Ag.	32
Figure 2.2: A schematic illustration of a typical heating profile used in TSMG.	33
Figure 2.3: A single grain of (RE)BCO.	33
Figure 2.4: Heating profiles of a) JY-01 input to the furnace, b) JY-01 measured at the centre of the furnace, c) JY-02 input to the furnace and d) JY-02 measured at the centre of the furnace...	35
Figure 2.5: Plots of the variation in J_c value with field at a constant temperature of 77 K for sub-specimens from within one sample.	37

Figure 2.6: Plots of the variation in normalised magnetic moment with temperature for sub-specimens from within one sample.....	38
Figure 2.7: Schematic showing the orientation of the approximate dimensions of the pieces cut for analysis in the SQUID, dimensions in mm.	39
Figure 2.8: Schematic of the axes imaged using the optical microscope.	40
Figure 2.9: Image of: a) The microstructure of a YBCO-Ag sample at 50x magnification, b) The thresholded image used to identify pores, c) the thresholded image used to identify Ag agglomerates.	43
Figure 3.1: The heating profiles used for both conventional TSMG and recycling of a) YBCO, b) GdBCO-Ag and c) SmBCO-Ag, inset is the region highlighted in yellow.	46
Figure 3.2: Single grains of: a) primary grown YBCO, b) recycled YBCO, c) primary grown GdBCO-Ag, d) recycled GdBCO-Ag, e) primary grown SmBCO-Ag and f) recycled SmBCO-Ag.....	47
Figure 3.3: Trapped field profiles measured at the top surface of single grains of; a) recycled YBCO, b) recycled GdBCO-Ag, c) primary grown GdBCO-Ag and d) recycled SmBCO-Ag. .	48
Figure 3.4: A schematic illustration of the labelling of each piece cut from the centre of the bulk.	51
Figure 3.5: A labelled SEM image showing an (RE)-123 matrix including a number of labelled features.....	53
Figure 3.6: SEM images along the a/b-axis of a primary grown GdBCO-Ag sample approximately 1 mm below the seed at 2000x magnification, inset is a schematic of the axes along which the images were taken.	54
Figure 3.7: SEM images along the central c-axis of a primary grown GdBCO-Ag sample at 2000x magnification, inset is a schematic of the axes along which the images were taken.....	55

Figure 3.8: SEM images along the a/b-axis of a recycled GdBCO-Ag sample approximately 1 mm below the seed at 2000x magnification, inset is a schematic of the axes along which the images were taken.....	56
Figure 3.9: SEM images along the central c-axis of a recycled GdBCO-Ag sample at 2000x magnification, inset is a schematic of the axes along which the images were taken.....	57
Figure 3.10: Micrograph image showing regions 1 and 2 in which the composition was measured.	59
Figure 3.11: Graphs showing the variation in atomic fraction of the elements Cu, Ba and RE... ..	61
Figure 3.12: Graphs showing the ratios of Y : Ba and Y : Cu with distance from the seed.	62
Figure 4.1: XRD spectra showing the component phases present in a) Precursor powder, b) LR2, c) LR 3, d) LR 4.....	67
Figure 4.2: DTA plots showing the temperatures at which phase changes occur in a) LR 2, b) Sintered liquid-rich powder, LR 3, c) Y-211 powder and d) Yb-123 powder.....	69
Figure 4.3: The heating profile used to grow single grains of 25 mm diameter of YBCO.	71
Figure 4.4: Photographs of the samples with observations labelled by the yellow arrows: a) JY-01 with a double facet line, b) JY-02 with a small secondary grain, c) JY-03 with lots of cracking and not fully grown to the base, d) JY-04 base with post-oxygenation cracking, e) JY-05 base showing post oxygenation cracking, f) JY-06 base showing post oxygenation cracking, g) JY-07, h) JY-08, i) JY-09 with a double facet line, j) JY-10, k) JY-11 with a secondary grain, l) JY-12 with a double facet line, m) JY-13 with a secondary grain due to seed failure, n) JY-14, o) JY-15 with a secondary grain nucleated from the ZrO ₂ rod, p) JY-16 with cracking, q) JY-17 with a double facet line.....	74
Figure 4.5: Characteristic trapped field profiles for the base of samples JY-02 and JY-09.....	75
Figure 4.6: Trapped field profiles for samples JY-06 and JY-10 grown with and without a buffer pellet.....	77

Figure 4.7: Trapped field profiles of samples grown with and without additional liquid phase. .	78
Figure 4.8: Trapped field profiles of samples grown with different liquid-rich powders.	79
Figure 4.9: Trapped field profiles of samples with precursor pellets sintered at a number of temperatures.....	80
Figure 4.10: A graph showing the difference in maximum trapped field due to the sintering temperature of the precursor powder pellet.	81
Figure 4.11: A schematic of the locations of the sub-specimens cut from each bulk.....	81
Figure 4.12: A plot to show the relationship between average density and trapped field.	83
Figure 4.13: Low magnification images of samples a) JY-02 no sintering and no additional liquid-phase-rich powder, b) JY-04 no sintering with LR 2, c) JY-07 sintered at 1043 °C with LR 2 and d) JY-09 no sintering with LR 3, all four samples are approximately 21 mm in diameter.	84
Figure 4.14: Optical microscope images along the a/b-axis of sample JY-02 approximately 1.5 mm from the base at 50x magnification.	86
Figure 4.15: Optical microscope images along the a/b-axis of sample JY-09 approximately 1 mm from the base at 50x magnification.....	87
Figure 4.16: Optical microscope images along the a/b-axis of sample JY-02 approximately 1.5 mm from the base at 1000x magnification.	88
Figure 4.17: Optical microscope images along the a/b-axis of sample JY-09 approximately 1 mm from the base at 1000x magnification.....	89
Figure 4.18: Optical microscope images along the c-axis of sample JY-02 and JY-09 from approximately 1 mm directly below the seed at 50x magnification.	90
Figure 4.19: Optical microscope images along the c-axis of samples JY-02 and JY-09 from approximately 1 mm directly below the seed at 1000x magnification.	91

Figure 4.20: Graphs showing the variation in normalised atomic fraction of the elements Cu, Ba and Y at 1 mm intervals from the expected amount with distance from the seed along the three lines imaged using the SEM. JY-02 was grown by conventional TSMG, JY-09 was provided with additional liquid-phase-rich powder.	93
Figure 4.21: Graphs showing the ratios Y : Ba and Y : Cu with distance from the seed at 1 mm intervals along the three directions imaged using the SEM, these ratios correlate with the ratios of Y-123 and Y-211 present.	94
Figure 5.1: A schematic of the relationship between growth rate and undercooling. The solid line in the plot corresponds to the region through which slow cooling takes place in CCIH.....	100
Figure 5.2: A schematic of the undercooling as a function of time.	101
Figure 5.3: A schematic of the general cooling profile used for CCIH.	102
Figure 5.4: A schematic of the general undercooling profile used for CCIH.	102
Figure 5.5: DTA of YBCO and YBCO-Ag precursor powder.	104
Figure 5.6: The assembly post-heating did not show any visible grain growth.	105
Figure 5.7: A schematic of the heating profile used in the CCIH process, superimposed in red is the heating profile conventionally used in single-stage isothermal holding.....	106
Figure 5.8: The cooling profile used for CCIH in this work.	106
Figure 5.9: The undercooling profile used for CCIH in this work.	107
Figure 5.10: Photographs of the samples grown for the calculation of growth rate. The dashed lines show the edge of the single grain regions.	108
Figure 5.11: The measurements taken of the single grain region a) Top view where the two side lengths are averaged, b) Side cross-section.	109
Figure 5.12: A plot of the predicted growth length and the actual recorded growth length for a) the a/b-axis direction and b) the c-axis direction after two-step cooling to a final undercooling ΔT	

with a subsequent isothermal hold (as shown in Fig. 5.9). Each colour marker represents a different value of T_i . The dotted line represents $y=x$, if the points lay on this line then the predicted and measured values would match perfectly. 111

Figure 5.13: A plot of the growth rate models predicted for YBCO-Ag, based upon two-step undercooling to a final undercooling ΔT 112

Figure 5.14: A cross-section of a single grain illustrating the locations of the silver-deficient and silver-rich regions observed in the YBCO-Ag samples..... 113

Figure 5.15: An optimised heating profile derived from the growth rate data for the successful growth of a single grain of 17 mm diameter of YBCO-Ag, a fully grown sample is shown inset. 114

Figure 5.16: The heating profiles used for the growth of a) 20 mm, b) 25 mm and c) 30 mm diameter assemblies of YBCO-Ag..... 116

Figure 5.17: YBCO-Ag single grains of diameter (top row) 17 mm, (middle row) 21 mm and (bottom row) 26 mm. 117

Figure 5.18: Whole cross-sections at 50x magnification of partially grown single grains grown with T_i of: a) 970 °C, b) 962 °C, c) 956 °C and d) 952 °C. 118

Figure 5.19: Optical microscope images at 500x magnification of a number of the growth rate samples both behind and ahead of the growth front. 119

Figure 5.20: Optical microscope images at 50x magnification showing the regions in the growth rate sample both ahead (below the white line) of and behind the growth front (above the white line). 120

Figure 5.21: Optical microscope images taken at 50x magnification along the c-axis directly below the seed..... 121

Figure 5.22: Optical microscope images taken at 500x magnification along the c-axis directly below the seed..... 122

Figure 5.23: The entire central cross section of an oxygenated single-grain of YBCO-Ag. This was produced by assembling a large number of images taken at 50x magnification using an optical microscope.	124
Figure 5.24: Optical microscope images of a sample post-oxygenation taken at 50x magnification along the c-axis directly below the seed.	124
Figure 5.25: Optical microscope images of a sample post-oxygenation taken at 500x magnification along the c-axis directly below the seed.	125
Figure 5.26: The composition within partially grown single grains with T_i of: a) 970 °C, b) 962 °C, c) 956 °C and d) 952 °C alongside the composition expected based on the precursor powder composition.	126
Figure 5.27: Y/Ba and Y/Cu ratios for partially grown single-grains with T_i of: a) 970 °C, b) 962 °C, c) 956 °C and d) 952 °C. These ratios correlate with the ratios of Y-123 and Y-211 present	127
Figure 6.1: Heating profiles used for the growth of 30 mm diameter assemblies of a) YBCO-Ag and b) YBCO and LR YBCO by TSMG.	131
Figure 6.2: The fully grown single grains of a) YBCO, b) LR YBCO and c) YBCO-Ag.	132
Figure 6.3: Whole cross-sections of single grains of: a) YBCO, b) LR YBCO, and c) YBCO-Ag.	133
Figure 6.4: A plot of the average maximum trapped field recorded on the top and bottom surface of 26 mm diameter samples of YBCO and LR YBCO and a range of sizes of YBCO-Ag.	136
Figure 6.5: A schematic of the locations of the sub-specimens cut from each bulk.....	136
Figure 6.6: Histograms to enable comparison between corresponding sub-specimens for: a) T_c , b) ΔT_{90} , and c) J_c values.	138
Figure 6.7: Optical microscope images taken at 50x magnification corresponding to approximately the centre of each of the sub-specimens.	141

Figure 6.8: Optical microscope images along the central c-axis of a YBCO sample at 500x magnification.	142
Figure 6.9: Optical microscope images along the central c-axis of a LR YBCO sample at 500x magnification.	143
Figure 6.10: Optical microscope images along the central c-axis of a YBCO-Ag sample at 500x magnification.	144
Figure 6.11: A plot of the area occupied by pores in each image of the sub-specimen, as derived using threshold analysis.	145
Figure 6.12: Plots of the area occupied by pores, and where relevant, silver in each image with the J_c value for the sub-specimen superimposed for: a) a YBCO sample, b) a LR YBCO sample, and c) a YBCO-Ag sample.	148
Figure 6.13: The relative average pore size, and where relevant, silver agglomerate size in each image taken from the centre of each of the sub-specimens.	149
Figure 7.1: The fully grown single grains of YBCO, LR YBCO and YBCO-Ag.....	152
Figure 7.2: Whole cross-sections of single grains of: a) YBCO, b) LR YBCO, and c) YBCO-Ag.	153
Figure 7.3: A schematic of the three-point bend test setup.....	154
Figure 7.4: A schematic of the locations of the beams used for mechanical testing.	155
Figure 7.5: A typical load-displacement curve exhibited by the YBCO, LR YBCO and YBCO-Ag beams during the three-point bend test.	156
Figure 7.6: The average flexural strength of each beam in (a) slice 1, (b) slice 2 and (c) slice 3. The error bars correspond to the maximum and minimum recorded failure stress at each location.	158

Figure 7.7: Optical microscope images taken at 50x magnification corresponding to approximately the centre of each of the beams.....	160
Figure 7.8: The average variation in porosity between the beams considered in terms of a) the average area occupied by pores and b) the average size of the pores present at each location. .	163
Figure 7.9: The relationship between flexural strength and area occupied by pores in slice 1 of: a) YBCO, b) LR YBCO, c) YBCO-Ag and d) the area occupied by silver in YBCO-Ag.	165
Figure 7.10: The relationship between flexural strength and relative average pore size in slice 1 of: a) YBCO, b) LR YBCO, c) YBCO-Ag and d) the area occupied by silver in YBCO-Ag. ..	166
Figure 10.1: Recycled grains of a) Top view of YBCO, b) Side view of YBCO, c) Top view of GdBCO-Ag (note the 2 grains on the left and one grain on the right of the middle row are primary grown samples), d) Side view of GdBCO-Ag, e) Top view of SmBCO-Ag and f) Side view of SmBCO-Ag.....	182
Figure 10.2: Plots of the magnetic moment evolution during a temperature sweep used to find T_c values and ΔT_{90} for sub-specimens of a) primary YBCO, b) recycled YBCO, c) primary GdBCO-Ag, d) recycled GdBCO-Ag, e) primary SmBCO-Ag, f) recycled SmBCO-Ag sample 1, and g) recycled SmBCO-Ag sample 2.....	183
Figure 10.3: Plots of the variation in J_c values at a 77 K for: a) Primary grown YBCO, b) Recycled YBCO, c) Primary grown GdBCO-Ag, d) Recycled GdBCO-Ag, e) Primary grown SmBCO-Ag, f) Recycled SmBCO-Ag grain 1, and g) Recycled SmBCO-Ag grain 2	184
Figure 10.4: Optical microscope images along the a/b-axis of a primary grown YBCO sample approximately 1 mm below the seed at 500x magnification.	185
Figure 10.5: Optical microscope images along the central c-axis of a primary grown YBCO sample at 500x magnification.	185
Figure 10.6: Optical microscope images along the a/b-axis of a recycled YBCO sample approximately 1 mm below the seed at 500x magnification.	186

Figure 10.7: Optical microscope images along the central c-axis of a recycled YBCO sample at 500x magnification.	186
Figure 10.8: SEM images along the a/b-axis of a primary grown SmBCO-Ag sample approximately 1 mm below the seed at 2000x magnification.	187
Figure 10.9: SEM images along the central c-axis of a primary grown SmBCO-Ag sample at 2000x magnification.	187
Figure 10.10: SEM images along the a/b-axis of recycled SmBCO-Ag grain 1 approximately 1 mm below the seed at 2000x magnification.	188
Figure 10.11: SEM images along the central c-axis of recycled SmBCO-Ag grain 1 at 2000x magnification.	188
Figure 10.12: SEM images along the a/b-axis of recycled SmBCO-Ag grain 2 approximately 1 mm below the seed at 2000x magnification.	189
Figure 10.13: SEM images along the central c-axis of the recycled grain 2 at 2000x magnification.	189
Figure 11.1: Plots of the variation in normalised magnetic moment with temperature for: a) Sample JY-02, b) Sample JY-09.....	190
Figure 11.2: Plots of the variation in J_c value with field at a constant temperature of 77 K for a) Sample JY-02, the standard TSMG sample, b) Sample JY-09, the sample grown by TSMG with additional liquid-phase.....	191
Figure 11.3: Optical microscope images along the a/b-axis of sample JY-02 approximately 1 mm below the seed at 50x magnification.....	192
Figure 11.4: Optical microscope images along the a/b-axis of sample JY-09 approximately 1 mm below the seed at 50x magnification.....	192
Figure 11.5: Optical microscope images along the a/b-axis of sample JY-02 approximately 1 mm below the seed at 1000x magnification.....	193

Figure 11.6: Optical microscope images along the a/b-axis of sample JY-09 approximately 1 mm below the seed at 1000x magnification.....	193
Figure 12.1: Plots of the variation in normalized magnetic moment with temperature, used to determine the transition temperature of the sub-specimens from: a) a YBCO sample, b) a LR YBCO sample, and c) a YBCO-Ag sample.....	194
Figure 12.2: Plots of the variation in J_c values with field for the sub-specimens from: a) a YBCO sample, b) a LR YBCO sample, and c) a YBCO-Ag sample.	195
Figure 12.3: Optical microscope images along the central c-axis of a YBCO sample from a position just below the seed at 50x magnification.	196
Figure 12.4: Optical microscope images along the central c-axis of a LR YBCO sample from a position just below the seed at 50x magnification.	196
Figure 12.5: Optical microscope images along the central c-axis of a YBCO-Ag sample from a position just below the seed at 50x magnification.	197
Figure 12.6: Optical microscope images along the a/b-axis of a YBCO sample approximately 1.5 mm from the top at 50x magnification.	197
Figure 12.7: Optical microscope images along the a/b-axis of a LR YBCO sample approximately 1.5 mm from the top at 50x magnification.	198
Figure 12.8: Optical microscope images along the a/b-axis of a YBCO-Ag sample approximately 1.5 mm from the top at 50x magnification.	198
Figure 12.9: Optical microscope images along the a/b-axis of a YBCO sample approximately 1.5 mm from the base at 50x magnification.	199
Figure 12.10: Optical microscope images along the a/b-axis of a LR YBCO sample approximately 1.5 mm from the base at 50x magnification.	199
Figure 12.11: Optical microscope images along the a/b-axis of a YBCO-Ag sample approximately 1.5 mm from the base at 50x magnification.	200

Figure 13.1: Optical microscope images along the central c-axis of a YBCO sample from a position just below the seed at 50x magnification.	201
Figure 13.2: Optical microscope images along the central c-axis of a LR YBCO sample from a position just below the seed at 50x magnification.	201
Figure 13.3: Optical microscope images along the central c-axis of a YBCO-Ag sample from a position just below the seed at 50x magnification.	202
Figure 13.4: Optical microscope images along the a/b-axis of a YBCO sample approximately 1.5 mm from the top at 50x magnification.	202
Figure 13.5: Optical microscope images along the a/b-axis of a LR YBCO sample approximately 1.5 mm from the top at 50x magnification.	203
Figure 13.6: Optical microscope images along the a/b-axis of a YBCO-Ag sample approximately 1.5 mm from the top at 50x magnification.	203
Figure 13.7: Optical microscope images along the a/b-axis of a YBCO sample approximately 1.5 mm from the base at 50x magnification.	204
Figure 13.8: Optical microscope images along the a/b-axis of a LR YBCO sample approximately 1.5 mm from the base at 50x magnification.	204
Figure 13.9: Optical microscope images along the a/b-axis of a YBCO-Ag sample approximately 1.5 mm from the base at 50x magnification.	205
Figure 13.10: Optical microscope images along the central c-axis of a YBCO sample at 500x magnification.	205
Figure 13.11: Optical microscope images along the central c-axis of a LR YBCO sample at 500x magnification.	206
Figure 13.12: Optical microscope images along the central c-axis of a YBCO-Ag sample at 500x magnification.	206

List of tables

Table 1.1: A table showing the typical T_c and J_c values of the common (RE)BCO bulk superconducting materials [45].	23
Table 2.1: The seed material used for each system.	29
Table 2.2: The composition of the precursor powder used for each system.	29
Table 2.3: The heating profiles used for the oxygenation process.	34
Table 3.1: The maximum trapped fields recorded at the top and bottom surface of recycled and primary grown bulk single grains.	49
Table 3.2: T_c , ΔT_{90} and J_c values from YBCO and recycled YBCO samples.	50
Table 3.3: T_c , ΔT_{90} and J_c values from GdBCO-Ag and recycled GdBCO-Ag samples.	50
Table 3.4: T_c , ΔT_{90} and J_c values from one SmBCO-Ag sample and two recycled SmBCO-Ag samples.	51
Table 4.1: A table summarising the growth conditions and the post-growth observations for each sample grown in the optimisation process.	73
Table 4.2: Maximum trapped field measurement at the surface, measured using a single Hall probe and corrected for use in liquid nitrogen.	76
Table 4.3: A table showing the values of the superconducting properties for each sub-specimen derived from the SQUID data.	82
Table 5.1: The undercooling profile and growth length functions for each region of the general CCIH case.	103
Table 5.2: The growth lengths measured in the a/b -axis direction and c -axis direction for each growth condition.	109

Table 5.3: A table of the estimated values of alpha for YBCO-Ag grown by the CCIH process.
..... 110

Table 5.4: The percentage of total growth length that occurs in each region of cooling as
predicted using the models for the YBCO-Ag system grown by CCIH..... 112

Table 5.5: A table of the mass of each powder used during pressing of different sized samples.
..... 115

Table 6.1: The values of maximum trapped field recorded at the top and base of a number of
single grains of YBCO, LR YBCO and YBCO-Ag. 135

Table 6.2: T_c , ΔT_{90} and J_c values of the sub-specimens of YBCO, LR YBCO and YBCO-Ag 137

Table 7.1: The flexural strength of each beam from each of the three types of sample. 157

List of abbreviations

Ag	Silver
at %	Atomic percentage
Ba	Barium
CCIH	Continuous cooling and isothermal hold
Ce	Cerium
Cu	Copper
2D	Two dimensional
3D	Three dimensional
DC	Direct current
DTA	Differential thermal analysis
EDX	Energy dispersive X-ray spectroscopy
FC	Field cooling
Fe	Iron
Gd	Gadolinium
GdBCO	Gadolinium barium copper oxide, Gd-Ba-Cu-O
GdBCO-Ag	Gadolinium barium copper oxide with silver, Gd-Ba-Cu-O-Ag
h	Hours
HTS	High temperature superconductor
IG	Infiltration growth
La	Lanthanum
Mg	Magnesium or Mega-gram
MgB ₂	Magnesium diboride
mol %	Molar percentage
Nd	Neodymium
NdBCO	Neodymium barium copper oxide, Nd-Ba-Cu-O
O	Oxygen
PFM	Pulse field magnetisation

Pt	Platinum
(RE)	Rare earth element including Y, Gd or Sm
RE-123	(RE)Ba ₂ Cu ₃ O _{7-δ} superconducting matrix
RE-211	(RE) ₂ BaCuO _x non-superconducting inclusions
(RE)BCO	Rare earth barium copper oxide, (RE)-Ba-Cu-O
SEM	Scanning electron microscope
Sm	Samarium
SmBCO	Samarium barium copper oxide, Sm-Ba-Cu-O
SmBCO-Ag	Samarium barium copper oxide with silver, Sm-Ba-Cu-O-Ag
Sn	Tin
SQUID	Superconducting quantum interference device
Sr	Strontium
T	Tesla
TSMG	Top seeded melt growth
wt %	Weight percentage
XRD	X-ray diffraction
Y	Yttrium
Yb	Ytterbium
Yb-123	Ytterbium barium copper oxide, YbBa ₂ Cu ₃ O _x
YBCO	Yttrium barium copper oxide, Y-Ba-Cu-O
YBCO-Ag	Yttrium barium copper oxide with silver, Y-Ba-Cu-O-Ag
ZFC	Zero field cooled
Zr	Zirconium

List of symbols

a	Shortest side length in the a/b -plane or flaw half-length
b	Longest side length in the a/b -plane or width of the test beam used in a three-point bend test
B	Magnetic field strength
b_{σ}	An empirical constant
c	Dimension in the c -direction
d	Spacing between atom layers or the depth of the test beam used in a three-point bend test
d_{211}	Diameter of RE-211 inclusions
D_L	Diffusivity in liquid
E	Voltage generated
F	Load at failure
F_c	Corrected trapped field
F_D	Drag force
F_I	Force due to interfacial energy
F_L	Force on a magnetic flux quanta
F_m	Measured trapped field
ΔH	Change in enthalpy
h	Average height
H	Magnetic field strength
H_{c1}	Lower critical value of applied magnetic field
H_{c2}	Upper critical value of applied magnetic field
J	Current density
J_c	Critical current density
K_{IC}	Fracture toughness
l	Support span in the three-point bend test
L	Growth length
L_a	Growth length in the a/b -axis direction

L_c	Growth length in the c -axis direction
Δm	Difference in magnetic moment
m	Sample mass
M	Magnetisation
n	An integer
P_v	Volume of pores
r^*	Critical radius
r	Modified mean radius or average radius
R	Growth rate
R_a	Growth rate of the ac -plane
R_c	Growth rate of the ab -plane
R_{ih}	Growth rate during the isothermal hold period
t	Time
T	Temperature
ΔT	Undercooling
ΔT_{90}	Temperature range over which the magnetic moment reduces to 90 % of its original value
T_c	Transition temperature
T_i	Isothermal hold temperature
T_m	Melting temperature
T_p	Peritectic temperature
v	Velocity of each fluxon
V_{211}	Volume of RE-211 inclusions
Y	Constant dependent on flaw location and shape
α	Constant in Ostwald ripening or constant in growth rate equation
β	Constant in growth rate equation
σ	Strength at a given porosity
$\Delta\sigma_0$	Interfacial energy
σ_0	Pore-free strength
σ_f	Flexural strength at failure
η	Melt viscosity

Γ	Gibbs-Thomson coefficient
λ	Wavelength
θ	Angle of incidence

1 Introduction

1.1 Superconductors

High temperature superconducting (HTS) materials have a large number of potential technological applications. The existing forms of these superconductors can be grouped into three main categories: wires and tapes, thin films and bulk materials. These materials can be used to produce wires with high critical current densities (J_c) able to transport large electrical currents with minimal power losses, and tapes which are able to generate high magnetic fields. These materials can be used for thin films utilized in superconducting devices that rely upon quantum phenomena; these include superconducting quantum magnetic interference devices (SQUIDs) and quantum computers. The final category, upon which this work is focused, are bulk, single grain materials which are used primarily for levitation and shielding purposes.

1.1.1 Bulk high temperature superconductors for applications

HTS single grains have the ability to trap large magnetic fields of over an order of magnitude greater than those of conventional permanent magnets. They also have the ability to provide stable levitation [1]. As a result, there are a wide range of potential applications for these materials, classified into 3 main categories: levitation devices, rotating machines and a class of devices that use the high magnetic field directly. Levitation devices include Maglev trains, flywheels and seismic isolation devices. Rotating machines include motors and generators. The class of devices that use high magnetic field directly includes applications such as sputtering systems, separators, drug delivery systems and nuclear magnetic resonance (NMR) systems [2-4].

Bulk applications require materials with high J_c values. The J_c value is the highest DC current density a superconductor can support while retaining zero resistance. A high J_c value is crucial to the practical application of a bulk superconductor because the current circulating within the material is responsible for the magnitude of the trapped field generated. Depending on the application, either the trapped field itself or the levitation force provided due to the trapped field is the most important parameter. A large J_c value enables a large trapped field to be produced by the bulk superconductor and a large levitation force results. In addition, the resistance must be

retained at zero to enable the superconducting current to continue to flow. Any resistance in the bulk superconductor will dissipate energy, reduce the current circulating and the trapped field, and hence decrease the levitation force over time following magnetisation.

The value of J_c is strongly dependent upon the microstructure and is not an intrinsic property of the material. This property is heavily dependent upon the processing conditions; in order to produce bulk superconductors with high J_c values, a uniform, continuous matrix containing a homogeneous dispersion of defects is required [5-8]. Initially, sintering methods used in the fabrication process resulted in the production of polycrystalline samples. Polycrystalline samples have low J_c values because high angle grain boundaries form weak links to the flow of supercurrent [3,4]. The practical application of these sintered polycrystalline samples was limited due to low J_c values, hence single grain samples that contain fewer weak links are more desirable for practical applications [6, 9, 10]. Current research into HTS bulk superconductors is focused on improving their superconducting and mechanical properties. During the growth process there are a substantial number of interdependent variables, many of which are determined empirically from research and experience. It is, therefore, difficult to optimise the processing conditions and so further research into the fabrication of single grains is required to improve the growth process, both in terms of the reliability and the properties of the material produced [11].

Single grain RE-Ba-Cu-O [(RE)BCO], where RE (rare earth) = Y, Gd or Sm, is one of the most widely studied bulk HTS materials. There are many growth processes that have been developed to enable single-grain fabrication of (RE)BCO bulk superconductors.

1.1.2 Fabrication and superconducting properties of (RE)BCO

(RE)BCO has an oxygen deficient perovskite structure with layers of CuO_2 [8]. The structure of YBCO is shown in Fig. 1.1. The non-superconducting tetragonal structure is transformed post-processing to a superconducting orthorhombic structure during oxygenation. (RE)BCO compounds have a layered structure. The anisotropic nature of the structure causes both the mechanical and superconducting properties to be very anisotropic. Charge carriers are only able to propagate in the CuO_2 plane, referred to as the a/b -plane. Therefore, the achievable J_c value is significantly higher in the a/b -plane than along the crystallographic c -axis direction [8, 12]. The

anisotropy in superconducting properties necessitates the fabrication of single grains with a controlled orientation. The control of lattice orientation during melt processing is provided by a single grain seed, which is used to nucleate and grow a large, single grain sample.

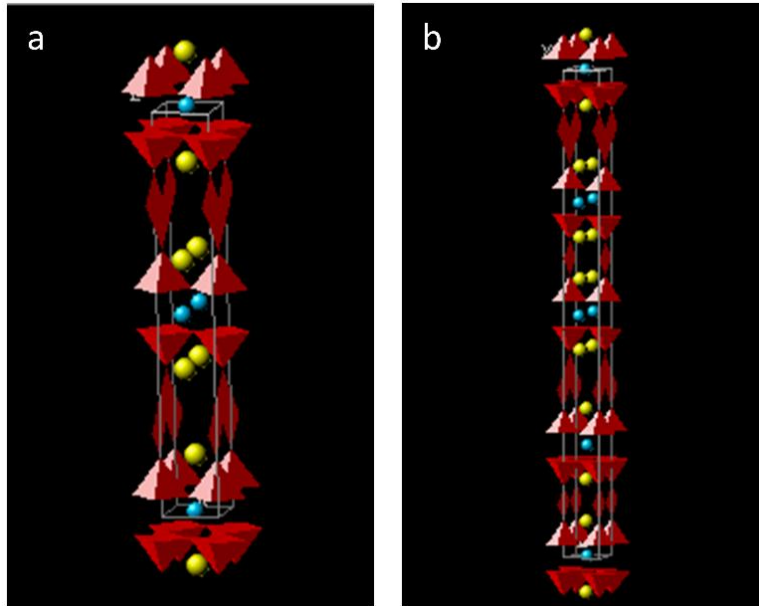
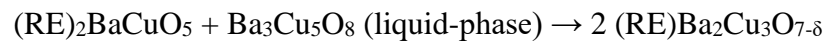


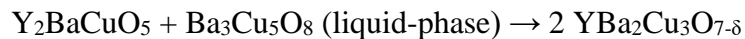
Figure 1.1: The structure of YBCO: a) non-superconducting tetragonal phase and b) superconducting orthorhombic phase, with the atoms in colours: Blue=Y, Yellow=Ba, Red=Cu and Grey=O [13].

1.2 Crystal growth of single grain bulk (RE)BCO

Many melt processing techniques have been developed in order to fabricate large single grains of (RE)BCO. These techniques are based upon the peritectic reaction:



in the case of the YBCO system the peritectic reaction:



occurs at approximately 1000 °C [13].

The corresponding phase diagram is shown in Fig. 1.2, with the region of interest in the majority of fabrication processes being the section corresponding to 20 to 50 mol % on the x -axis of the diagram.

The two melt processing techniques regularly used for the fabrication of large single grains of (RE)BCO are the so-called top seeded melt growth (TSMG) and infiltration growth (IG) processes [5, 14].

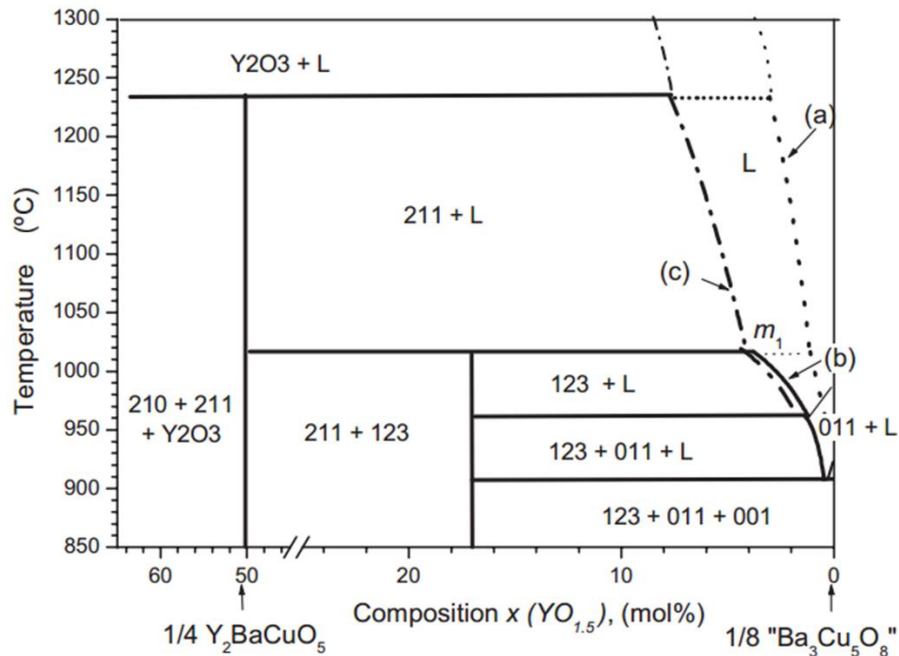


Figure 1.2: The phase diagram for the YBCO system [14].

TSMG is one of the simplest and most widely used methods for the fabrication of large, single grain bulk (RE)BCO [5, 14]. In this process a precursor powder pellet is pressed from pre-mixed powders consisting of a combination of $(RE)Ba_2Cu_3O_{7-\delta}$ (RE-123), which forms the superconducting matrix, $(RE)_2BaCuO_5$ (RE-211), which predominantly forms non-superconducting inclusions, and alloying elements such as CeO_2 and Pt that improve the microstructure and properties [4].

The sample and seed assembly is heated and held above the peritectic decomposition temperature (T_p) of the target RE-123 phase. The powder decomposes into a secondary RE-211 solid phase and

a residual Ba-Cu-O liquid-phase. Slow, controlled undercooling in the presence of a suitable seed crystal enables a single grain to be fabricated successfully.

The infiltration growth (IG) technique is an alternative fabrication technique for the growth of large single grains of (RE)BCO. The assembly used typically consists of a RE-211 preform pellet placed above a liquid-phase-rich source pellet of a slightly larger diameter. In some cases the RE-211 preform is sintered before assembly to ensure it retains the required shape during processing. Recently, a buffer has been placed between the RE-211 preform and the single grain NdBCO seed [7]. The assembly is heated according to a heating profile similar to that used in TSMG. During heating the liquid-phase-rich source pellet melts while the RE-211 preform pellet remains solid. The liquid infiltrates upwards into the preform and reacts with the RE-211 phase to form the RE-123 matrix on cooling [15]. Nucleation occurs at the seed in order to enable single grain growth. Although this process has a number of advantages, it is more difficult to implement successfully due to the additional processing parameters involved.

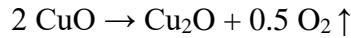
Each of the processing techniques described have a number of associated advantages and disadvantages. A trade-off between the ease of processing and the sample properties must be considered. TSMG is able to produce large, high quality, single grains. However, during the growth process, a large amount of liquid outflow occurs, as does a significant amount of shrinkage. The extended period at high temperature facilitates the undesirable coarsening of RE-211 pinning centres. In addition, some research groups have reported that the chemical composition of the samples grown by TSMG tend to be more inhomogeneous than those grown by IG, and that this is due to the growth process and the liquid outflow during processing [4, 7]. However, this view is not shared by all researchers in the field given that developments in TSMG of bulk superconductors have enabled reliable growth of bulk single grains with a very homogeneous microstructure.

Single grains grown by seeded IG exhibit negligible shrinkage and distortion, which enables near-net shape fabrication. In addition, in comparison with the TSMG process, the size of the RE-211 precipitates can be refined more easily in the IG process and the number and density of pores, cracks and RE-211 deficient regions is much lower in single grains produced by IG compared to

TSMG [4, 7]. The high level of porosity found in samples grown by TSMG is partially due to the evolution of oxygen gas during peritectic decomposition of Y-123 in the reaction:



The CuO decomposes according to:



Oxygen gas which is produced at the edge of the sample is able to diffuse out, but bubbles of gas produced within the interior of the sample become trapped and form pores. It has been observed that a higher heating rate produces larger pores in the TSMG process [7].

The pores formed in samples grown by TSMG can retain pools of liquid at high temperatures and, on cooling, this liquid may react with surrounding RE-211 particles to form the RE-123 matrix. This reaction within and surrounding the pores produces large RE-211 deficient regions. This process does not occur in samples grown by IG [7].

Although the IG process results in samples with lower porosity, fewer RE-211 precipitate-free regions, and finer and more controlled RE-211 size and shape than the TSMG process, the samples grown by IG show a reduced uniformity in the microstructure. In turn, the uniformity of the J_c value throughout the sample is more variable than in samples grown by TSMG. It is also more difficult to reliably produce high-quality single grain samples using the IG process.

1.3 Improvement of mechanical properties

It has been widely reported that the mechanical and superconducting properties of (RE)BCO can be improved by alloying with other elements or compounds [16-19]. Until recently, most studies have focused on improving the superconducting properties of (RE)BCO bulk superconductors, but, in most cases, the limitation is their mechanical properties [20]. The ceramic-like nature of (RE)BCO materials makes them inherently brittle [16, 20]. On magnetisation, samples experience large Lorentz forces, which, if sufficiently large, cause fatal cracking. This limits the maximum magnetisation and hence, in turn, the mechanical properties limit the achievable superconducting

properties [17]. This subsequently reduces the suitability of these materials for applications involving relatively high magnetic fields [16, 20].

(RE)BCO bulk superconductors are anisotropic and the ab -plane is the first cleavage plane under mechanical stress. In YBCO, bending about axes in this plane leads to the lowest flexural strength; estimated to be 8.6 MPa [21], compared to between 24 MPa [22] and 70 MPa [23] for bending about the c -axis. Although the material has the lowest strength for bending about axes in the ab -plane, this does not need to be considered in detail as the largest stresses induced by the Lorentz force produce radial and hoop stresses but no significant longitudinal stresses.

Brittle fracture is critical in the case of (RE)BCO bulk superconductors. Brittle fracture is initiated by pre-existing flaws within the material, such as pores, surface scratches, inclusions or other types of inhomogeneity [24]. These materials inherently contain a large number of pores and a number of cracks; many of these are created during the growth and oxidation process, as explained later. The presence of these pores and cracks weakens this material significantly. Pores act as stress concentration sites, and so promote both fracture initiated from another source and fracture due to the introduction of micro-cracks. Therefore, an increase in pore volume reduces the elastic modulus, fracture toughness [25-27] and the strength of the material [28]. There are a number of models for the strength at a given porosity, σ , for example one model gives;

$$\sigma = \sigma_0 e^{-b_\sigma P_v} \quad (1.1)$$

where P_v is the volume of pores, σ_0 is the pore-free strength and b_σ is an empirical constant [29].

In addition to the amount of porosity, the shapes, sizes and locations of pores affect the fracture properties of the single grain material [30]. This is illustrated by the equation below, in which the shape and size of the crack are critical when the fracture toughness, K_{IC} , of the material is fixed:

$$K_{IC} = Y\sigma\sqrt{\pi a} \quad (1.2)$$

where Y is dependent on the flaw location and shape, σ is the remote stress and a is the flaw half-length. Therefore, the failure of bulk superconductors by fast-fracture is determined by a number of variables related to the intrinsic flaw size.

The compound effect of all of these variables must be considered when studying the mechanical properties of these materials. Alongside the pores, the presence of cracks within the microstructure is detrimental to the mechanical properties of bulk superconductors. Cracks are generally much more dangerous given that they are more difficult to detect and are much sharper, but are also generally much smaller in size.

The (RE)-211 agglomerates are responsible for some of the cracking present within the single grain microstructure. The (RE)-211 agglomerates are pushed by the growth front during grain growth. The pushing and final location of each of these agglomerates depends upon the size of the agglomerate and the speed at which the growth front advances. This generally leads to an inhomogeneous distribution of the (RE)-211 agglomerates throughout the bulk sample. These samples are stress-free at high temperatures and in a semi-molten state, but, on cooling, large stresses are created within the material. This is due to the difference in the coefficient of thermal expansion between the (RE)-123 matrix and (RE)-211 agglomerates. It is estimated that these stresses reach values of 50 to 100 MPa in YBCO [31], which is significantly higher than the flexural strength of the material, so this can cause micro-cracks in the ab -plane. In addition, this thermal expansion mis-match can enable the creation of cracks directly around the (RE)-211 agglomerates [31]. However, the growth of these cracks is usually limited, so this is unlikely to lead to the failure of large samples.

Oxygen annealing, which is carried out to convert the non-superconducting tetragonal structure of the (RE)-123 matrix to the octahedral superconducting structure, is also responsible for introducing macro- and micro-cracks to the sample microstructure [32, 33]. During oxygen annealing of YBCO, the c -axis length of the unit cell shrinks when the x value in $YBa_2Cu_3O_x$ increases [34, 35]. The increase in oxygen concentration leads to the generation of large mechanical stresses within the material. This is due to the RE-211 particles providing constrains on the movement and extension of the c -axis length. In addition, the oxygen diffusion coefficient in the ab -plane is 10^4

to 10^6 times larger than in the c -direction [36]. Therefore, these stresses tend to open-up cracks within the ab -plane.

The evolution of oxygen gas during peritectic decomposition is responsible for the creation of the characteristically large number of pores present within each sample.

The predominant failure of these materials is caused by crack initiation and growth: either from a pre-existing crack or from a defect present within the structure. There are a number of competing factors involved in crack growth. Crack growth ahead of the crack tip is promoted by intrinsic microstructural damage. In these ceramic-like materials the microstructural damage includes pores and cracks already present within the microstructure. Crack growth is impeded, in general, behind the crack tip by extrinsic mechanisms. In order to reduce crack propagation under load, therefore, these intrinsic and extrinsic features should be modified appropriately [37].

The initiation and propagation of cracks for a given remote applied stress can be reduced by improving the intrinsic material properties. In single grain bulk superconductors, this can be achieved by reducing the size and volume fraction of pores present within the single grain, and by reducing the number and size of the cracks present within the microstructure. This is difficult to achieve, and so the crack initiation and propagation in these materials is inhibited predominantly by providing and enhancing extrinsic mechanisms. In general, these are used to shield the crack tip from high stress intensities [38, 39], thus increasing the fracture toughness of the material. Some materials undergo an in-situ phase transformation at the crack tip. This is not the case in YBCO, but is observed extensively in zirconia [39]. Another approach is to use micro-crack toughening, whereby the stress at the crack tip causes the micro cracking of small particles present within the microstructure at the advancing crack tip [39]. A more important, but similar approach, vital for crack growth reduction in YBCO single grains, is the ability of the Y-211, or other particles introduced into the single grain, to cause crack branching and crack meandering due to crack deflection at these particles. This can have an even bigger effect in multi-grain materials since the interfaces are able to provide crack deflection. In addition, crack bridging by fibres, or if the crack is engineered to intersect a ductile phase that undergoes plastic deformation as the crack passes, provides another way of improving the strength of the material [38, 39].

The extrinsic shielding is, critically, dependent on the crack size and geometry [37]. Therefore, in order to improve the mechanical properties, at the lowest level, the porosity and cracks within a sample should be as small as possible and there should be as few as possible, as will be determined by the growth process. At a more complex level, particles or fibres should be added to provide crack deflection and crack bridging [37].

In order to achieve as many of these positive effects as possible, the pores and cracks should generally be filled, and it would be beneficial for the material used to do so to be ductile. Silver is commonly introduced to the bulk microstructure of GdBCO and SmBCO to enable significant improvement in the mechanical properties of these single grains [40, 41]. The addition of silver increases the fracture toughness [42] and bending strength [41, 43] without degrading the superconducting properties [40, 42, 44, 45]. A significant increase in the fracture toughness (K_{IC}) from $1 \text{ MPa m}^{1/2}$ to over $2.4 \text{ MPa m}^{1/2}$ can be achieved by the addition of 30 wt% Ag_2O to the melt. This increase in fracture toughness is, in part, due to the increase in the ability of the sample to deform plastically with an increase in the volume percentage of silver added, shown in Fig. 1.3 [16]. This graph shows that the addition of silver enables a higher stress and strain to be reached before failure, and with a volume of 92 % silver the material is able to behave in a ductile manner rather than behaving as a brittle material. In addition, the metallic silver introduced is able to occupy locations that would otherwise have been pores in the final microstructure [41]. A number of studies have suggested silver within the melt fills some of the pores in the single grain microstructure [40, 46]. Many studies have also suggested that the Ag precipitates present within the structure modify the distribution of residual stresses [47]; these residual stresses are leading factors in the propagation of dislocations and cracks [44].

The incorporation of silver into the pores and cracks within the structure is important for the improvement of the mechanical properties [48]. The Ag precipitates modify the residual stress distribution within the bulk sample. This occurs because strains are generated within the microstructure during cooling due to the different thermal expansion coefficients of Y-123 and Ag [49]. It has also been discovered that large stresses are created around Ag and Y-211 inclusions after processing [50]. Ceramic materials subjected to compressive stress are less likely to crack or fail than when subjected to tensile stresses. This provides the opportunity to engineer the sample

microstructure via the addition of silver to optimise the intrinsic resilience to such potentially destructive forces.

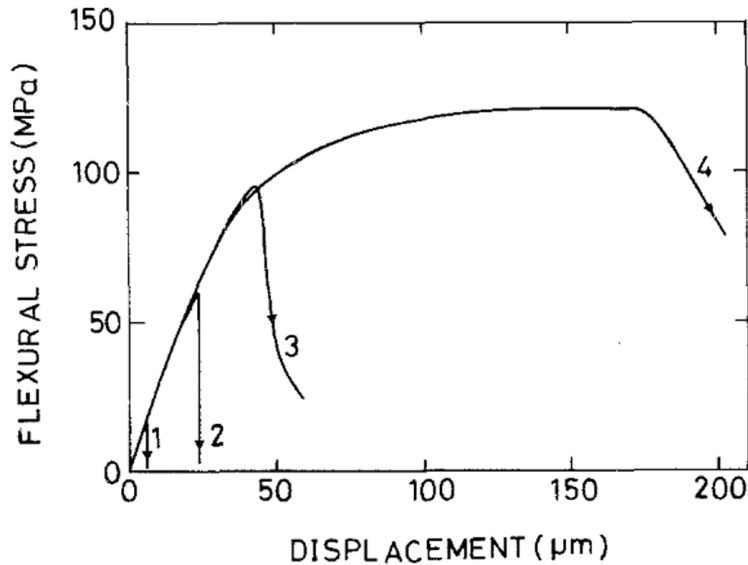


Figure 1.3: A plot of the flexural stress against displacement for YBCO alloyed with: 1) 0 %, 2) 50 %, 3) 67 % and 4) 92 % by volume Ag [25].

The fabrication of large, single grain bulk samples by batch processing has been achieved successfully for $\text{YBa}_2\text{Cu}_3\text{O}_7$ (YBCO) and both the $\text{GdBa}_2\text{Cu}_3\text{O}_7\text{-Ag}$ (GdBCO-Ag) and $\text{SmBa}_2\text{Cu}_3\text{O}_7\text{-Ag}$ (SmBCO-Ag) systems [51]. However, successful and reliable batch processing of $\text{YBa}_2\text{Cu}_3\text{O}_7\text{-Ag}$ (YBCO-Ag) has yet to be achieved due to the greater complexity of the growth process of YBCO-Ag. The addition of greater than 5 wt% silver to the melt causes a large reduction in the peritectic temperature [20, 52] of approximately 30 °C in the YBCO system [53]. The reduction in the peritectic temperature of YBCO-Ag in comparison to the YBCO system leads, in turn, to a considerable narrowing of the temperature window available for successful single grain growth. Hence, a substantially different heating profile is required for the growth of YBCO-Ag single grains to that of the YBCO single grains that do not contain silver. A reduction in the maximum processing temperature affects many aspects of the growth process, including initial decomposition [42], solute diffusion and interface kinetics. This therefore reduces the growth rate of YBCO-Ag in comparison to YBCO. [20] The reduction in processing temperature also significantly increases the likelihood of spontaneous nucleation of secondary grains [20] and further complications arise due to the low solubility of silver in the melt [53]. In addition, the diffusion of Y to the growth front is much slower than that of Gd or Sm. Therefore, a further

reduction in the diffusion speed due to the reduction in processing temperature will reduce the growth rate further, hence making it more difficult to fabricate single grains of YBCO-Ag than GdBCO-Ag or SmBCO-Ag.

If the likelihood of successful single grain growth of YBCO without silver can be improved, this will increase the likelihood of successful growth of YBCO-Ag. The successful growth of YBCO-Ag provides an opportunity to improve the mechanical properties of the YBCO system and reduce the limitation that the mechanical properties place upon the superconducting properties in the YBCO system.

1.4 Models related to the growth of (RE)BCO single grains

Solidification models are usually based upon a diffusion limited model and, on some occasions, a model limited by interfacial kinetics. In the growth of single grains of (RE)BCO, both the diffusion and interfacial kinetics limit growth to some extent. Many of the diffusion-limited models assume that primary crystallisation is due to a balance between the mass flow through an interface and flow originating from the RE-211 particles dissolving ahead of the growth front within the melt. In addition, the facet lines produced during growth show that, to some extent, kinetics also influence crystal growth. Facet lines are growth sector boundaries, each of these growth sectors grow from the seed in a given orientation until they fill the space available to them.

Crystal growth is initiated by nucleation from the single grain seed. It is therefore important that the seed has an elevated melting temperature in comparison to the maximum temperature used in the heating profile. In addition, the seed must have a similar lattice structure to RE-123 in order to ensure lattice misfit does not prevent single grain growth. The extent of this problem has, however, been reduced effectively by the use of a buffer pellet placed between the seed and precursor pellet.

The undercooling temperature during the growth process influences the growth rate; a higher growth rate is produced by a greater undercooling and so larger grains can be produced. However, larger undercooling also increases the likelihood of undesirable nucleation and growth occurring at points other than the seed. This leads to the growth of secondary grains.

1.4.1 Push-trap theory

Movement of the RE-211 particles occurs during the growth of (RE)BCO from a melt of RE-123 with an excess of RE-211. As a result, the quantity of RE-211 in the single grain increases with distance from the seed. The distribution of RE-211 within the RE-123 matrix can be modelled by the so-called Push-trap theory. The RE-211 particles can be modelled as inert particles at an advancing growth front. The dominant forces acting upon the RE-211 particles are the drag force (F_D), due to viscous flow around the particle, and the force arising due to interfacial energy ($\Delta\sigma_0 = \Delta\sigma_{sp} - \Delta\sigma_{lp} - \Delta\sigma_{sl}$, where the subscripts s, p and l represent solid, particle and liquid, respectively) which is the difference between three interface energies and should be positive in order for particle pushing to occur. Particles of RE-211 with a radius greater than the critical radius (r^*) are trapped as the single grain grows. Particles smaller than the critical radius are pushed, and move with the solidification front. The relationship between the growth rate and critical radius is:

$$R \propto \frac{\Delta\sigma_0}{\eta r^*} \quad (1.3)$$

where R is the growth rate and η is the melt viscosity [54, 55]. A schematic of the forces involved is shown in Fig. 1.4.

The general trend whereby the content of RE-211 increases with distance from the seed is in agreement with this model. During the initial stages of nucleation, the growth rate is low and so the critical radius of the RE-211 particles is large, hence the majority of the RE-211 particles are pushed with the advancing solidification front. As the grain growth proceeds, the undercooling increases, hence the growth rate increases. This reduces the critical radius and so enables smaller and more RE-211 particles to be trapped with increasing distance from the seed [56].

Although this model is in agreement with the general trend, care must be taken with its use to model the growth process of the (RE)BCO system. This model assumes the particles modelled are inert whereas, in the case of excess RE-211 in a RE-123 melt, some of the RE-211 dissolves and reacts with the liquid at the growth front, so the assumption of inert particles is only valid for conditions of high undercooling.

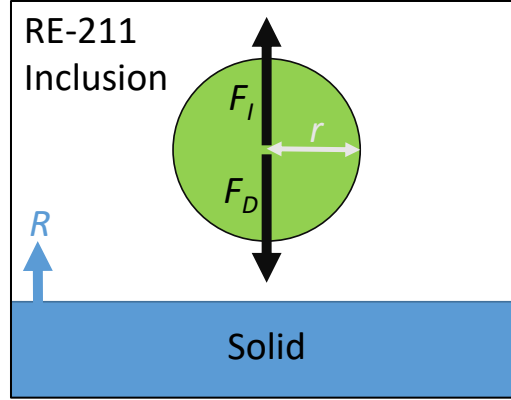


Figure 1.4: A schematic illustration of the forces acting on a particle in front of the solid/liquid interface; F_D is the drag force due to viscous flow around the particle and F_I is the force due to interfacial energy.

1.4.2 Diffusion theory

One of the models of crystal growth is based upon the solute diffusion model. In the case of the (RE)BCO system this states that the growth of a RE-123 single grain depends upon the diffusion of RE^{3+} ions which dissolve in RE-211. The dissolving of RE^{3+} ions is driven by the concentration gradient of RE^{3+} at the solidified RE-123/liquid-interface and RE-211/liquid-interface [54, 56, 57]. The diffusion of RE^{3+} ions within the melt to the solidification front is proportional to the square of the undercooling (ΔT^2). Therefore the undercooling temperature determines the growth rate of single grain samples growing according to this theory [58].

1.4.3 Ostwald ripening

The elevated maximum processing temperature and extended hold time at high temperature causes coarsening of the Y-211 particles [55]. This coarsening is undesirable as many small RE-211 particles are preferred to a small number of large RE-211 particles. The coarsening of RE-211 particles scales in proportion to the cube root of the time held at an elevated temperature, t . Coarsening can be modelled by the Ostwald ripening theory with an adapted mean radius, which accounts for the fact that the RE-211 particles are rod-like rather than spherical. This is given by:

$$r = \alpha(D_L \Gamma t)^{\frac{1}{3}} \quad (1.4)$$

where r is the modified mean radius, α is a constant, D_L is diffusivity of (RE) in the liquid and Γ is the Gibbs-Thomson coefficient, this is valid when the initial radius is small compared to the

current radius [8, 59]. The coarsening of the RE-211 particles is governed by both the diffusion of solute through the liquid and the reaction at the interface between the coarsening particle and the liquid-phase.

The addition of a small quantity of CeO₂ or Pt can reduce the coarsening of the Y-211 particles during melt processing carried out under the same conditions. With this addition, the value of $D_L \Gamma$ in the Ostwald ripening model is altered, this alters the coarsening rate of the Y-211 particles in the Y-123 melt [54].

1.4.4 Secondary nucleation

Secondary nucleation occurs when a second grain is nucleated at a point other than the seed. This produces a multi-grain sample. Multi-grain samples are undesirable as the undisturbed area over which the critical current can flow is significantly reduced in comparison to a single grain sample of the same size. Grain boundaries provide a physical barrier to the flow of superconducting current [58]. The formation of secondary grains may occur for a number of reasons, these include: aggregates of a powder present due to poor mixing of precursor powders, foreign particles entering the powder between the stages of mixing and melt growth, seed failure (if the seed is not uniform in shape or not a single grain), and nucleation occurring from another solid part of the assembly.

The likelihood of secondary grain formation can be significantly reduced by careful control of the undercooling during the growth process. Larger undercooling provides a larger driving force for nucleation. In order to reduce the likelihood of secondary nucleation it is preferable to reduce the undercooling. However, the undercooling is also responsible for the single grain growth rate. The heating profile must be carefully optimised to control the undercooling and account for the trade-off between high growth rates and reducing the likelihood of the nucleation of secondary grains to an acceptable level. The undercooling and driving force for nucleation are related by the equation for Gibbs free energy:

$$\Delta G(T) = \frac{\Delta H(T)}{T_m} \Delta T \quad (1.5)$$

where ΔG is the driving force, ΔH is the change in enthalpy, T_m is the melting temperature and ΔT is the undercooling [58].

1.5 Superconductivity theory

Superconductivity was discovered in 1911 when Kamerlingh Onnes observed that mercury lost all resistance to the flow of DC electrical current when cooled below 4.2 K [60]. Superconductivity was observed in many other metals immediately after this discovery. However, until 1930, the highest temperature at which the transition to the superconducting state (T_c) had been observed was only 9.2 K. These discoveries led to a number of theories and models to explain and predict this behaviour. These included models based upon the behaviour of electrons, the Messiner effect, penetration depth and coherence length [60]. The first non-phenomenological theory, the BCS theory, was proposed in 1957, which explained superconductivity through the formation of Cooper pairs [61]. Many further theories were subsequently proposed to explain low temperature superconductivity. In 1986 the interest in superconductivity was revived by the discovery of high temperature superconductivity by Bednorz and Muller in the $\text{La}_{2-x}\text{Sr}_x\text{CuO}_4$ compound. This was followed by further discoveries; YBCO in 1987 [62], other (RE)BCO high temperature superconductors (HTSs) and, most recently, with the discovery of MgB_2 [63] and Fe-based compounds [64].

High temperature superconductors typically have a T_c greater than 90 K, which is substantially higher than the boiling point of liquid nitrogen of 77 K. Liquid nitrogen is much easier to handle and significantly less expensive than the liquid helium required for cooling of low temperature superconductors. Therefore, from an industrial perspective, HTS materials are much more desirable for practical applications.

1.5.1 Fundamental characteristics of superconductivity

There are three fundamental characteristics associated with superconductivity [60]. One of the most well-known characteristics is the ability of a superconductor to abruptly lose all resistance to the flow of DC electrical current when cooled below T_c . The second important characteristic is the ability of a superconductor to exhibit perfect diamagnetism. Screening currents flowing near to the surface of the material prevent magnetic flux penetrating the sample, which gives superconductors

the ability to completely exclude magnetic flux from their interior, at least at relatively low field. This ability which cannot be explained by Faraday's law, is widely accepted to be due to a phase transition, determined by thermodynamics, which occurs within the material. The exclusion of magnetic flux from the interior is referred to as the Meissner effect. The final characteristic is that all superconducting materials exhibit a discontinuous increase in specific heat when the material is cooled towards T_c . This characteristic provides support for the idea that superconductivity can be associated with a thermodynamic phase change, as suggested by the Meissner effect [60].

1.5.2 Types of superconductors

So-called Type I superconductors exhibit perfect diamagnetism. They generate an induced magnetic field in a direction opposing that of an externally applied magnetic field. Screening currents flowing near the surface of the superconductor prevent magnetic flux penetrating into the sample. The superconducting ability of a material is abruptly destroyed when the strength of the applied field exceeds a critical value, H_{C1} . This behaviour is shown in Fig. 1.5. Type I superconductors are typically pure metals.

Type II superconductors behave in the same way as Type I superconductors up to a lower critical value of applied field, H_{C1} , with screening currents flowing near the surface preventing magnetic flux penetrating into the bulk. Once the magnetic field is above H_{C1} , unlike in Type I, the magnetic field is able to penetrate into the material in the form of flux vortices, producing a 'mixed state' comprising both normal and superconducting regions causing the magnetisation to decrease. Once the upper critical field, H_{C2} , is reached, superconductivity is suppressed, and the system becomes non-superconducting. The behaviour of both an ideal and a real Type II superconductor are shown in Figs. 1.5 and 1.6, respectively. The ideal curves are for a geometry with a demagnetisation factor of zero; this corresponds to an infinitely long rod orientated parallel to an applied field. Type II superconductors include some metals, and many alloys and oxides, including the (RE)BCO family of compounds. Practical Type II superconductors are typically mechanically harder than Type I superconductors and exhibit significantly higher J_c values.

1.5.3 *M-H* curves

The *M-H* curve for a typical type II superconductor at a temperature below T_c is shown in Fig. 1.5. The initial straight line region, which begins at the origin, shows that when a small magnetic field is applied, screening currents flow near the surface and these are able to completely screen the interior of the sample from the applied magnetic field. The gradient of this line is (-1) in the absence of demagnetisation effects and this region is often referred to as the Meissner state.

Above H_{c1} , in an ideal type II superconductor, the interior of the sample is no longer completely screened, and the magnetic field begins to penetrate into the sample in the form of flux vortices. The ideal case is shown as the red line in Fig. 1.5.

With increasing applied field, an increasing field is able to penetrate into the superconductor. At H_{c2} the flux is able to fully penetrate, and the material is no longer superconducting. The region between H_{c1} and H_{c2} is known as the ‘Mixed state’, and is shown in Fig. 1.5.

Practical Type-II materials such as YBCO do not behave as ideal superconductors, and they do not follow the reversible curve exhibited by an ideal superconductor due to the presence of flux pinning inclusions. The flux movement is no longer reversible due to the pinning of the flux lines by the flux pinning inclusions. This produces a hysteretic magnetisation curve rather than a reversible one. The form of the hysteretic magnetisation curve can be predicted from the critical state model. Fig. 1.6 shows the hysteresis curves modelled by both the Bean and Kim models, with the latter including the dependence of J_c on B , the magnetic flux density. As a result, the Kim model produces curves much closer in shape to real materials than the Bean model. The Bean model, on the other hand, assumes the amount of flux penetration is proportional to B .

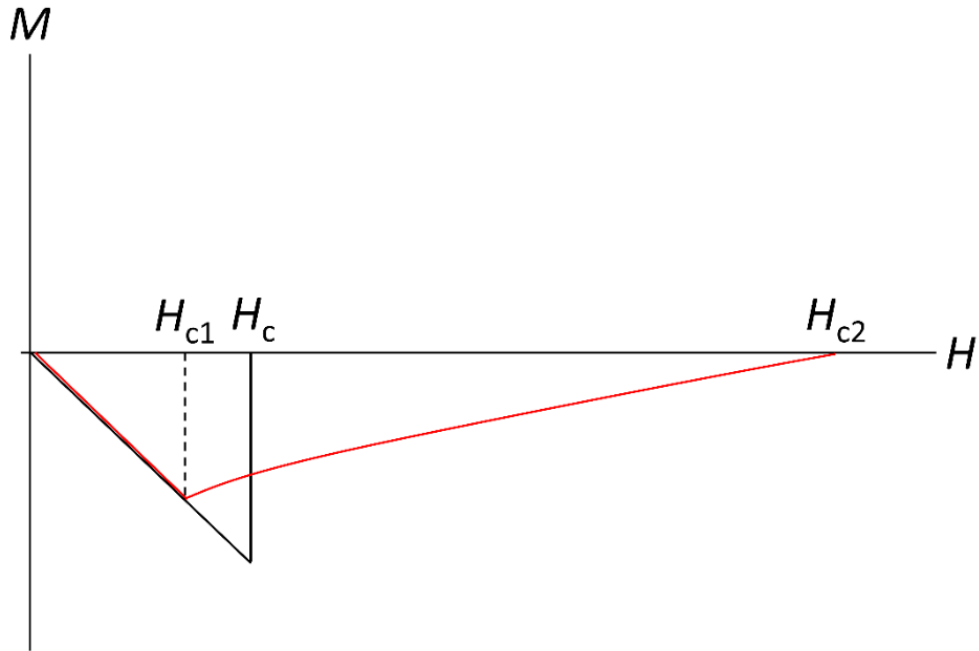


Figure 1.5: An M-H curve for a typical ideal superconductor showing: (black) an ideal Type I superconductor, (red) an ideal Type II superconductor.

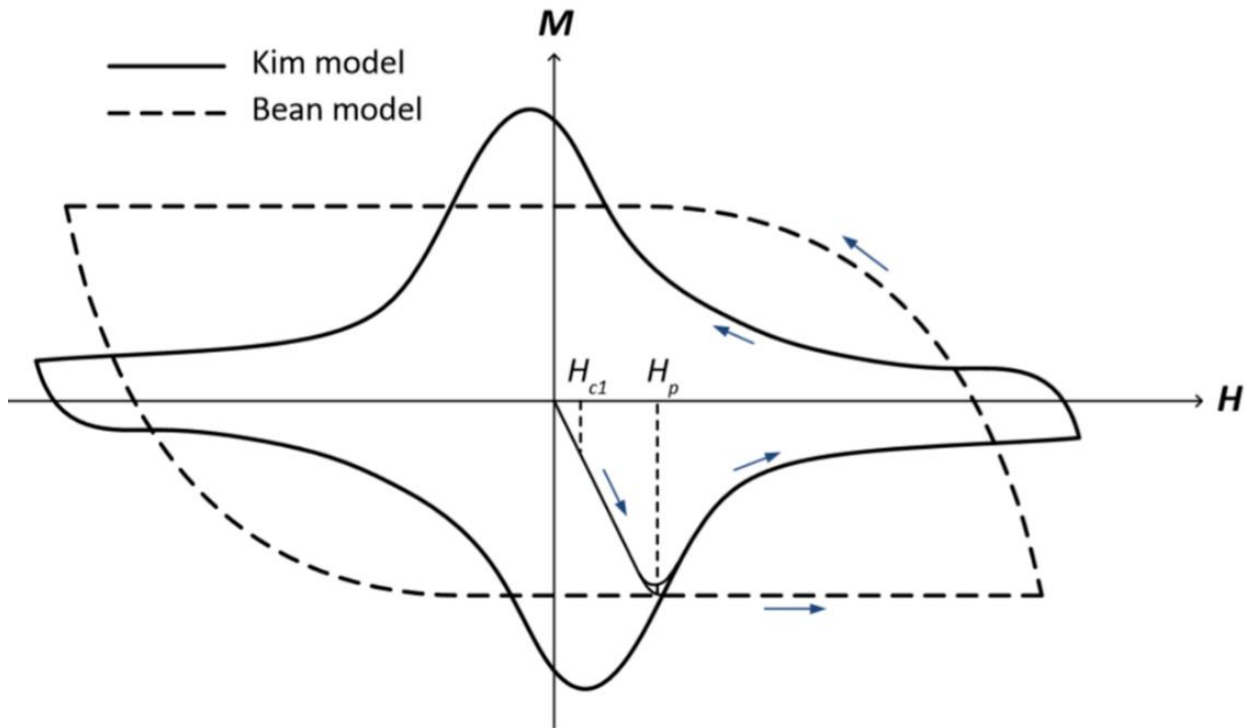


Figure 1.6: An M-H loop for practical superconducting Type II materials showing loops predicted using the Bean model and the Kim model (including the dependence of J_c on B , the magnetic flux density) [51].

1.5.4 Magnetisation

There are three main types of magnetisation; zero field cooling (ZFC), field cooling (FC) and pulse field magnetisation (PFM). In ZFC the sample is cooled in the absence of an applied field. A magnetic field is then applied on reaching a temperature below T_c . The trapped magnetic field is measured on removal of the external magnetic field.

In FC an external magnetic field is applied whilst the sample is cooled from room temperature to below T_c . The trapped magnetic field is measured on removal of the external magnetic field. In this magnetisation process, the magnetic field present within the sample before cooling is trapped within the interior of the material by the shielding currents present at the surface when the sample is cooled below T_c .

PFM is widely used for magnetisation in-situ within a device since it is simple, relatively cheap, quick and can be carried out by a compact magnetising assembly. The sample is cooled initially and then a series of intense pulses of current are sent to a pulsed field coil. The pulsed field coil generates short, intense bursts of magnetic field enabling magnetisation of the sample.

Cooling and application of an external magnetic field induces an electromotive force within the bulk. The electromotive force, in turn, induces eddy currents into the sample which circulate within the layers of the a/b -plane. The eddy currents generate a magnetic field in opposition to the field responsible for their induction. When the external magnetic field is removed the eddy currents reverse and a remanent magnetic field remains. Upon removal of the external magnetic field, the trapped field at the top and base can be measured to give an indication of the superconducting ability of the sample.

1.5.5 Transition temperature and critical current density

Both T_c and J_c are important superconducting properties used to define whether a superconducting material is suitable for practical application. T_c is the temperature below which the resistance of the sample to DC current reduces to zero. J_c is defined as the highest DC current density a superconductor is able to support whilst retaining zero resistance and is dependent upon the

presence of flux-pinning inclusions within the sample. The T_c value for a sample can be measured directly and is generally similar for every sample within the same (RE)BCO system. The value of J_c is widely estimated by the Bean Model [65] and varies significantly between samples and between sub-specimens within the same system and within the same sample. The J_c value is heavily influenced by the fabrication technique and microstructure of the material [11].

1.5.6 The Bean Model

The extended Bean model is widely used to estimate the J_c value for small, cuboid samples subjected to a magnetic field [65]. The Bean model assumes an applied field is able to penetrate into the superconductor when the field is above the lower critical field (H_{c1}) and a persistent supercurrent is able to flow when the flux lines are pinned against the Lorentz force.

The Bean model is used to describe a superconductor in the critical state, i.e. when it has a supercurrent density of either 0 or J_c everywhere within the material, implying that there are no localised magnetic dipoles present in the sample microstructure. It is assumed that there is no flux creep within the sample and that J_c value is independent of the magnetic field and so has a constant value across the entire superconductor. In general, in practical cases, the value of J_c is not independent of the magnetic field; the value of J_c usually decreases with increasing applied field. Although the assumptions of the model are not completely valid for the practical case, they are a good approximation, and so the extended Bean model is widely used to estimate the value of J_c of a specimen.

1.5.7 The effect of pinning centres

The magnitude of the achievable trapped field is determined by J_c . The larger the magnitude of the critical current, the greater the trapped field achieved. The magnitude of the critical current in (RE)BCO bulk superconductors is determined primarily by flux pinning [66]. Defects and non-superconducting inclusions of the same order of size as the fluxoid are able to act as pinning centres. The main contribution to flux pinning in the (RE)BCO system is provided by RE-211 non-superconducting inclusions [67]. The interaction of a fluxoid with a pinning centre lowers the energy of the fluxoid and so enables the fluxoid to be pinned. If movement of the fluxoid is to occur, it must gain the energy that it released upon being pinned. No flux pinning occurs in ideal,

reversible Type II superconductors, when a current density of J flows in the superconductor in the presence of a magnetic field and each of the magnetic flux quanta penetrating into the sample is subjected to a force of $F_L = J \times B$, where F , J and B are vectors. The movement of fluxoids in a direction perpendicular to the current, caused by the Lorentz force, generates a voltage of $E = v \times B$, where v is the velocity of each fluxon and E , v and B are vectors. The voltage generated creates resistance, and hence loss, within the superconductor. The effect of pinning of these fluxoids is extremely important in allowing the superconducting phenomenon to occur in practical applications of these materials [8].

Single grains that exhibit optimum superconducting properties require a uniform distribution of nano-sized defects and inclusions to be present within the superconducting matrix. These small defects and inclusions are able to provide effective flux pinning. To ensure the greatest effectiveness for flux pinning, the size of the pinning centres should be of the order of size of the coherence length [68, 69]. The coherence length in the YBCO system is of the order of nanometres [70, 71], whereas the Y-211 inclusions typically have a size of the order of micrometres. Although the size of the inclusions in the YBCO system are three orders of magnitude larger than the coherence length, these inclusions are still able to enhance the flux pinning, and hence improve the magnitude of the J_c value [72]. The pinning occurs in these systems at the interface of the Y-211 inclusions, and smaller pinning centres have a higher effectiveness. Hence, for optimum pinning the Y-211 inclusions should be engineered to be as small as possible [67]. The J_c value has been reported to increase with the V_{211}/d_{211} ratio, where V_{211} is the volume fraction of Y-211 and d_{211} is the average size of the Y-211 particles [72, 73]. The Y-211 inclusions provide a major contribution to flux pinning in the YBCO system, so the uniformity and magnitude of critical current depends on the distribution and density of Y-211 within the superconducting Y-123 matrix. A greater uniformity in J_c values is produced by a more uniform distribution of Y-211 particles and a larger magnitude of J_c value is produced by a higher density of small Y-211 inclusions. There is a limit to the effectiveness of increasing the density of Y-211 inclusions on the increase in magnitude of J_c , since increasing the volume fraction of Y-211 decreases the volume fraction of superconducting Y-123 matrix within which the superconducting current is able to flow.

The growth process is highly influential in determining the superconducting properties of a bulk superconductor. The composition of the sample, particle size within the precursor powder and the variables modified within the growth process determine the microstructure of the sample. The flux pinning ability of each sample depends, in turn, upon the microstructure and hence this determines the achievable value of J_c [41, 54].

1.5.8 Superconducting properties of (RE)BCO

Table 1.1 gives the typical transition temperature and critical current density for a range of common (RE)BCO materials. Although both the T_c and J_c values are lower in the YBCO system than in the other systems listed in the table, YBCO is a very useful material and in many applications these lower values are not limiting. In addition, YBCO precursor powders are less expensive and more widely available from suppliers. This system has also been more widely researched and so more detailed information is available on this system.

Material	T_c (K)	$J_c(0)$ at 77 K (kA cm ⁻²)
NdBa ₂ Cu ₃ O ₇	95.0	40-50
SmBa ₂ Cu ₃ O ₇	93.5	40-50
GdBa ₂ Cu ₃ O ₇	92.5	50-60
YBa ₂ Cu ₃ O ₇	92.0	20-30

Table 1.1: A table showing the typical T_c and J_c values of the common (RE)BCO bulk superconducting materials [45].

1.6 A review of the developments in processing of (RE)BCO

Superconducting (RE)BCO materials were first discovered in 1987 by Bednorz and Müller [74]. Initially these materials were fabricated in polycrystalline form, and these exhibited relatively poor superconducting properties due to their granular structure and small grain size [9, 10, 75-77]. The need to enhance the J_c value of these materials was not realised immediately. The J_c value is strongly microstructure dependent, not an intrinsic material property, and so while granularity was a problem there was no focus on improving the value of J_c . In addition, a number of features including the 2D structure and the short coherence length of the material caused major problems in the enhancement of the J_c value.

The development and optimisation of the growth process and the development of a basic understanding of the solidification and crystallisation mechanisms occurred in parallel when the need to fabricate large grains of (RE)BCO was understood. A good understanding of the solidification process and the optimisation of the growth process are both interdependent and important in achieving an effective growth process. There are a large number of considerations when studying the growth process. Some of these are similar to those of the solidification of metals, whereas others are similar to those of oxides. However, these considerations are further complicated by the fact that (RE)BCO is a multi-element system [8].

This detailed study of the growth process has enabled the development of a number of models for the growth of (RE)BCO single grains, as described in detail in section 1.4. The information has enabled the development and optimisation of a number of melt growth techniques to enable the growth of large single grains.

Practical applications of bulk superconductors require large single grains with high and uniform J_c values and these materials must be able to be fabricated reliably. A number of melt processing techniques have been developed and optimised to produce large single grains [2, 5, 8, 13, 76, 78, 79]. The most popular and simplest melt processing techniques are top seeded melt growth and infiltration growth; as described in detail in section 1.2.

The melt growth techniques have been optimised to enhance the J_c values of the resultant material by optimising the size and distribution of the intrinsic (RE)-211 inclusions. The heating profile can be optimised to achieve this, although this is rather limited by the growth process [76, 80]. Both the size and distribution of these (RE)-211 inclusions can be further optimised in samples grown by TSMG. An excess of (RE)-211 powder was added to the precursor powder, and this increased the amount of (RE)-211 inclusions present within the microstructure of the as-processed single grain and hence the number of flux pinning inclusions [67]. The addition of a small quantity of elements or compounds such as Pt [81-83], BaSnO₃ [84] or CeO₂ [19, 83, 85] are able to alter both the size and shape of these inclusions. Another technique investigated to increase flux pinning was irradiation, whereby the internal structure is damaged slightly due to the irradiation and this damage formed pinning centres [86]. The addition of Pt or CeO₂ is widely used to control the size

of the (RE)-211 inclusions and increase the value of J_c as it is effective and it does not significantly increase the complexity of the growth process.

The reliability of the growth process is important in addition to the need to produce single grains with a high J_c value. The growth of a single large grain is difficult as there are a number of competing factors. The seeding process is vital to the success of the growth of a single grain. Initially a hot-seeding process was used, which involved heating the sample to enable decomposition, and then cooling to just above the peritectic temperature and applying a seed while the sample was in a molten state [87]. This was complex, and often failed, but enabled self-seeding (eg. using an NdBCO seed to seed an NdBCO sample [88]). The use of a self-seed prevented complications due to lattice mis-match. A simpler method for seeding is the cold-seeding method. This requires a less complex furnace arrangement, however, due to the high temperatures involved in the heating process, this seed required a significantly higher melting temperature than the precursor powder, and so prevented the use of self-seeding [87]. In addition there are further complexities since the seeds did not have the same lattice structure because they required a significantly higher melting temperature. Additionally, the long period of heating enabled the diffusion of pollutants between the seed and precursor powder which, in turn, lowered the melting temperature of the seed. The reduction in the melting temperature of the seed was significant in the case of silver diffusion from the precursor powder and often resulted in the melting and failure of the seed. However, two approaches have been developed to enable cold seeding. Materials were developed with high melting temperatures that had similar lattice structures relative to the known (RE)BCO compounds of the samples to be grown. The latest development was that of a generic, multi-purpose seed with a very high melting temperature in relation to the known (RE)BCO compounds [87]. In addition, the use of a buffer pellet has been developed and employed successfully. The buffer pellet effectively insulates the seed from pollutants within the precursor powder whilst also reducing complications due to the lattice mis-match between the seed and sample [89-94]. The use of buffer pellets is described in more detail in Chapter 2. Both of these techniques enable more reliable growth and the use of a simpler seeding technique in the TSMG process.

A significant amount of research has been carried out to glean a greater understanding of the growth process and to enable optimisation of the growth of large single grains of (RE)BCO. At this time the growth process has been well optimised. It generally results in the reliable growth of large single grains of (RE)BCO with high J_c values and a reasonably uniform distribution of J_c values. One of the current limitations on the use of (RE)BCO materials in practical applications is their mechanical properties. On magnetisation, samples experience large Lorentz forces, which, if sufficiently large, cause fatal cracking. This limits the maximum magnetisation, and hence the mechanical properties limit the achievable superconducting properties [17]. A limited amount of research has investigated improving the mechanical properties of (RE)BCO and, as a result, silver is now commonly introduced to the bulk microstructure of GdBCO and SmBCO to enable significant improvement in the mechanical properties of these single grains [40, 41]. However, only a limited amount of research into improving the mechanical properties of YBCO bulk superconductors has been undertaken due to the high complexity of the growth of YBCO when mixed with other elements.

1.7 An outline of the work

The overall aim of this work was to improve the mechanical properties of YBCO bulk superconductors without causing a significant detrimental effect on the superconducting properties of the material. It is widely acknowledged that large single grains of GdBCO and SmBCO fabricated with silver can be successfully batch processed to produce large single grains with superior mechanical properties to GdBCO or SmBCO grown by standard TSMG. However, the successful, reliable growth of large single grains of YBCO-Ag by TSMG is significantly more difficult and had not been documented. YBCO has a significantly lower peritectic temperature than that of GdBCO or SmBCO, which is then reduced further by addition of silver to the melt, which makes the growth of single grains of YBCO-Ag more complex. This work approached the successful and reliable single grain growth of YBCO-Ag in a number of incremental stages.

The first stage investigated the use of additional liquid-phase in a novel recycling process for the multi-grain samples of YBCO, GdBCO-Ag and SmBCO-Ag. It is understood that one of the reasons the recycling process was very reliable in successfully producing large single grains is due to the addition of liquid-phase, which promotes re-growth from the failed samples and prevents

sub-grains forming from the bottom of the sample. In addition, the superconducting properties of the recycled single grains were good. The properties of these recycled grains were investigated in detail to gain understanding as to why the processing had a high success rate in the hope this could be used to successfully and reliably grow single grains of YBCO-Ag.

In a second stage, the provision of additional liquid-phase was trialled in the primary growth of YBCO by TSMG in order to investigate its effect on the primary growth process. This resulted in a higher reliability of the growth of large single grains. In addition, these single-grains had superconducting properties of magnitude comparable to, or higher than, those of YBCO grown by standard TSMG. They also retained the improvement in the uniformity of the superconducting properties observed in the recycled samples.

The increase in reliability, and in the tolerance to silver-rich agglomerates attributed to the provision of additional liquid-phase in the TSMG process, suggested this technique may enable the successful growth of single grains of YBCO-Ag. Initially the growth rate of YBCO-Ag was investigated for the first time. A suitable heating profile is essential for TSMG and this provided data to enable the derivation of a suitable heating profile. This also generated the first published data on the growth rate of the YBCO-Ag system. Large single grains of YBCO-Ag were then successfully and reliably grown using heating profiles derived from the growth rate models.

The adaptation of the TSMG growth process and the growth rate data enabled the reliable growth of YBCO-Ag to be achieved. The development of a reliable growth process for YBCO-Ag enabled a large number of large single grains to be grown, and the superconducting properties to be measured. In addition, this development enabled the mechanical properties of YBCO-Ag to be analysed in detail for the first time.

2 Experimental methods

In this work a number of single grains of (RE)BCO and (RE)BCO-Ag were grown by variations of the TSMG technique. The superconducting properties of these single grains were measured and their microstructure and compositions were studied. In addition, the mechanical properties of YBCO-Ag were studied using a three-point bend test.

2.1 Top seeded melt growth

The assembly for fabrication by TSMG consists of a precursor powder pellet supported by ZrO₂ rods. These rods are stabilised for use with (RE)BCO to reduce the likelihood of any points of physical contact acting as nucleation points. Materials such as single grain MgO are more suitable for providing a stabilisation layer as they are more stable and so are less likely to act as nucleation points. However, this material is very expensive so is not widely used. Seeding of the melt growth process is provided by a small single grain seed. The seed must have a lattice structure similar to that of the (RE)BCO single grain lattice and a higher melting temperature than the precursor powder [87]. The type of seed used with each of the systems in this work are given in Table 2.1. A buffer pellet is often placed between the seed and the precursor powder pellet to reduce the diffusion of contaminants between the seed and precursor pellet. The buffer pellet improves the likelihood of successful single grain growth and improves the properties of the grain in the region directly below the seed [89-94].

In this work the buffer pellet is pressed uniaxially from 0.15 g of precursor powder to a diameter of 5 mm. The buffer pellet improves the reliability of seeding and successful single grain growth [89-94]. The buffer pellet is able to provide a barrier to diffusion of impurities between the seed and the melt [91]. Any impurities are captured within the buffer pellet rather than moving into either the seed or the main precursor powder pellet. The buffer pellet is also able to reduce the lattice mismatch between the seed crystal lattice structure and the growing (RE)BCO single grain, thus increasing the likelihood of successful single grain growth [91, 92]. The composition of the buffer pellet is the same as that of the standard precursor powder for an additive-free sample, ie. (RE)-123 and (RE)-211 powders in the same ratio as the precursor powder but without Ag or Pt.

System	Seed material
YBCO	NdBCO
YBCO-Ag	Thin film seed
GdBCO-Ag	NdBCO-MgO generic seed [87]
SmBCO-Ag	NdBCO-MgO generic seed [87]

Table 2.1: The seed material used for each system.

Precursor powder was mixed from the constituent powders for 2 h using a mechanical pestle and mortar. This ensured the powder was thoroughly mixed and ground to the appropriate size. The standard precursor powder composition for each system is summarised in Table 2.2. The precursor powder was prepared from 99.9 % purity powders, high purity is essential in order to reduce the likelihood of impurities reducing the likelihood of successful single grain growth.

System	Precursor powder composition
YBCO (Chapter 3 only)	70 g $\text{YBa}_2\text{Cu}_3\text{O}_7$ + 30 g Y_2BaCuO_5 + 0.5 g CeO_2
YBCO	75 g $\text{YBa}_2\text{Cu}_3\text{O}_7$ + 25 g Y_2BaCuO_5 + 0.5 g CeO_2
YBCO-Ag	75 g $\text{YBa}_2\text{Cu}_3\text{O}_7$ + 25 g Y_2BaCuO_5 + 0.5 g CeO_2 + 10 g Ag_2O
GdBCO-Ag	75 g $\text{GdBa}_2\text{Cu}_3\text{O}_7$ + 25 g $\text{Gd}_2\text{BaCuO}_5$ + 1 g Pt + 1 g BaO_2 + 15 g Ag_2O
SmBCO-Ag	75 g $\text{SmBa}_2\text{Cu}_3\text{O}_7$ + 25 g $\text{Sm}_2\text{BaCuO}_5$ + 1 g CeO_2 + 2 g BaO_2 + 10 g Ag_2O

Table 2.2: The composition of the precursor powder used for each system.

The liquid-phase-rich powder, which provides additional liquid during the growth process, was prepared by mixing the constituent powders for 3 h in a Turbulator. The preferred liquid-phase-rich powder has the composition Yb_2O_3 : $\text{Ba}_3\text{Cu}_5\text{O}_8$: BaO_2 in a molar ratio of 5.0 : 5.6 : 1.0 and was subsequently calcined once at 850 °C for 5 h.

Sintering of the liquid-phase-rich powder changes the composition. It is often important to know which phases are likely to be responsible for the behaviour of a powder during the TSMG process

so X-ray powder diffraction (XRD) was used to determine the composition of a number of powders.

XRD is a technique used to identify the phases present within a crystalline material, usually in powder form. XRD analysis uses an instrument consisting of an X-ray tube, a sample holder and an X-ray detector. A small quantity of powder is loaded into a holder and the sample and detector are rotated through a given range of angles. The intensity of the reflected X-rays are recorded at angular intervals. The technique is based upon the Bragg equation, below, which relates the wavelength of electromagnetic radiation to the diffraction angle and the lattice spacing within the sample:

$$n\lambda = 2d \sin \theta \quad (2.1)$$

where n is an integer, λ is the wavelength of the X-ray, d is the spacing between atom layers and θ is the angle of incidence of the X-ray.

A crystalline sample acts as a three-dimensional diffraction grating. When the spacing of planes within the lattice becomes similar to the wavelength of the X-rays constructive interference occurs, thus producing a high intensity of reflected X-rays. The recorded reflected X-ray intensity at each angle can be converted into the d -spacing of the crystal lattice. The d -spacing is unique for every crystalline material and for every phase of the material. This technique enables the material and phases present in a powder sample to be identified using reference data for d -spacing of crystalline materials.

The current and voltage settings used were 20 mA and 35 kV, respectively. Measurements were taken within the range of 20° to 80° rotation. The analysis of powders of known composition provided reference spectra to enable the relevant peaks in the powders studied to be identified.

In addition to determining the powder's composition, for the TSMG process it is critical to know the peritectic temperature of the powder. Differential thermal analysis (DTA) is a technique used to determine phase transformations within a sample, including glass transitions, crystallisation,

melting and sublimation. DTA analysis uses a sample holder, thermocouples, a furnace, temperature programmer, inert sample material such as Al_2O_3 and a recording system. Two thermocouples are connected via a voltmeter; one thermocouple is placed in a sample of the material of interest whilst the other is placed in the inert reference material. During heating the sample of interest may undergo phase changes. When a phase transition occurs, the temperature of the inert material will increase while the temperature of the material undergoing the phase change will not rise as heat will be incorporated as latent heat. The thermocouples are connected through a voltmeter and so this will produce a sharp deflection in the voltmeter reading. Therefore, a phase change can be identified by a sudden sharp peak on the graph and the corresponding temperature of this phase change can be determined. In the TSMG fabrication process knowledge of the peritectic temperature of the precursor powder used, as well as the phase transition temperatures of powders used, alongside the liquid-rich source, are fundamental to developing an effective process.

DTA was undertaken on a range of precursor and liquid-phase-rich powders. DTA was carried out without additional gas flow. This data was used to identify the peritectic temperature of each of the powders studied.

Once the composition and peritectic temperature of these powders was known, samples were pressed and assembled. The assembly used for conventional TSMG is shown schematically in Fig. 2.1 a. The assembly used for recycling used a failed sample, this has had the top and bottom surface ground flat and parallel to expose clean, new surfaces, in the place of the precursor powder and used an additional pressed pellet of liquid-phase-rich powder above a layer of Yb_2O_3 powder, as shown in Fig. 2.1 b. The assembly used for growth of LR YBCO and YBCO-Ag has a layer of the additional liquid-phase-rich powder layer pressed into the same pellet as the precursor powder pellet, as shown in Figs. 2.1 c and 2.1 d, respectively.

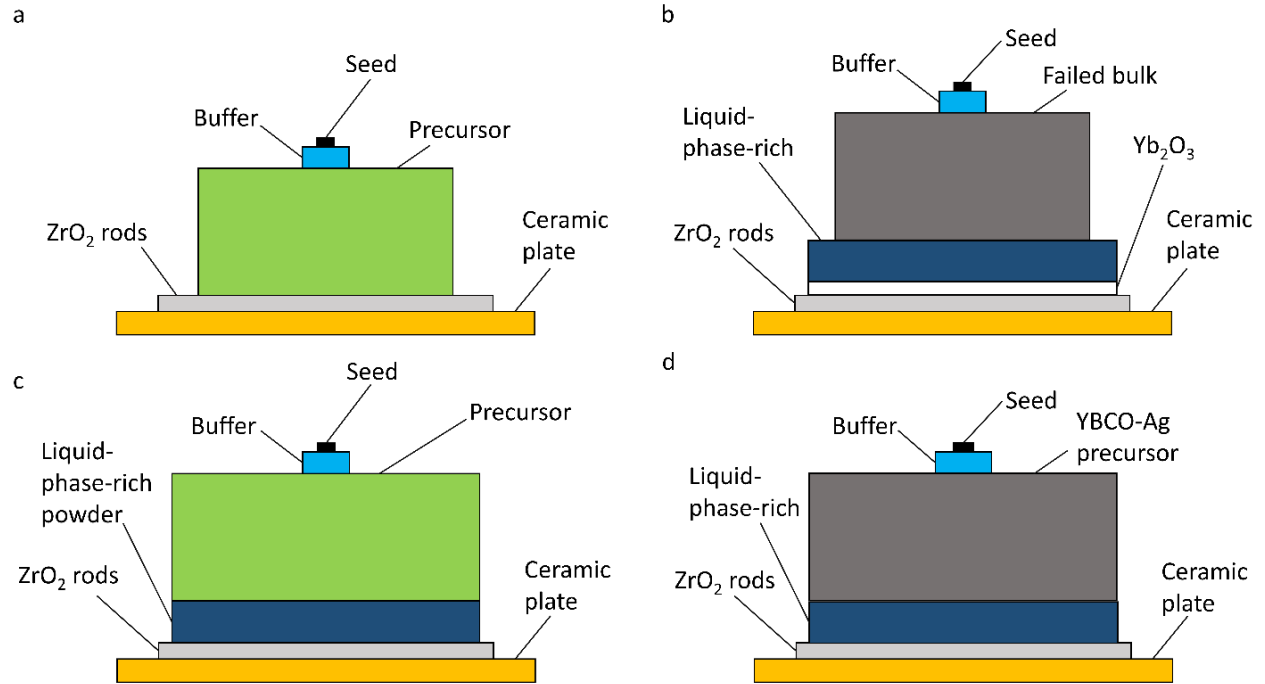


Figure 2.1: The assembly used for: a) conventional TSMG, and b) the recycling process, c) LR YBCO, d) YBCO-Ag.

The sample and seed assembly were heated and held above the peritectic decomposition temperature (T_p) of the target (RE)-123 phase in a box furnace under atmospheric pressure and gas composition. The powder decomposed into a secondary (RE)-211 solid phase and a residual Ba-Cu-O liquid-phase, a minimum of approximately 50 % of the sample mass is always solid, hence a mould is not required during melting. The melt is first cooled to T_{g1} to provide rapid undercooling and to generate a supersaturated molten state with respect to the equilibrium state. Rapid undercooling reduces the likelihood of the growth of (RE)-211 precipitates, which originate from the additional (RE)-211 in the precursor powder. Therefore, this encourages a dispersion of fine (RE)-211 particles in the fully processed bulk superconductor. The undercooling, $\Delta T = T_p - T$, is further limited to enable solidification under controlled thermal conditions. The controlled undercooling ensures that the seed acts as a single nucleation point during the melt process. Controlled undercooling takes place until the entire sample is solidified at T_{g2} , from there it is rapidly cooled to room temperature. This provides a single grain (RE)-123 matrix with the desired crystallographic orientation containing a distribution of discrete (RE)-211 phase inclusions [5, 95]. The temperature profile required during solidification to produce a single grain is specific to a

particular system and a given size of sample, a schematic illustration is shown in Fig. 2.2. A single grain is shown in Fig. 2.3.

During the growth process the buffer pellet melts in the same way as the main precursor powder pellet. The single grain grows from the seed outwards and downwards through the buffer pellet and then the single grain continues to grow through the larger pressed pellet. The resulting single grain and the buffer pellet have the same crystallographic orientation.

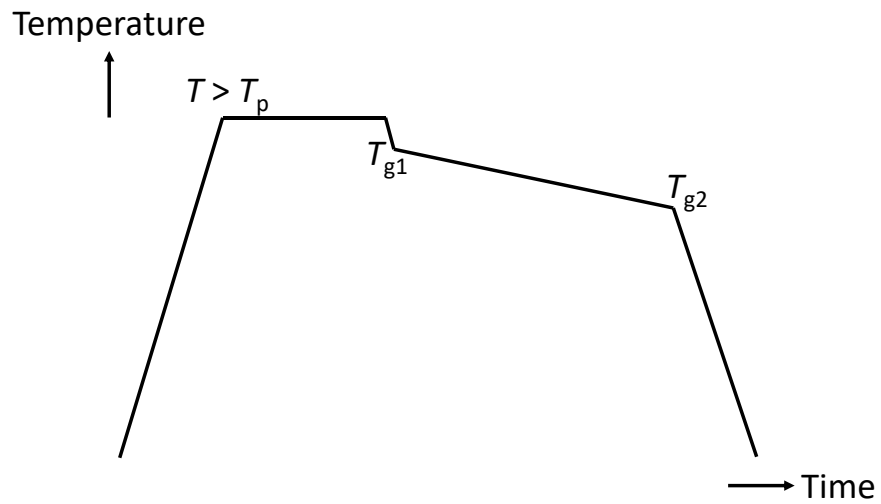


Figure 2.2: A schematic illustration of a typical heating profile used in TSMG.



Figure 2.3: A single grain of (RE)BCO.

The melt growth process described above produces large, single grain samples of a RE-123 matrix with embedded RE-211 inclusions. Directly after melt processing, the RE-123 matrix is in the non-

superconducting tetragonal phase, which must undergo a transformation to the orthorhombic phase to become superconducting. The oxygenation process involves heating the single grain in an oxygen-rich environment. Oxygen is able to diffuse into the sample and this is significantly enhanced by the presence of micro-cracks parallel to the a/b -plane and the c -plane [96]. The phase transition occurs when the oxygen content in $(RE)Ba_2Cu_3O_{7-\delta}$ (RE-123) exceeds approximately 6.5 (when $7-\delta > 6.5$) [59].

All samples successfully grown as single grains were oxygenated in an oxygen-rich environment in a tube furnace. The oxygenation heating profiles for each system are given in Table 2.3.

System	Heating
YBCO	450 °C for 10 days
YBCO-Ag	450 °C for 10 days
GdBCO-Ag	400 °C for 10 days
SmBCO-Ag	360 °C for 10 days

Table 2.3: The heating profiles used for the oxygenation process.

The actual temperature recorded within a box furnace may be offset from the temperature values input into the controller. In order for work on the growth process and derivation of optimised heating profiles to be useful in academia and industry, the actual temperatures experienced by a sample in the furnace must be known. A standard heating profile for 25 mm diameter YBCO samples was input into the controller of the furnace. A thermocouple placed close to the sample was used to record the heating profile experienced within the processing zone. This was repeated for two full heating profiles and the data were used to estimate the temperature offset of the furnace.

The thermocouple recorded the air temperature close to the surface of the assembly. This method of temperature measurement does not provide data on the temperature distribution within the sample itself. The ability to record the temperature distribution and release of latent heat in the assembly itself would provide a greater insight as to how the size of the samples will change the heating profile required for successful growth of a single grain.

The plots of the heating profile input to the controller and the measured furnace temperature profile are shown in Fig. 2.4 for two separate cycles. The furnace offset at the maximum temperature within the heating profile was approximately 17 °C higher than the temperature input. Therefore, the temperature input to the controller should be 17 °C lower than the actual temperature required in the furnace.

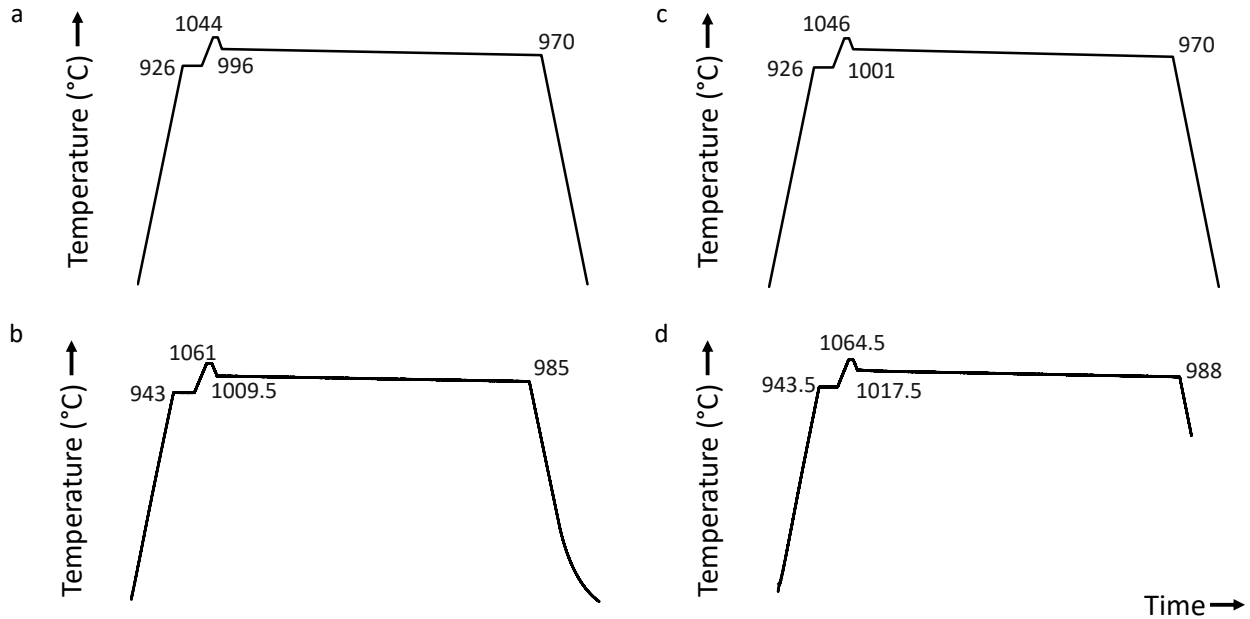


Figure 2.4: Heating profiles of a) JY-01 input to the furnace, b) JY-01 measured at the centre of the furnace, c) JY-02 input to the furnace and d) JY-02 measured at the centre of the furnace.

2.2 Trapped field measurement

In order to measure the trapped field, any excess, unreacted liquid-phase-rich powder or Yb_2O_3 stabilising layer was cut from the base of each sample. The seed and buffer pellet was cut from the top of the sample, then the top and base of each sample was polished flat and parallel.

Each sample was field cooled. A magnetic field of 1.4 T was applied using a DC electromagnet and then liquid nitrogen was used to cool the sample to 77 K. Once the sample had been cooled, the field was removed and the maximum trapped field at the top and base of the sample was recorded using a Hall sensor at a distance of 0.5 mm from the surface.

The trapped field profile at the top and base of each sample was measured using a rotating array of 20 Hall probes. The temperature of the sample was maintained at 77 K for the duration of the measurements. The height of the array of Hall probes is adjusted on a per-sample basis after loading, so the entire array of probes are located at a distance of 1.0 ± 0.5 mm from the surface. It is important to ensure the Hall probes on the array are not in direct contact with the surface as they are required to rotate, so the values recorded using the Hall probe array were used to study the lines of contour of the trapped field rather than the absolute values. The maximum value recorded using the Hall probe array is typically between 0.1 T to 0.3 T lower than the maximum value recorded using the single hand-held Hall probe due to the increase in distance between the sample and the probe surface.

2.3 Superconducting quantum interference device measurements

The measurement of magnetic moment using a superconducting quantum interference device (SQUID) magnetometer is carried out indirectly from measurements of current and voltage. The sample is moved through superconducting detection coils which are at the centre of the magnet but outside the sample chamber. As the sample is moved through the coils, the magnetic moment produced by the sample induces an electric current in the detection coils. These detection coils, along with the connecting coils and SQUID input coil, form a closed superconducting loop. A change of flux in the detection coils produces a change in the persistence current in the detection coils. The change in persistence current in the detection coils is proportional to the change in the magnetic flux. The variation in this current produces a variation in the SQUID output voltage, which is proportional to the magnetic moment of the sample.

Small cuboids cut from bulk samples can be analysed using a SQUID magnetometer to measure the T_c and to define the value of J_c of each small specimen. Samples are zero field cooled to 77 K in the SQUID before a magnetic field is applied in a direction parallel to the c -axis of the sample. A temperature sweep at a constant field of 1.6 kAm^{-1} (i.e. much lower than H_{C1}) is applied to determine the transition temperature of the specimen. This is followed by a field sweep at a constant temperature of 77 K (below the T_c value of the sample) to produce an M - H hysteresis loop to enable estimation of the value of J_c for each sub-specimen. In both cases the magnetic moment

is measured. The range of temperature and field used for the sweeps are generally well-established from previous research.

The extended Bean model has been used to estimate the J_c value for each small sample measured. The extended Bean model is given by:

$$J_c = \frac{20 \times 10^{-5} \Delta m}{a \left(1 - \frac{a}{3b}\right) abc} \quad (2.3)$$

in Am^{-2} and where Δm is the difference in magnetic moment derived from the M - H hysteresis loop measured in emu, a is the shortest side length in the a/b -plane, b is the longest side length in the a/b -plane and c is the dimension in the c -direction all measured in cm [97]. An example of a plot of J_c -field is shown in Fig. 2.5, all other plots of this type are given in the appendix.

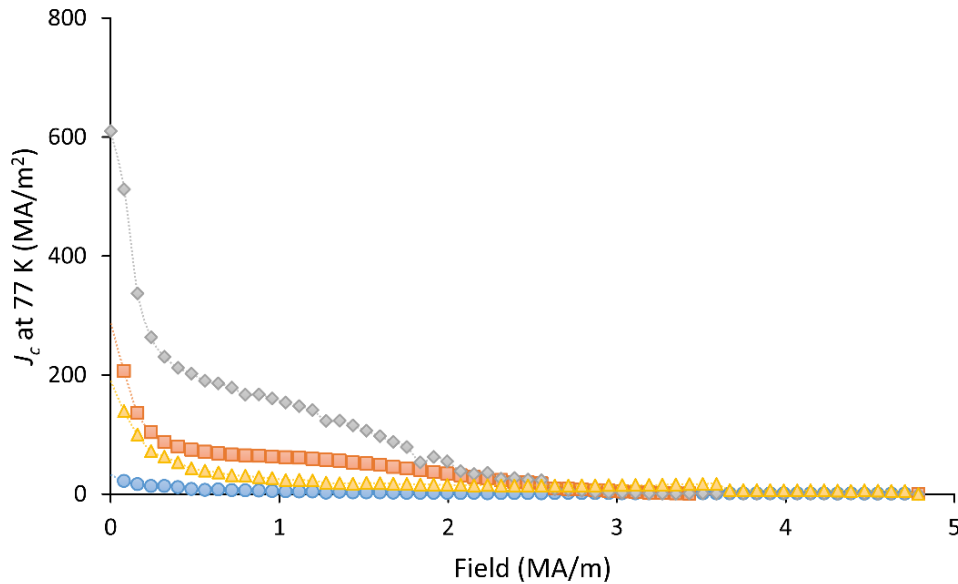


Figure 2.5: Plots of the variation in J_c value with field at a constant temperature of 77 K for sub-specimens from within one sample.

The value of T_c can be determined as the temperature at which the resistance decreases to zero on a plot of temperature against magnetic moment. In this work the T_c value has been determined using the data from the temperature sweep as the lowest temperature at which the magnetic moment becomes zero. A further characterisation of the quality of the superconductor can be

calculated from this graph, the so-called ΔT_{90} value. ΔT_{90} is the temperature range over which the magnetic moment reduces to 90 % of its original value. In this work 100 % of the magnetic moment was determined as the maximum magnitude magnetic moment in the temperature sweep data. Superconductors of high quality have a small value of ΔT_{90} which signals a narrow temperature range over which the transition to the superconducting state occurs. In plots of the magnetic moment evolution during a temperature sweep, the magnetic moment is normalised by dividing the dataset for the sub-specimen by the maximum magnetic moment the sub-specimen experiences. An example plot of magnetic moment evolution during a temperature sweep for a number of sub-specimens from one sample is shown in Fig. 2.6, all other plots are shown in the appendix.

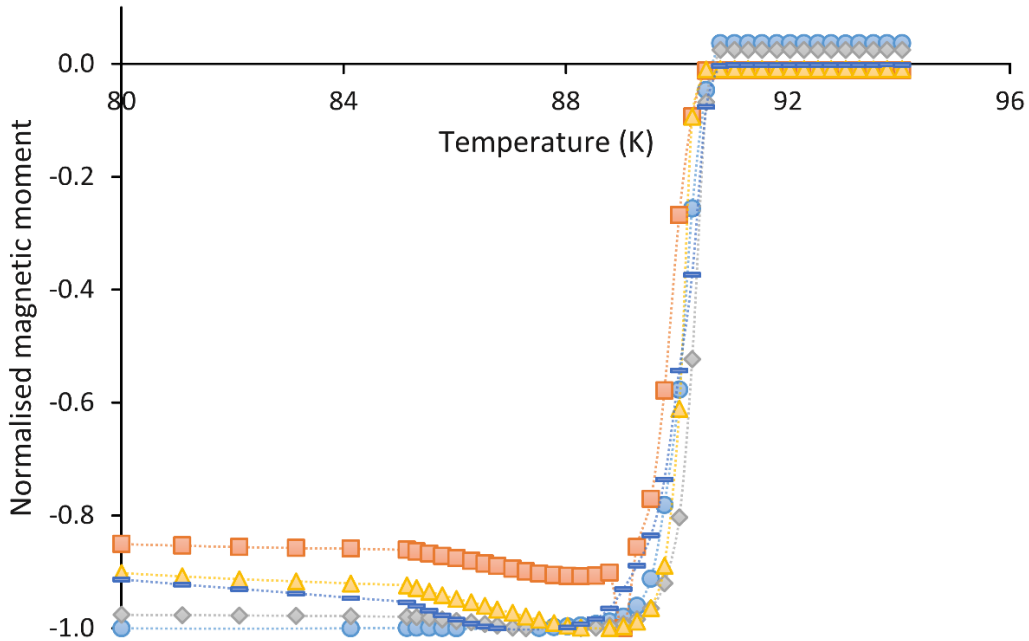


Figure 2.6: Plots of the variation in normalised magnetic moment with temperature for sub-specimens from within one sample.

The samples tested using a SQUID magnetometer must be small. In this work each sample was cut in half to expose a rectangular cross-section. A slice approximately 1.2 mm thick was cut from one of the halves from the region directly below the seed. This was then further cut into cuboids with approximate dimensions 1.5 mm x 2.0 mm x 1.2 mm. The orientation of the dimensions are shown in Fig. 2.7. The sub-specimen is orientated with the c -axis mounted parallel to the magnetic field in all measurements.

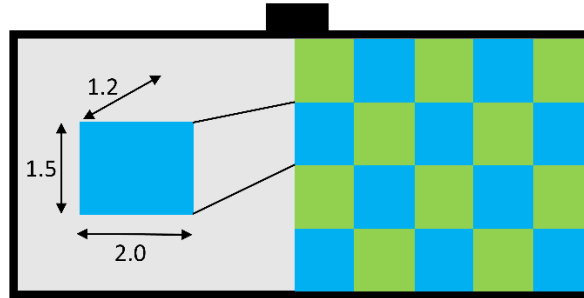


Figure 2.7: Schematic showing the orientation of the approximate dimensions of the pieces cut for analysis in the SQUID, dimensions in mm.

2.4 Microscopy

Each sample to be imaged was cut in half to expose a rectangular cross section. The cross-section of one of the cut halves was polished using progressively finer silicon carbide paper followed by a range of finer diamond paste. Each sample was studied under a Nikon Eclipse ME600 optical microscope (Nikon, Tokyo, Japan) with a Motic Multicam Pro 282A camera (Motic, Hong Kong, China) at a variety of magnifications including 50x, 100x, 200x, 500x and 1000x, in order to identify the microstructural features present. The Y-211 particles could be best seen at magnifications of 200x or above. At 1000x magnification it was difficult to obtain a clear image, so 500x magnification was chosen to systematically study the distribution of Y-211 inclusions.

Only one half of the a/b -axis was imaged as it was assumed that, since the sample is symmetric and nucleated from the centre, the microstructure will be similarly symmetric. A schematic illustration of the axes is shown in Fig. 2.8.

In addition to optical microscopy, scanning electron microscopy (SEM) can be used to produce a higher magnification image of a conducting sample. A voltage of chosen magnitude is applied to enable a focused beam of electrons to be accelerated towards the sample surface. Reflection of the beam of electrons from the sample surface and from layers a short distance below the surface produce back scattered electrons. Secondary electrons are produced by the ejection of electrons from bonds and bands within atoms at the surface of the sample. Images of the surface and the layer just beneath can be produced by collection of backscattered or secondary electrons produced by the incident beam.

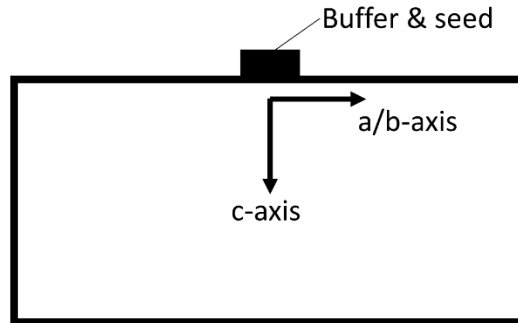


Figure 2.8: Schematic of the axes imaged using the optical microscope.

Samples imaged using SEM must be conducting to enable electrons from the incident beam to escape to earth to prevent a build-up of static charge on the sample's surface. A build-up of static charge will cause the incoming beam of electrons to be deflected, thus causing distortion of the image produced. The sample must also be contained inside a vacuum chamber, since molecules within the air will cause deflection of the electron beam. (RE)BCO samples, as analysed in this investigation, do not conduct at room temperature and are therefore unable to provide a path for the electrons from the incident beam to be conducted away to earth. To reduce the likelihood of charge build-up on the surface of the YBCO samples, and thus to reduce the distortion produced, a single line of silver conducting paint was painted on three sides of each sample to allow the electrons to be conducted away to earth.

Scanning electron microscopy was used on a number of occasions because it was able to provide greater magnification and greater resolution than the optical microscope. The samples were polished, then imaged using a Hitachi S-3400 SEM at 2000x magnification. An acceleration voltage of 25 kV was chosen along with backscattered electron mode because it produced a reasonable image of all three systems.

2.5 Energy dispersive X-ray spectroscopy

Energy dispersive X-ray spectroscopy (EDX) can be used to analyse the composition of a sample. A beam of high energy charged particles, usually electrons or protons, are fired at the surface of the sample and the wavelength of the X-rays emitted is measured. The high energy beam interacts with a stationary atom at the surface of the sample. At rest each atom contains electrons in discrete energy levels bound to the nucleus. Upon incidence of the high energy beam, an electron in an

inner electron shell may become excited and be ejected from the shell creating an electron hole. This electron hole may be filled by an electron from a higher energy shell. There will be an associated change in energy due to the movement of an electron from a higher energy shell to a lower energy shell and this difference in energy may be released in the form of an X-ray.

Each element has a unique atomic structure and so produces a unique set of peaks on its X-ray emission spectrum. This allows the elements present to be identified from the energies of the emitted X-rays, provided the difference between the energies of the emitted X-rays are sufficiently large. The energy of the accelerated electrons can be varied by changing the acceleration voltage applied. The appropriate acceleration voltage is determined from experience or preliminary investigation. The quantity of each element present can be found from the number of X-rays of the characteristic energy produced in a given time frame.

EDX analysis was used on the Hitachi S-3400 to measure the average composition of some small areas and over an area of approximately $40\ \mu\text{m} \times 40\ \mu\text{m}$ at each location imaged using the SEM. This setup has a spatial resolution on the order of 1 to $5\ \mu\text{m}$, this is therefore suitable for measurement of the average composition of the large area, but is less suitable for analysing the smaller regions of (RE)-211 or (RE)-123 accurately.

The composition data were normalised with respect to the atomic percentages of Y, Ba and Cu present at each location by dividing each of the individual atomic percentages of (RE) or Ba or Cu by the total sum of the atomic percentages of (RE), Ba and Cu over the total area of the individual image (or for the YBCO-Ag samples dividing by the total sum of the atomic percentages of (RE), Ba, Cu and Ag). The average expected amount of each element present, given the powder composition of the precursor powder pellet, was plotted and compared to the measured composition at each location. The normalised values of (RE), Ba and Cu were used in comparisons in order ensure the fluctuation in oxygen content throughout the sample did not limit the comparison of the distribution of the other elements present. In addition, the ratios of Y:Ba and Y:Cu correlate directly with the amount of Y-211 present in the sample microstructure. These ratios have been used to identify trends in the distribution of (RE)-211 inclusions throughout the samples. These data, when used alongside the trapped field data, J_c and T_c values and the optical

and SEM images, can provide explanations as to why each sample behaves as it does with respect to: the superconducting properties it exhibits, the differences between systems, and between primary and recycled growth samples, and the effect composition has on the microstructure, and vice versa.

In addition to analysis of the average composition across a wide area, unknown phases present in the sample, along with Ce-rich phases, were analysed to determine the composition. These data will allow any anomalies to be identified, as many of the images contained a large area of an unknown phase which may, in some cases, alter the average composition by a significant amount.

2.6 Threshold analysis

ImageJ software [98] was used to analyse a number of images of the sample microstructure to quantify the area fraction occupied by pores and, where relevant, silver agglomerates. In addition, the average size of the pores and silver agglomerates in each image was recorded.

The *colour threshold* tool was adjusted to highlight the pores or silver agglomerates in an image. The brightness level of the pores and silver in comparison to each other and the Y-123 matrix were very different and, hence, allowed thresholding to easily highlight the particles. Then the *analyse particle* tool was used to collect data on the average size and area of the image occupied by these pores or agglomerates. A microscope image and the associated thresholded images are shown in Fig. 2.9.

Although this technique has provided a good quantitative indication of the pores and Ag agglomerates present within the structure, some of the very small Ag particles and some of the small pores may not have been included in the thresholding.

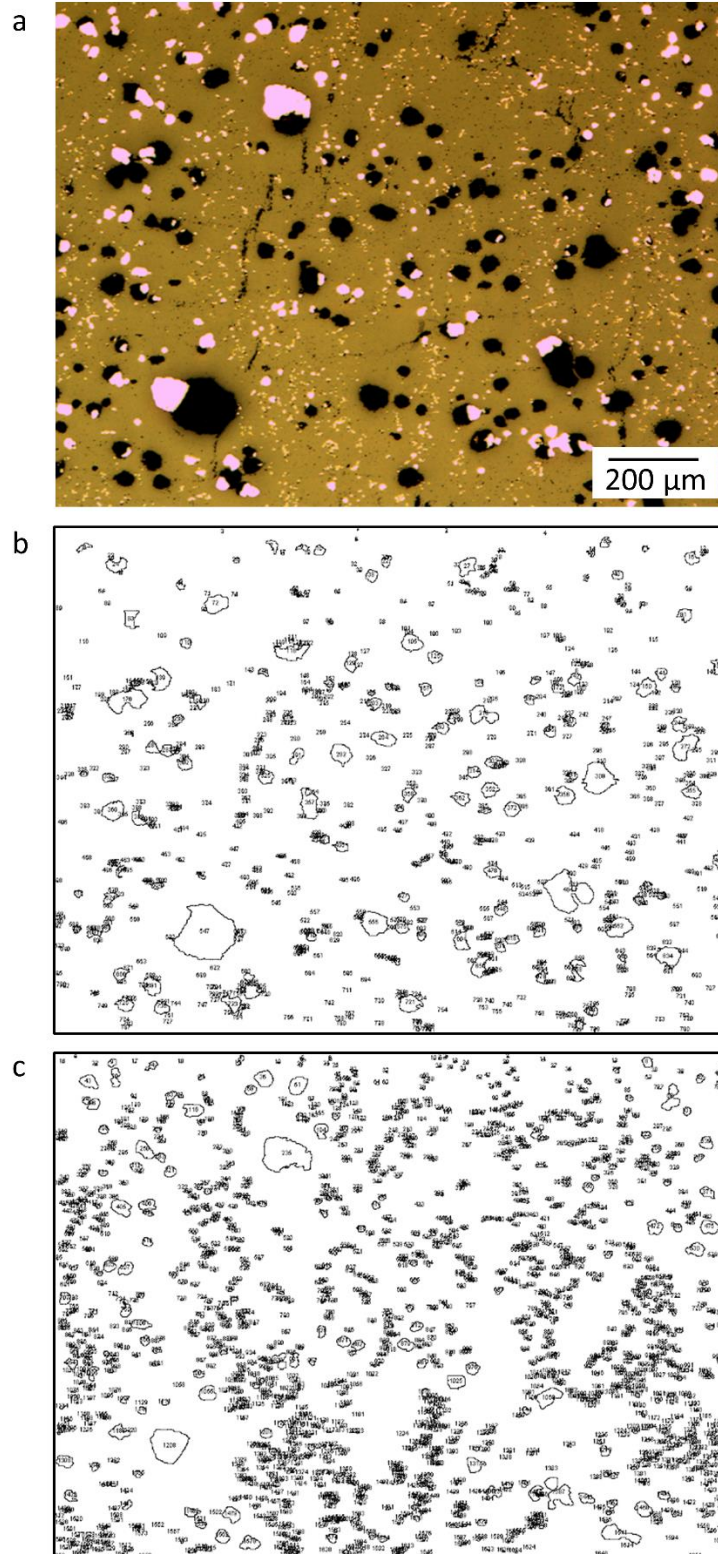


Figure 2.9: Image of: a) The microstructure of a YBCO-Ag sample at 50x magnification, b) The thresholded image used to identify pores, c) the thresholded image used to identify Ag agglomerates.

3 The provision of additional liquid-phase in the recycling of YBCO, GdBCO-Ag and SmBCO-Ag bulk superconductors

The successful growth of single grain (RE)BCO bulk superconductors is very sensitive to changes in the growth variables. This makes the likelihood of failure of single grain growth relatively high, frequently resulting in the production of multi-grain samples. These multi-grain samples are usually discarded as a waste product since they contain high-angle grain boundaries and hence exhibit low J_c values, so are generally useless for practical applications. The rare-earth precursor powders used in the TSMG process are typically of high purity (99.9 %) and so are reasonably expensive. In addition, expensive alloying elements such as Pt or Ag are used to improve the properties of (RE)BCO single grains. Waste, in the form of samples that fail to grow as single grains, is both expensive and an inefficient use of material resources. As a result, recycling of these failed samples is highly desirable and increases both the economic viability and environmental sustainability of the production of (RE)BCO single grains. A successful recycling process will, in turn, significantly increase the viability of bulk superconductors for use in practical applications.

A recycling technique has been developed by the Bulk Superconductivity Group at the University of Cambridge [99]. This technique is both inexpensive and easy to apply, and has been found to be reliable in the fabrication of complete single grains. The recycling process has drawn inspiration from the so-called IG process [100]. The initial stage of the recycling process involves IG where the failed sample replaces the pressed pellet of mixed (RE)BCO powder and an additional pellet containing liquid-phase (Ba-Cu-O) is placed beneath the failed sample. This additional liquid provides liquid-phase to replenish some of the liquid lost during the failed primary growth process.

The recycling process is able to reliably produce single grain samples. However, the reasons for the success of this recycling technique were not clear. In order to explain the reasons for success, the recycling process has been repeated systematically for the YBCO, GdBCO-Ag and SmBCO-Ag systems. The superconducting properties of the resulting samples have been measured to confirm they are comparable to primary grown samples from the same system. A detailed analysis of the microstructure has been undertaken along both the a/b and c -axis directions. The fluctuations

in composition along both these axes have also been compared with primary grown samples. Reasons for the success of the recycling process have been investigated in detail with a view to providing additional liquid to enable the reliable growth of primary grown grains of YBCO.

3.1 The growth process

Two YBCO, three GdBCO-Ag and five SmBCO-Ag samples were grown by conventional TSMG. 40 g of the precursor powder was pressed uniaxially in a 25 mm diameter cylindrical die.

Fourteen YBCO, 19 GdBCO-Ag and 30 SmBCO-Ag samples were recycled as part of this investigation. Liquid-phase-rich powder was mixed from $\text{Yb}_2\text{O}_3 : \text{CuO} : \text{BaCuO}_2$ in the molar ratio 1 : 6 : 10 for 2 h in a Turbulator. This liquid-phase-rich powder was used as the liquid source for the IG process by Li et. al. [100] with the Y_2O_3 replaced by Yb_2O_3 which has a lower peritectic temperature. A 30 mm diameter liquid-phase-rich powder pellet was pressed uniaxially to recycle a failed sample approximately 25 mm in diameter. For larger diameter samples, the diameter and mass of the additional pellet was scaled in proportion to the area of the base. For the 25 mm failed sample, this 30 mm diameter pellet contained 4 g of Yb_2O_3 powder below 11 g of the liquid-phase-rich powder.

The heating and oxygenation profiles used were the same for both the conventional TSMG process and the recycling, as shown in Fig. 3.1. This enabled primary grown and recycled samples to be processed at the same time, in the same furnace, for purposes of comparison.

Of the recycled samples, 10 of the YBCO samples, 15 of the GdBCO-Ag samples and 22 of the SmBCO-Ag samples grew successfully into single grains. A selection of the samples are shown in Fig. 3.2. Single grains were distinguished by characteristic four fold facet lines which extend along the top face and down the sides towards the base. These facet lines, or so-called growth sector boundaries, form the boundary between the growth sectors in these quasi single crystals. Of the primary grown grains, neither of the two YBCO assemblies, two of the three GdBCO-Ag assemblies and four of the five SmBCO-Ag assemblies were successfully grown as single grains.

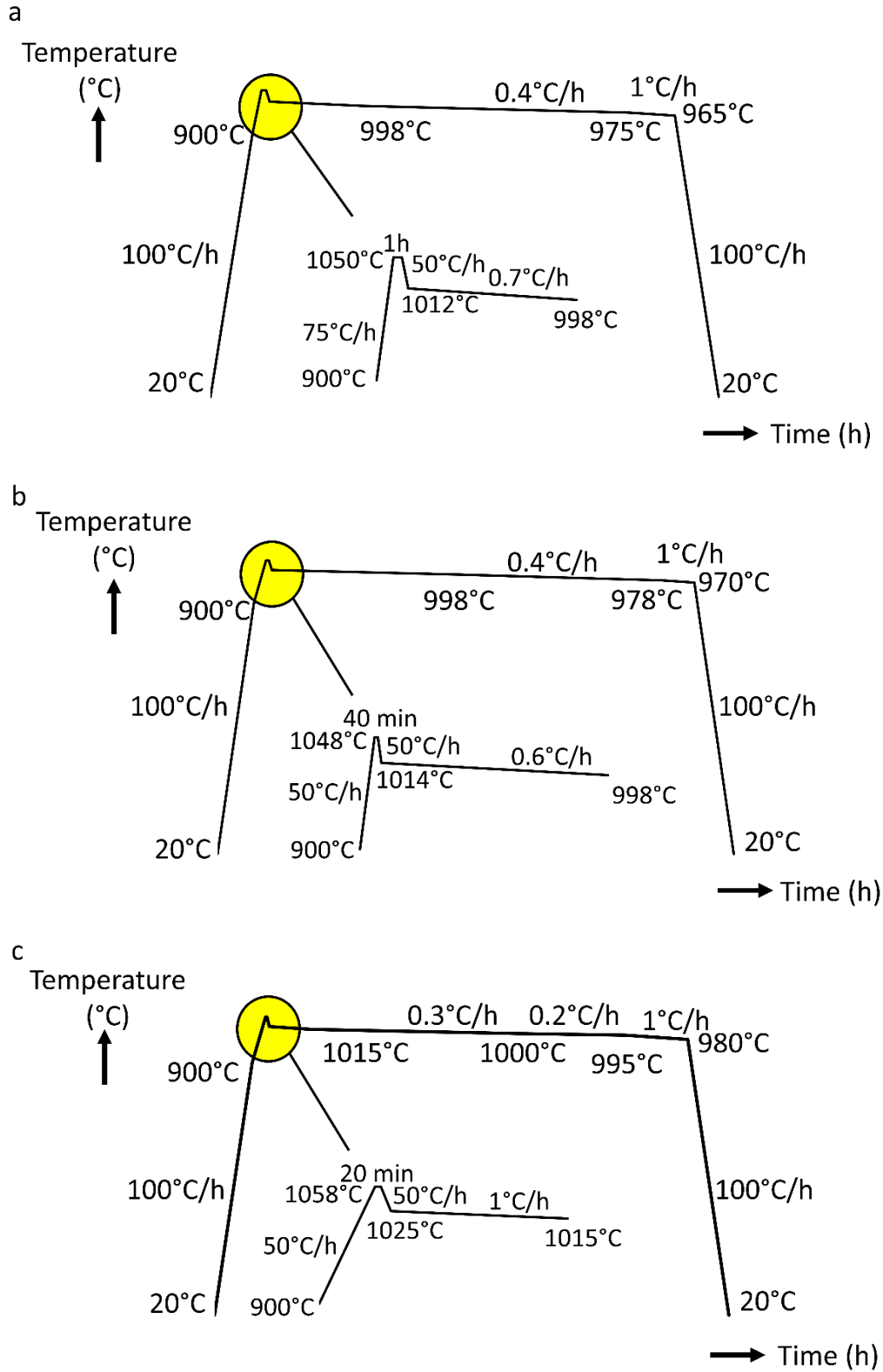


Figure 3.1: The heating profiles used for both conventional TSMG and recycling of a) YBCO, b) GdBCO-Ag and c) SmBCO-Ag, inset is the region highlighted in yellow.

To enable comparison, a primary grown YBCO sample was acquired from the group, this was processed in the same way as described in Chapter 2. The success of the recycling process was high, at an average 75 % for across all samples and 71 %, 79 % and 73 % for YBCO, GdBCO-Ag and SmBCO-Ag, respectively. In most cases the reason for failure of the recycling process was the seeding.

Although this was investigated on a relatively small batch of samples, these data suggest the recycling process has a higher success rate of single grain production than the primary growth process. The recycling process is also simple, easy and low cost.

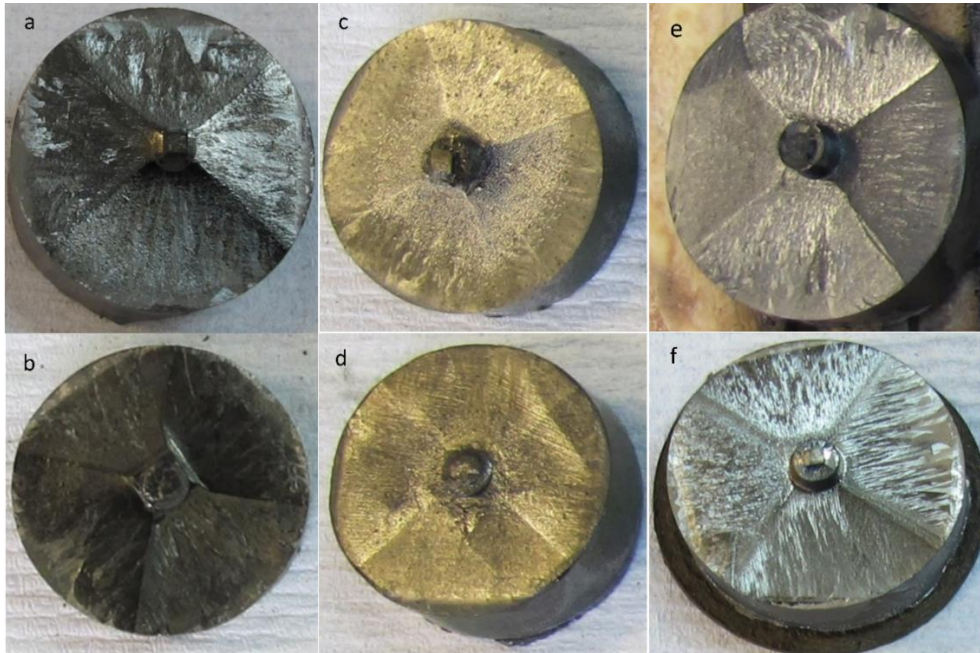


Figure 3.2: Single grains of: a) primary grown YBCO, b) recycled YBCO, c) primary grown GdBCO-Ag, d) recycled GdBCO-Ag, e) primary grown SmBCO-Ag and f) recycled SmBCO-Ag.

3.2 Superconducting properties

One recycled and one TSMG-grown sample was chosen at random from each of the three systems be studied, with the exception of the SmBCO-Ag system. Two recycled samples of SmBCO-Ag were analysed in detail. Two were studied because the SmBCO-Ag system generally shows more variation between samples and it was hypothesised that this may also be the case for the recycled samples in the SmBCO-Ag system. The samples were then oxygenated.

3.2.1 Trapped field

The maximum trapped field and trapped field profile of each of the 7 samples were measured. The trapped field profiles exhibited at the top and base of each of the samples are characteristic of single grain samples. They each have a single peak that decreased continuously with radial distance from the centre, as shown in Fig. 3.3. The maximum trapped field values are given in Table 3.1. The trapped field was not measured for the primary grown YBCO sample as data are widely available on the trapped field of YBCO grains grown by conventional TSMG. The trapped field was also not measured for a primary grown SmBCO-Ag single grain as the trapped field values vary widely between samples. Measurements within the Bulk Superconductivity Group at the University of Cambridge have varied between 0.35 to 0.81 T. It can be concluded that the recycled samples typically exhibit a maximum trapped field approximately 15 % lower than primary grown samples.

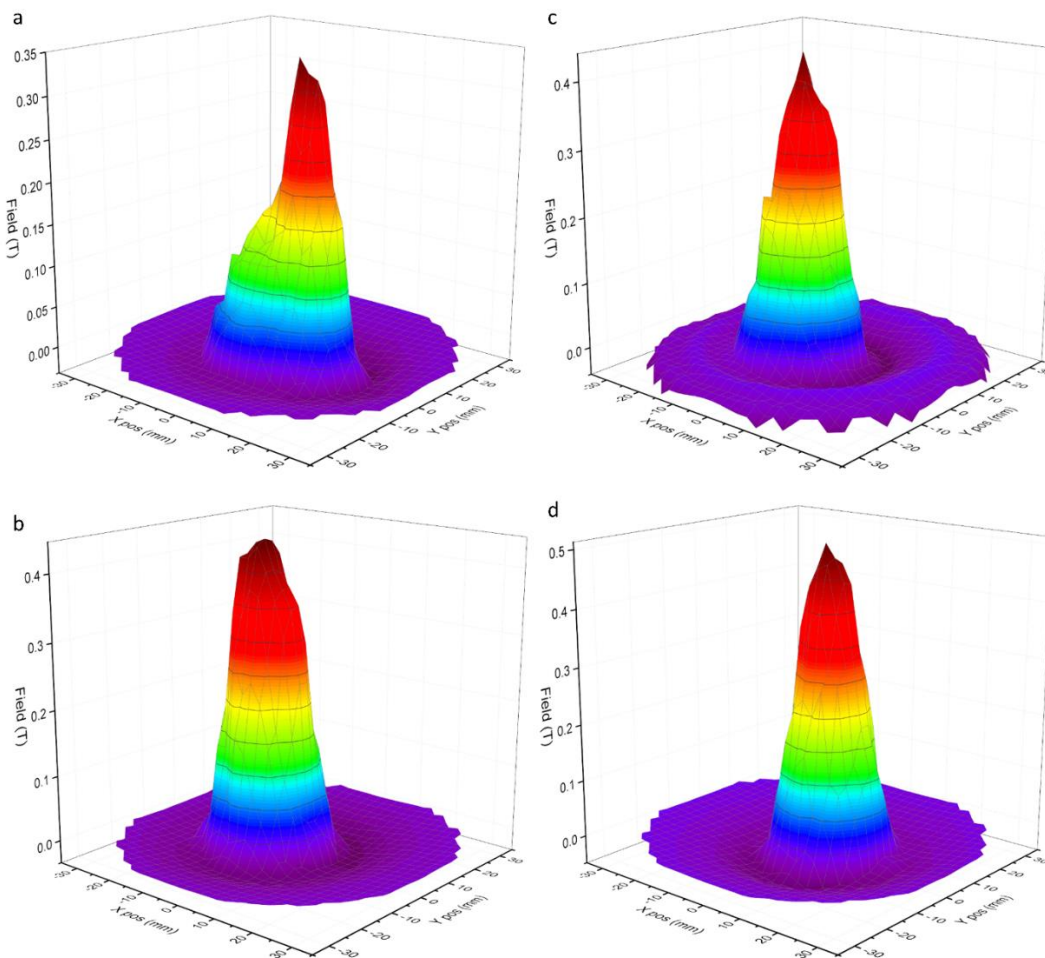


Figure 3.3: Trapped field profiles measured at the top surface of single grains of; a) recycled YBCO, b) recycled GdBCO-Ag, c) primary grown GdBCO-Ag and d) recycled SmBCO-Ag.

Sample	Trapped field at top (T)	Trapped field at base (T)
YBCO recycled	0.61	0.36
GdBCO-Ag primary	0.85	0.65
GdBCO-Ag recycled	0.77	0.75
SmBCO-Ag recycled	0.72	0.70

Table 3.1: The maximum trapped fields recorded at the top and bottom surface of recycled and primary grown bulk single grains.

3.2.2 Transition temperature and critical current density

Samples were cut and analysed as described in Chapter 2. Four sub-specimens from each sample were analysed to study the variation in the values of J_c and T_c throughout each sample, and to enable the variation in the primary grown and recycled samples from each system to be compared. The location of each piece is shown schematically in Fig. 3.4. The value of T_c for each sub-specimen is given in Tables 3.2 to 3.4 alongside the value of ΔT_{90} .

All samples have a T_c value significantly higher than 77 K, so liquid nitrogen would be a suitable cryogen for low temperature characterisation. All values of T_c were within the range 90 K to 94 K and the variation for each of the sub-specimens from an individual bulk was less than 2 K. There was a large difference in T_c values between different systems; YBCO had the lowest average T_c values. The GdBCO-Ag and SmBCO-Ag systems had very similar T_c values with averages for each sample varying less than 1 K within each single grain.

The recycled sample for each of the (RE)BCO systems had a slightly lower average T_c value than the primary grown sample. There was one exception for the SmBCO-Ag recycled samples; one had a T_c value 1 K higher than the primary grown sample. No relationship between ΔT_{90} and whether the grain was primary grown or recycled was observed.

Sample	T_c (K)	ΔT_{90} (K)	J_c (MA m ⁻²)
Primary			
1tb	92	2.2	370
1td	90	0.9	404
4ta	90	3.5	227
4tc	90	0.5	681
Average	91	1.8	420
Recycled			
1ta	90	1.4	458
1tc	91	0.7	508
4ta	90	1.2	364
4tc	90	1.0	280
Average	90	1.1	403

Table 3.2: T_c , ΔT_{90} and J_c values from YBCO and recycled YBCO samples.

Sample	T_c (K)	ΔT_{90} (K)	J_c (MA m ⁻²)
Primary			
1ta	93	0.6	392
1tc	93	0.4	381
4ta	93	0.5	430
Average	93	0.5	401
Recycled			
1ta			102
1tc	93	1.3	221
1tc repeat	93	0.5	211
3tc	93	0.4	250
4ta	93	0.9	369
Average	93	0.8	231

Table 3.3: T_c , ΔT_{90} and J_c values from GdBCO-Ag and recycled GdBCO-Ag samples.

Sample	T_c (K)	ΔT_{90} (K)	J_c (MA m ⁻²)
Primary			
1ta	93	1.9	703
1tc	93	1.3	572
2ta	92	5.6	
2tc	93	1.7	563
3ta	92	5.3	473
3tc	93	2.1	647
Average	93	3.0	592
Recycled 1			
1ta	93	1.2	368
1tc	94	1.0	391
4ta	93	4.1	
4tb	94	2.4	397
4tc	94	2.1	382
Average	94	2.2	385
Recycled 2			
1ta	92	8.6	200
1tc	93	6.3	225
4ta	92	5.2	294
4tc	92	5.1	143
Average	92	6.3	215

Table 3.4: T_c , ΔT_{90} and J_c values from one SmBCO-Ag sample and two recycled SmBCO-Ag samples.

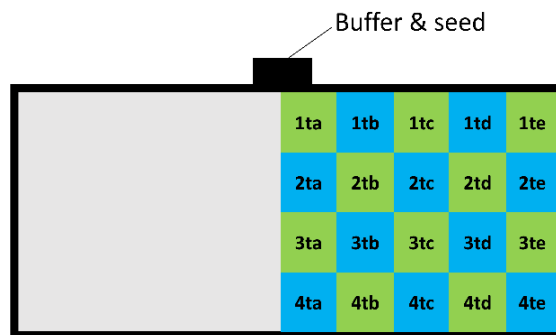


Figure 3.4: A schematic illustration of the labelling of each piece cut from the centre of the bulk.

The $J_c(0)$ value can be used to provide a direct quantitative comparison of the J_c values. The value of $J_c(0)$ for each sub-specimen is given in Tables 3.2 to 3.4.

The average value of J_c across all sub-specimens in the YBCO samples is very similar for both the primary-grown and recycled samples (420 MA m⁻² and 403 MA m⁻², respectively). However, in the GdBCO-Ag and SmBCO-Ag systems the average value of J_c is significantly lower in the recycled sample than in the primary grown sample. The average value of J_c in the recycled sample is 42 % lower than the conventional TSMG grown sample in the GdBCO-Ag system and differs by 65 % between the primary grown and recycled sample with the lowest J_c value in the SmBCO-Ag system. The average $J_c(0)$ value varies significantly between the bulk samples of SmBCO-Ag studied.

The $J_c(0)$ values were more consistent throughout an individual recycled bulk sample, except for the GdBCO-Ag system, although this may be because fewer sub-specimens were analysed. The variation in the values of J_c throughout the sample in the primary grown samples was generally much larger than the variation across the sub-specimens for the recycled samples in the YBCO and SmBCO-Ag systems. This suggests that the distribution of flux pinning centres in the recycled samples is more uniform.

3.3 Microstructure

The rectangular cross section of one half of each of the seven samples was imaged using the optical microscope. Images were taken at intervals of 2 mm along the a/b -axis 1 mm vertically below the seed and along the central c -axis directly below the centre of the seed. In addition, these samples were imaged using the SEM along the same axes at intervals of 1 mm, as shown schematically in Chapter 2. This reduction in interval size was chosen because the images taken were at higher magnification and so this enabled a more detailed analysis of the variation in the microstructure throughout each sample.

The SEM image in Fig. 3.5 is labelled with a number of different features including (RE)-211, a pore, a silver agglomerate and a crack within a (RE)-123 superconducting matrix. The SEM images shown in Figs. 3.6 and 3.8 reveal that the density of RE-211 particles increases with distance from the seed in the horizontal direction, as predicted by particle pushing-trapping theory [54, 55]. The growth rate is low in the early stages of growth and so only large particles can be trapped, so the majority of the RE-211 particles are pushed. As the growth front advances, the

growth rate increases and so the reduction in critical radius means that smaller, and so more, RE-211 particles are trapped. A similar increase in RE-211 particle density is also observed in the vertical direction in all the primary grown (RE)BCO and (RE)BCO-Ag single grain samples, as shown in Figs. 3.7 and 3.9. The other samples show this behaviour and the additional images are shown in Appendix 1.

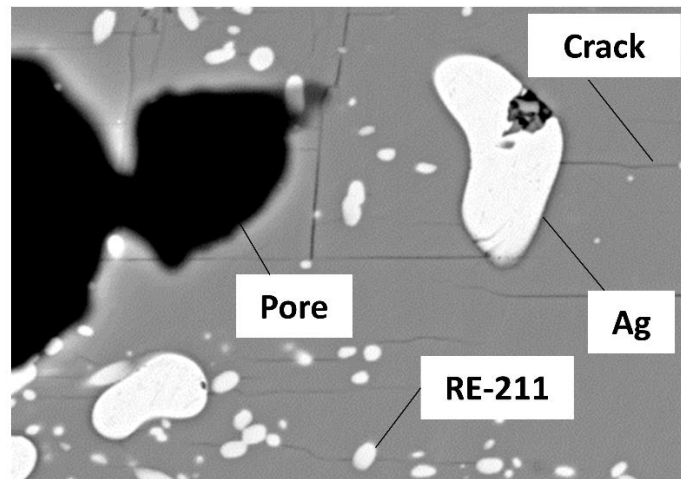


Figure 3.5: A labelled SEM image showing an (RE)-123 matrix including a number of labelled features.

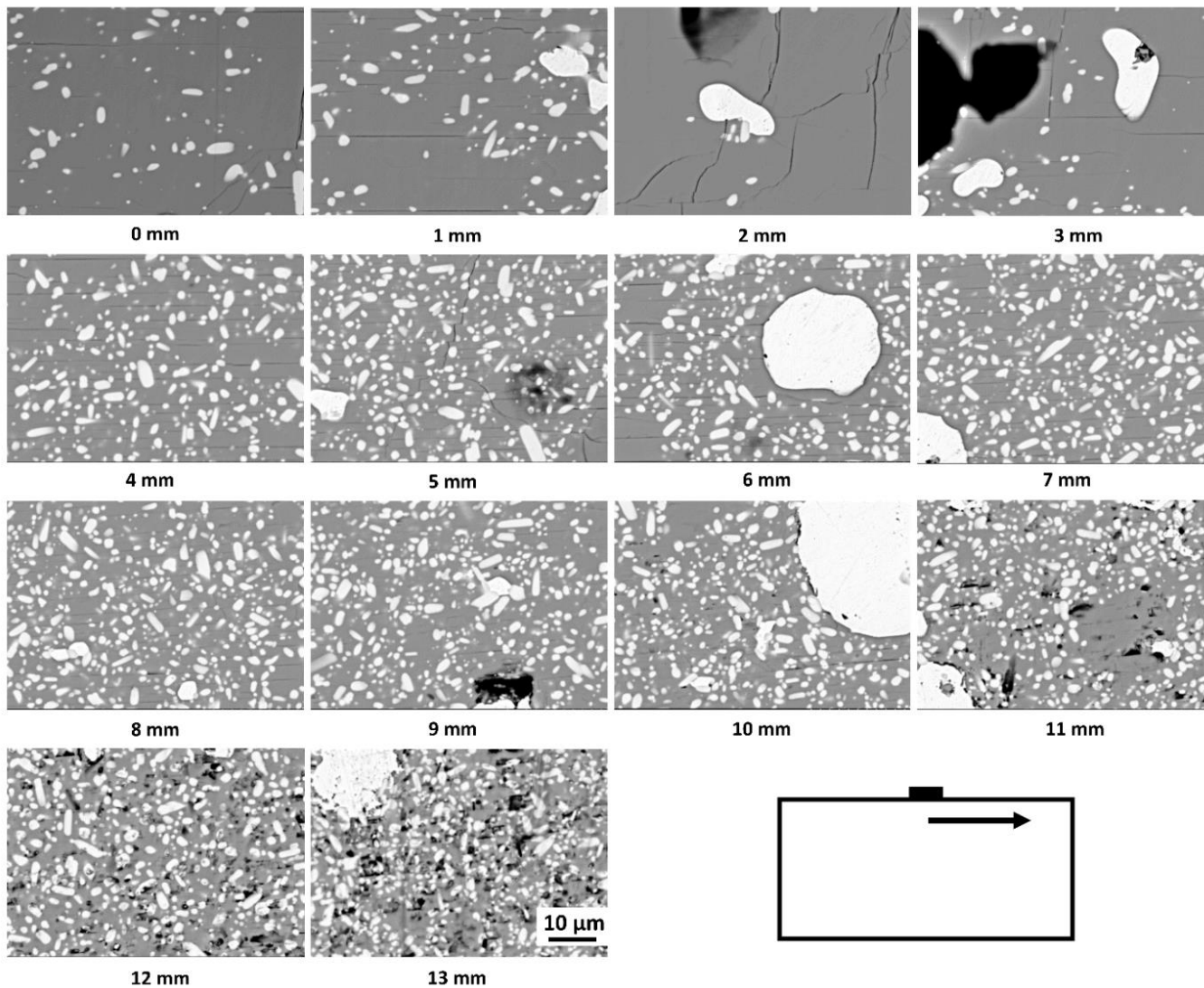


Figure 3.6: SEM images along the a/b -axis of a primary grown GdBCO-Ag sample approximately 1 mm below the seed at 2000x magnification, inset is a schematic of the axes along which the images were taken.

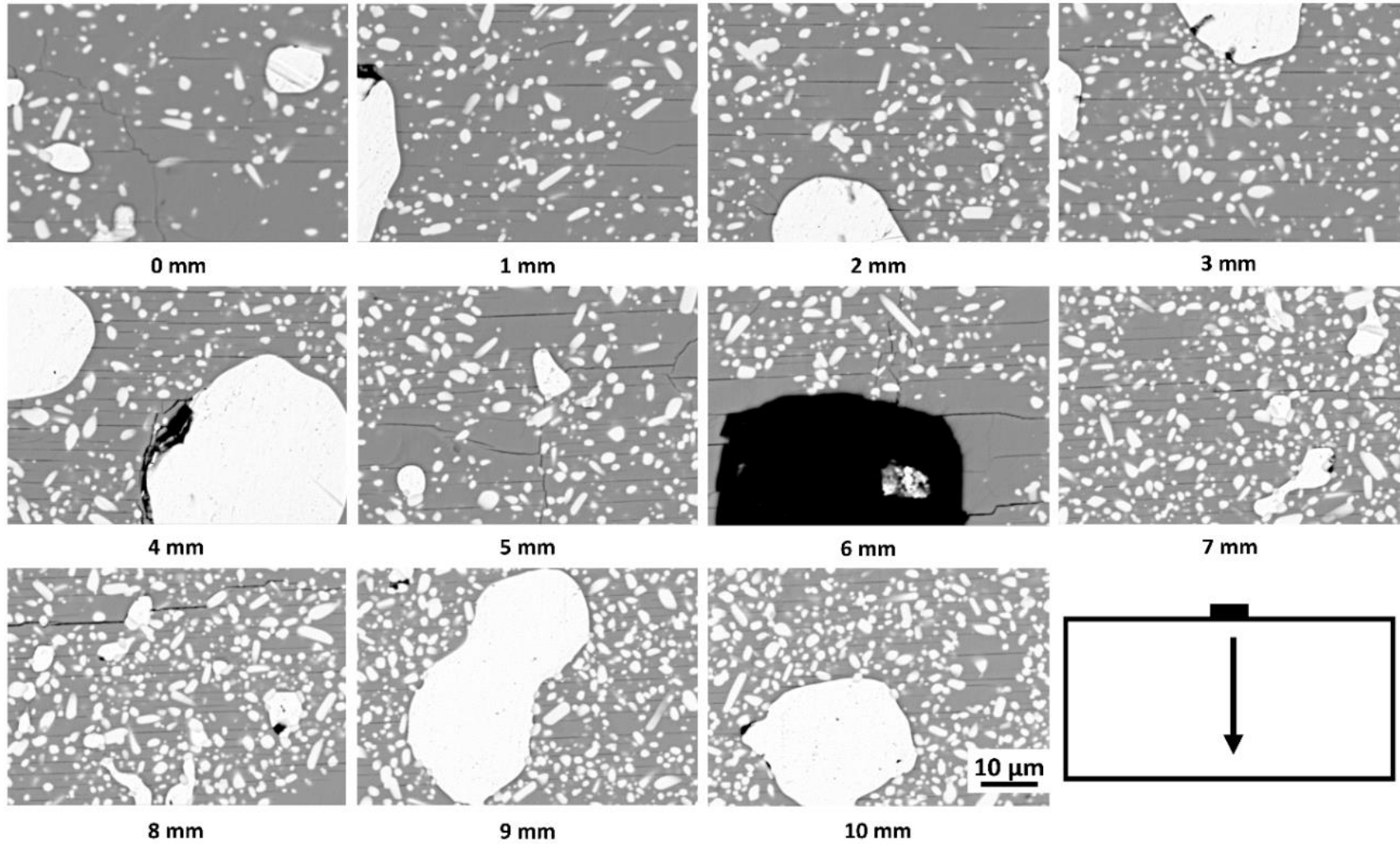


Figure 3.7: SEM images along the central c-axis of a primary grown GdBCO-Ag sample at 2000x magnification, inset is a schematic of the axes along which the images were taken.

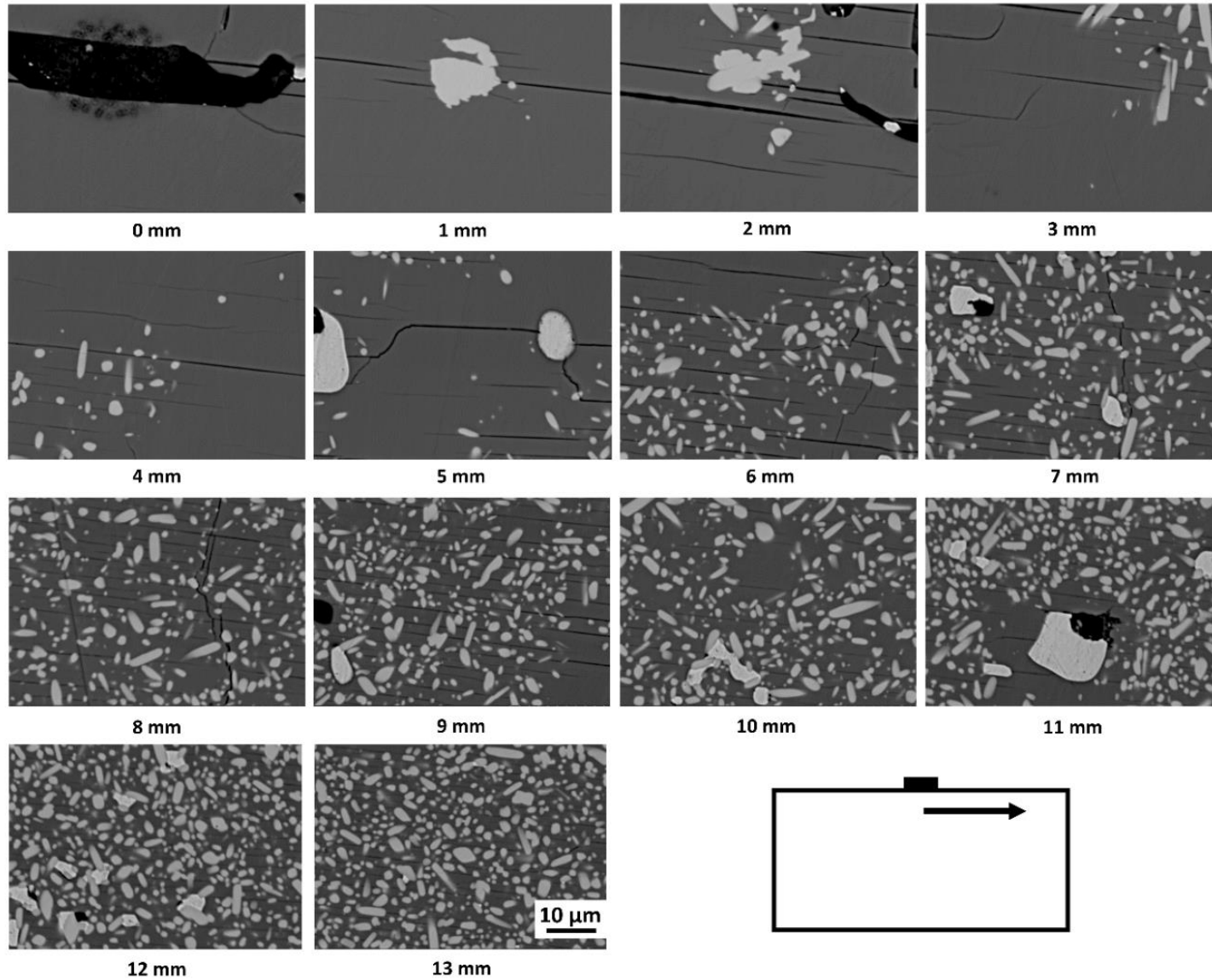


Figure 3.8: SEM images along the a/b -axis of a recycled GdBCO-Ag sample approximately 1 mm below the seed at 2000x magnification, inset is a schematic of the axes along which the images were taken.

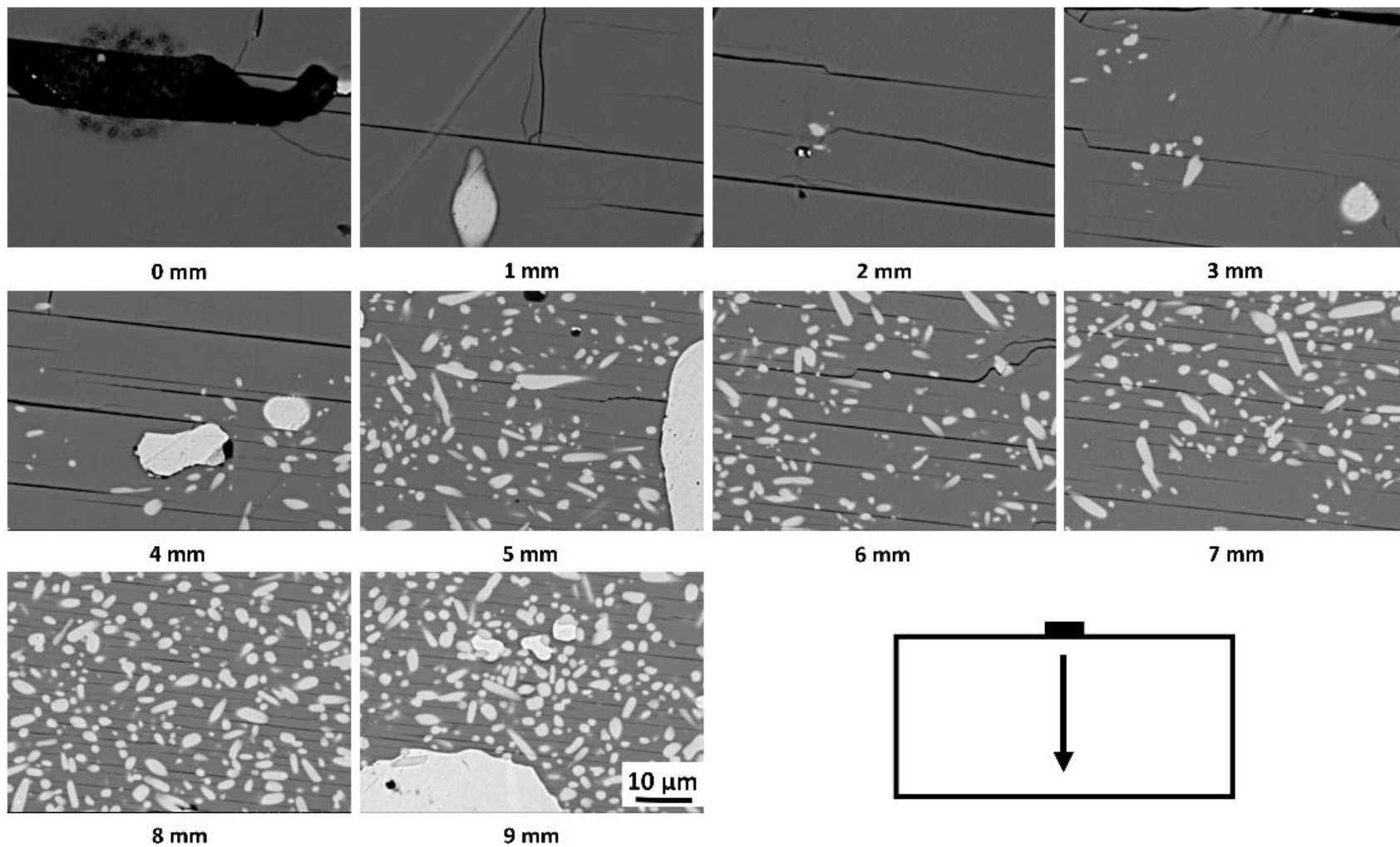


Figure 3.9: SEM images along the central c-axis of a recycled GdBCO-Ag sample at 2000x magnification, inset is a schematic of the axes along which the images were taken.

The magnitude of J_c is determined by the ability of the sample microstructure to pin magnetic flux (i.e. a fluxoid). A larger macroscopic J_c value produces a larger trapped field [66]. Both nano-sized defects and non-superconducting inclusions act as particularly effective pinning centres in bulk (RE)BCO superconductors. Un-reacted, un-dissolved small (RE)-211 particles are typically trapped in the as-grown (RE)-123 single grain phase matrix during peritectic solidification, which creates (RE)-211/(RE)-123 interfaces that form effective flux pinning centres and so improves J_c of the single grains [67]. In particular, the value of J_c is reported to increase with the V_{211}/d_{211} ratio, where V_{211} is the Y-211 volume fraction and d_{211} is the average size of the Y-211 particles [72, 73]. The more uniform the distribution of (RE)-211 particles, the more uniform the critical current, and the higher the density of small-sized (RE)-211, the larger the magnitude of the critical current. The ratio of V_{211} and d_{211} can be quantitatively analysed using threshold analysis software, as described in section 2.6.

The density of RE-211 particles has been observed to increase with distance from the seed in all the systems investigated in this study. However, the distribution of RE-211 particles is more uniform for the recycled samples and the uniformity of the distribution increases from Y to Gd to Sm. This suggests that the provision of adequate liquid-phase during the grain solidification process, which is achieved during the recycling process, enables the peritectic reaction to continue to progress to the edge of the sample. This, in turn, enables growth of the single grain to continue to the edge of the sample to produce a more uniform sample, which is highly desirable for practical applications.

The RE-211 inclusions become both larger with increasing distance from the seed, and noticeably elongated during the recycling process, these inclusions are noticeably elongated in Figs. 3.8 and 3.9. This is likely due to the samples having been held at high temperature for twice the time period of those grown by primary TSMG. These samples have experienced one heating and cooling cycle during the failed growth process and then an additional heating and cooling cycle in the recycling process. The increase in pinning due to the increase in pinning centre size will typically be less than if there were a larger number of smaller pinning centres (of equivalent volume). This is likely to be the reason why the recycled samples exhibit a lower maximum J_c value than the primary grown samples of the same system.

3.4 Composition

The average composition of the area of each image taken using SEM was analysed, along with the composition of a number of the individual phases present. The image in Fig. 3.10 shows the regions of Gd-211 and Gd-123 in which the composition was measured. In this example, the ratio of Gd: Ba: Cu in region 1 was 1.9: 1.0: 1.0, whilst in region 2 the ratio was 1.0: 2.0: 2.9. This is very close to the expected ratios of Gd-211 and Gd-123.

The composition data for all three systems for the recycled and primary grown samples are shown in Fig. 3.11. Composition analysis, in conjunction with the SEM images, has been used to identify the phases present in the microstructure, which include cerium-rich, silver-rich, RE-123, and RE-211 phases. Analysis of the average composition at each location has revealed that the average composition at most locations in the single grain samples fluctuates around the expected average composition calculated from the precursor powder compositions. Large fluctuations from the expected composition for a given image can be explained using the SEM images. In many cases the SEM images reveal the presence of large agglomerates, large pores, cracks, or regions of abnormal microstructure.

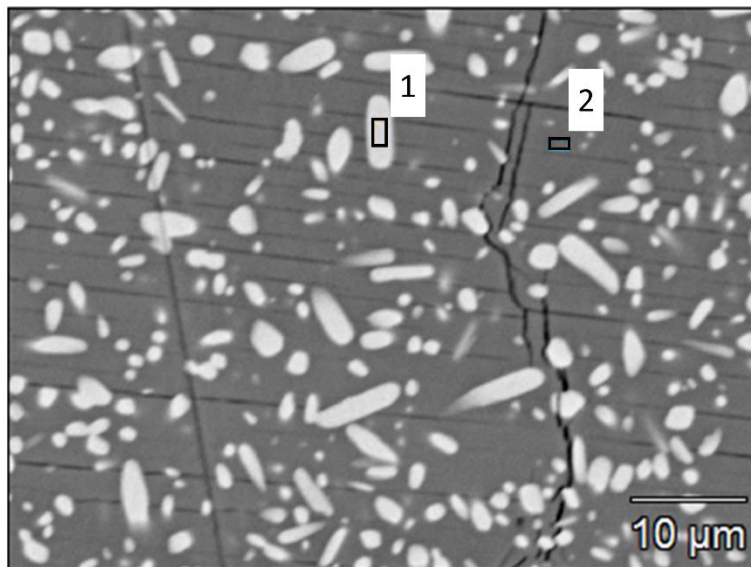


Figure 3.10: Micrograph image showing regions 1 and 2 in which the composition was measured.

Each position along either the a or c -axis direction within a single-grained sample fabricated by TSMG corresponds to an equivalent point in time during the solidification of the growth front. The

growth of (RE)BCO single grains can be interpreted by a “black box” approach given that changes in composition during the growth process itself are difficult to detect. For this reason, it is commonly assumed that the local composition on completion of solidification is the same as that during the growth process.

The general trend in composition seen in Fig. 3.11 is that of a reduction in the normalized atomic percentage of Cu, indicating the shortage of liquid-phase (liquid-phase composition: $\text{Ba}_3\text{Cu}_5\text{O}_8$) and an increase in the atomic percentage of (RE) element with increasing distance from the seed in both the horizontal and vertical direction. The level of barium, however, remains constant throughout the sample, suggesting that the atomic percentage of the (RE)-211 phase increases with distance from the seed, whereas the atomic percentage of the (RE)-123 phase decreases with distance from the seed. This can also be seen in the optical microscope and SEM images of the single grain samples. The ratios of RE/Cu and RE/Ba represent the trend in (RE)-211 concentration and are shown for each location in Fig. 3.12. The data shows that both ratios increase with distance from the seed and this increase is much larger in the horizontal direction than in the vertical direction for all systems. This suggests that there is a much greater change in the ratio of (RE)-123 and (RE)-211 in the horizontal direction.

The ratios of RE/Cu and RE/Ba in the recycled grains are more consistent between neighbouring locations than in the primary grown samples. The curves in the former are more parallel with each other. This suggests that the overall compositions of the (RE)-123 and (RE)-211 phases are more uniform throughout the recycled samples than in the primary-grown samples, causing the more uniform superconducting properties of the recycled material. The additional liquid-phase is thought to be responsible for the greater uniformity in the composition obtained in the recycled samples.

The large Ag-rich, Ce-rich and combined Ce and Ag-rich clusters apparent in a number of the SEM images are thought to be a major reason for the failure of single grain growth. These clusters are often generated due to poor mixing of the precursor powders used in the primary growth process. The high success rate of the recycling process is likely to be because this process is tolerant to the presence of these Ag, Ce and Ag- and Ce-rich clusters. This is due to the provision

of adequate quantities of liquid-phase, which enables Y, Gd, or Sm to be more readily available at the growth front. This additional liquid-phase allows the grain to continue to grow as a single grain, even when there is a sudden significant change in the liquid-phase composition.

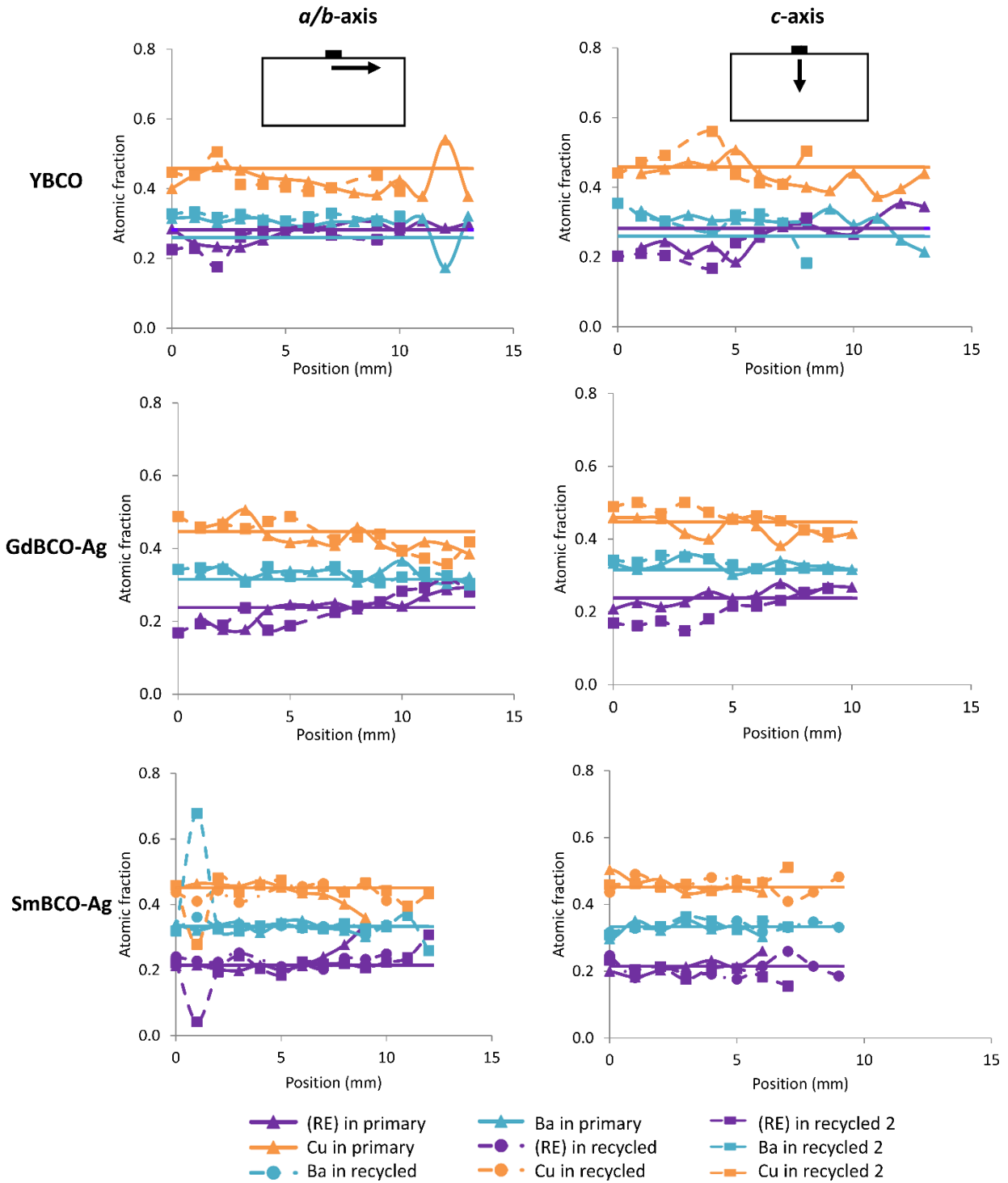


Figure 3.11: Graphs showing the variation in atomic fraction of the elements Cu, Ba and RE.

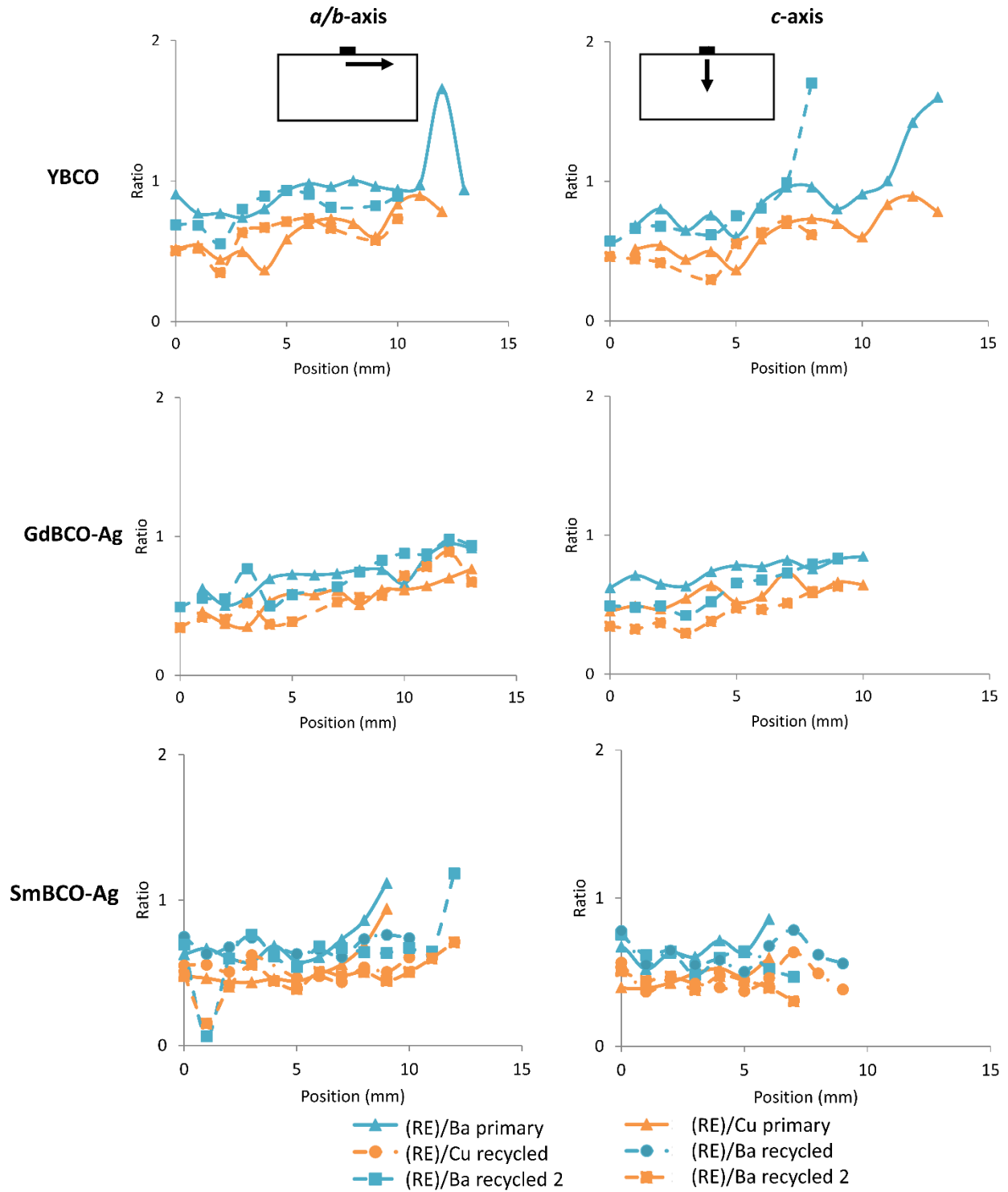


Figure 3.12: Graphs showing the ratios of Y : Ba and Y : Cu with distance from the seed.

3.5 Conclusions

It has been demonstrated that failed YBCO, GdBCO-Ag and SmBCO-Ag melt processed samples can be recycled successfully and reliably by the controlled replenishment of liquid-phase lost during the primary growth process. SEM and EDX have been used to observe and analyse the composition of the growth front of primary and recycled single grains of all three systems post-processing. The uniformity of both the (RE)-123 superconducting matrix and the distribution of the flux pinning, non-superconducting (RE)-211 inclusions are critical for the uniformity of the superconducting properties. Analysis using EDX has revealed relatively large fluctuations from the composition of the precursor powders. This has been explained by a variety of processing features, including the presence of Ce and Ag-rich agglomerates and pores and cracks at specific locations within the single grain samples. The compositional analysis suggests that the growth mechanisms are the same for both the primary grown and recycled grains in all three systems investigated.

The additional liquid-phase provided in the recycling process dissolves the RE element (Y, Gd, Sm) to form the RE-123 phase at the growth front, which is fundamental to the growth of single grains. The provision of adequate liquid-phase yields sufficient RE element concentration at the growth front to enable single grain samples to grow easily, to provide a more uniform composition at the growth front and to support growth in the presence of agglomerates of Ag and Ce-rich phases.

The additional liquid-phase provided in the recycling process has produced recycled samples with a more uniform composition than the primary grown samples. This increased uniformity has yielded recycled samples that have more uniform superconducting properties throughout the superconducting bulk microstructure. It may be possible to adapt the method used to recycle failed samples to improve the uniformity of the superconducting properties of primary grown samples and to increase the success rate of the primary single grain growth process.

The recycling method provides adequate liquid-phase without leakage and therefore provides an adequate concentration of RE element at the growth front, which, in turn, enables the recycled samples to grow fully and easily. In addition, and significantly, the recycling technique is tolerant

to failed samples containing relatively large, localised agglomerations of Ce or Ag-rich phases. It has been found that the liquid-phase that carries the RE element is important to produce fully grown single grains. As some liquid-phase is always lost during the primary growth TSMG process, this suggests that any method that can reduce liquid loss or compensate for the liquid loss during primary grain growth would help the fabrication of good quality single grains.

4 The provision of additional liquid-phase to enhance the growth of YBCO single grains by TSMG

In the previous chapter the provision of additional liquid-phase was shown to be instrumental to the reliable growth of high-quality single grain samples. The additional liquid is typically provided by a liquid-source pellet, similar to that used in the IG process. The additional liquid supplied during recycling is able to replenish the liquid lost during the failed growth process. The additional liquid-phase infiltrates upwards into the failed grain on heating. This formed additional RE-123 at the growth front and so enabled a single grain to grow more easily. Significantly, the recycling process was observed to be more reliable in the successful fabrication of single grain samples than the primary TSMG process.

In addition to the increase in reliability of single grain growth, the recycling process produced single grains with a more uniform and homogeneous distribution of RE-211 particles throughout the sample microstructure. This is considered to be directly due to the provision of additional liquid-phase. The increase in uniformity of the RE-211 inclusions produced an increase in the uniformity of the superconducting properties throughout the sample. However, the magnitude of the critical current density was, on-average, only 4 % lower in recycled YBCO samples than in YBCO samples grown by conventional TSMG. The reduction is due to the size of the non-superconducting RE-211 inclusions; they are elongated in the recycled samples. The RE-211 inclusions grow in size during the heating process and, after the recycling process, the samples have been held at high temperature for twice the time period of those grown by primary TSMG; one cycle during the failed growth process and then an additional cycle in the recycling process.

The recycling process can reliably produce large single grains with very uniform superconducting properties but these are of reduced magnitude. The major difference between the recycling process and conventional TSMG is the provision of additional liquid-phase. Therefore, it was hypothesised that the addition of liquid-phase to conventional TSMG would result in more reliable single grain growth. In addition, these single grains should have more uniform superconducting properties of a similar magnitude to those of single grains grown by conventional TSMG.

This chapter describes the preliminary work on the investigation of different liquid-phase source powders and small process adaptations to optimise the conventional TSMG processing technique. It then describes the preparation of samples using conventional and liquid-phase-enriched TSMG. The superconducting properties and microstructure of samples grown with and without additional liquid-phase are compared. The relationship between the superconducting properties, microstructure and composition is then explained. Conclusions have been drawn on the effect of the provision of additional liquid-phase to samples fabricated by TSMG.

4.1 Powder preparation and analysis

A number of liquid-phase-rich powders were investigated in this study. Liquid-phase-rich powder 1 (LR 1) had the molar ratio $\text{Yb}_2\text{O}_3 : \text{CuO} : \text{BaCuO}_2$ of 1 : 6 : 10 as used in IG by Li et al [100], with the Y_2O_3 replaced by Yb_2O_3 . Liquid-phase-rich powder 2 (LR 2) had the molar ratio $\text{Yb}_2\text{O}_3 : \text{Ba}_3\text{Cu}_5\text{O}_8 : \text{BaO}_2$ of 5.0 : 5.6 : 1.0. The powder was mixed for 2 h in a Turbulator with ZrO_2 balls to ensure thorough mixing of the component powders. A further liquid-phase-rich powder composition was produced by sintering LR 2 for 5 h at 850 °C to form LR 3, ramping up and down at a rate of 100 °C/h. A fourth liquid-phase-rich powder was produced by sintering a second time (LR 4). The powder was heated in air in a box furnace and then ground by hand using a pestle and mortar.

The four compositions of liquid-phase-rich powders and the YBCO precursor powder (produced as described in Chapter 2) were analysed using XRD, in order to determine the component phases present and to identify changes in composition which took place upon calcination of the liquid-phase-rich powders. Alongside this, the as-supplied constituent powders of CuO , BaO_2 , BaCuO_2 , Yb_2O_3 , Y_2BaCuO_5 , $\text{YBa}_2\text{Cu}_3\text{O}_7$, Y_2O_3 and $\text{Ba}_3\text{Cu}_5\text{O}_x$ were analysed and this provided reference spectra to enable the relevant peaks in the liquid-phase-rich powders to be identified. The spectra for the precursor powder and a number of the liquid-phase-rich phase are shown in Fig. 4.1.

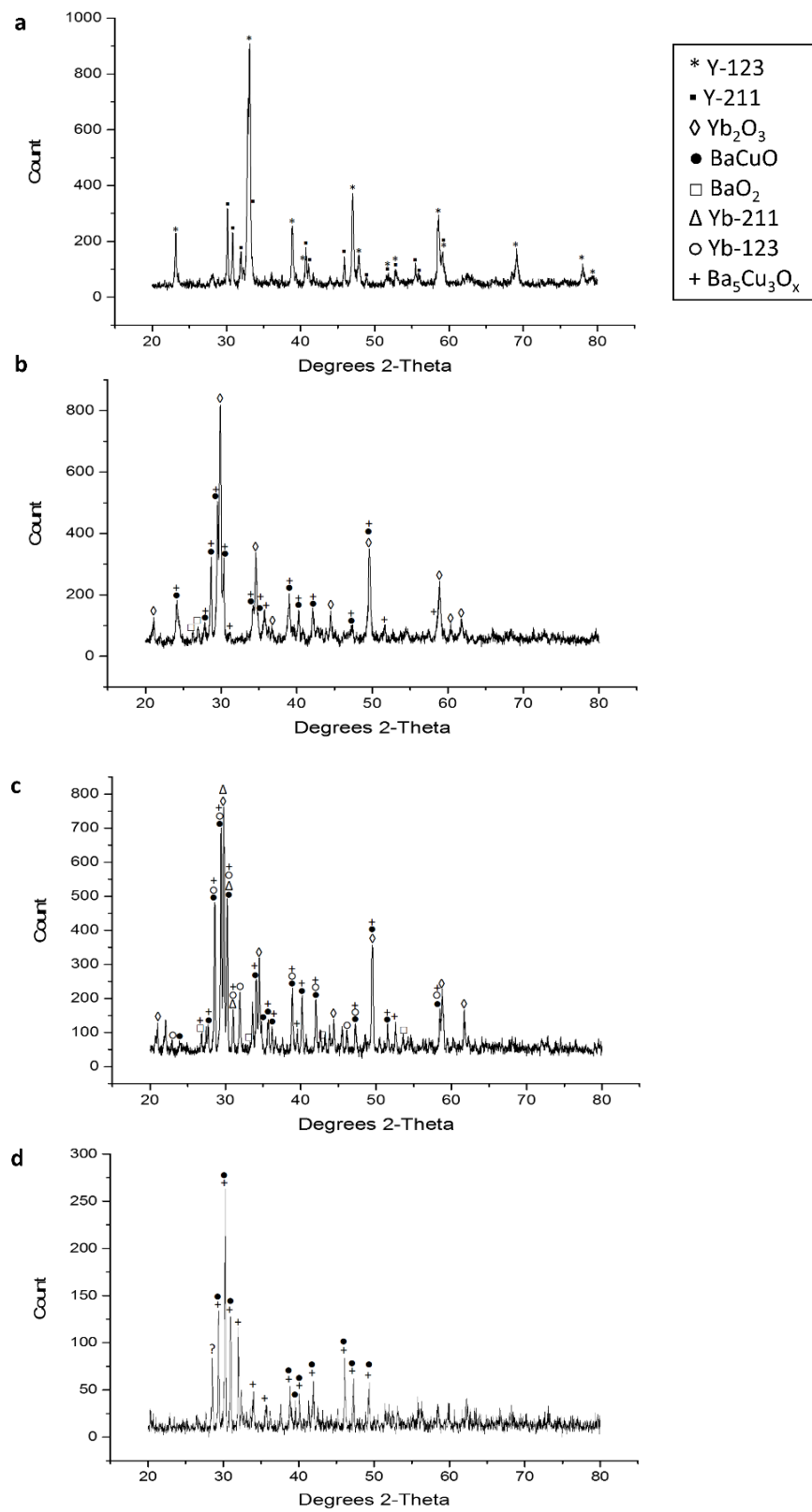


Figure 4.1: XRD spectra showing the component phases present in a) Precursor powder, b) LR2, c) LR 3, d) LR 4.

Fig. 4.1 shows that the precursor powder contains predominantly Y-123 and Y-211. The spectra of LR 2, LR 3 and LR 4 shows that the un-sintered liquid-phase-rich powder contains Yb_2O_3 , $\text{Ba}_5\text{Cu}_3\text{O}_x$, BaCuO and BaO_2 . After sintering this liquid-phase-rich powder for 5 h at $850\text{ }^\circ\text{C}$ all of the above phases remain but additional phases of Yb-123 and Yb-211 are formed, while, after further sintering for an extended period at $850\text{ }^\circ\text{C}$, only BaCuO_2 and $\text{Ba}_3\text{Cu}_5\text{O}_8$ remain. These XRD results show the sintering of the liquid-phase-rich powder alters the component phases present within the powder.

In addition to XRD analysis, the powders LR 2 and LR 3 were analysed using DTA alongside as-supplied Y-211 and lab-produced, impure Yb-123 powders. The results are shown in Fig. 4.2. This enabled the temperatures at which phase changes occurred in each of these powders to be identified. It should be noted that the Yb-123 powder had undergone a number of calcination stages and contained a small amount of contamination from Y powders, which the mixing bottle had originally contained, and thus is only a good approximation of the DTA profile for Yb-123.

The plot for the un-sintered powder, LR 2, is very similar to that of Yb-123 powder with one additional peak at $850\text{ }^\circ\text{C}$ corresponding to a peak at this temperature in the Y-211 plot. After a single calcination stage the profile produced is similar to that of the un-sintered liquid-phase-rich powder with some small differences; a more continuous region between 1000 and $1100\text{ }^\circ\text{C}$, a reduction in the peak amplitude at $840\text{ }^\circ\text{C}$ and the loss of a peak at $790\text{ }^\circ\text{C}$. These differences correspond to a change in the phases present before and after calcination and so result in a change in the phase transitions the material will experience when it is heated or cooled in DTA. Comparison of the liquid-phase-rich DTA profiles with that of the as-supplied Y-211 powder show the melting temperature of the liquid-phase-rich powder is much lower than that of the Y-211 powder. The temperatures at which phase changes within the powders take place are important parameters which set the temperature parameters used for the growth process, ensuring that the required phase changes take place and no unexpected phase changes take place during the growth process. The lower melting temperature of the liquid-phase-rich powders in comparison with the precursor powder will enable infiltration to occur before growth by TSMG. The liquid-phase-rich powder will melt first and the additional liquid-phase, BaCuO_5 , will be able to move into the

powder pellet before it has fully decomposed. In addition, as the liquid-phase-rich powder melts first, this will prevent the powder from acting as additional solid nucleation points.

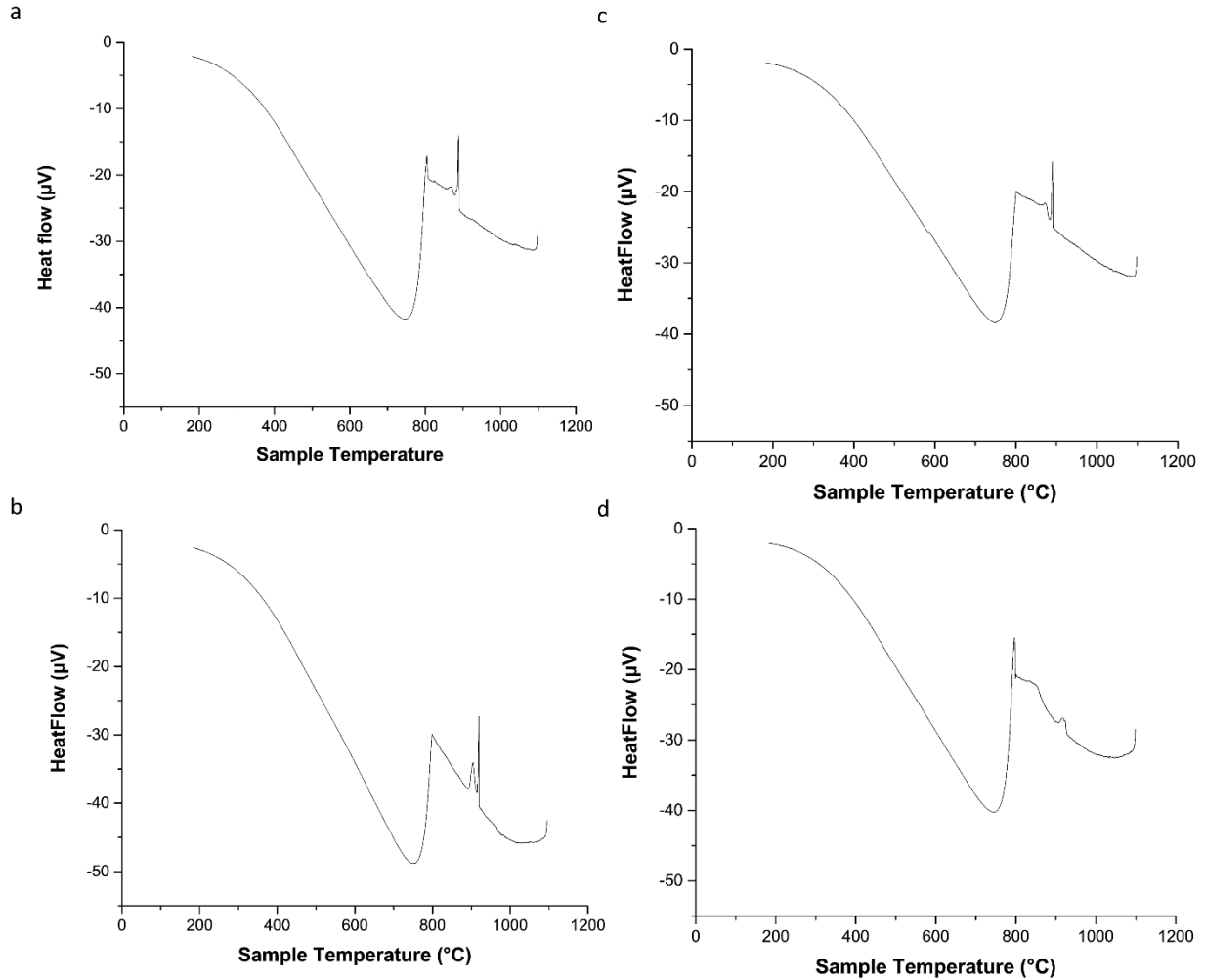


Figure 4.2: DTA plots showing the temperatures at which phase changes occur in a) LR 2, b) Sintered liquid-rich powder, LR 3, c) Y-211 powder and d) Yb-123 powder.

4.2 Incremental optimisation of sample growth

A series of samples were grown with incremental changes to the processing conditions. This was carried out to systematically identify the impact of a number of parameters and variables involved in the growth process.

The first stage used a small sample grown by the conventional TSMG process with a buffer pellet. This sample was pressed uniaxially from 22 g of the precursor powder in a 25 mm diameter cylindrical die. A layer of Yb_2O_3 was mixed to a paste with ethanol and painted onto the base to reduce the likelihood of secondary grain formation at the base. The assembly was heated according to the heating profile shown in Fig. 4.3. This sample developed a secondary facet line and so, to reduce the likelihood of secondary facet line production, the rate of cooling was reduced for the second sample. The second sample successfully grew as a single grain. This sample will be the standard sample, representative of samples grown by the current buffer-aided TSMG method.

The next samples were provided with additional liquid-phase-rich powder LR 2. A layer consisting of 3 g of liquid-phase-rich powder was pressed below the precursor powder and a layer of 1.5 g of Yb_2O_3 was used to replace the painted paste at the base. The Yb_2O_3 powder layer is thought to provide greater stabilisation during the growth process; the liquid-phase may be easily lost from the base of the sample during heating. This assembly was also heated according to the heating profile shown in Fig. 4.3.

The growth with LR 2 successfully produced a single grain, so this was followed by investigation of the effect of sintering the precursor pellet. It has been shown that the temperature, at which pre-sintering of Y-211 precursor pellets in the IG process takes place, significantly affects the final pore density and distribution within the bulk superconductor. Increasing the sintering temperature increases the density of the bulk material. Higher sintering temperatures produce a more homogeneous microstructure with regards to the pore distribution, and hence higher and more homogeneous J_c values [101].

Precursor powder pellets of mass 22 g were pressed in a die of 25 mm diameter. The precursor powder pellet was sintered for 4 h in a box furnace under atmospheric pressure and atmospheric gas composition; the ramp rate was 100 °C/h. The precursor powder pellet alone was sintered at temperatures of 943 °C, 993 °C and 1043 °C. Whilst the precursor powder pellets were being sintered pellets of 25 mm diameter were uniaxially pressed in a die from a layer of 1.5 g of Yb_2O_3 below 3 g of liquid-phase-rich powder. These samples were then assembled as described in Chapter 2. All three of these samples grew successfully, although the facet lines did not extend

fully to the base. Each sample was oxygenated and, on oxygenation, a large amount of material was lost from the base of one of these samples due to cracking, so an identical growth process was repeated.

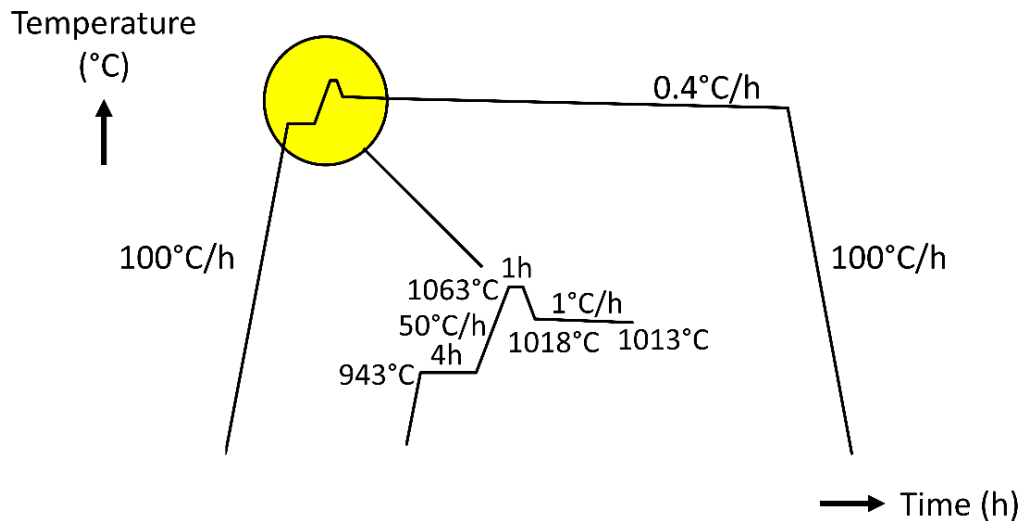


Figure 4.3: The heating profile used to grow single grains of 25 mm diameter of YBCO.

The effect of the composition of the additional liquid-phase-rich powder was investigated for the samples successfully grown with LR2. It was observed that a number of grains exhibited double facet lines and, in some cases, there was tilting of the facet lines that resulted in tilting of the *c*-axis, although it was unclear why this had happened. One possible reason was the buffer pellet may have impeded the grain nucleation and growth process. The precursor powder pellet used for the sample with the greatest tilting of the facet lines had been sintered at 993 °C and so in the next stage of the investigation this sample was grown under the same conditions without a buffer pellet. An additional sample grown by the conventional TSMG process was also grown without a buffer pellet for comparison with the standard sample. These were assembled as described in Chapter 2 except the seed was placed directly onto the top surface of the precursor powder pellet.

After single grain samples with reasonable trapped fields had been produced, larger samples were grown using the optimised processing conditions. The growth of larger single grain samples amplified the scale of problems observed in the smaller samples. This was particularly noticeable for cracking that occurred at the base of the sample and the excess liquid-phase-rich powder. The cracking was thought to be due to the stresses induced by the difference in shrinkage of the pressed

Yb₂O₃ powder stabilising layer and the precursor pellet during melt growth. The layer of pressed Yb₂O₃ powder was removed to reduce the magnitude of the cracking. Initially this powder was completely removed, which resulted in a secondary grain nucleation from a ZrO₂ rod. In order to eliminate this secondary grain nucleation from a rod, a thin layer of Yb₂O₃ was painted on by mixing with ethanol, as carried out for the base of the precursor powder pellet in conventional buffer-aided TSMG. This reduced the thickness of the stabilising layer and so the stresses induced by differential shrinkage, and thus the likelihood and extent of cracking at the base.

The optimisation stages and the resulting outcomes of these samples of 20 to 21 mm in diameter are given in Table 4.1 and images of each sample are shown in Fig. 4.4. The effect of each optimisation stage on the properties of the samples are discussed in the sections below.

Sample	Growth conditions	Observations post-growth
JY-01	Standard buffer aided TSMG	Double facet line
JY-02	Standard buffer aided TSMG, cooling rate reduced	Small secondary grain
JY-03	Buffer aided TSMG with 3 g LR 2 powder, small die	Lots of cracks and not fully grown to the base
JY-04	Buffer aided TSMG with 3 g LR 2	Fully grown
JY-05	Buffer aided TSMG with 3 g LR 2, precursor sintered at 943 °C	Fully grown
JY-06	Buffer aided TSMG with 3 g LR 2, precursor sintered at 993 °C	Fully grown, but facet lines do not all extend to the base
JY-07	Buffer aided TSMG with 3 g LR 2, precursor sintered at 1043 °C	Fully grown, less offset of facet lines
JY-08	Buffer aided TSMG with 3 g LR 1	Fully grown
JY-09	Buffer aided TSMG with 3 g LR 3	Double facet line
JY-10	TSMG with 3 g LR phase, no buffer, precursor sintered at 993 °C	Fully grown
JY-11	TSMG, no buffer and no LR phase	Small secondary grain
JY-12	Buffer aided TSMG with 3 g LR 2, precursor sintered at 943 °C	Double facet line
JY-13	TSMG, no buffer, with 3 g LR 3	Small secondary grain due to seed failure
JY-14	Buffer aided TSMG with 4.62 g of LR 3, 1 inch diameter sample	Fully grown
JY-15	Buffer aided TSMG with 3 g LR 3, no Yb ₂ O ₃	Secondary grain nucleated from rod
JY-16	Buffer aided TSMG with 3 g LR 3, Yb ₂ O ₃ mixed with ethanol painted on base	Fully grown
JY-17	Buffer aided TSMG with 4.62 g LR 3, Yb ₂ O ₃ mixed with ethanol painted on base, 1 inch sample	Double facet line at top, small angle grain boundaries on top surface
JY-18	Buffer aided TSMG with 4.62 g LR 3, Yb ₂ O ₃ mixed with ethanol painted on base, 1 inch sample, reduced cooling rate	Secondary grain nucleated from rod, more straight and parallel lines on top surface (less misalignment of low angle grain boundaries)

Table 4.1: A table summarising the growth conditions and the post-growth observations for each sample grown in the optimisation process.

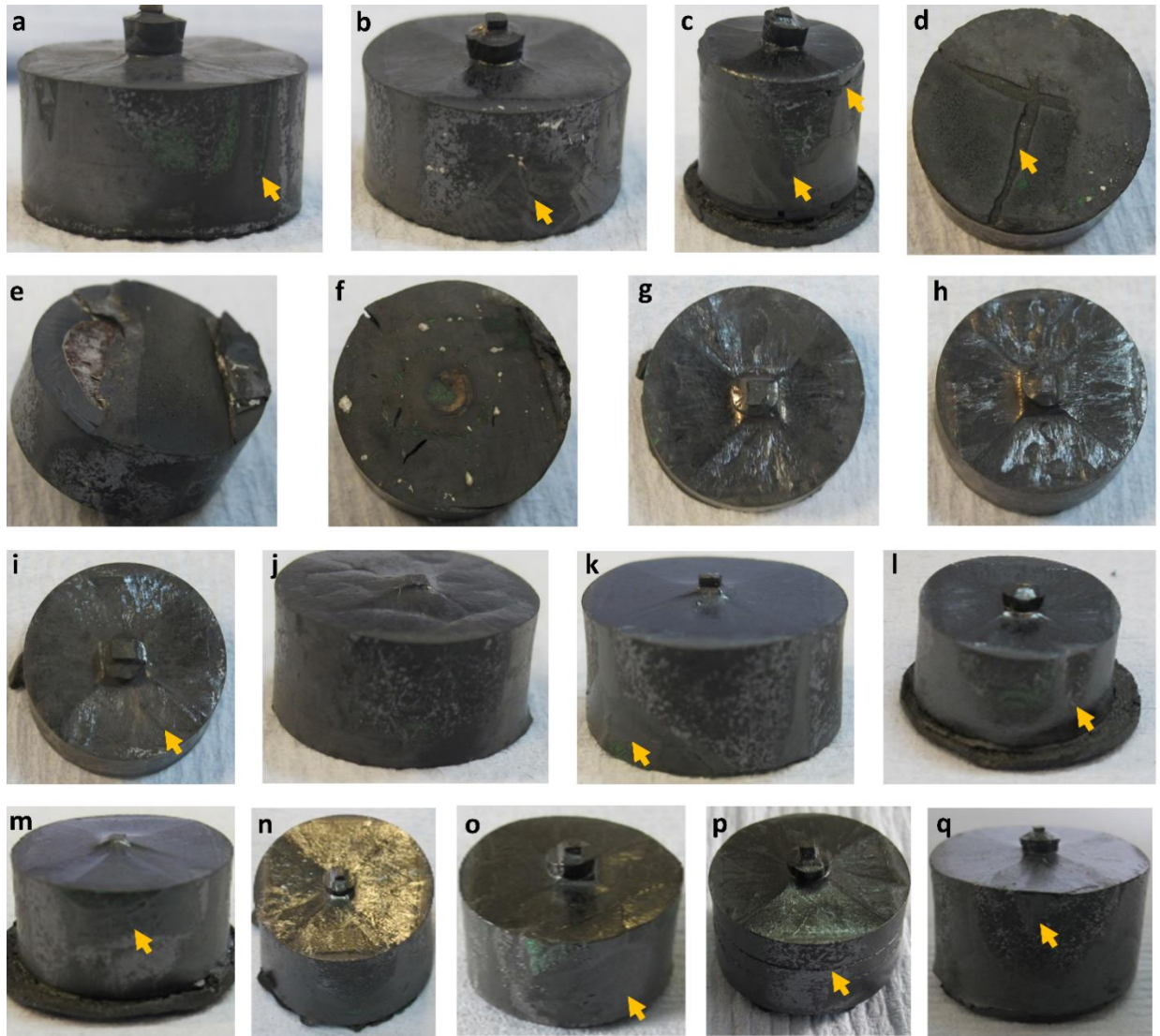


Figure 4.4: Photographs of the samples with observations labelled by the yellow arrows: a) JY-01 with a double facet line, b) JY-02 with a small secondary grain, c) JY-03 with lots of cracking and not fully grown to the base, d) JY-04 base with post-oxygenation cracking, e) JY-05 base showing post oxygenation cracking, f) JY-06 base showing post oxygenation cracking, g) JY-07, h) JY-08, i) JY-09 with a double facet line, j) JY-10, k) JY-11 with a secondary grain, l) JY-12 with a double facet line, m) JY-13 with a secondary grain due to seed failure, n) JY-14, o) JY-15 with a secondary grain nucleated from the ZrO_2 rod, p) JY-16 with cracking, q) JY-17 with a double facet line.

4.3 Superconducting properties

All samples were oxygenated and the trapped field of a large number of these samples was then measured. The J_c and T_c values of a number of sub-specimens cut from JY-02 and JY-09 were measured to enable the effect of additional liquid-phase-rich powder on the superconducting properties to be studied.

4.3.1 Trapped field

A typical trapped field profile of a single grain sample is shown in Fig. 4.5. Single grains typically exhibit a characteristic trapped field profile consisting of a single peak that decreases radially and continuously with distance from the seed. The maximum trapped field values measured at the top and base of each sample are given in Table 4.2 alongside their difference. Sample JY-03 was not measured as it was pressed in a smaller die and so will not produce results comparable to the other samples. JY-05 had a very large crack after oxygenation and could also not be used to form a fair comparison to the other samples.

Due to the variability between samples, even those processed under the same conditions using the same powder, care must be taken when interpreting the results. Typical single grains of YBCO processed under the same conditions often exhibit differences in maximum trapped field of 0.05 T. Therefore, it is important to note that some of the observed differences may just be due to sample to sample variation, to improve the evidence for the conclusions drawn from the data many more samples of each type should be produced, this was not carried out in this study due to time constraints; each sample takes at least a week to produce and each sample is produced individually.

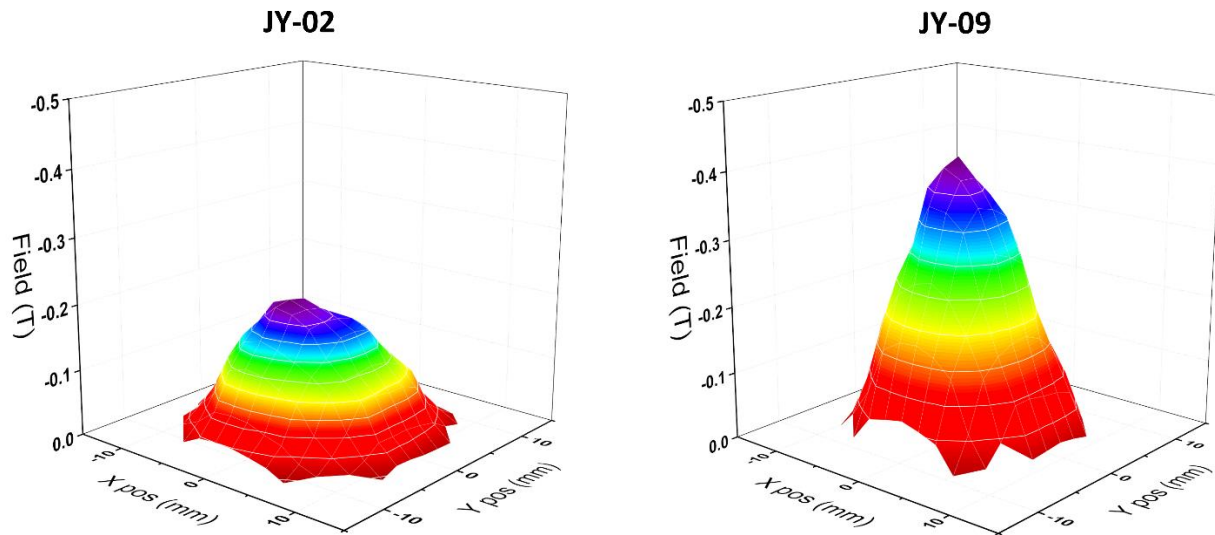


Figure 4.5: Characteristic trapped field profiles for the base of samples JY-02 and JY-09.

Sample	Maximum trapped field (T)		
	Top	Bottom	Difference
JY-01	0.45	0.35	0.10
JY-02	0.53	0.26	0.27
JY-03	-	-	-
JY-04	0.54	0.48	0.06
JY-05	-	-	-
JY-06	0.52	0.39	0.14
JY-07	0.52	0.42	0.10
JY-08	0.51	0.46	0.05
JY-09	0.60	0.55	0.05
JY-10	0.36	0.27	0.09
JY-11	0.38	0.25	0.13
JY-12	0.49	0.50	0.01
JY-13	0.43	0.39	0.04
JY-14	0.72	0.50	0.21
JY-15	0.54	0.38	0.16
JY-16	0.53	0.41	0.12
JY-17	0.56	0.57	0.01
JY-18	0.65	0.44	0.21

Table 4.2: Maximum trapped field measurement at the surface, measured using a single Hall probe and corrected for use in liquid nitrogen.

The trapped field profiles for JY-06 and JY-10, sintered samples grown with and without a buffer pellet, respectively, are shown in Fig. 4.6. These profiles show that the plot for the top surface of the single grain with a buffer exhibits more circular contour lines, and so a more uniform trapped field distribution. The maximum trapped field values at both the top and base were higher for the sample grown with a buffer (0.52 T compared to 0.36 T and 0.39 T compared to 0.27 T respectively). The same behaviour was observed for samples JY-02 and JY-11, grown by the conventional TSMG process with and without a buffer pellet; and for samples JY-09 and JY-13, grown using additional liquid-phase-rich powder with and without a buffer pellet. These data suggest the use of a buffer pellet improves the magnitude and uniformity of the superconducting properties at the top of the sample. It also suggests that the use of a buffer may have a slight

positive, albeit limited, effect on the trapped field exhibited at the base, when the absolute magnitude of the trapped field in each set of samples is considered.

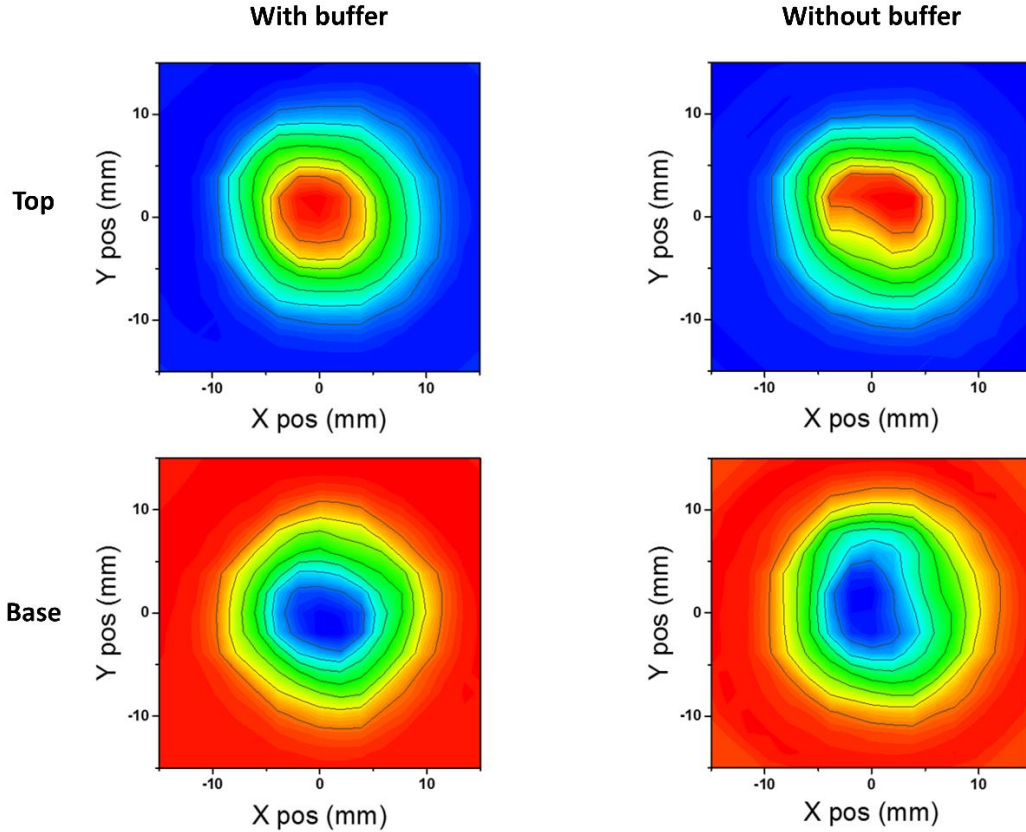


Figure 4.6: Trapped field profiles for samples JY-06 and JY-10 grown with and without a buffer pellet.

The trapped field profile for sample JY-02, fabricated without liquid-phase-rich powder, and JY-04, provided with LR 2, are shown in Fig. 4.7. The maximum trapped field at the top of both samples is similar, 0.53 T in JY-02 and 0.54 T in JY-04. The trapped field profiles for both samples show a similar distribution of trapped field at the top surface. This suggests additional liquid-phase has no effect on the trapped field at the top of the sample. At the base of the sample provided with additional liquid-phase, the maximum trapped field was significantly higher than the value recorded for the standard sample, 0.48 T compared to 0.26 T. The trapped field profile at the base of the sample provided with additional liquid-phase was more uniform than that for the standard sample. This is shown by the more circular and evenly distributed lines within the trapped field profile. This suggests the provision of additional liquid-phase produces samples with a larger magnitude and more uniform trapped field at the base.

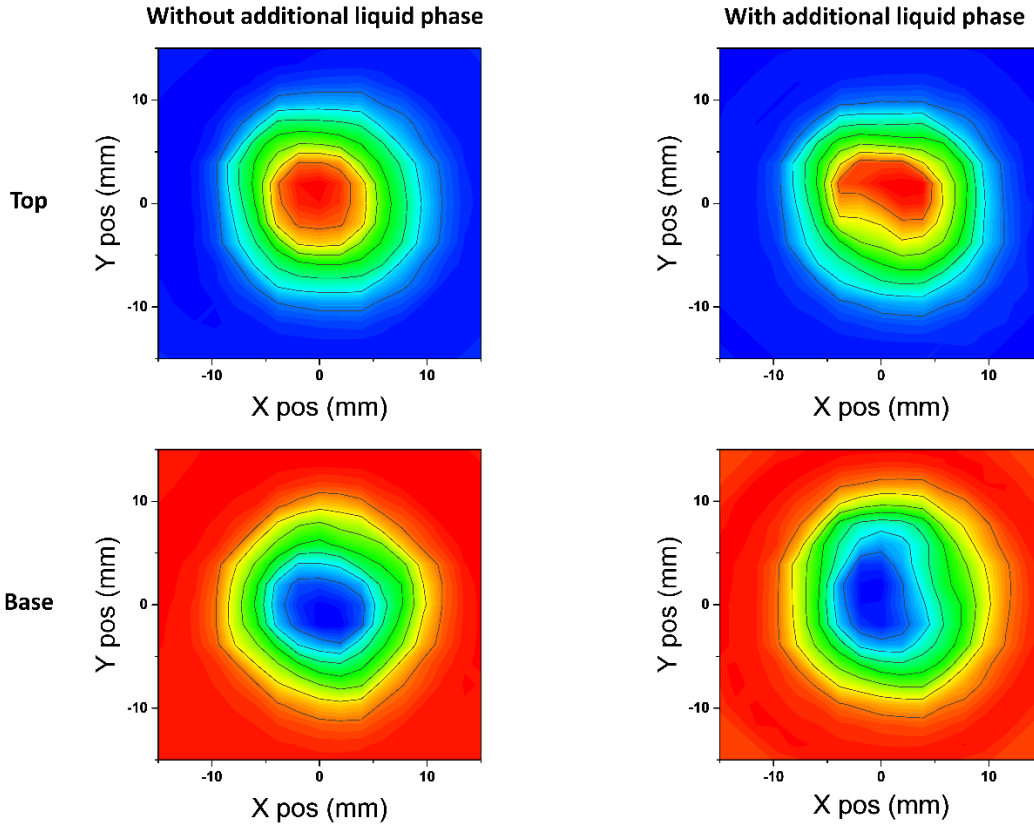


Figure 4.7: Trapped field profiles of samples grown with and without additional liquid phase.

The trapped field profiles of JY-04, grown with LR 2, JY-08, grown with LR 1, and JY-09, grown with LR 3 are shown in Fig. 4.8. These plots show the addition of liquid-phase has no effect on the trapped field profile at the top surface of the samples. However, at the base of each of the samples the uniformity of the trapped field is much higher than for samples grown by standard TSMG. The provision of additional liquid-phase-rich powder of any of the types increases the maximum trapped field at the base and so reduces the difference in maximum trapped field between the top and base of the sample. The largest maximum trapped field at the base occurred for the sample provided with LR 3, at 0.55 T compared to 0.48 T in JY-04 and 0.46 T in JY-08. This suggested LR 3 was the optimum liquid-phase-rich powder composition to use to achieve the highest magnitude of trapped field at the base of the sample. However, it should be noted the trapped field values are quite similar, so this difference may be due to the random variation in the superconducting properties between samples of the same type.

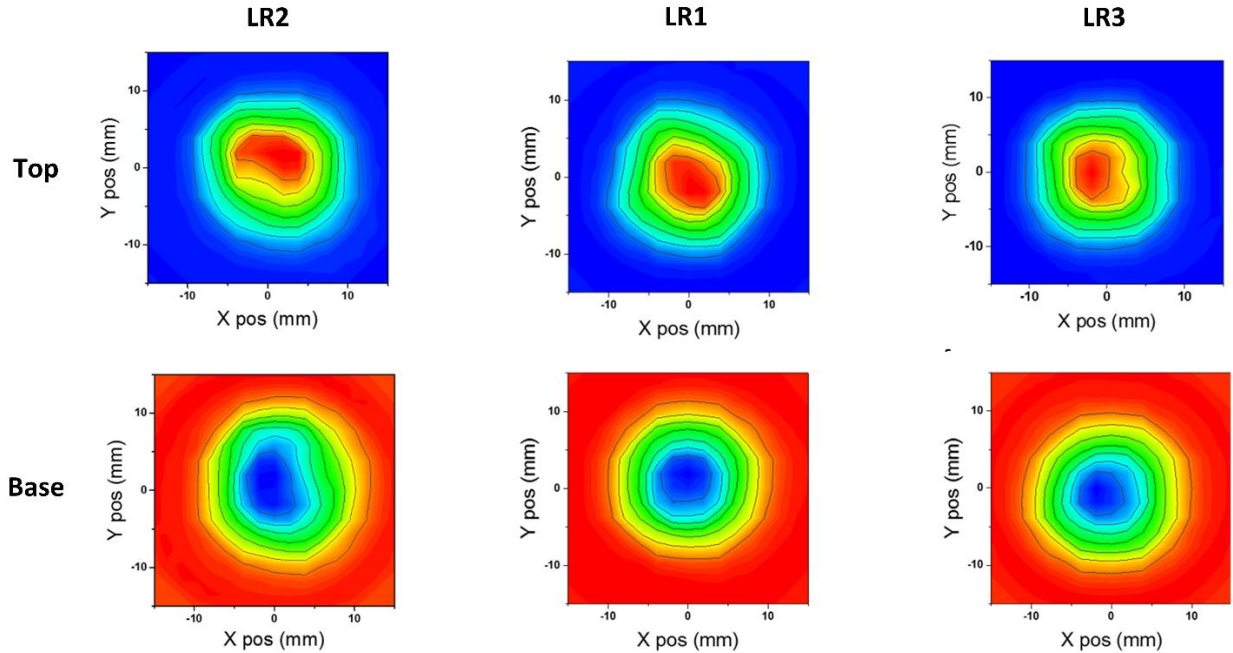


Figure 4.8: Trapped field profiles of samples grown with different liquid-rich powders.

The trapped field profiles for sample JY-04, where the precursor powder pellet has not been sintered, and samples JY-12, JY-06 and JY-07, where the precursor powder pellet has been sintered for 4 h at 943 °C, 993 °C and 1043 °C, respectively, are shown in Fig. 4.9. A plot of the maximum trapped field values at the top and base are shown in Fig. 4.10. The trapped field profiles have shown that sintering of the precursor powder pellet did not noticeably improve the uniformity of the trapped field profile. The plot in Fig. 4.10 shows that sintering of the precursor powder pellet has a limited effect on the magnitude of the trapped field. It was concluded that sintering of the precursor pellet was not necessary since the sintering of the precursor pellet does not have a significant positive effect on the trapped field, and adds extra complexity to the processing.

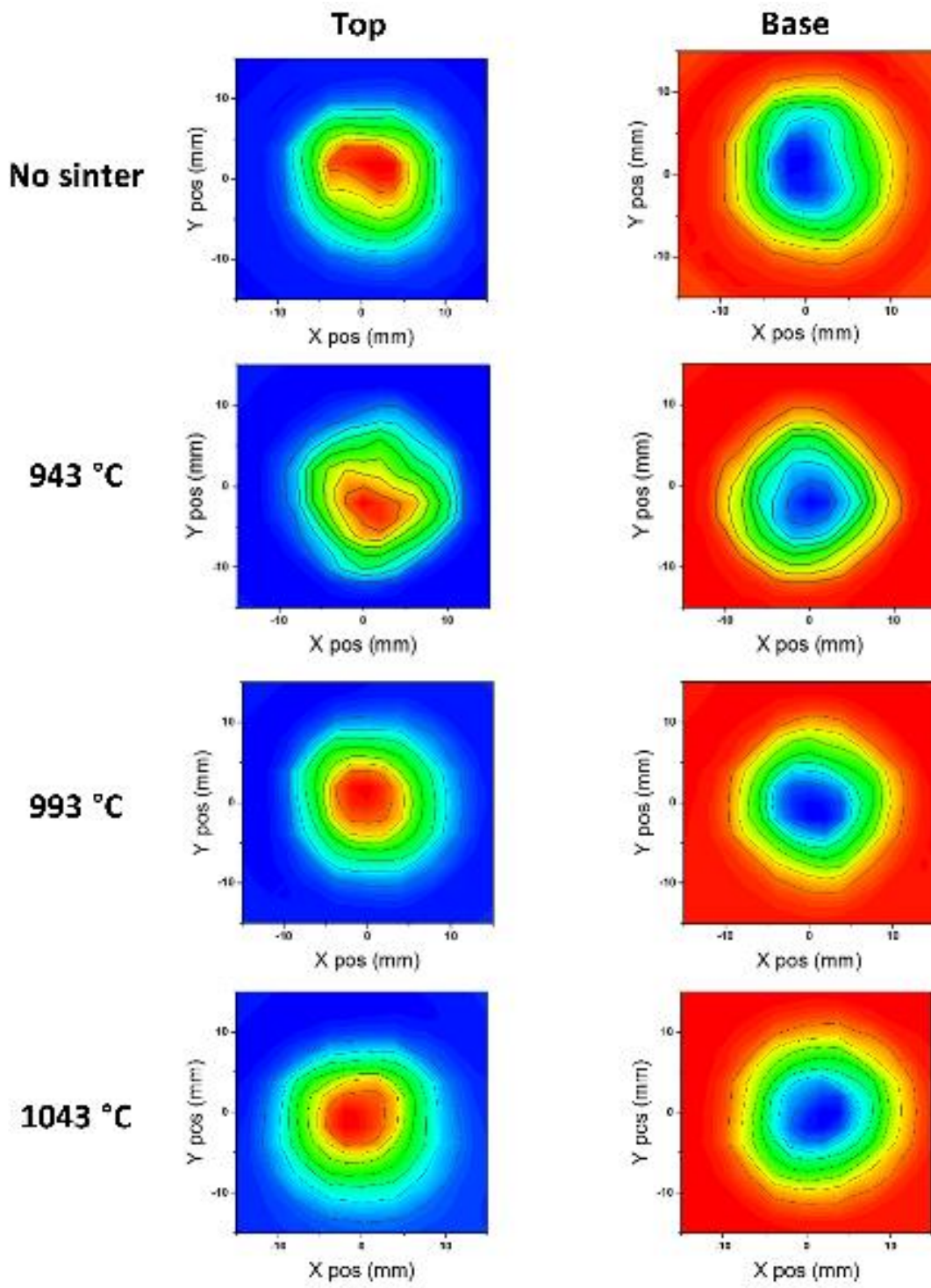


Figure 4.9: Trapped field profiles of samples with precursor pellets sintered at a number of temperatures.

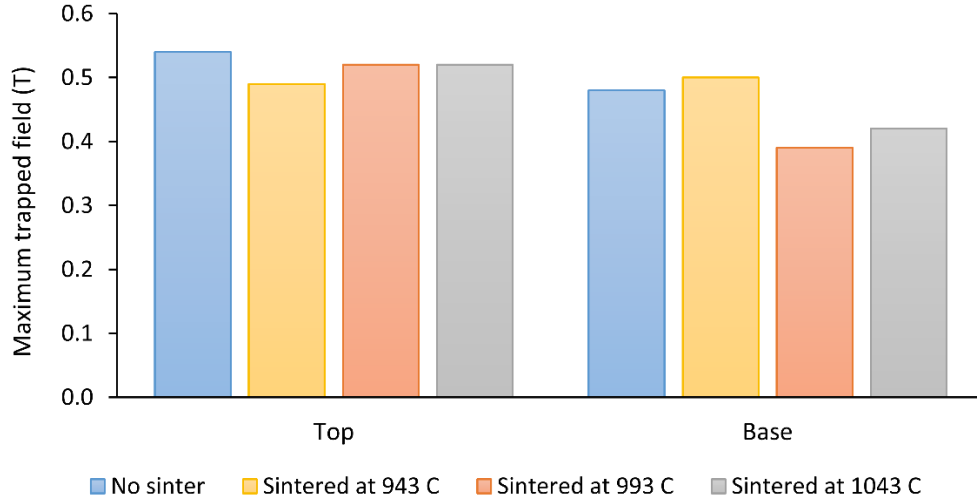


Figure 4.10: A graph showing the difference in maximum trapped field due to the sintering temperature of the precursor powder pellet.

4.3.2 Transition temperature

Samples were cut and analysed as described in Chapter 2. A number of sub-specimens from each sample were analysed to study the variation in the values of T_c along the c -axis. The location and labelling of each piece is shown schematically in Fig. 4.11.

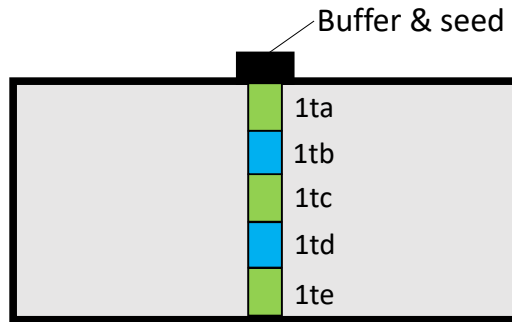


Figure 4.11: A schematic of the locations of the sub-specimens cut from each bulk.

The value of T_c for each sub-specimen measured is given in Table 4.3. The value of T_c is very similar in all sub-specimens within each sample; in all cases it is between 90 K and 91 K. This consistency in the measured values of T_c is expected.

An additional parameter, ΔT_{90} , is used to characterise the quality of single grain YBCO. The ΔT_{90} value has exhibited a larger variation between sub-specimens and between samples than the value

of T_c . It can be seen from the shallower gradient of the transition that the ΔT_{90} value increases with distance from the seed for both samples and then reduces at the base for JY-09. The corresponding 1te sub specimen could not be analysed for JY-02 because this sub specimen was outside the single grain region. The distribution of ΔT_{90} suggests that the provision of additional liquid-phase has a significant impact upon improving the quality and uniformity of superconducting properties at the base of the sample in comparison to a sample grown by conventional TSMG.

Sample	Sub-specimen	T_c (K)	ΔT_{90} (K)	$J_c(0)$ (MA m ⁻²)
JY-02	1ta	90	1.8	32
	1tb	91	2.6	287
	1tc	91	2.9	610
	1td	91	4.3	190
JY-09	1ta	91	1.5	369
	1tb	91	1.7	388
	1tc	91	2.2	446
	1td	91	3.4	217
	1te	91	2.0	161

Table 4.3: A table showing the values of the superconducting properties for each sub-specimen derived from the SQUID data.

4.3.3 Critical current density

The values of J_c were calculated as described in Chapter 2. The maximum J_c values for each sub-specimen are given in Table 4.3. The maximum J_c value is higher for all corresponding sub-specimens from sample JY-09 than from sample JY-02, except for the 1tc sub-specimen where the maximum J_c value is much higher for sample JY-02. A trend of increasing maximum J_c value with distance from the seed until midway along the c -axis of the specimen can be seen, after which point the maximum J_c value decreases with distance from the seed. As in the case of the T_c value measurement, the J_c value for sub-specimen 1te could not be measured for sample JY-02 because this region was not part of the single grain region.

4.4 Density and Porosity

The mass and dimensions of the samples after polishing were recorded. These values were used to calculate the approximate density of each of the samples using:

$$\rho = \frac{m}{\pi R^2 h} \quad (4.1)$$

where m is the sample mass, R is the average radius and h is the average height.

The samples were polished before measurements were taken to ensure the sample was a cylinder to enable simple calculation of the volume and to remove any excess liquid-phase which remained as this may have a very different microstructure and so would not allow the density to be accurately compared with samples grown by conventional TSMG.

The density of each sample is shown in Fig. 4.12. It can be seen that the sample with the precursor powder pellet sintered at 993 K and provided with LR 2, sample JY-06, had the highest density. This plot shows that for the growth conditions investigated, there is no correlation between the average density and the maximum trapped field observed.

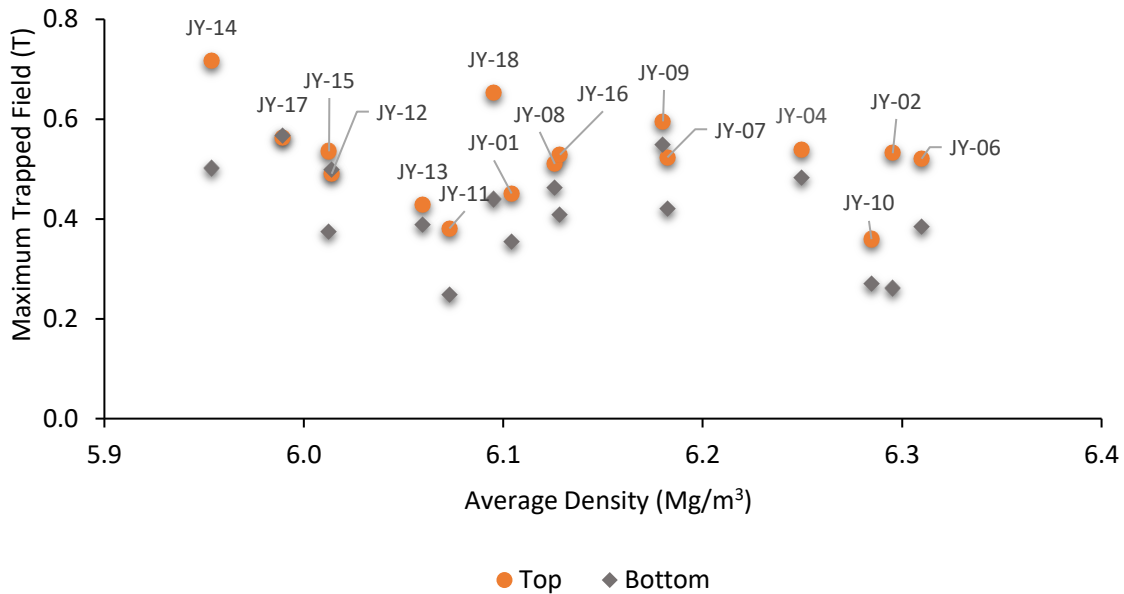


Figure 4.12: A plot to show the relationship between average density and trapped field.

The porosity of a number of the samples was analysed using a low magnification microscope to identify the effect of sintering and different compositions of liquid-phase-rich powders on the porosity of the final sample. The samples were prepared as described in Chapter 2. Four samples; JY-02 grown without additional liquid-phase, JY-04 grown with LR 2, JY-07 with a sintered precursor powder pellet and JY-09 with LR 3 were studied to observe the differences in porosity. Images of the four samples are shown in Fig. 4.13. These images show JY-02 had not fully grown to the base. There is no significant observable difference in the amount or distribution of pores between the samples. It is also apparent that there are less pores at the edges of all of the samples; this is because the gas is able to diffuse out easily at the edges but cannot diffuse fast enough from the centre to escape from the sample before solidification occurs.

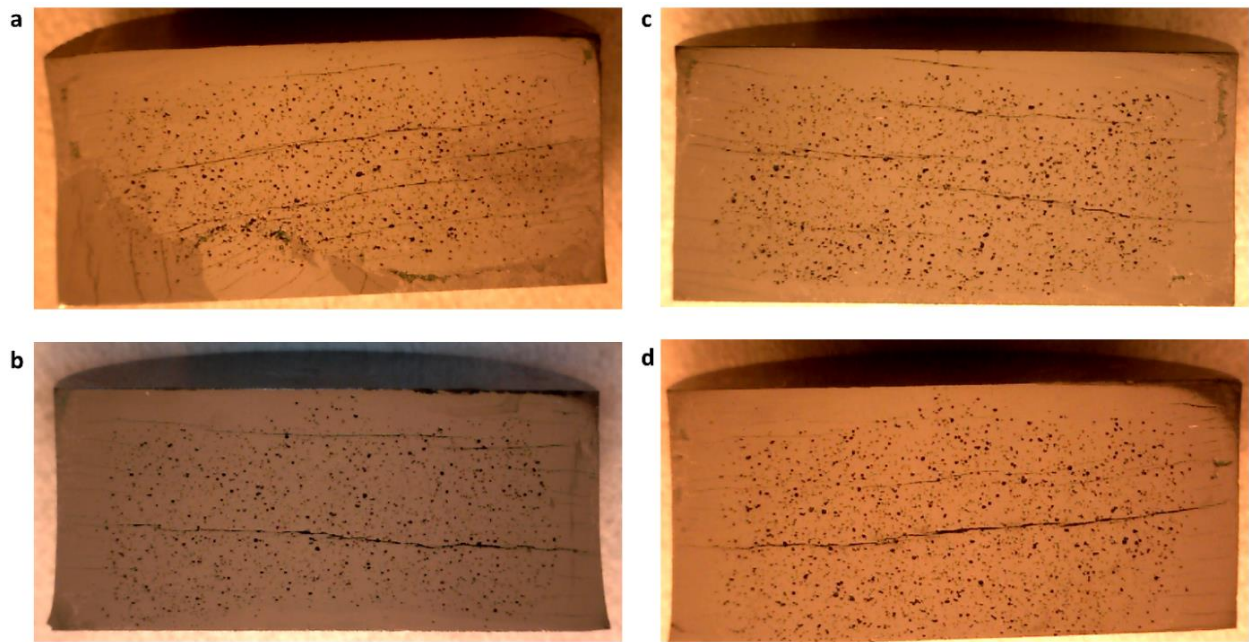


Figure 4.13: Low magnification images of samples a) JY-02 no sintering and no additional liquid-phase-rich powder, b) JY-04 no sintering with LR 2, c) JY-07 sintered at 1043 °C with LR 2 and d) JY-09 no sintering with LR 3, all four samples are approximately 21 mm in diameter.

4.5 Microstructure

The rectangular cross section of one half of each of JY-02 and JY-09 was imaged using the optical microscope. Images were taken at millimetre intervals along the a/b -axis at 1 mm from the top and along the central c -axis, sample JY-02 was imaged at 1.5 mm from the base, whereas sample JY-09 was imaged at 1 mm from the base, to ensure images were taken within the single grain region.

Magnifications of 5x and 50x were used to observe the pore and crack distribution (shown in black in the optical microscope images) while a magnification of 1000x was used to observe the size of the Y-211 inclusions and their distribution (shown in grey in the optical microscope images). In addition, these two samples were imaged using the SEM at 1 mm intervals along the *a/b*-axis approximately 1 mm from the top and base and along the central *c*-axis.

At the top of the sample the porosity reduces with distance from the seed in the horizontal direction. Each image reveals a similar pore size, pore distribution and area fraction of pores in both samples, these images are shown in the appendix. In both samples the area occupied by Y-211 particles increased with distance from the seed with some Y-211 deficient regions present in both samples, as explained, in part, by the push-trap theory. These results suggest that provision of additional liquid-phase has relatively little, if any, effect on the microstructure at the top of the sample. The relevant images are shown in the appendix. However, at the base of the sample, there are significant differences between the two samples; the most obvious being that the single grain region does not fully extend to the base for the sample grown without additional liquid-phase powder. When the single grain regions at the base were compared, as shown in Figs. 4.14 and 4.15, at 50x magnification it can be seen that the pore distribution is much more uniform in the sample provided with additional liquid-phase and that this sample also exhibits less cracking. The 1000x magnification images show that in both samples there is a trend of increasing area occupied by Y-211 particles with horizontal distance from the seed. Sample JY-09, grown with the additional liquid-phase-rich powder, has a much more uniform distribution of Y-211 particles throughout the sample while sample JY-02, grown without additional liquid-phase-rich powder has large regions completely deficient in Y-211 particles. The Y-211 particles within sample JY-09 are larger, showing an elongated shape in comparison to the Y-211 particles seen in sample JY-02, as shown in Figs. 4.16 and 4.17. As sample JY-09 has a more uniform distribution of Y-211 particles and exhibits less porosity and cracking, then there will be more superconducting Y-123 phase present in this sample and this is more uniformly distributed.

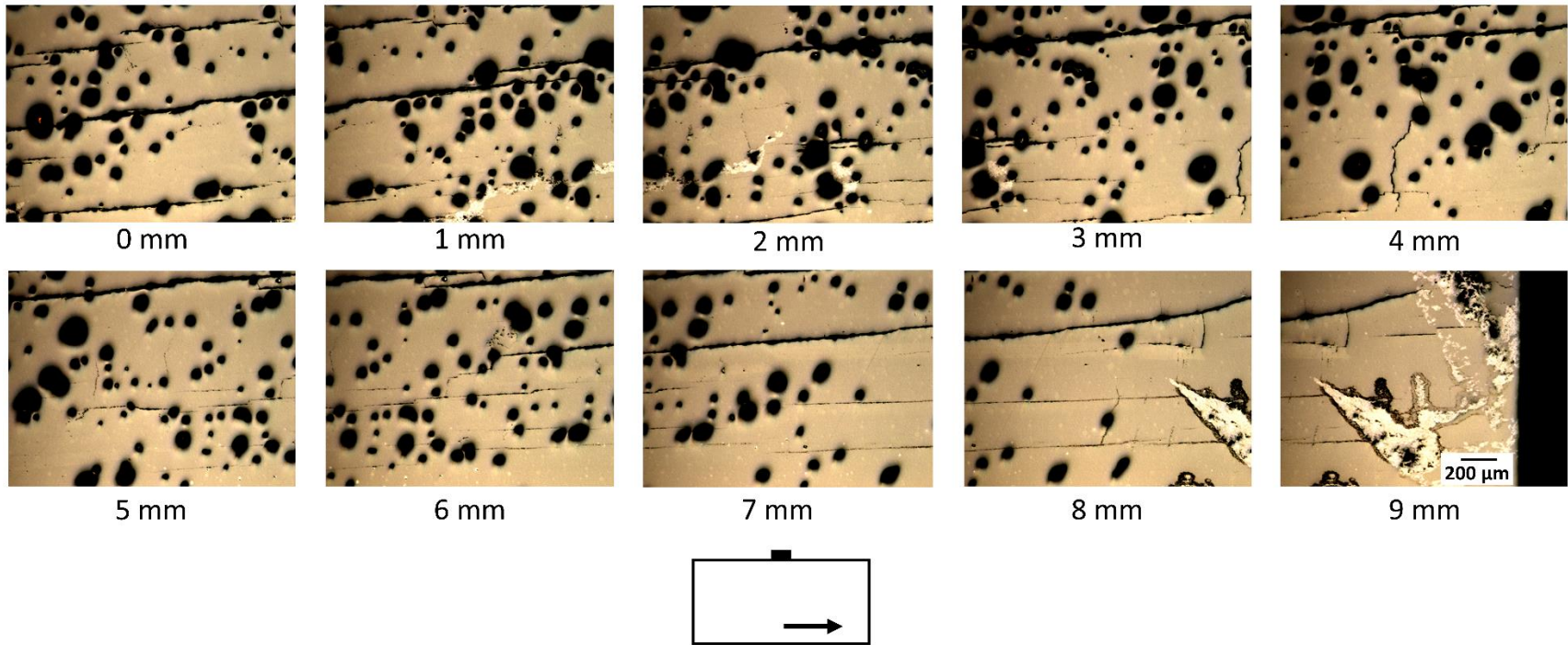


Figure 4.14: Optical microscope images along the a/b -axis of sample JY-02 approximately 1.5 mm from the base at 50x magnification.

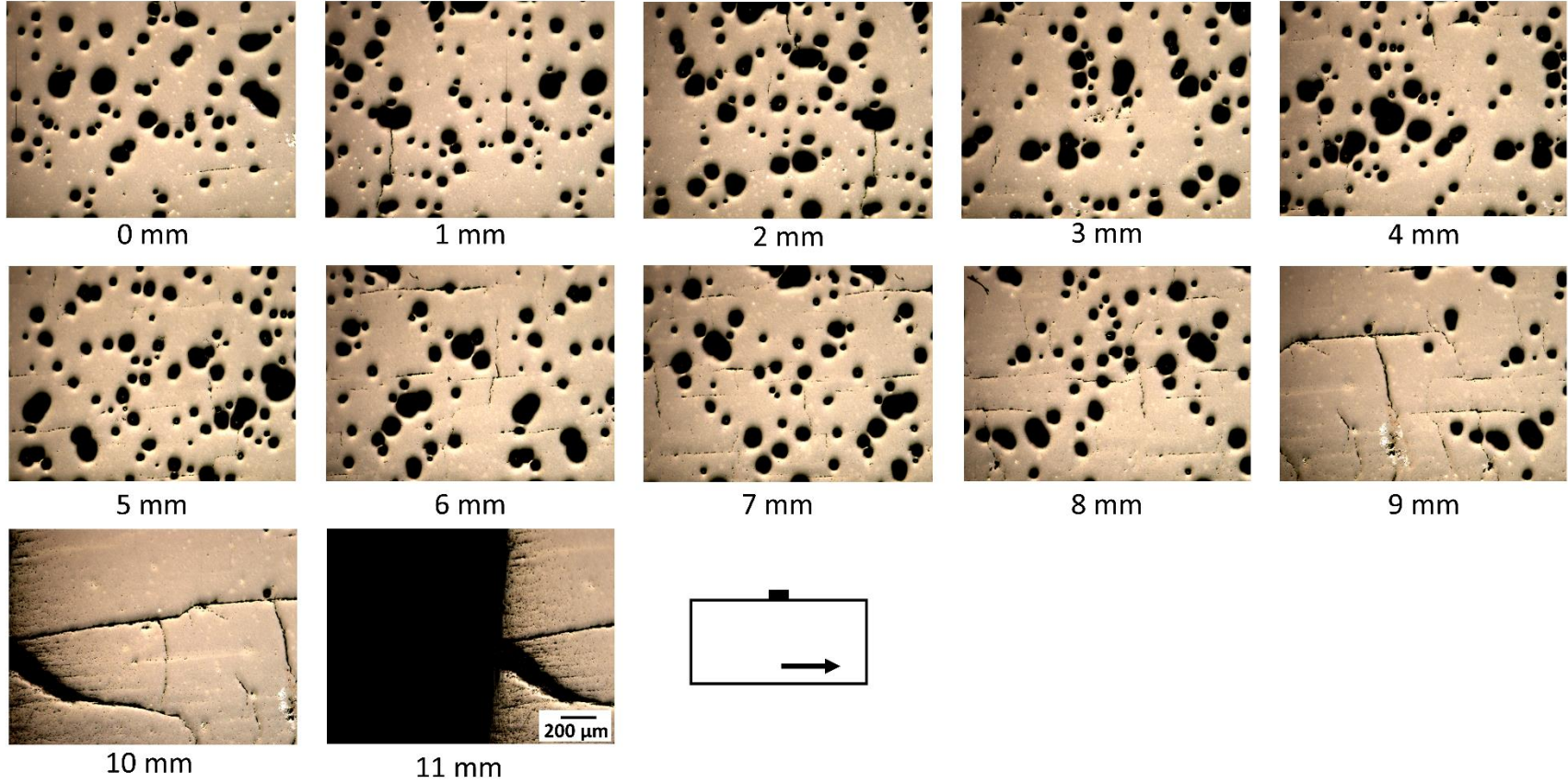


Figure 4.15: Optical microscope images along the a/b -axis of sample JY-09 approximately 1 mm from the base at 50x magnification.

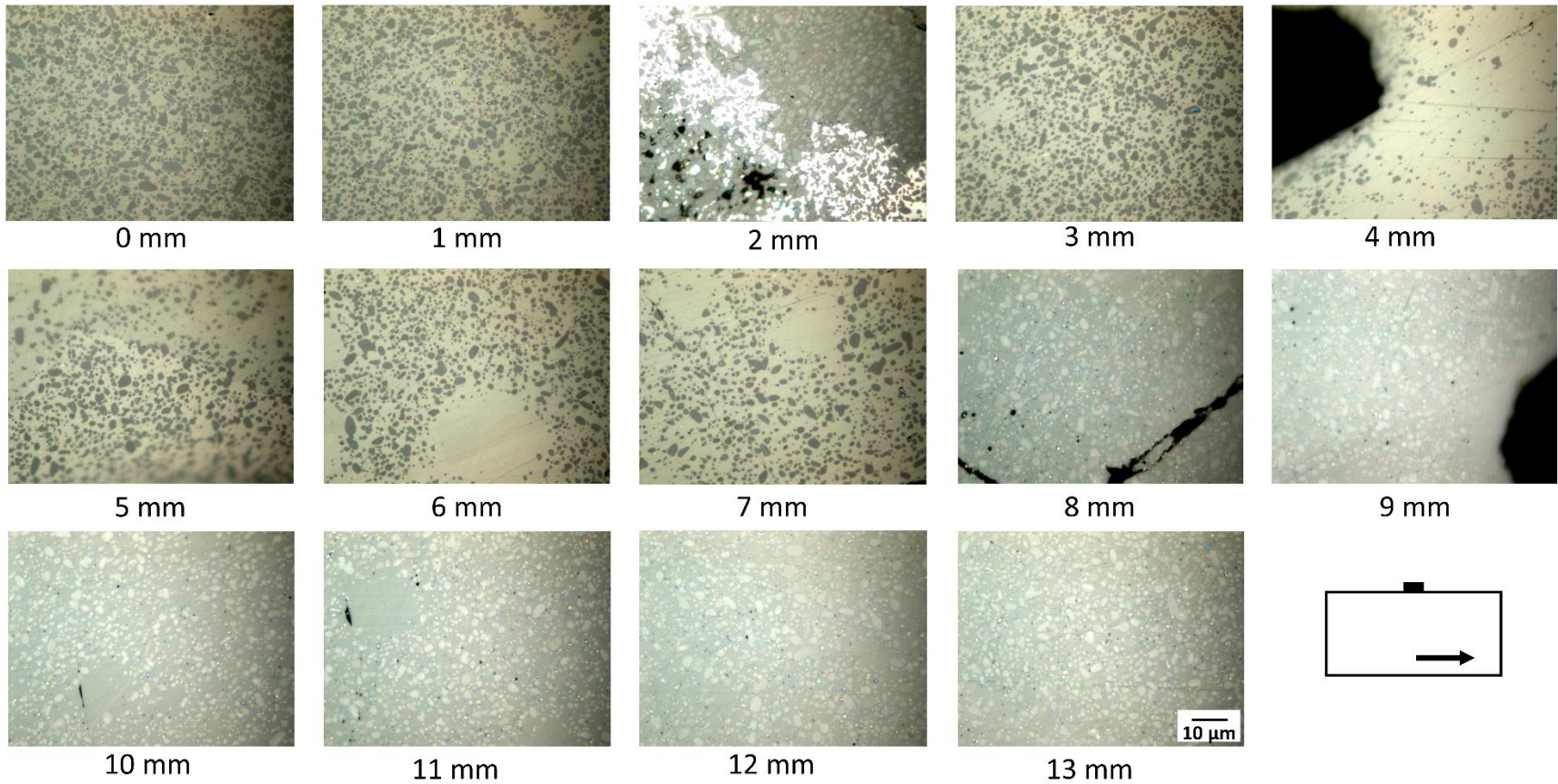


Figure 4.16: Optical microscope images along the a/b -axis of sample JY-02 approximately 1.5 mm from the base at 1000x magnification.

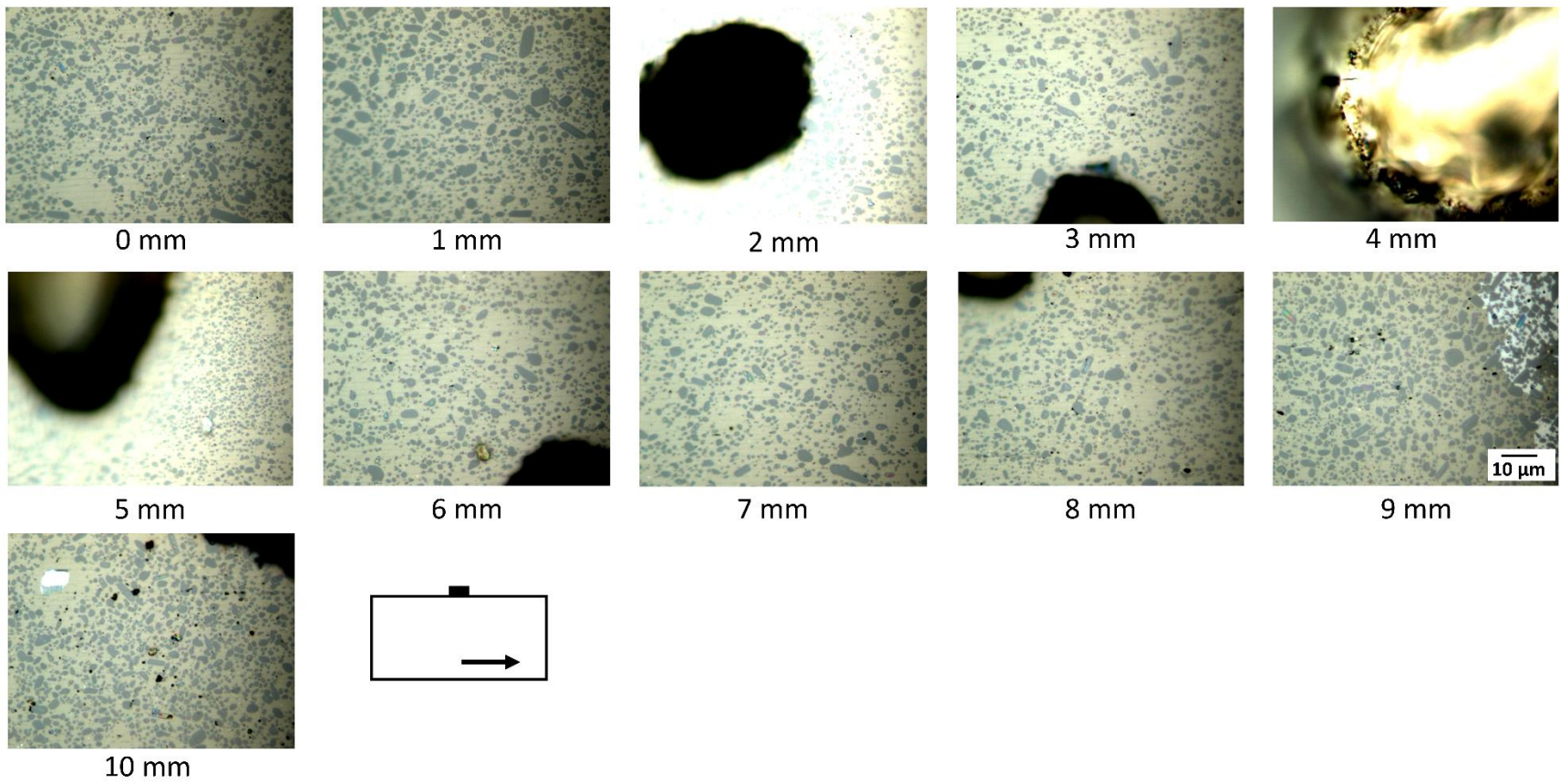


Figure 4.17: Optical microscope images along the *a/b*-axis of sample JY-09 approximately 1 mm from the base at 1000x magnification.

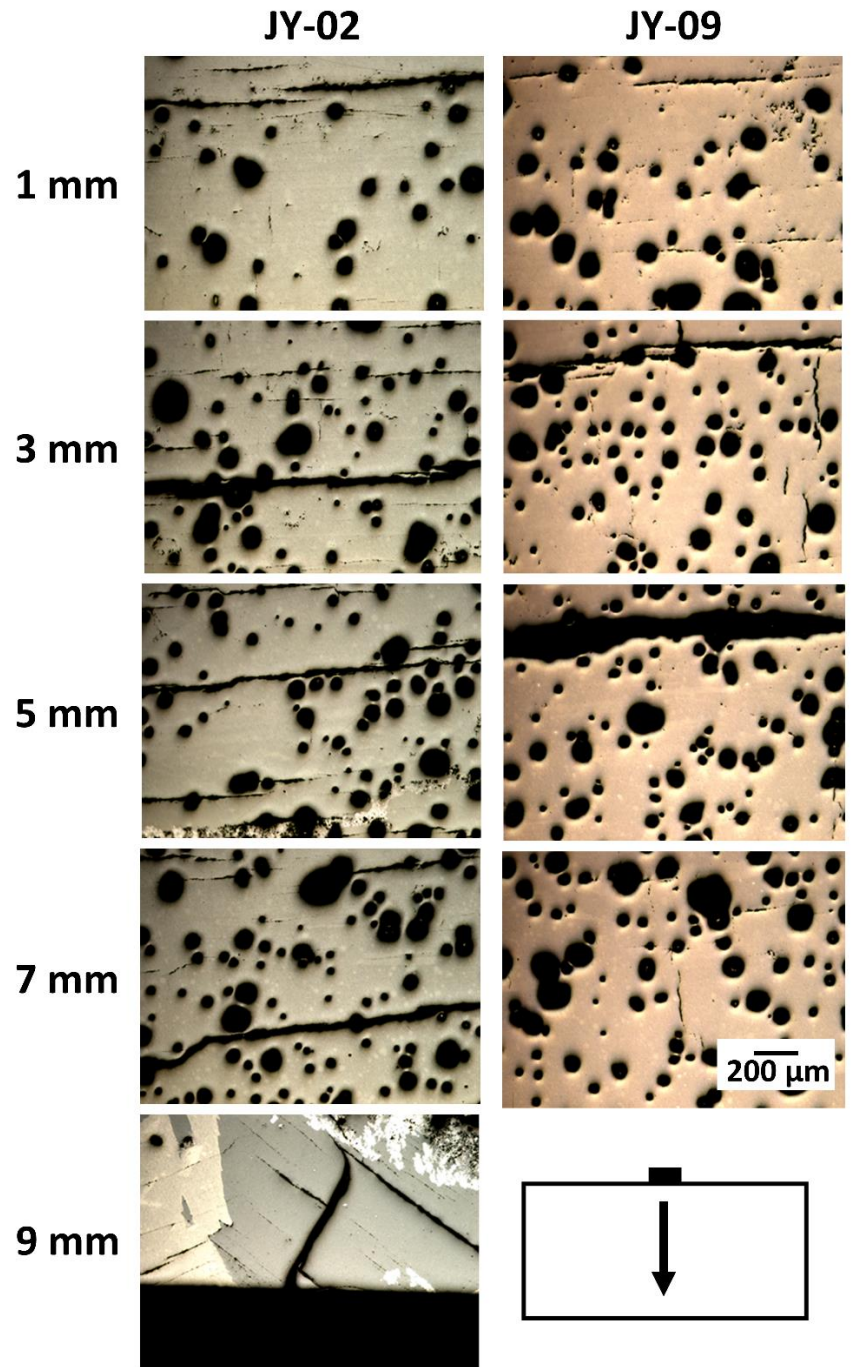


Figure 4.18: Optical microscope images along the c-axis of sample JY-02 and JY-09 from approximately 1 mm directly below the seed at 50x magnification.

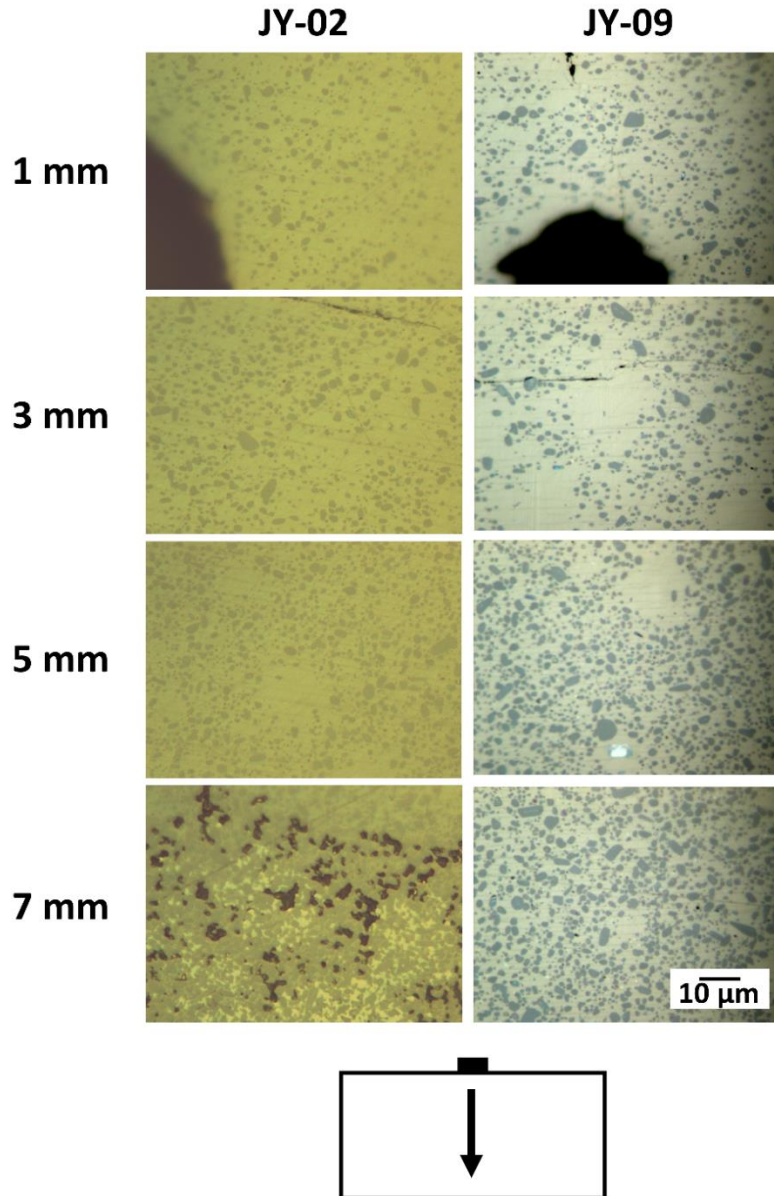


Figure 4.19: Optical microscope images along the c -axis of samples JY-02 and JY-09 from approximately 1 mm directly below the seed at 1000x magnification.

The images taken along the c -axis, shown in Fig. 4.18, indicate that sample JY-02 was not fully grown to the base, as seen in the image at 9 mm in the figure. Sample JY-09, on the other hand, was fully grown to the base. This suggests that provision of additional liquid-phase enables the growth of the single grain region to extend to the base of the sample. Sample JY-09 shows less cracking than sample JY-02. This is likely to be due to the ability of the additional liquid-phase to infiltrate into the sample filling pores and cracks, thus enabling more Y-123 phase to be present. The distribution of Y-211 particles is much more uniform in the c -axis direction for sample JY-09

than for sample JY-02, as shown in Fig. 4.19, suggesting that the additional liquid-phase also has an effect upon the distribution of the Y-211 particles.

Comparison of the top and base of both samples shows there is greater porosity at the base of the sample with more small pores present. It can be seen that the microstructure of JY-09 is more similar at the top and base of the sample than JY-02, which shows that the provision of additional liquid-phase predominantly affects the base of the sample and that liquid is lost from the base during the TSMG process. In sample JY-02 there are more Y-211 deficient regions at the base than at the top of the sample.

The trend in distribution of Y-211 observed in the SEM images was the same as those observed using the optical microscope, so these images have not been included here.

4.6 Composition

EDX analysis was carried out at each of the locations imaged using the SEM. Composition analysis has shown that the average composition at each location fluctuates from the expected stoichiometric composition, although in the majority of samples, at the majority of the locations imaged, the composition tends to fluctuate around the expected stoichiometric composition. In all three directions imaged, both samples show decreasing normalised Cu at %, almost constant normalised Ba at % and increasing normalised Y at % with distance from the seed, as shown in Fig. 4.20. This shows that the amount of liquid-phase ($\text{Ba}_3\text{Cu}_5\text{O}_8$) available at the growth front during processing reduces characteristically with distance from the seed. Sample JY-02 has slightly larger fluctuations between neighbouring locations and the composition is slightly further from the expected composition. However, these samples show limited differences in the normalised atomic fraction of the elements present at each location.

The location of the edge of the single grain region can be identified using EDX analysis as the point where the normalised Cu and normalised Y begin to strongly converge. This is shown in Fig. 4.20 at a location 11 mm along the horizontal direction at the top in sample JY-02. It should be noted, however, that the distribution of Y-211 was not observed to change suddenly in the microscope images as is suggested by this rapid convergence.

The ratios Y : Ba and Y : Cu from each image have been plotted in Fig. 4.21. The ratios Y : Ba and Y : Cu increase with distance from the seed in all three directions in both samples. Sample JY-02 showed greater fluctuations from the overall trend than sample JY-09, except at the top in the horizontal direction where the ratios are similar and show a similar trend. This suggests that the provision of additional liquid-phase has no effect upon the top of the sample, whereas the provision of additional liquid-phase does have an effect upon the ratio of Y-211 particles to Y-123 matrix with increasing distance down the *c*-axis of the sample. The additional liquid-phase provided has likely enabled an increase in the uniformity of the distribution of Y-211 particles and Y-123 phase towards the base of the sample.

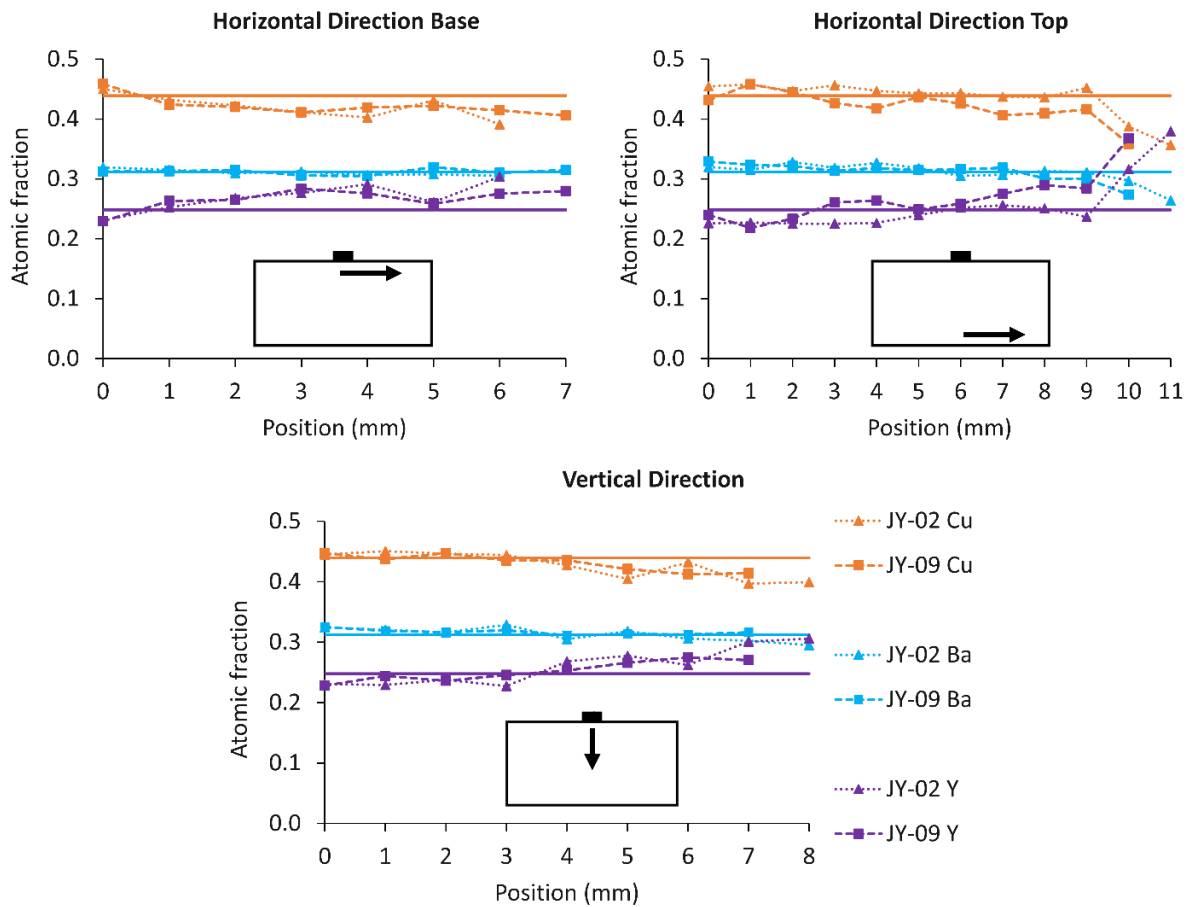


Figure 4.20: Graphs showing the variation in normalised atomic fraction of the elements Cu, Ba and Y at 1 mm intervals from the expected amount with distance from the seed along the three lines imaged using the SEM. JY-02 was grown by conventional TSMG, JY-09 was provided with additional liquid-phase-rich powder.

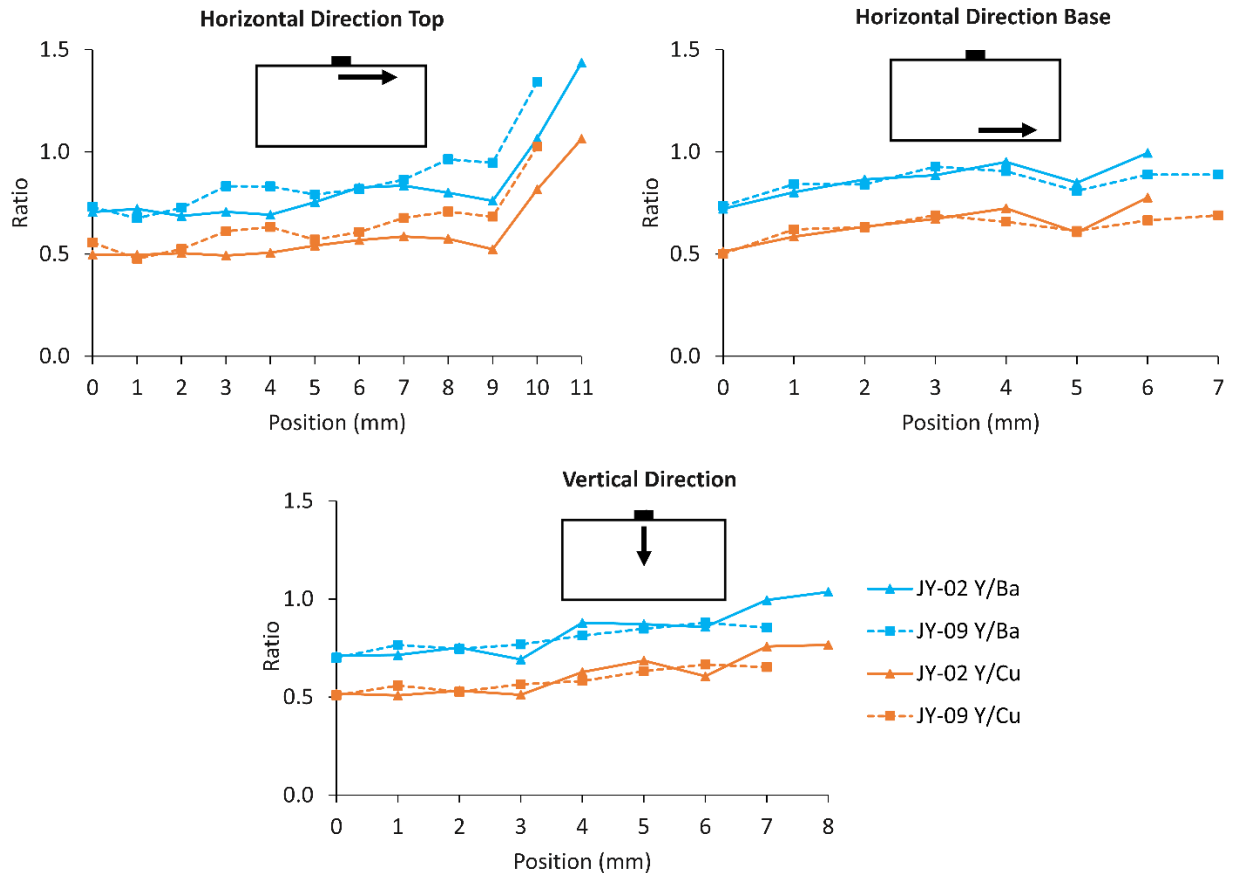


Figure 4.21: Graphs showing the ratios $Y : Ba$ and $Y : Cu$ with distance from the seed at 1 mm intervals along the three directions imaged using the SEM, these ratios correlate with the ratios of Y-123 and Y-211 present.

4.7 Comparison of superconducting properties, microstructure and composition

Provision of additional liquid-phase to the precursor powder pellet during the TSMG growth process has enabled extension of the single grain region in the c -axis direction all the way to the base of the sample. This provision has increased the reliability of full through-thickness growth and has increased the size of the single grain region. This suggests that the provision of additional liquid-phase will enable the peritectic reaction to continue to the edge of the sample in both the c -axis and a/b -axis directions. The liquid-phase carries the Y element and so additional liquid-phase enables a sufficient quantity of Y to be carried to the growth front of the sample. As the growth of a single grain is limited by diffusion of the Y element at the growth front, this additional Y concentration increases the uniformity of the composition at the growth front and provides more reliable growth, and an extended growth region. As the composition at the growth front has a much

greater uniformity, the regions to which the additional liquid is able to infiltrate to provide this effect, predominately the base of the sample, show a much greater uniformity in the Y-211 particle distribution, and thus a much more uniform distribution of Y-123 superconducting phase than for samples grown without additional liquid-phase.

Samples produced by the conventional TSMG process show a decrease in the amount of liquid-phase present with increasing distance from the seed, especially at the base and with greater distances along the c -axis of the sample. The large decrease towards the base of the sample is likely to be due to the loss of liquid-phase during the melt process. The increased uniformity in the liquid-phase distribution and the higher levels of liquid-phase exhibited in the sample provided with additional liquid-phase is likely to be due to the ability of this additional liquid-phase to infiltrate upwards, given that the pellet is placed beneath the base of the pressed precursor powder. Comparison of the two samples has shown that the provision of additional liquid-phase has no effect upon the top of the surface. This suggests that either there is less liquid lost from the top of the sample during conventional TSMG than from the base or that there is less infiltration of additional liquid to the top of the sample during growth with liquid-phase-rich powder. Nucleation occurs during the growth process at the seed on the top surface of the bulk, so the first part of the sample to solidify is the top surface. As the top centre is the first region to solidify, initially there is sufficient liquid-phase, and hence sufficient Y, carried by the liquid when the top surface solidifies. A more uniform composition is observed at the top surface, but as solidification proceeds, the amount of liquid-phase, and thus the amount of Y, arriving at the growth front reduces with distance along the c -axis of the sample. In turn, this reduces the uniformity of both the composition and in the distribution of Y-211 inclusions within the Y-123 matrix.

Alongside the increased uniformity in composition, the provision of additional liquid-phase provides liquid that is able to fill the pores and cracks. The microstructure at the base of the sample and in the lower region of the c -axis of the sample grown with additional liquid-phase exhibits a lower porosity and less cracking than that of a sample grown by conventional TSMG. This is likely to improve both the superconducting properties and the mechanical properties of the sample. The provision of additional liquid-phase increased the trapped field at the base of the sample by 0.29 T.

The small, unreacted Y-211 particles trapped within the Y-123 matrix during peritectic solidification create Y-211/Y-123 interfaces which are able to act as effective flux pinning centres. The increase in uniformity of the trapped field profile at the base of the sample provided with additional liquid-phase can be explained by: the increase in homogeneity of the Y-211 inclusions producing an improved homogeneity of the flux pinning, and the increased homogeneity of Y-123 phase present at the base of the sample. The increase in magnitude of the maximum trapped field measured at the base of the sample provided with additional liquid-phase can be partly explained by the increase in J_c value due to increased uniformity of the Y-211 inclusion distribution. However, it is predominately due to the reduction in porosity and cracking. Also, in this sample, the single grain region extends to the base, and so there is a much larger area over which the superconducting current is able to flow at the base. The magnitude of the trapped field correlates directly with the area available for the superconducting current to flow, with the largest magnitude trapped field occurring for the largest a - b growth sector.

4.8 Conclusions

A number of parameters associated with the widely-used TSMG process have been investigated. These include: the use of a buffer pellet, sintering of the precursor powder pellet prior to TSMG, provision of additional liquid-phase and the use of a mechanically stabilising Yb_2O_3 layer. The effect of these variables and parameters on the successful growth of a single grain of YBCO and its superconducting properties have been investigated. This has enabled a number of parameters to be optimised. The optimum conditions for the growth of a single grain of YBCO by TSMG are: a buffer pellet, additional liquid-phase-rich powder, no prior sintering of the precursor powder pellet, and a stabilising layer of Yb_2O_3 mixed with ethanol painted onto the base.

The provision of additional liquid-phase during the TSMG process has significantly increased the reliability of through-thickness growth. In addition, by providing a more uniform composition at the growth front, it has produced a more uniform distribution of Y-211 particles within the Y-123 superconducting matrix. This increased the quality of the superconducting properties: T_c , J_c and trapped magnetic field values, predominantly at the base of the sample. This provision enabled greater homogeneity in the superconducting properties throughout the sample.

The composition of additional liquid-phase can be further optimised by sintering to produce samples with better superconducting properties. The provision of additional liquid-phase-rich powder during growth is a simple change to the conventional TSMG process which has led to improved reliability of growth and improved sample performance.

5 Optimisation of growth rate for fabrication of large single grains of YBCO-Ag

The addition of silver is reported to significantly improve the mechanical properties [40, 41] of single grain bulk (RE)BCO by increasing the fracture toughness [102] and bending strength [41, 43] of the samples without degrading their superconducting properties [40, 44, 45]. In order to successfully grow single grains of (RE)BCO with other added elements, a good understanding of the growth process is critical. This, in turn, enables a suitable heating profile to be determined which is vital to the growth process.

The successful, reliable, single grain growth of YBCO-Ag is much more difficult to achieve than growth of single grains of YBCO, GdBCO-Ag and SmBCO-Ag [51]. The fabrication of large, single grain bulk samples by batch processing has been achieved successfully for YBCO, and both the GdBCO-Ag and SmBCO-Ag systems [51], but for YBCO-Ag has yet to be achieved, due to the greater complexity of the growth of YBCO-Ag single grains. The addition of 5 wt% silver to the precursor powder reduces the peritectic temperature [103] by approximately 30 °C [42]. This significantly reduces the size of the temperature window available for the growth of single grains. The reduction in maximum processing temperature has many effects on the growth process, including on the decomposition [42], solute diffusion and interface kinetics. This, therefore, causes an overall reduction in the growth rate [103]. In addition, the reduction in processing temperature increases the likelihood of undesired spontaneous grain nucleation at points other than the seed. There are further difficulties associated with the low solubility of silver in the melt in the peritectically decomposed state [53]; yttrium diffuses much more slowly to the growth front than gadolinium or samarium during the growth process as it is not able to easily diffuse through the melt. Further reductions in yttrium diffusion, due to the reduction in temperature, makes the fabrication of single grains of YBCO-Ag much more difficult than those of YBCO, GdBCO-Ag and SmBCO-Ag. This highlights the need for a very different heating profile for the successful growth of YBCO-Ag than for growth of YBCO, GdBCO-Ag and SmBCO-Ag. A carefully optimised heating profile, therefore, is crucial to the successful growth of single grain bulk superconductors by TSMG [104, 105], and this is particularly important for YBCO-Ag.

The provision of additional liquid-phase to recycle (RE)BCO, samples and to YBCO samples processed without silver, has enabled much more reliable fabrication of large single grains of YBCO. The additional liquid provides a sufficient concentration of the (RE) element at the growth front, enabling an improved tolerance to the presence of Ce and Ag-rich clusters that typically form during the melt process [99]. For this reason, liquid-phase enriched TSMG has been used to assist in the reliable fabrication of large single grains of YBCO-Ag that would otherwise have been difficult to fabricate by conventional TSMG.

A number of studies have been carried out on the growth rate of the YBCO system fabricated without silver [57, 106]. It has been established that the relationship between growth rate and undercooling can be modelled by:

$$R_a = 4.5 \times 10^{-7} \Delta T^{1.9} \quad (4.1)$$

$$R_c = 2.8 \times 10^{-6} \Delta T^{1.3} \quad (4.2)$$

where R_a is the growth rate of the ac -plane in mm/second, R_c is the growth rate of the ab -plane in mm/second and ΔT is the undercooling. Experimental results have been found to be in good agreement with these relationships [106].

The measurement of the growth rate for (RE)BCO systems investigated to date has involved predominantly a single period of simple isothermal growth [57, 106, 107], and are based on assuming that the growth length of a single grain is proportional to the holding time. However, for the YBCO-Ag system, isothermal growth is unreliable and it has proven difficult to grow single grains in this way.

Measurements of advance of the growth front have been made using a new, two-stage method, based on continuous cooling and isothermal holding (CCIH), in which a period of continuous cooling is followed by a holding period at a constant temperature. A slow-cooled period enables nucleation to occur. It is thought that a slow-cooled period is required because close to the

peritectic temperature the growth rate is very low while nucleation and the first stages of growth occur. This corresponds to the solid line in the plot of growth rate and temperature shown in Fig. 5.1.

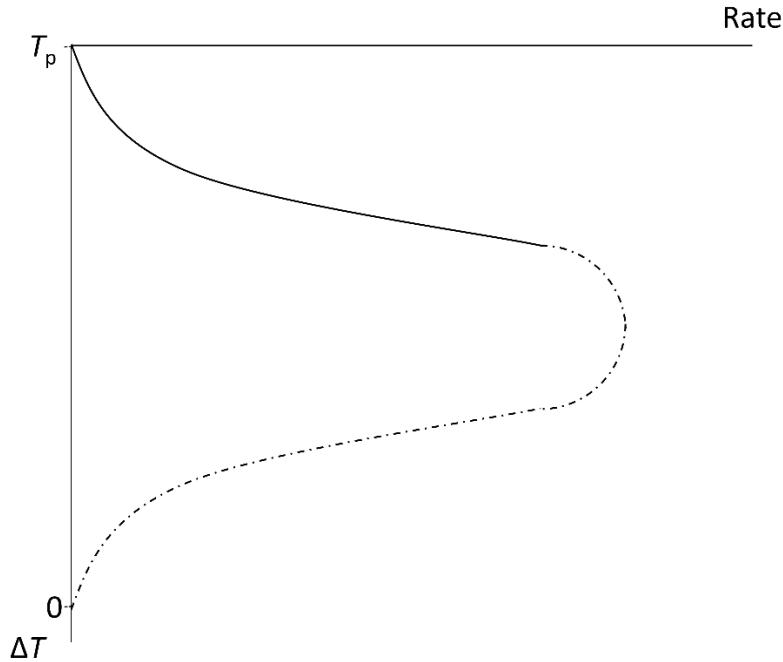


Figure 5.1: A schematic of the relationship between growth rate and undercooling. The solid line in the plot corresponds to the region through which slow cooling takes place in CCIH.

Previous studies involving a single isothermal hold period have shown the growth rate can be modelled by the expression:

$$R = \alpha(\Delta T)^\beta \quad (4.3)$$

where R is the growth rate, ΔT is the undercooling and α and β are constants that vary with composition of the precursor powder. In the diffusion-limited crystal growth model, β is expected to be approximately equal to two for the YBCO system, assuming that YBCO crystal growth is controlled by the diffusion rate of the Y element in the liquid-phase ($\text{Ba}_3\text{Cu}_5\text{O}_8$).

The growth rate in the thermal profile used in CCIH is not fully defined by the growth rate model for an isothermal growth process. In this case the expression required to model the growth rate

becomes more complex because the additional continuous cooling periods must also be considered as they occur below the peritectic temperature of the system. The definition of growth rate must be considered:

$$R = \frac{dL}{dt} \quad (4.4)$$

where L is the growth length and t is the time over which growth occurs.

In general, the undercooling can be modelled as a function of time, $\Delta T(t)$, so the growth length due to a given undercooling profile, such as that shown in Fig. 5.2, can be calculated using:

$$L = \int_0^L dL = \int_0^t \alpha (\Delta T(t))^\beta dt \quad (4.5)$$

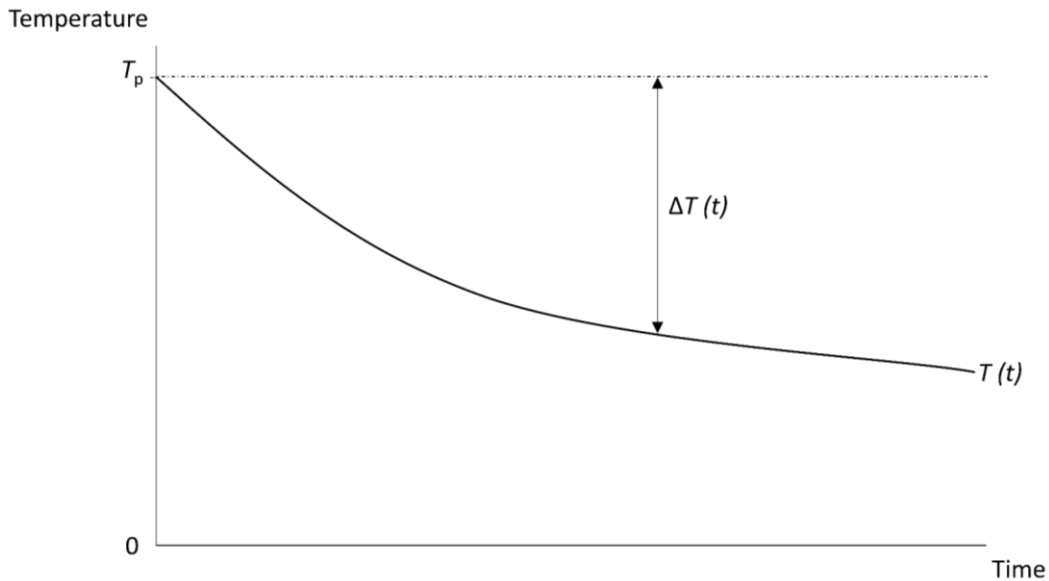


Figure 5.2: A schematic of the undercooling as a function of time.

The CCIH growth process is divided into three parts: rapid cooling from the peritectic temperature (between $t=0$ and t_1), slower continuous cooling (between $t=t_1$ and t_2) and an isothermal hold period (between $t=t_2$ and t_3). A schematic of the cooling profile is shown in Fig. 5.3 and a schematic of the undercooling profile is shown in Fig. 5.4.

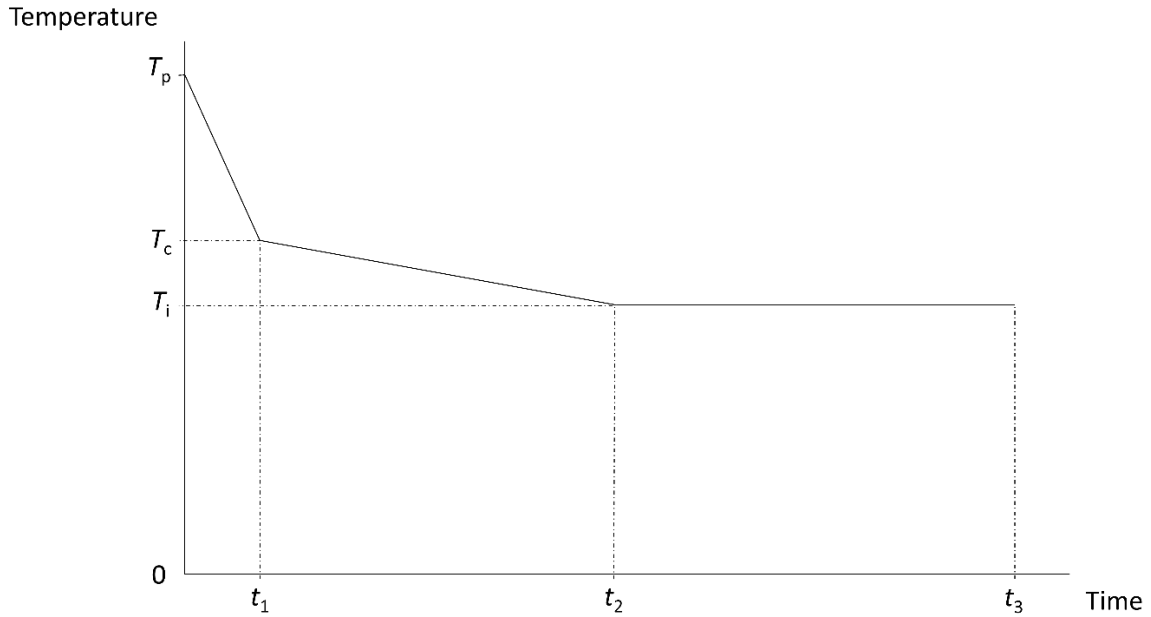


Figure 5.3: A schematic of the general cooling profile used for CCIH.

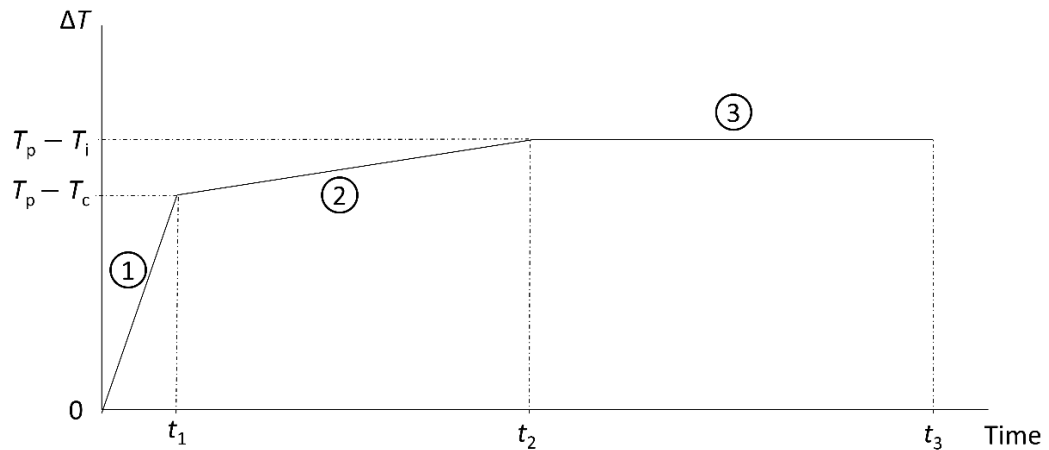


Figure 5.4: A schematic of the general undercooling profile used for CCIH.

The functions of ΔT and L for each region shown in the general CCIH case, as labelled in Fig. 5.4, are given in Table 5.1. The variables T_c and t_1 are coupled by the cooling rate between $t=0$ and t_1 . In addition, the variables T_i and t_2 are coupled by the cooling rate between $t=t_1$ and t_2 and the variables T_c and t_1 .

Region	$\Delta T(t)$	L
1	$\left(\frac{T_p - T_c}{t_1}\right) t$	$\int_0^{t_1} \alpha \left[\left(\frac{T_p - T_c}{t_1}\right) t\right]^\beta dt$
2	$\left(\frac{T_c - T_i}{t_2 - t_1}\right) (t - t_1)$	$\int_0^{t-t_1} \alpha \left[\left(\frac{T_c - T_i}{t_2 - t_1}\right) (t - t_1)\right]^\beta dt$
3	$(T_p - T_i)$	$\int_0^{t-t_2} \alpha [(T_p - T_i)]^\beta dt$

Table 5.1: The undercooling profile and growth length functions for each region of the general CCIH case.

The overall growth rate equation for CCIH then becomes:

$$\int_0^L dL = \int_0^{t_1} \alpha \left[\left(\frac{T_p - T_c}{t_1}\right) t\right]^\beta dt + \int_0^{t-t_1} \alpha \left[\left(\frac{T_c - T_i}{t_2 - t_1}\right) (t - t_1)\right]^\beta dt + \int_0^{t-t_2} \alpha [(T_p - T_i)]^\beta dt \quad (4.6)$$

The parameters α and β can be found for each growth condition. The value of β has been taken to be 2.2, as defined for the ratio of 25:75 of Y-211:Y-123 [57].

The liquid-phase enrichment technique [108] has been used to enable the successful fabrication of single grains of YBCO-Ag. The growth rate was approximated by using a new method in which thermal processing, comprising continual cooling and isothermal holding, was followed by measurement of the side lengths of the single grain region. The time periods of continuous cooling and isothermal hold have been varied for a series of YBCO-Ag samples. Measurement of the growth rate of small samples has provided a large amount of information on the growth process at a low relative cost, and because the samples used in the study are small, the time required for growth is short. The study of the growth rate in the YBCO-Ag system has subsequently enabled a suitable heating profile to be defined for the growth of YBCO-Ag single grains of a variety of sizes up to 26 mm in diameter. In addition, the microstructure and composition along both the a/b -axis and c -axis of the single grains was observed, and trends in the distribution of the silver

agglomerates and the Y-211 and Y-123 discussed. Both the microstructure of samples prior and post-oxygenation were observed. Conclusions have been drawn on the effect of the addition of silver to YBCO on the microstructure of the resulting large single grains.

5.1 The growth process

The peritectic temperature of both standard YBCO precursor powder and YBCO-Ag precursor powder were measured using DTA. The peritectic temperature of the YBCO-Ag precursor powder was measured to be 989 °C, which is 40 °C lower than that of the YBCO precursor powder. The heating and cooling profile from DTA are shown in Fig. 5.5.

Assemblies of YBCO-Ag were produced in a 20 mm die from 1.5 g of liquid-phase-rich powder below 10 g of YBCO-Ag precursor powder, as described in chapter 2. A layer of Yb_2O_3 paste was painted onto the base of each compact to avoid sub-grain formation.

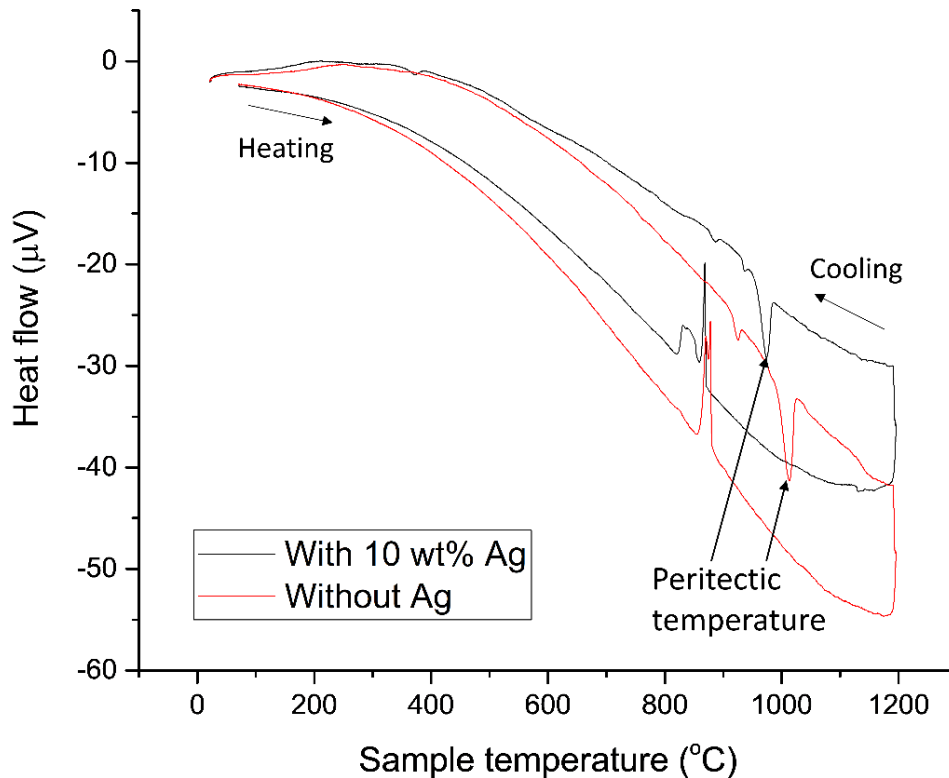


Figure 5.5: DTA of YBCO and YBCO-Ag precursor powder.

Initially, the conventional single-stage isothermal hold growth process was investigated. Samples were heated above the peritectic temperature in a box furnace. This was followed by rapid cooling to 970 °C, which is below the peritectic melting point (989 °C). Following this the melt was held isothermally at 970 °C for 10 h.

The samples did not grow when the conventional isothermal hold process was used, as observed in the sample shown in Fig. 5.6, so an additional slow cooling period was inserted between the rapid cooling to 970 °C and the isothermal hold stage. The slow cooled period had a cooling rate of 0.5 °C/h. This region enabled nucleation and growth initiation to take place. Each sample was cooled to the isothermal hold temperature (T_i) in the range 970 °C to 952 °C. The sample was then held isothermally for a given time period (t_i) of between 45 minutes and 10 h. The isothermal hold time was varied to ensure the side length of the partially grown single grain could be measured. Each sample was quenched to ambient temperature at the end of the isothermal hold period. It was assumed that heat dissipation at the growth front was large in comparison to the growth rate, so the quenching enabled the growth dimensions and microstructure at the end of the isothermal hold period to be preserved. A schematic illustration of the overall heating profile can be seen in Fig. 5.7, superimposed is the heating profile with a single isothermal hold period conventionally used to measure growth rate.



Figure 5.6: The assembly post-heating did not show any visible grain growth.

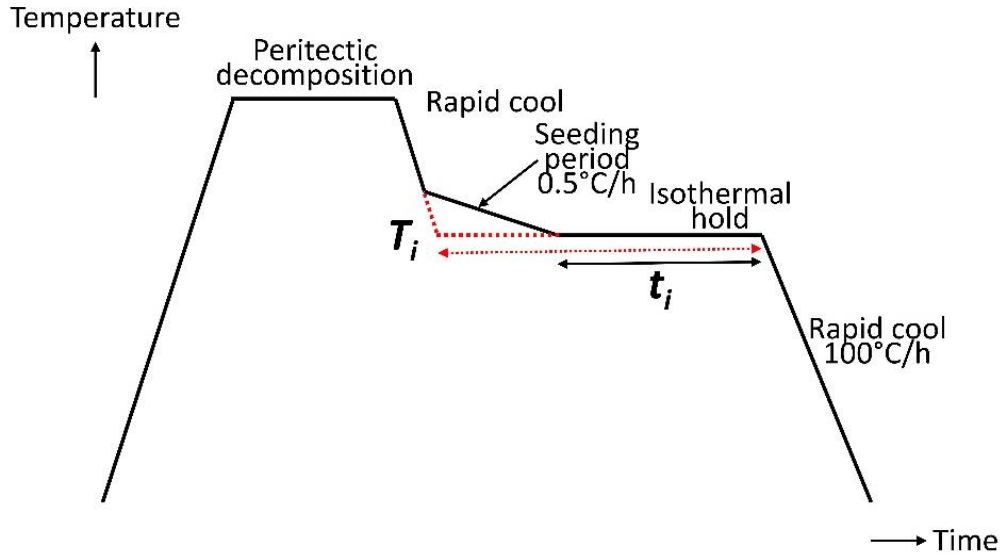


Figure 5.7: A schematic of the heating profile used in the CCIH process, superimposed in red is the heating profile conventionally used in single-stage isothermal holding.

The CCIH cooling profile with the temperatures, cooling rates and timings used in this work is shown in Fig. 5.8. In addition, the undercooling profile used for this work is shown in Fig. 5.9. T_i was varied which produced a variation in t_2 , in addition t_1 was varied.

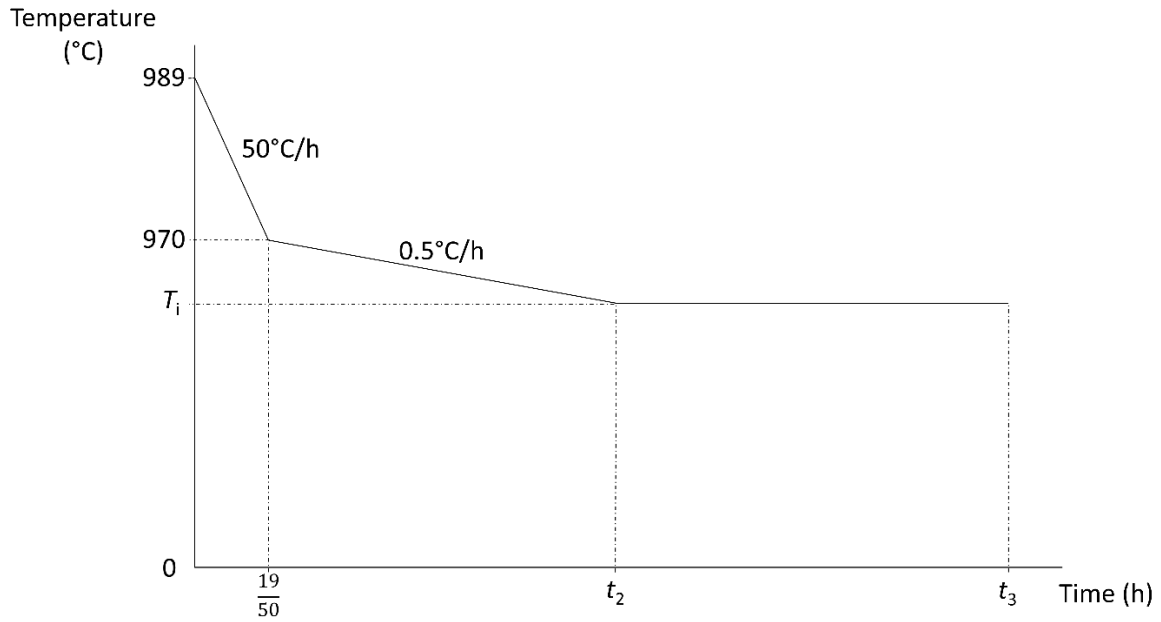


Figure 5.8: The cooling profile used for CCIH in this work.

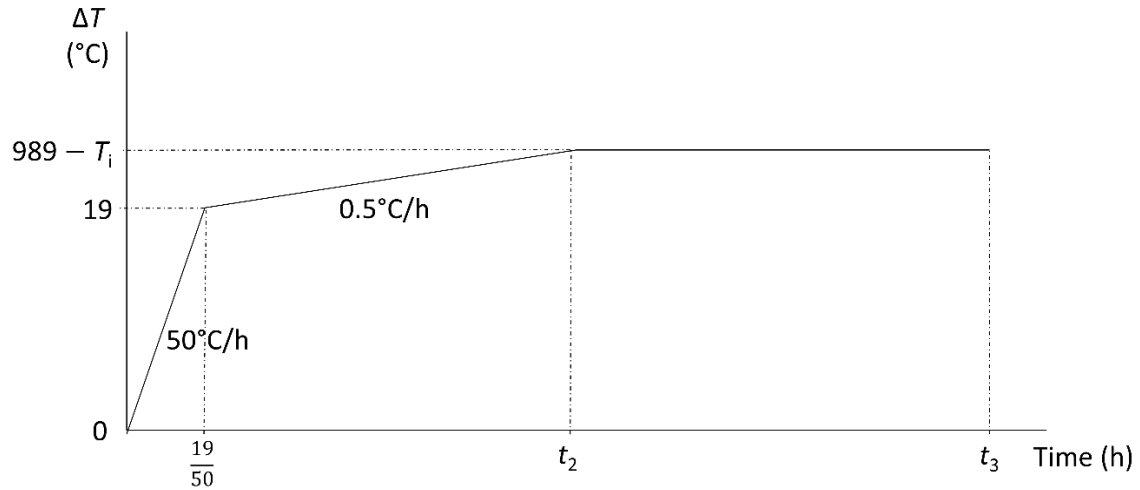


Figure 5.9: The undercooling profile used for CCIH in this work.

All nine samples were grown successfully. The top surface and cross-section of each sample is shown in Fig. 5.10. The edge of each of the single grain regions is indicated by a yellow dotted line.

The side length of the square single grain region was measured on the top surface of each sample and the average of the two perpendicular side lengths recorded as grain growth in the a/b -axis direction. Each sample was then cut in half to enable the extent of growth in the c -axis direction to be measured as the vertical distance from the top of the buffer pellet to the edge of the single grain region observed in the rectangular central cross section at the centre of the sample. The positions of the measurements taken on each sample cross-section are illustrated in Fig. 5.11. The side lengths of the single grain regions are given in Table 5.2.

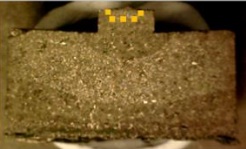
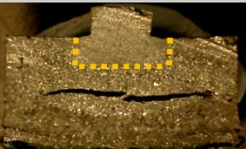
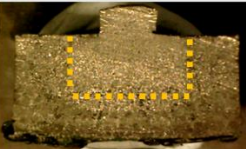
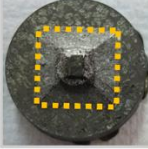
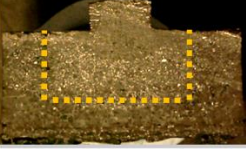
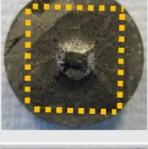
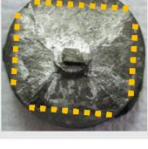
T_i (°C)	t_i (hours)	Top of sample	Cross section of sample
970	10		
967	10		
962	10		
960	10		
958	8		
956	6		
954	3		
954	2		
952	0.75		

Figure 5.10: Photographs of the samples grown for the calculation of growth rate. The dashed lines show the edge of the single grain regions.

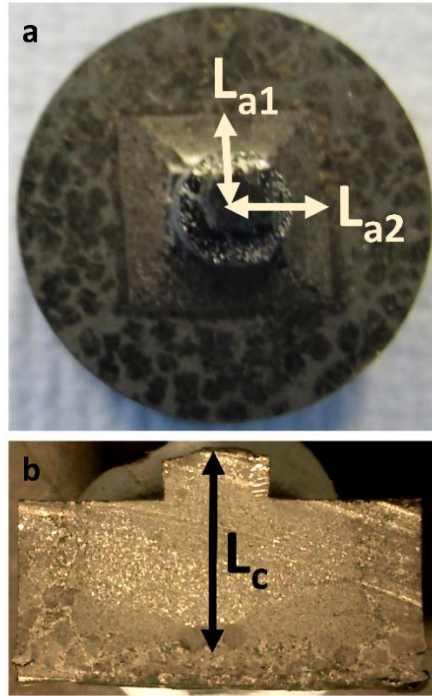


Figure 5.11: The measurements taken of the single grain region a) Top view where the two side lengths are averaged, b) Side cross-section.

T_i (°C)	t_i (h)	L_a (mm)	L_c (mm)
970	10	1.13	0.75
967	10	1.08	1.40
962	10	2.86	4.10
960	10	3.90	6.09
958	8	4.72	6.70
956	6	5.35	8.19
954	3	6.49	9.01
954	2	5.89	8.23
952	0.75	7.17	9.15

Table 5.2: The growth lengths measured in the a/b -axis direction and c -axis direction for each growth condition.

An approximation of β was taken to be 2.2, as explained earlier. The values of α for both growth in the a/b -axis direction and c -axis direction were calculated for each sample using an equation derived from equation 4.6. The calculated values of α for each of the growth conditions are given in Table 5.3.

T_i (°C)	t_i (h)	$\alpha_{a/b}$	α_c
970	10	1.72×10^{-4}	1.14×10^{-4}
967	10	0.789×10^{-4}	1.02×10^{-4}
962	10	0.946×10^{-4}	1.36×10^{-4}
960	10	1.01×10^{-4}	1.57×10^{-4}
958	8	1.06×10^{-4}	1.50×10^{-4}
956	6	1.06×10^{-4}	1.62×10^{-4}
954	3	1.19×10^{-4}	1.66×10^{-4}
954	2	1.14×10^{-4}	1.59×10^{-4}
952	0.75	1.20×10^{-4}	1.53×10^{-4}

Table 5.3: A table of the estimated values of alpha for YBCO-Ag grown by the CCIH process.

The average α value for each growth direction was used in the growth rate model. The values of α and β were input to give the models of the growth rate for the YBCO system containing 10 wt% Ag₂O of:

$$R_{a/b} = 1.1 \times 10^{-4}(\Delta T)^{2.2} \quad (4.7)$$

$$R_c = 1.4 \times 10^{-4}(\Delta T)^{2.2} \quad (4.8)$$

where $R_{a/b}$ is the growth rate in the a/b -axis direction, R_c is the growth rate in the c -axis direction and ΔT is the undercooling. The standard deviation between the α values is only 2.6×10^{-5} between all growth conditions for growth in the a/b -axis direction and only 2.2×10^{-5} for growth in the c -axis direction. Plots of the measured growth length against the growth length predicted by the model are shown in Fig. 5.12. These plots show that there is an almost linear relationship between the two values. This suggests that the growth length predicted by the growth rate model is a good approximation to the measured growth rate along both growth axes.

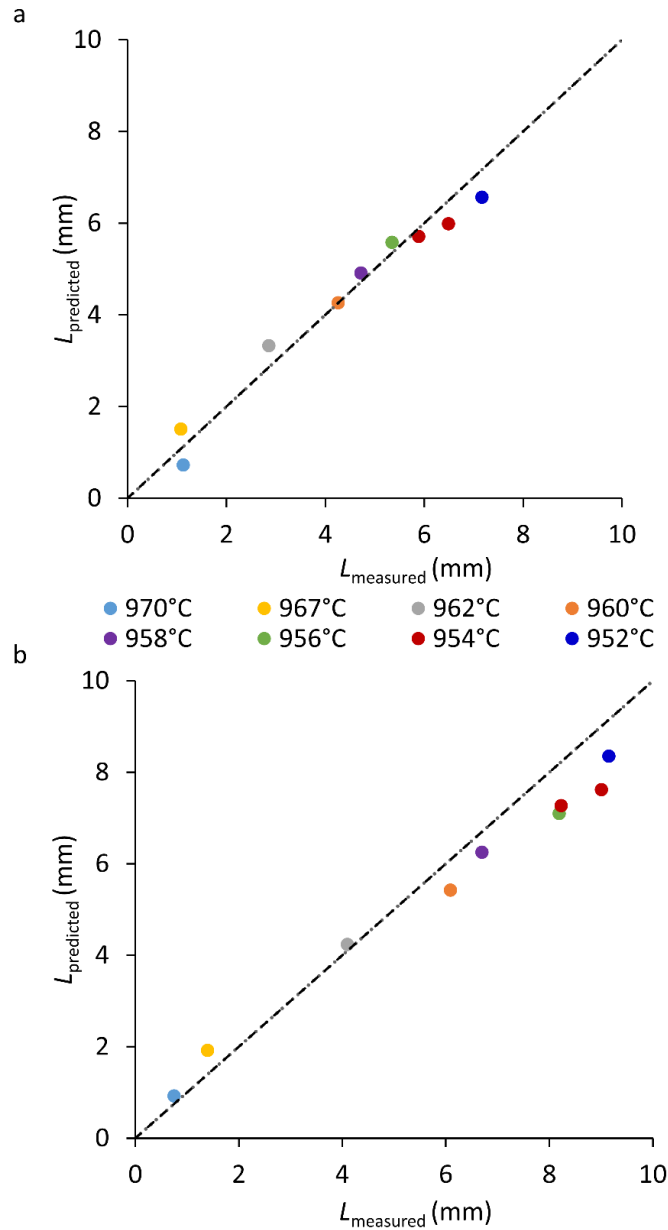


Figure 5.12: A plot of the predicted growth length and the actual recorded growth length for a) the a/b-axis direction and b) the c-axis direction after two-step cooling to a final undercooling ΔT with a subsequent isothermal hold (as shown in Fig. 5.9). Each colour marker represents a different value of T_i . The dotted line represents $y=x$, if the points lay on this line then the predicted and measured values would match perfectly.

The percentage of growth that occurred in each of the three cooling regions has been predicted using the growth rate model. This data is given in Table 5.4 and shows that during the rapid cooled period a negligible amount of growth occurs. At low levels of undercooling most of the growth occurs during the isothermal hold period, however, when the undercooling is increased a greater proportion of the growth occurs during the slow cooled period.

T_i (°C)	t_i (h)	Percentage of total growth		
		Region 1	Region 2	Region 3
970	10	0	4	96
967	10	0	36	64
962	10	0	54	46
960	10	0	58	42
958	8	0	66	34
956	6	0	74	26
954	3	0	86	14
954	2	0	91	9
952	0.75	0	96	3

Table 5.4: The percentage of total growth length that occurs in each region of cooling as predicted using the models for the YBCO-Ag system grown by CCIH.

The growth rate model for both the a/b -axis direction and the c -axis direction is shown graphically in Fig. 5.13.

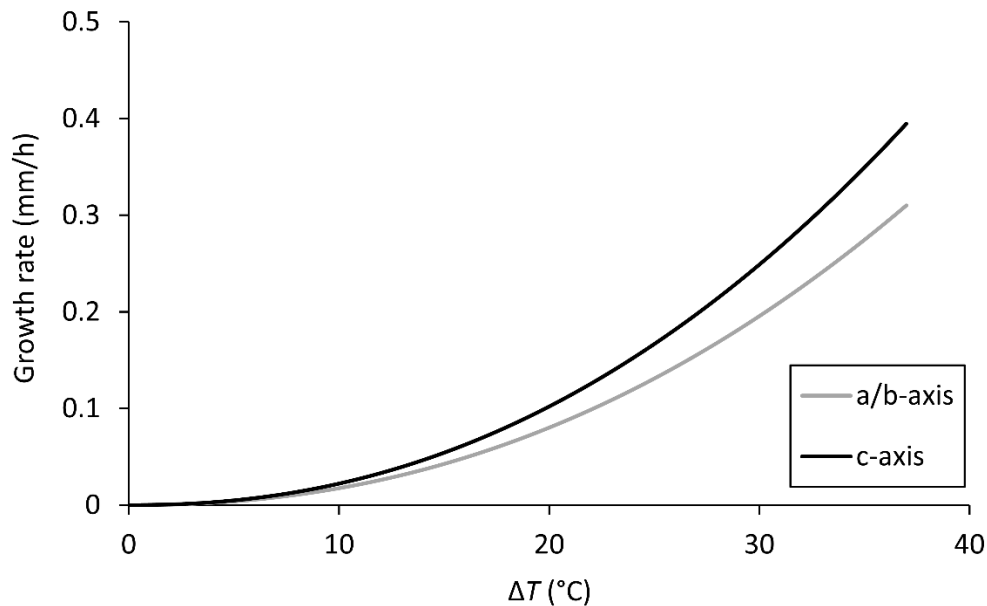


Figure 5.13: A plot of the growth rate models predicted for YBCO-Ag, based upon two-step undercooling to a final undercooling ΔT .

The plot in Fig. 5.13 suggest that there is a period of undercooling below the peritectic temperature within which the growth rate is very low. The need for the slow cooled period is suggested both in the structure of the bulk samples, and by the growth rate models. The region immediately below

the buffer appears to be deficient in silver compared to the central region, as shown in Fig. 5.14. In addition to the reduction in silver content, the size of the agglomerates present in the silver-deficient region are much smaller in size relative to those in the adjacent region towards the centre of the sample, which appears to be silver-rich.

It is thought that silver is forced to the growth front during the initial stages of growth, since it cannot be easily incorporated into the microstructure. As the growth front advances, too much silver is present to be pushed with the growth front, and so it is forced to move into the pores already present within the solidifying single grain structure. This discontinuity can be interpreted as the change from a silver deficient region to a silver-rich region where the silver agglomerates are much larger and fill some of the regions that were initially pores. The relatively low growth rate at low values of undercooling in the growth rate model provides further evidence of the importance of the seeding and growth initiation period required for successful nucleation and growth of the YBCO-Ag system. This region with a very low growth rate is approximately the same for both growth directions within the sample, suggesting that the slow cooling period is critical to achieving 3D growth and affects both growth directions to the same extent. This suggests that there is a nucleation barrier during the initial stages of growth of YBCO-Ag, so the growth cannot begin at low undercooling but a slow cool to a higher undercooling may enable this nucleation barrier to be overcome.

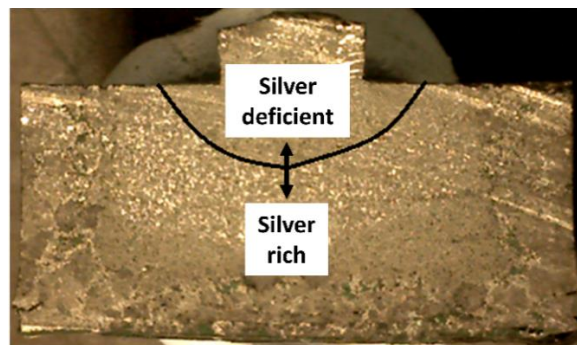


Figure 5.14: A cross-section of a single grain illustrating the locations of the silver-deficient and silver-rich regions observed in the YBCO-Ag samples.

The maximum recorded growth rate in the YBCO-Ag system is approximately 0.4 mm h^{-1} , which is significantly lower than the maximum growth rate of the YBCO system of 0.6 mm h^{-1} [57, 106]. This significant reduction in the growth rate when YBCO is alloyed with silver is one of the major

limitations to the ease with which large single grains can be grown successfully. This reduction in growth rate also necessitates a significantly different heating profile for successful single grain growth. The growth rate model has been used to derive suitable heating profiles for the successful growth of single grains of YBCO-Ag of various sizes.

Both the peritectic temperature measured using DTA and the growth rate at various values of undercooling enabled derivation of the appropriate heating profiles. A heating profile has been derived for growth of 20 mm as-pressed diameter grains of YBCO-Ag.

The initial heating, holding and rapid cooling region had already been used in the growth process and did not need to be changed. The initial slow cooling was carried out at a rate of 0.5 mm h^{-1} . In order to try to keep the heating profile as continuous and simple as possible, the isothermal hold period was replaced with a period of slow cooling, the length of which was calculated using the growth rate. This enabled an optimised heating profile to be derived and, as a result, a 20 mm diameter sample was successfully grown, as shown inset in Fig. 5.15.

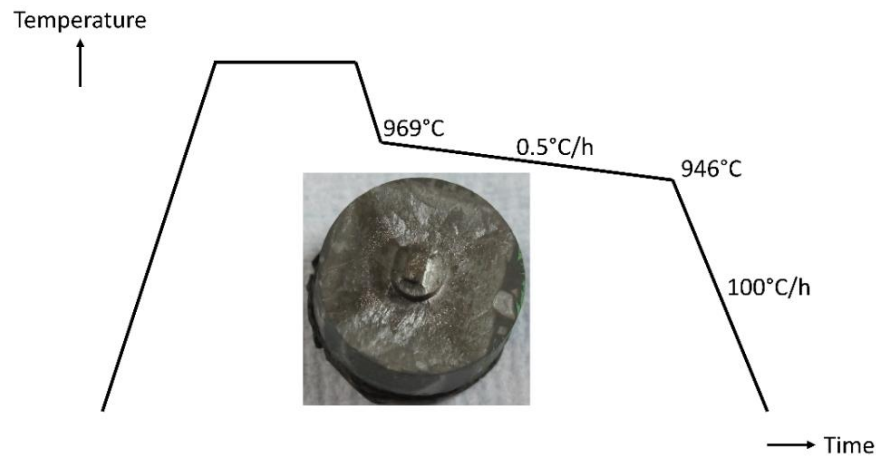


Figure 5.15: An optimised heating profile derived from the growth rate data for the successful growth of a single grain of 17 mm diameter of YBCO-Ag, a fully grown sample is shown inset.

After determination of an initial heating profile for the successful growth of 17 mm samples, as shown in Fig. 5.15, further optimisation stages were undertaken. Notably, a small increase in the processing temperatures before the first rapid cooling stage produced single grains with fewer visible low-angle grain boundaries. This translated to a slight change in the initial section of the heating profile. The slow cooling rate of $0.5 \text{ }^{\circ}\text{C/h}$ remained the same. This initial slow cooled

period enabled seeding and growth initiation. The temperature chosen for isothermal hold produced a reasonably high growth rate with an acceptably low risk of secondary grain growth. The length of the isothermal hold period was evaluated for each single grain and incrementally modified where necessary to ensure a fully-grown single grain was produced. Samples of YBCO-Ag were produced as described in Chapter 2 using the masses of powder given in Table 5.5. The final heating profiles used for the growth of 20 mm, 25 mm and 30 mm diameter samples are shown in Fig. 5.16. This successfully produced six 17 mm diameter, five 21 mm diameter and four 26 mm diameter samples as shown in Fig. 5.17. An additional sample of 25 mm diameter was grown in the same way and then oxygenated as described in Chapter 2.

Die diameter (mm)	Number pressed	Mass of precursor powder (g)	Mass of liquid-phase-rich powder (mm)
20	6	10	1.5
25	5	20	3.2
30	4	45	4.6

Table 5.5: A table of the mass of each powder used during pressing of different sized samples.

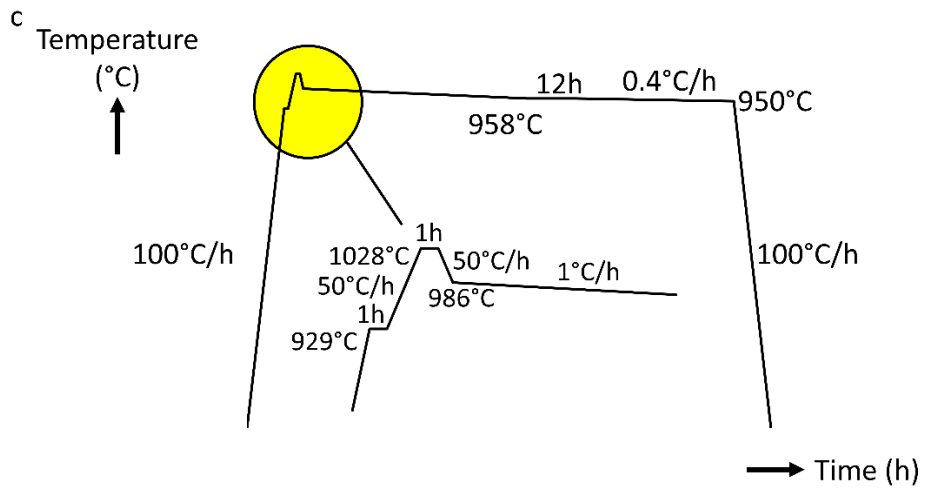
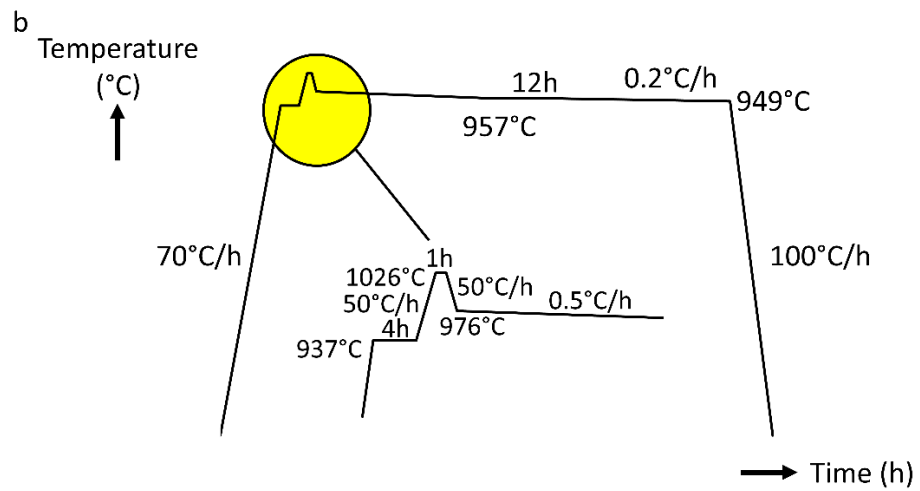
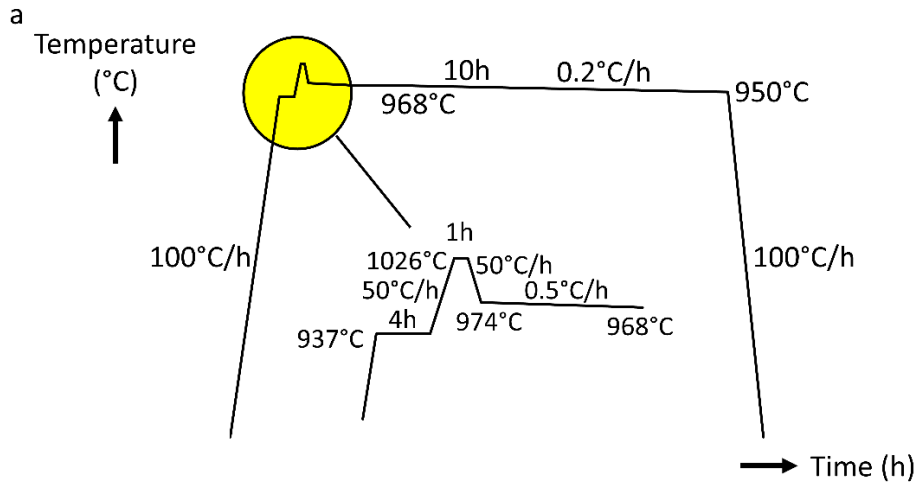


Figure 5.16: The heating profiles used for the growth of a) 20 mm, b) 25 mm and c) 30 mm diameter assemblies of YBCO-Ag.



Figure 5.17: YBCO-Ag single grains of diameter (top row) 17 mm, (middle row) 21 mm and (bottom row) 26 mm.

5.2 Microstructure prior to oxygenation

A number of samples used to study the growth rate were cut in half to expose a rectangular cross-section. The requirement for a slow-cooled seeding period, in addition to the isothermal hold period, is suggested by the structure of each of the cut samples. The cross-sections showed the same trend as described in earlier. The region directly below the buffer pellet appears to be silver-deficient in comparison to the central region.

Closer observation of the microstructure was undertaken for a number of the partially grown samples. Fig. 5.18 shows the entire cross-section of a number of the samples, each of these images has been assembled from individual microscope images taken at 50 \times magnification. In addition,

Fig. 5.19 shows the microstructure ahead of and behind the growth front at 500× magnification for a number of the growth-rate samples, and Fig. 5.20 shows the region of the growth front at 50× magnification. The distinction between the single grain region and the region outside of the single grain is clearly visible in the samples shown in Fig. 5.20 as the Y-123 matrix is more continuous.

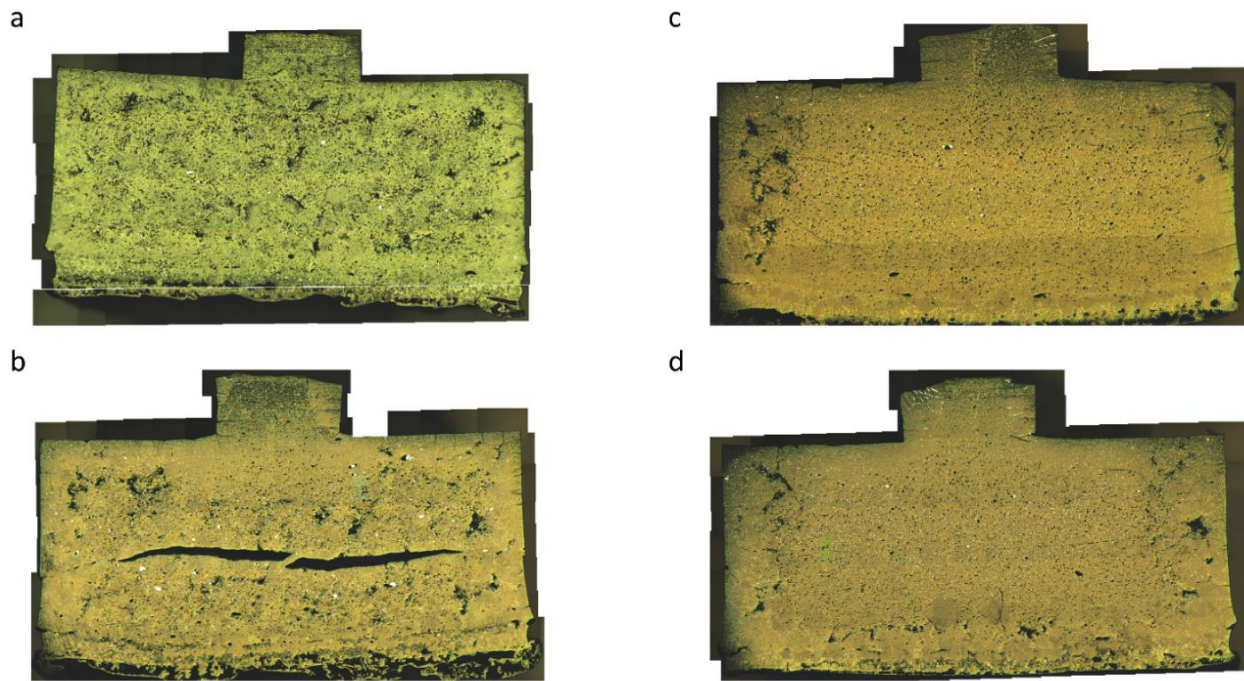


Figure 5.18: Whole cross-sections at 50x magnification of partially grown single grains grown with T_1 of: a) 970 °C, b) 962 °C, c) 956 °C and d) 952 °C.

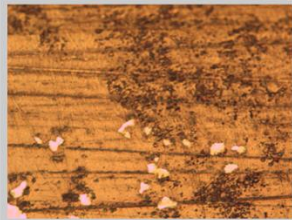
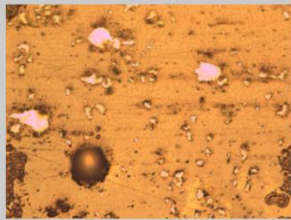
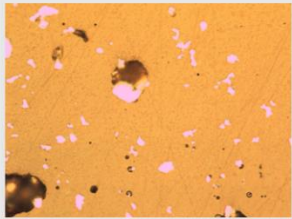
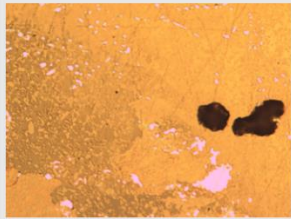
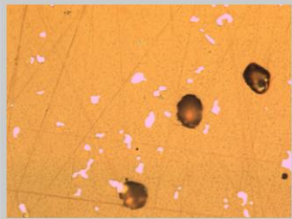
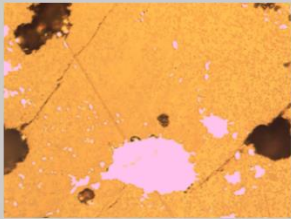
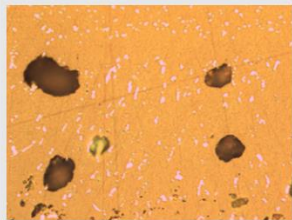
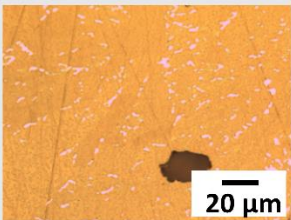
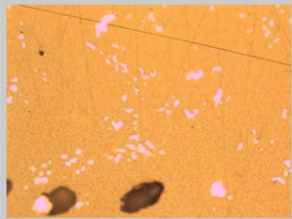
T_i (°C)	Behind growth front	Ahead of growth front
970		
962		
960		
956		
952		Grown almost to the edge, no image available

Figure 5.19: Optical microscope images at 500x magnification of a number of the growth rate samples both behind and ahead of the growth front.

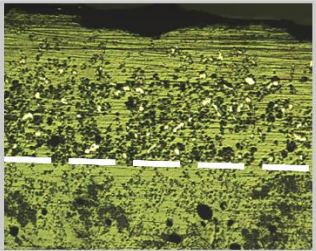
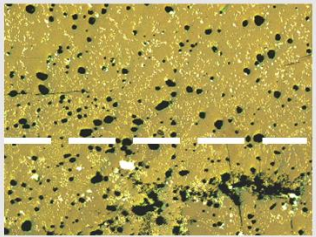
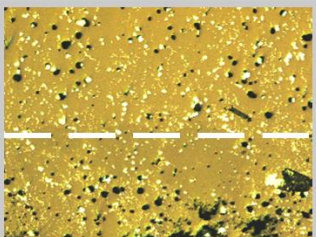
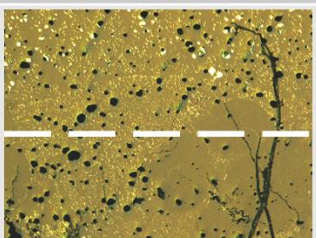
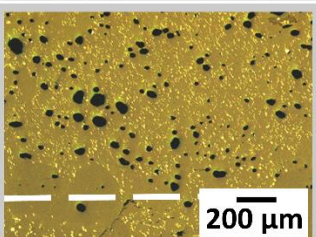
T_i (°C)	Growth front
970	
962	
960	
956	
952	

Figure 5.20: Optical microscope images at 50x magnification showing the regions in the growth rate sample both ahead (below the white line) of and behind the growth front (above the white line).

Fig. 5.21 shows optical microscope images of the almost fully grown sample before oxygenation, held at an undercooling of 18 °C for 45 minutes. This illustrates the distribution of silver agglomerates in the sample microstructure more clearly. The images taken at 0 mm and 1 mm from the top surface of the sample correspond to the region within the buffer pellet; this contains

a large number of small pores and a limited number of small silver agglomerates. The images at 2 mm and 3 mm lie within the region that appears to be silver deficient to the eye. It can be seen from these images that there are silver agglomerates present in this region. However, the silver agglomerates in the ‘silver-deficient’ appearing region are much smaller in size and there are fewer silver agglomerates in this region compared to the region that appears to be silver-rich.

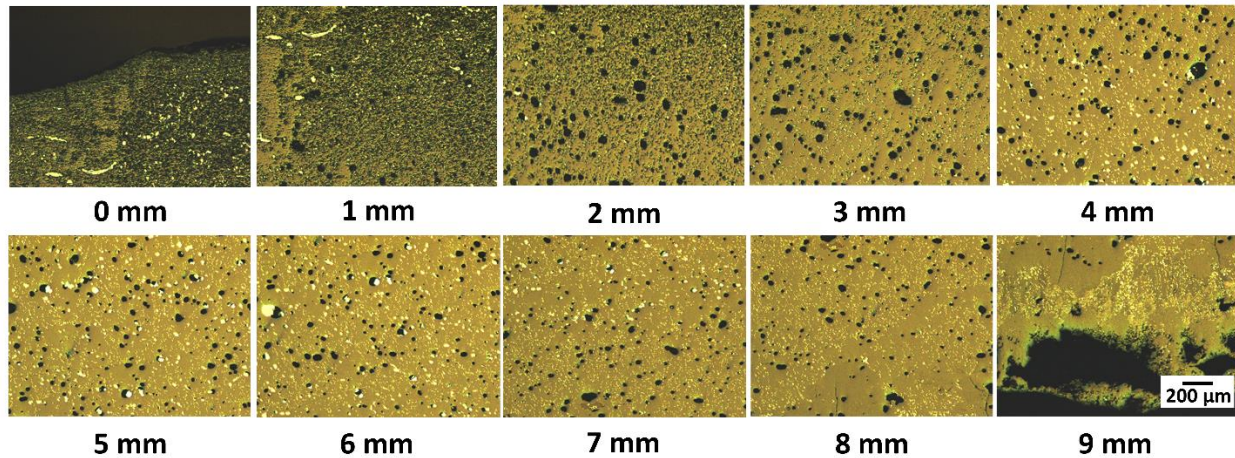


Figure 5.21: Optical microscope images taken at 50x magnification along the *c*-axis directly below the seed.

Fig. 5.22 shows optical microscope images of the same sample at 500x magnification. The Y-211 and silver distribution can be seen clearly in these images. The image taken at 0 mm from the top is within the buffer pellet, where many small pores (black) are present within the Y-123 matrix, and there are no visible silver agglomerates. The image labelled 1 mm is also within the buffer pellet and this does contain some silver agglomerates; these are shown as bright white-yellow regions. This indicates that some of the silver does move through the sample and into the buffer pellet and reinforces the point that it is essential to use a buffer to prevent seed failure. Elongated lines of silver are visible in the *a/b*-direction within the buffer pellet, although this is not observed throughout the bulk of the sample. The buffer pellet is also relatively porous. The movement of silver into the buffer pellet provides evidence that the buffer pellet is necessary to prevent seed failure due to silver contamination. The contamination of the seed by silver would significantly reduce the peritectic temperature of the seed, and therefore it would be unlikely to remain solid during the heating stages of processing.

The image at 2 mm from the top of the sample is towards the edge of the buffer and at the top of the sample, this region still contains a large number of small pores. The image taken at 3 mm along the *c*-axis direction lies in the ‘silver-deficient’ region, it contains: one relatively large pore (very dark grey), a small number of very small pores (black), a number of small silver agglomerates (white) and a uniform distribution of Y-211 particles (pale grey, not easily visible) within the Y-123 matrix. Much larger silver agglomerates are present with increasing distance from the seed in the ‘silver-rich’ region and more, larger pores are also present. This suggests that the silver initially fills pores that are present within the bulk single grain. Many of the large pores are filled by the additional liquid towards the base of the sample, so there are fewer pores in that region which are available to be filled by the silver. This is why there are smaller and fewer silver agglomerates in the lower region of the sample.

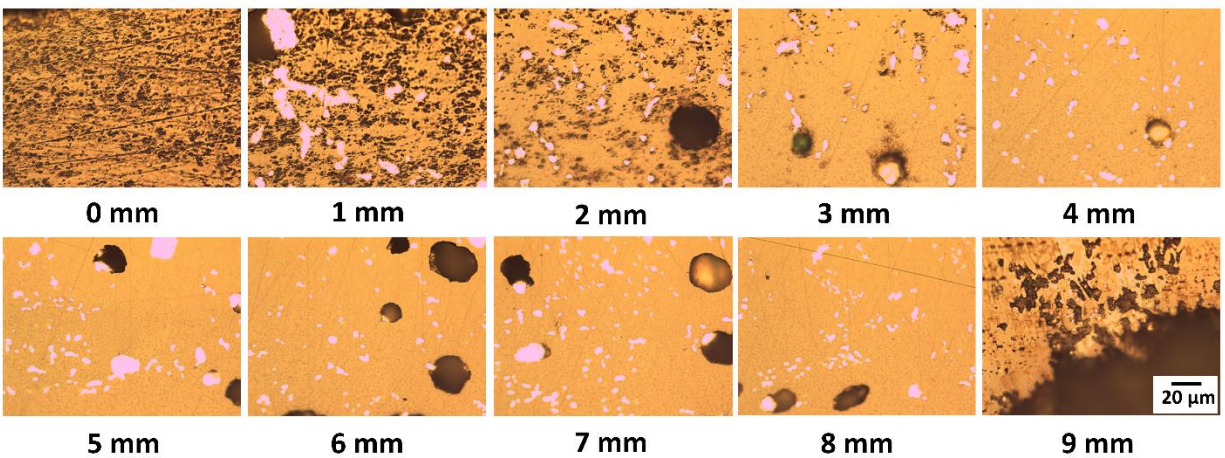


Figure 5.22: Optical microscope images taken at 500x magnification along the *c*-axis directly below the seed.

5.3 Microstructure of the oxygenated samples

The samples imaged in the previous section had not been oxygenated as they were only partially grown for the growth rate study, and their superconducting properties were not measured. However, bulk samples used in practical applications must be superconducting when cooled, so they will have been subjected to the oxygenation process. This involves prolonged heating at 450 °C. During this process oxygen diffuses into the sample, and a phase change occurs within the matrix. Silver may move during this heating process and cracks are often formed. The figures below show a 21 mm diameter single grain of YBCO-Ag which has been oxygenated. The buffer

pellet had been removed prior to cutting to enable trapped field measurements to be taken. The entire cross section is shown in Fig. 5.23. There are a greater number of cracks along the a/b -direction than observed in Fig. 5.21; this is expected. However, a similar dispersion of silver and pores are observed. When viewed from a distance this image shows the ‘silver-deficient’ looking region at the top and then a silver-rich looking region at the centre of the bulk as was observed in the un-oxygenated samples.

Images of the oxygenated sample at 1 mm intervals along the c -axis direction have been taken at both 50x magnification and 500x magnification using an optical microscope, as shown in Figs. 5.24 and 5.25. These images have enabled comparison between the porosity, silver and Y-211 distribution along the c -axis of a single grain before and after oxygenation. The images in Figs. 5.21 and 5.22 show a single grain prior to oxygenation. It should be noted that as the seed and buffer have been removed; 0 mm in Figs. 5.24 and 5.25 corresponds approximately to 3 mm in Figs. 5.21 and 5.22. The images at 0 mm and 1 mm in Fig. 5.25 clearly show a similar trend in the silver agglomerate size as the un-oxygenated sample; these silver agglomerates are much smaller than those seen further from the seed. Larger silver agglomerates begin towards the bottom of the image at 2 mm in this figure and in the images at 3 mm, 4 mm and 5 mm large silver agglomerates are present. However, there is a reduction in the size of the silver agglomerates present with greater distance from the seed. This corresponds with that observed in the bottom half of the image at 7 mm and the images recorded at a greater distance from the seed.

The images in Fig. 5.25 show a similar distribution in the silver content and size of the silver agglomerates as the images from the un-oxygenated sample in Fig. 5.22. However, the overall average size of the large silver agglomerates appear to be larger in the oxygenated sample. This is likely to be because the extended time period at high temperature experienced by the oxygenated sample has enabled greater diffusion of the silver. This has allowed larger agglomerates to form. Alternatively, due to the inherent variability in samples produced by TSMG, the sample which has been oxygenated may have initially had larger pores, hence allowing the silver agglomerates formed to be larger.

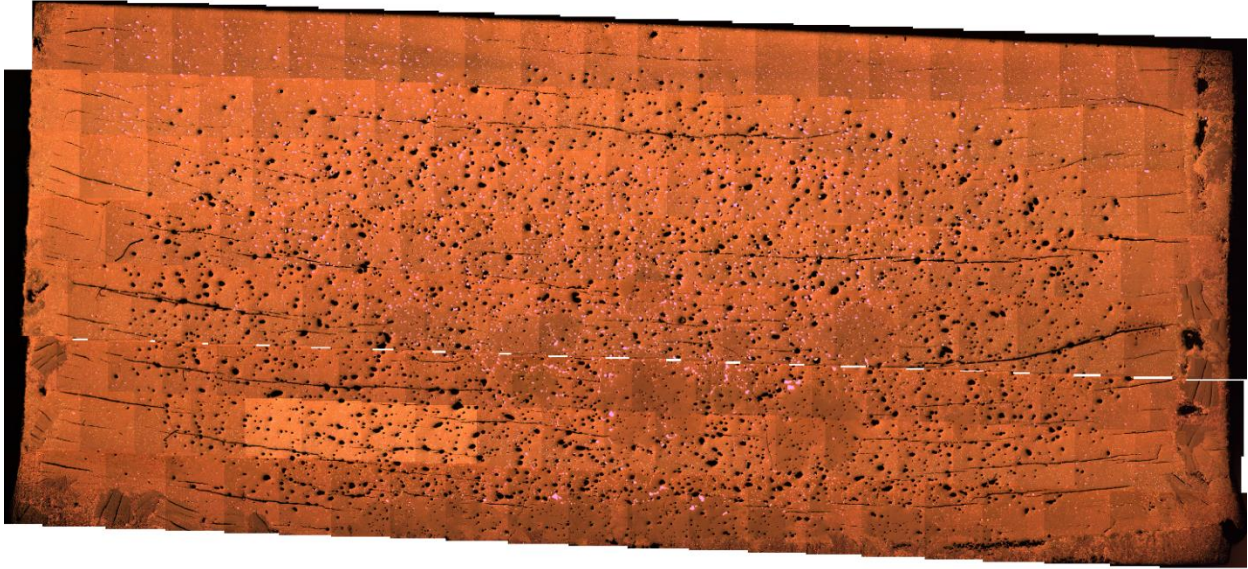


Figure 5.23: The entire central cross section of an oxygenated single-grain of YBCO-Ag. This was produced by assembling a large number of images taken at 50x magnification using an optical microscope.

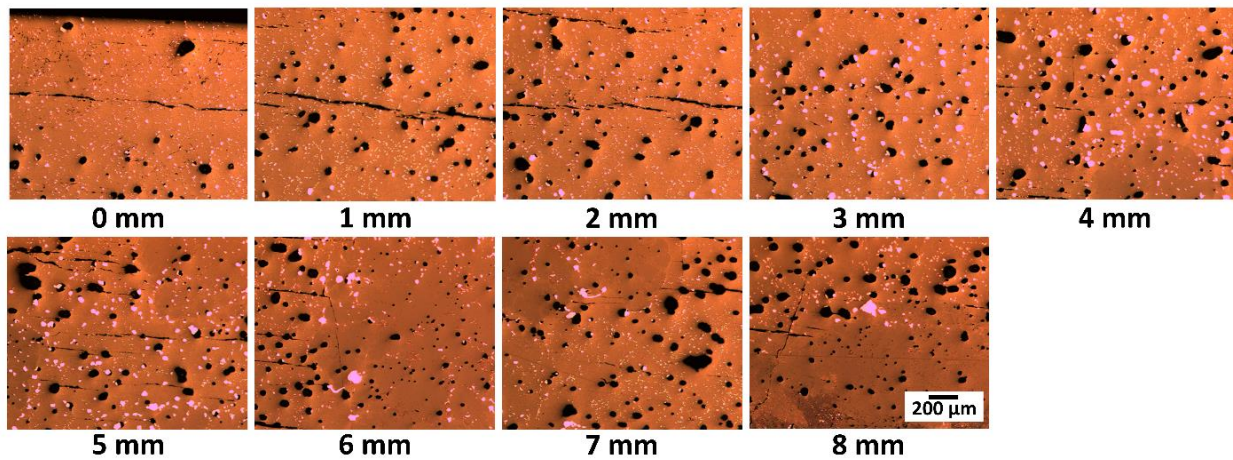


Figure 5.24: Optical microscope images of a sample post-oxygenation taken at 50x magnification along the c-axis directly below the seed.

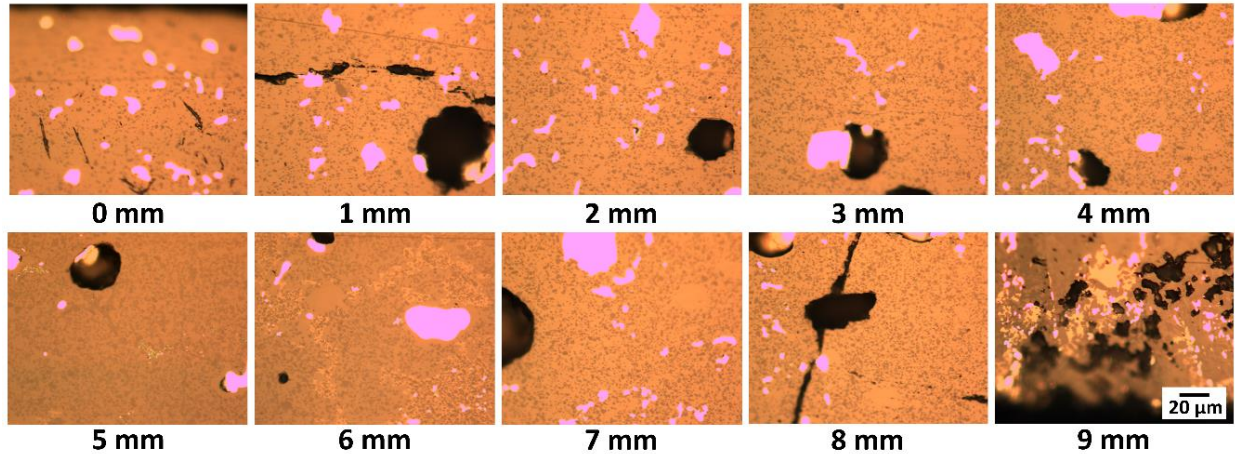


Figure 5.25: Optical microscope images of a sample post-oxygenation taken at 500x magnification along the *c*-axis directly below the seed.

5.4 Composition

The composition of the partially grown samples shown in Fig. 5.18 was analysed at intervals of 1 mm along the *c*-axis directly below the seed, as shown in Fig. 5.26. A sudden transition can be seen in the normalised at % of Y at the edge of the single grain region. The observed normalised at % of silver is as expected from the microscope images; at the top of the sample the at % of silver is low, but increases with distance into the ‘silver-rich’ region. More of the pores are filled as the distance from the seed increases further towards the region providing additional liquid, and the presence of silver agglomerates is less evident, those that are present are much smaller in size. The samples, which have not grown or have shown a very limited growth, exhibit a greater variation in composition between corresponding locations, as seen in Fig. 5.26 b and 5.26 c. With the exception of Ba and Cu, in all samples the normalised quantity of each element present fluctuates about the expected value based on the composition of the precursor powder. In the case of the normalised Ba and Cu, in the almost fully grown sample shown in Fig. 5.26 d, the amount of Cu and Ba present is, with the exception of one location, always higher than the expected value. This shows that, when growth occurs towards the base of the sample, some of the additional liquid-phase provided is taken into the sample and increases the overall Ba and Cu content within the single grain region.

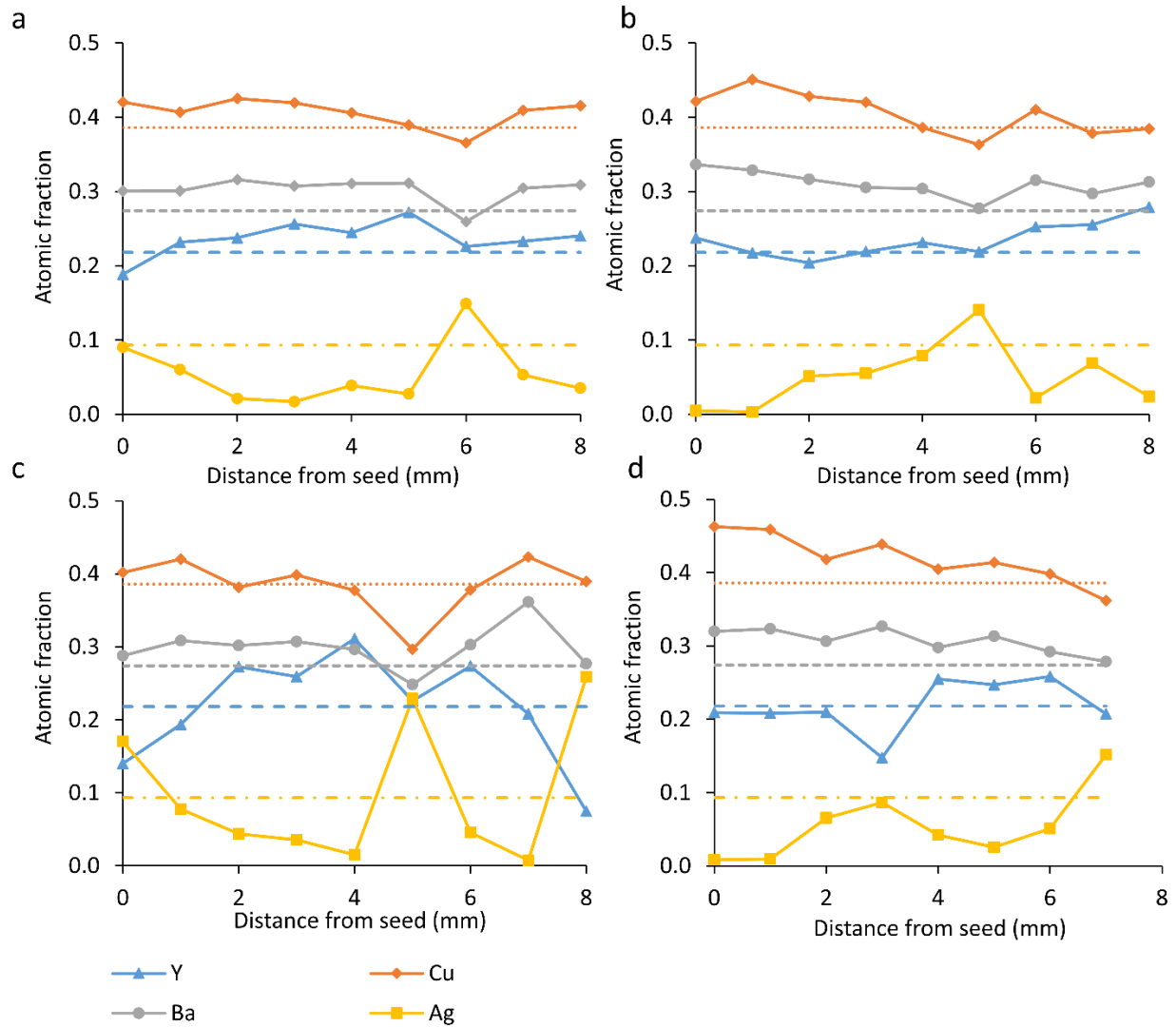


Figure 5.26: The composition within partially grown single grains with T_i of: a) 970 °C, b) 962 °C, c) 956 °C and d) 952 °C alongside the composition expected based on the precursor powder composition.

The ratios Y:Ba and Y:Cu from each location along the central c -axis have been plotted in Fig. 5.27. The quantity of Y-211 and Y-123 present correlates with these ratios, so these plots can be used to identify trends in the distribution of the Y-211 inclusions throughout the bulk and in the amount of Y-123 superconducting phase present. The sample from which the graphs in Fig. 5.27 a and Fig. 5.27 b are taken had only partially grown by a small amount, and so the majority of points will contain unreacted precursor powder. This accounts for the consistency in the ratios, and there are only small variations between each corresponding point. However, a larger portion of the samples, of which the composition is shown in Figs. 5.27 c and 5.27 d, had grown as a single grain. In Fig. 5.27 c both ratios show a general trend of increasing until 4 mm away from the seed.

This region is within the single grain region, and these ratios show that the amount of Y-211 increases whilst the amount of Y-123 decreases. This corresponds with the push-trap theory. With increasing distance from the seed after 4 mm away is the region that lies outside the single grain.

The sample whose composition is shown in Fig. 5.27 d is almost fully grown, so the majority of the points displayed in this graph are within the single grain region. In this sample there is a general trend of a slight increase in the ratios, showing there is a slight increase in the amount of Y-211 with distance from the seed. This increase is slight which suggests that both the distribution of Y-211 inclusions and the Y-123 matrix is relatively homogeneous throughout the *c*-axis direction at the centre of the sample. The point at 3 mm from the seed has a significantly different value for both ratios than all other points; this suggests there is a random fluctuation in the particular image taken using SEM. This may be due to the large increase in the silver content in the central region.

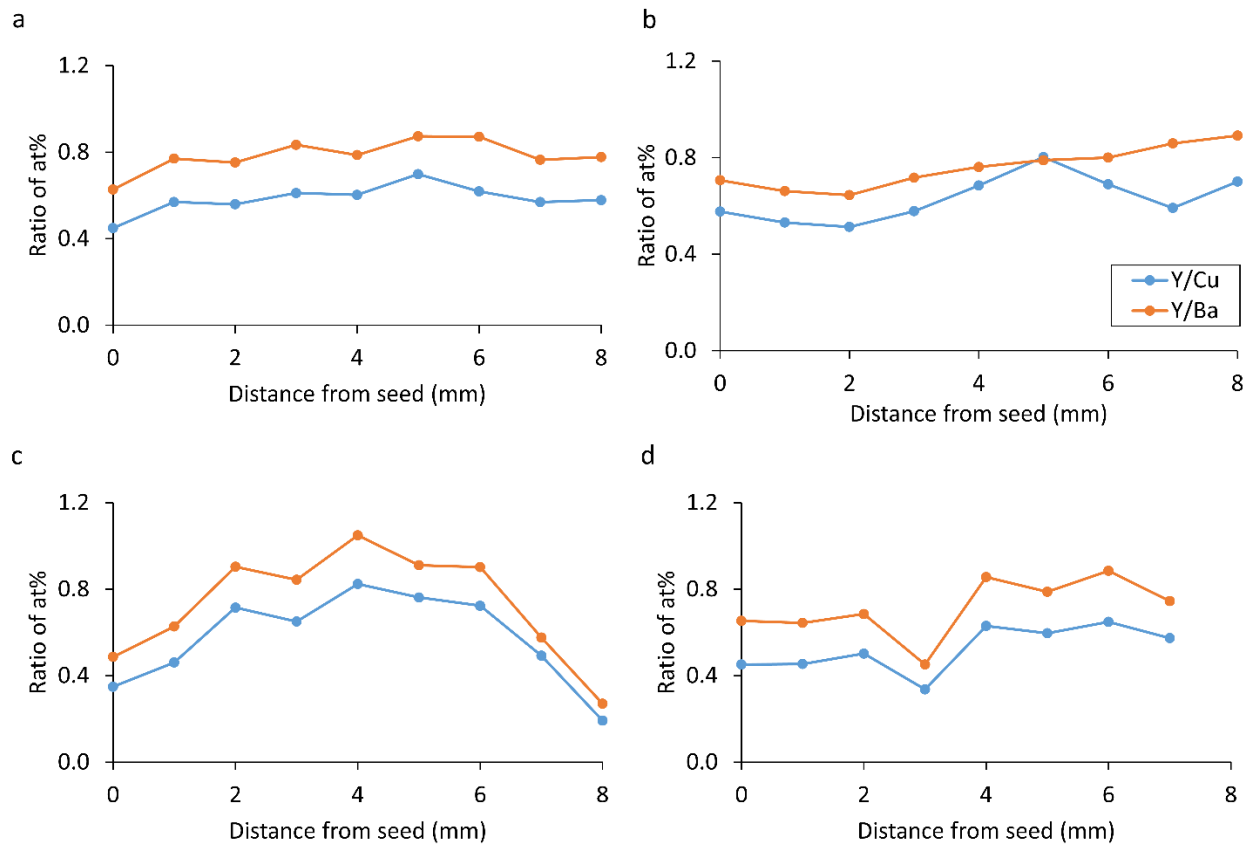


Figure 5.27: Y/Ba and Y/Cu ratios for partially grown single-grains with T_i of: a) 970 °C, b) 962 °C, c) 956 °C and d) 952 °C. These ratios correlate with the ratios of Y-123 and Y-211 present

5.5 Conclusions

The growth rate of single grains of YBCO-Ag has been investigated in detail. This has been studied using a new method based on continuous cooling and isothermal hold, which differs from previous studies of growth rate by providing a seeding and growth initiation period prior to the isothermal growth stage. This is the first time growth rate data has been reported in detail for the YBCO-Ag system.

This study has enabled optimum heating profiles to be derived for the growth of large single grains of YBCO-Ag. The distribution of silver is not uniform throughout the cross section of the bulk microstructure. It is difficult to incorporate the silver into the YBCO lattice during the initial stages of growth. In consequence, silver is pushed by the growth front, generating a silver deficient region below the seed that contains only a limited concentration of small silver agglomerates. Once the level of silver at the growth front reaches a threshold, however, silver is incorporated into the bulk microstructure to yield a discontinuity in the silver distribution. Many more and much larger silver agglomerates are present further away from the seed and fill regions that were initially pores. The filling of pores by the silver agglomerates reduces the porosity and therefore is likely to improve the strength of the initially brittle YBCO bulk material, which is important for practical applications of this material.

6 Comparison of the superconducting properties of YBCO and YBCO-Ag single grains

The widespread use of ceramic and single grain (RE)BCO superconductors is, in general, limited by their poor mechanical properties. The addition of alloying elements prior to processing is often implemented to improve the mechanical properties of conventional ceramic materials. However, the processing requirements of a single grain bulk superconductor limits the viability of the use of this method, and its ability to produce positive effects on the superconducting properties of the material. In addition, it is widely acknowledged that the inclusion of additional elements and compounds can be detrimental to the superconducting properties of a bulk single grain.

In order for the (RE)BCO material to have high J_c values and trap a large magnetic field, a large single grain must be produced. Sintered multi-grain (RE)BCO materials have a very limited magnitude of trapped field and J_c values [8, 109]. These sintered materials have a very low apparent density, they accumulate impurities at the grain boundaries and, critically, the grain boundaries act as weak links to the flow of superconducting current [6, 10]. Hence, a large single grain is required with a predominantly uninterrupted superconducting matrix in which the supercurrent can flow. In Chapter 5 the first challenge was overcome; the growth of large single grains of YBCO-Ag was achieved reliably.

Another important factor in maximizing the achievable J_c values of (RE)BCO materials is the provision of effective non-superconducting inclusions which are able to pin the magnetic flux lines within the superconducting matrix [66, 67, 72, 73]. The achievable J_c value is dependent on the distribution of these flux-pinning inclusions and their size; the value of J_c is directly proportional to the volume fraction of these inclusions and indirectly proportional to their size [80]. Although the optimum size of these inclusions is of the order of the coherence length, varying between single angstroms and tens of angstroms in Y-123 [71], larger inclusions are still able to provide pinning, albeit less effectively [8]. Y-211 inclusions are the predominant source of flux pinning in the Y-123 system [80]. In order to optimize the pinning, these inclusions should be as fine as possible

and dispersed uniformly throughout the single grain matrix [80]. It is difficult to achieve a fine and uniform distribution of these inclusions during the TSMG process, as explained in Chapter 1.

(RE)BCO bulk superconducting materials require relatively high onset T_c values, large J_c values and a sharp transition to the superconducting state. The key to the successful development of a new or improved material for use as a bulk superconductor in practical applications is an assurance that the properties and performance of this material are not inferior to those of YBCO single grains fabricated by TSMG. Hence, any mechanism used to improve the mechanical properties of (RE)BCO single grains must not significantly disturb the area of the superconducting matrix within which the supercurrent can flow. In addition, it should not have a negative effect on the uniformity of the Y-211 flux pinning inclusions or increase their size. It must also be ensured that the attempts to improve the mechanical strength do not have a negative effect on the T_c values, either as a direct result of alloying, or due to a reduction in the ability to oxygenate the material. Specifically, the Y-123 matrix must retain sufficient pores and cracks to assist in the diffusion of oxygen throughout the sample within a reasonable time frame to ensure oxygenation can be carried out effectively.

The optimization of pores and cracks present within the microstructure is important for both the oxygenation process, and hence the T_c value, but also for the magnitude of the J_c and trapped field values. Sufficient pores and cracks are required to enable oxygenation, although these have a detrimental effect on the value of J_c , and hence trapped field [56]. The presence of a/c -cracks and pores reduce the effective area of the superconducting matrix over which the supercurrent is able to flow [56], and these should be reduced to the minimum necessary to allow oxygenation.

In this chapter, the growth process developed in Chapter 5 has been used to fabricate large single grains of YBCO-Ag. The trapped field profile and maximum trapped field has been measured for a number of different sizes of YBCO-Ag single grains, and compared to that exhibited by single grains of YBCO and LR YBCO. In addition, the onset T_c value, sharpness of the transition to the superconducting state and the J_c value of a number of sub-specimens cut from one sample of each of YBCO, LR YBCO and YBCO-Ag have been derived and compared. The distribution of J_c values along the c -axis directly below the seed has then been compared with the pore and silver distribution in each of the single grains.

6.1 The growth process

The six 17 mm diameter, five 21 mm diameter and four 26 mm diameter samples grown in Chapter 5 (initially pressed using dies of diameter 20 mm, 25 mm and 30 mm, respectively) were used for measurement of the trapped field in a range of sizes of YBCO-Ag single grains. In addition, four samples of each of standard YBCO, liquid-phase-enriched (LR) YBCO and YBCO-Ag were pressed uniaxially in a 30 mm diameter die (to produce samples 26 mm in diameter following shrinkage). The standard YBCO samples were pressed from 46 g of standard precursor powder, the LR YBCO and YBCO-Ag samples were pressed from a layer of 4.6 g of liquid-phase-rich powder below 46 g of standard YBCO or YBCO-Ag precursor powder. Each sample was assembled and a layer of Yb_2O_3 paste was painted onto all surfaces of the compact except the top surface. Each assembly was heated according to the heating and cooling profiles used shown in Fig. 6.1. Each of the samples was oxygenated following the growth process.

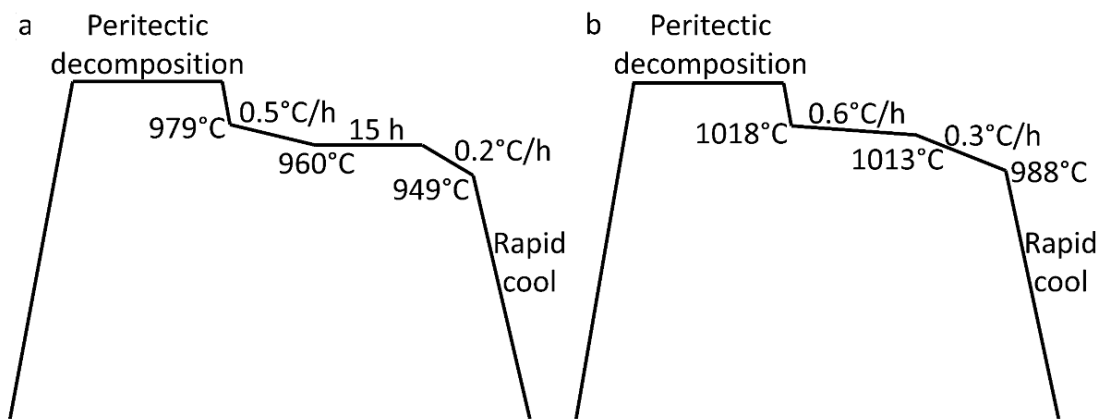


Figure 6.1: Heating profiles used for the growth of 30 mm diameter assemblies of a) YBCO-Ag and b) YBCO and LR YBCO by TSMG.

Each sample has successfully grown into a single grain, which is evident from the four-fold facet lines present on the top surface that extend to the base of each sample, these samples are shown in Figs. 5.17 and 7.1. The samples used for the measurement of T_c and J_c values are shown in Fig. 6.2. In addition, a representative example of the whole cross section built from individual 50x magnification images of the samples of YBCO, LR YBCO and YBCO-Ag used for the measurement of T_c and J_c values are shown in Fig. 6.3. The pore size is noticeably smaller throughout the YBCO-Ag sample in comparison with the YBCO and LR YBCO samples. There were fewer cracks observed in the YBCO-Ag sample than in the YBCO or LR YBCO sample and

those cracks present in the YBCO-Ag sample were characteristically much thinner and shorter. The assembled images at low magnification also show the distribution of silver within the sample. A number of large silver agglomerates are randomly distributed alongside many small silver agglomerates.

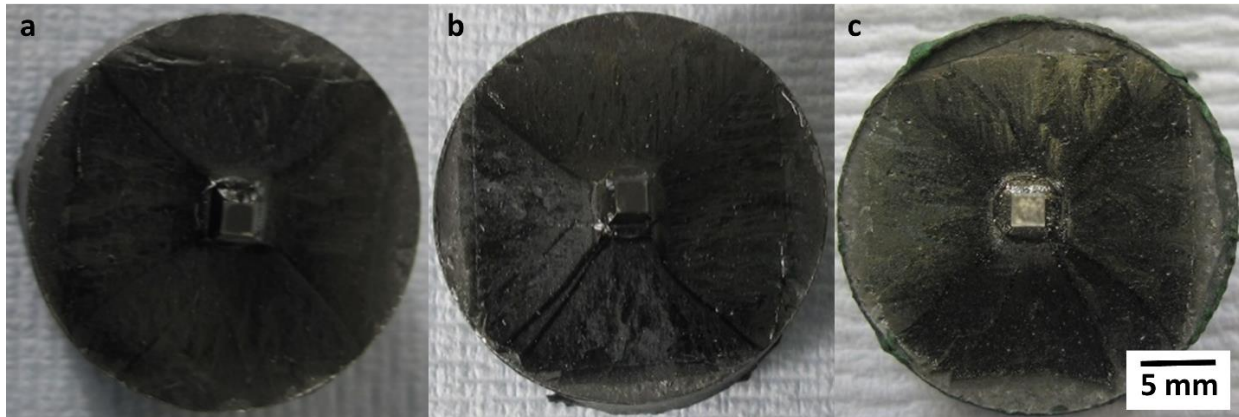


Figure 6.2: The fully grown single grains of a) YBCO, b) LR YBCO and c) YBCO-Ag.

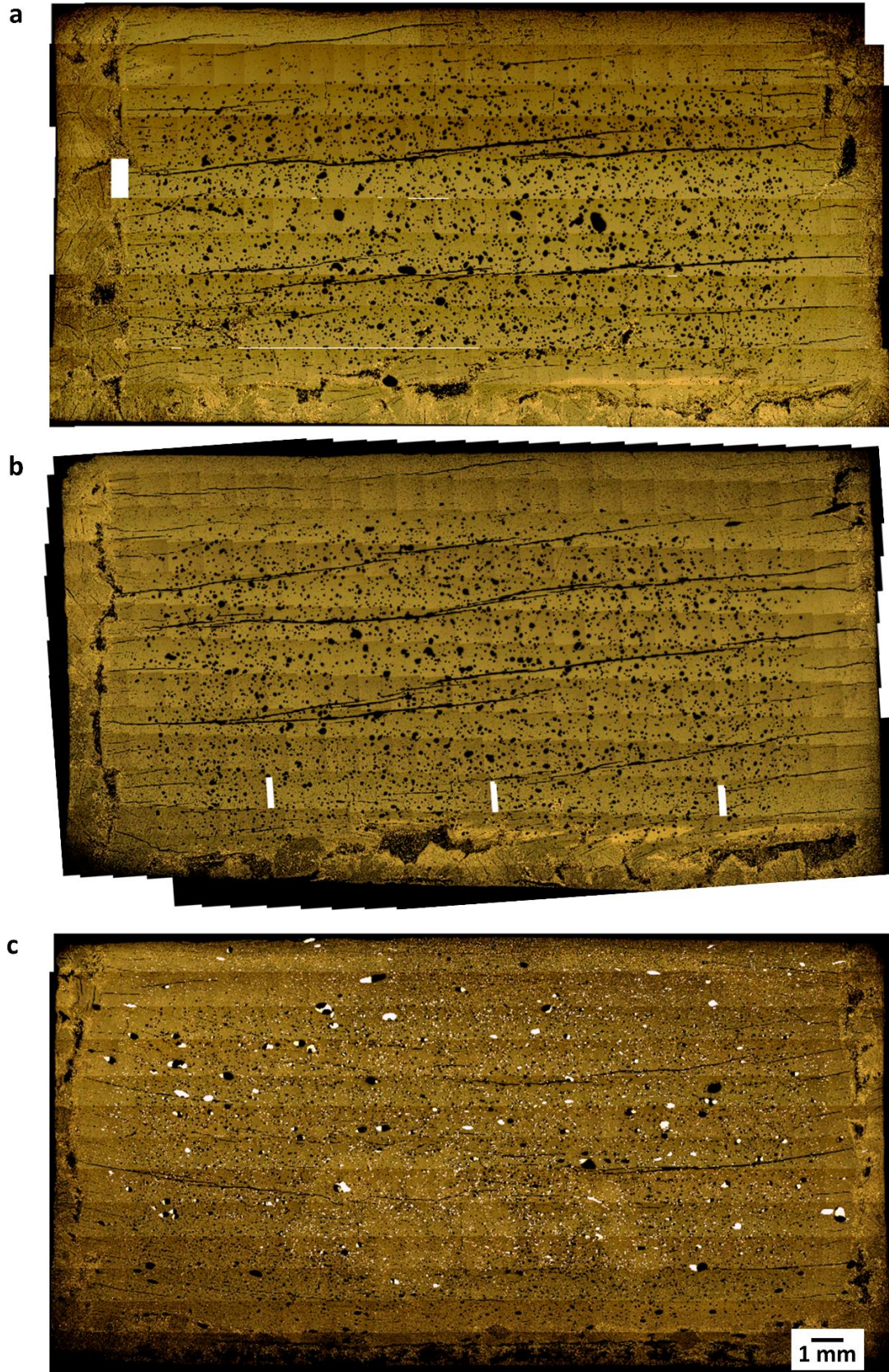


Figure 6.3: Whole cross-sections of single grains of: a) YBCO, b) LR YBCO, and c) YBCO-Ag.

6.2 Superconducting properties

6.2.1 Trapped field

The trapped field at the top and base of all samples were measured. All the samples exhibited a trapped field profile with a single peak and a smooth, continuously decreasing radial field gradient, characteristic of a single grain sample. The maximum trapped fields recorded on the top and bottom surfaces are given in Table 6.1. The average maximum trapped field for each size and type of sample is plotted in Fig. 6.4. The error bars in the figure represent the largest and smallest maximum trapped field value recorded for each type and size of sample.

The maximum trapped field recorded at the base of each of the samples was, in general, significantly lower than the trapped field recorded at the top surface, as expected. In addition, the smaller sized samples of YBCO-Ag had a significantly lower maximum trapped field than the 26 mm diameter samples of YBCO-Ag. This is also as expected; the larger the area over which the superconducting current can flow undisturbed, the larger the trapped field achievable for the sample.

The average maximum trapped field recorded for each of the 26 mm diameter samples is comparable across all three samples when the top or base is considered separately. There is, however, greater variation in the range of maximum trapped field of the YBCO-Ag than in either the LR YBCO samples or YBCO samples. The maximum trapped field at the top of one of the YBCO-Ag samples was over 0.05 T higher than the trapped field recorded in any of the YBCO samples.

Sample type	Sample diameter (mm)	Maximum trapped field (T)	
		Top	Base
YBCO-Ag	17	0.47	0.34
YBCO-Ag	17	0.30	0.24
YBCO-Ag	17	0.38	0.30
YBCO-Ag	17	0.41	0.21
YBCO-Ag	17	0.36	0.21
YBCO-Ag	17	0.28	0.22
YBCO-Ag	21	0.40	0.29
YBCO-Ag	21	0.40	0.31
YBCO-Ag	21	0.35	0.33
YBCO-Ag	21	0.36	0.27
YBCO-Ag	21	0.42	0.32
YBCO-Ag	26	0.58	0.23
YBCO-Ag	26	0.50	0.35
YBCO-Ag	26	0.64	0.37
YBCO-Ag	26	0.53	0.35
YBCO-Ag	26	0.68	0.51
YBCO-Ag	26	0.57	0.47
LR YBCO	26	0.54	0.36
LR YBCO	26	0.67	0.39
LR YBCO	26	0.63	0.39
LR YBCO	26	0.66	0.42
YBCO	26	0.61	0.42
YBCO	26	0.63	0.50
YBCO	26	0.58	0.45
YBCO	26	0.60	0.39

Table 6.1: The values of maximum trapped field recorded at the top and base of a number of single grains of YBCO, LR YBCO and YBCO-Ag.

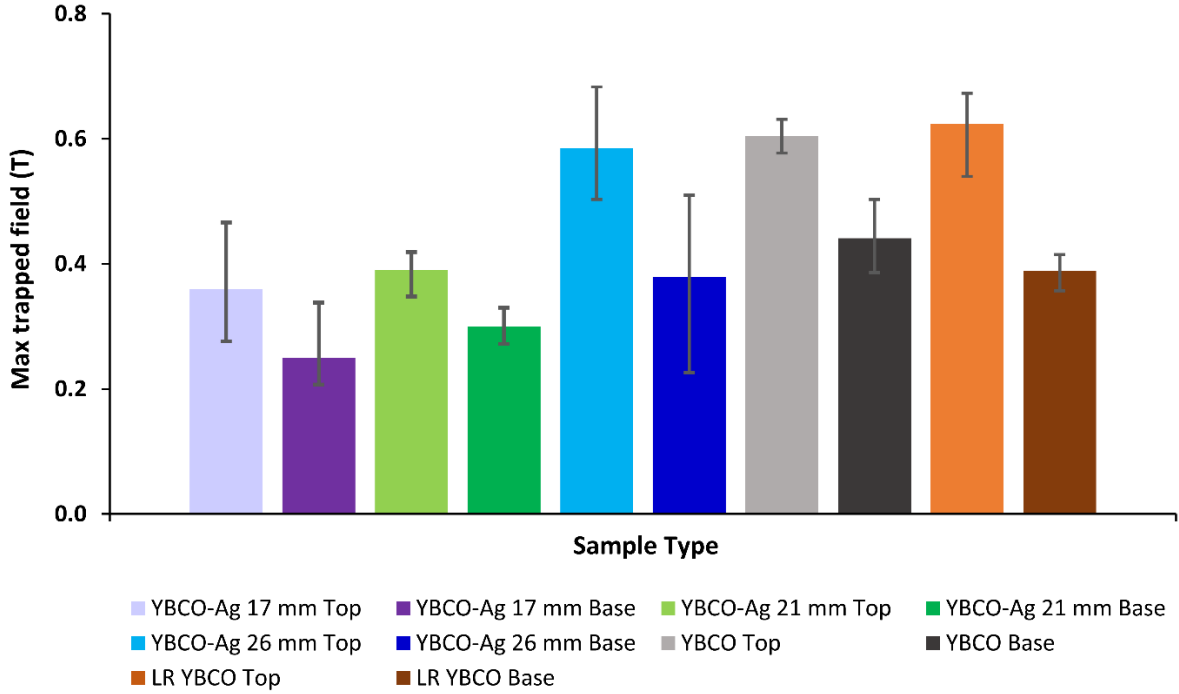


Figure 6.4: A plot of the average maximum trapped field recorded on the top and bottom surface of 26 mm diameter samples of YBCO and LR YBCO and a range of sizes of YBCO-Ag.

6.2.2 Transition temperature and critical current density

One of each of the 26 mm diameter samples of YBCO, LR YBCO and YBCO-Ag was chosen at random to be analysed using the SQUID. Sub-specimens were cut from along the c -axis directly below the seed and the locations were labelled as shown schematically in Fig. 6.5.

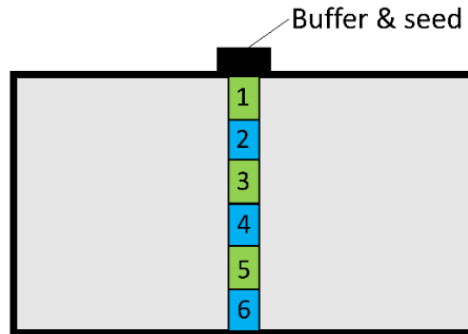


Figure 6.5: A schematic of the locations of the sub-specimens cut from each bulk.

The values of T_c and ΔT_{90} are given for each sub-specimen in Table 6.2. Histograms to enable comparison of these data for the different sub-specimen values are shown in Fig. 6.6. The value of T_c was at least 0.2 K higher for all corresponding sub-specimens of YBCO-Ag compared to the sub-specimens of YBCO. Conversely, the values of T_c for corresponding sub-specimens of LR

YBCO were comparable to those of the YBCO-Ag sub-specimens. The transition to the superconducting state was also sharper for sub-specimens of YBCO-Ag than for sub-specimens of YBCO and LR YBCO, with the exception of two and three equivalent sub-specimens, respectively.

Sub-specimen	YBCO			LR YBCO			YBCO-Ag		
	T_c (K)	ΔT_{90} (K)	$J_c(0)$ (MA m ⁻²)	T_c (K)	ΔT_{90} (K)	$J_c(0)$ (MA m ⁻²)	T_c (K)	ΔT_{90} (K)	$J_c(0)$ (MA m ⁻²)
1	91	1.2	394	91	1.4	482	92	1.2	417
2	92	1.1	413	92	1.2	386	92	0.7	465
3	92	1.1	454	92	1.5	371	92	0.5	495
4	92	0.8	412	92	1.0	400	92	1.9	160
5	91	3.7	267	92	1.2	380	92	3.0	145
6	91	0.7	401	92	0.9	326	92	1.7	287

Table 6.2: T_c , ΔT_{90} and J_c values of the sub-specimens of YBCO, LR YBCO and YBCO-Ag

The values of $J_c(0)$ are given in Table 6.2, the $J_c(0)$ value has been tabulated to provide a meaningful, single quantitative comparison of the J_c values between sub-specimens and types of sample. The highest value of $J_c(0)$ was recorded at the centre of the YBCO and YBCO-Ag samples (454 MA m⁻² and 494 MA m⁻², respectively), whereas in the LR YBCO sample this was recorded at the top (482 MA m⁻²). The largest overall maximum $J_c(0)$ value was recorded in a YBCO-Ag sub-specimen, this was 40 MA m⁻² higher than the maximum recorded in the YBCO sample and 12 MA m⁻² higher than recorded in the LR YBCO sample. The $J_c(0)$ value was extremely consistent across all sub-specimens from the LR YBCO sample to within ± 78 MA m⁻². The values of $J_c(0)$ were less consistent between sub-specimens of YBCO, varying within ± 94 MA m⁻², however, they were significantly less consistent between sub-specimens of YBCO-Ag which varied within ± 175 MA m⁻². Sub-specimens 1-3 of YBCO-Ag exhibited significantly higher values of $J_c(0)$ than the YBCO sub-specimens. Conversely, the values of $J_c(0)$ measured at the base of the samples were significantly and consistently higher in the YBCO sub-specimens.

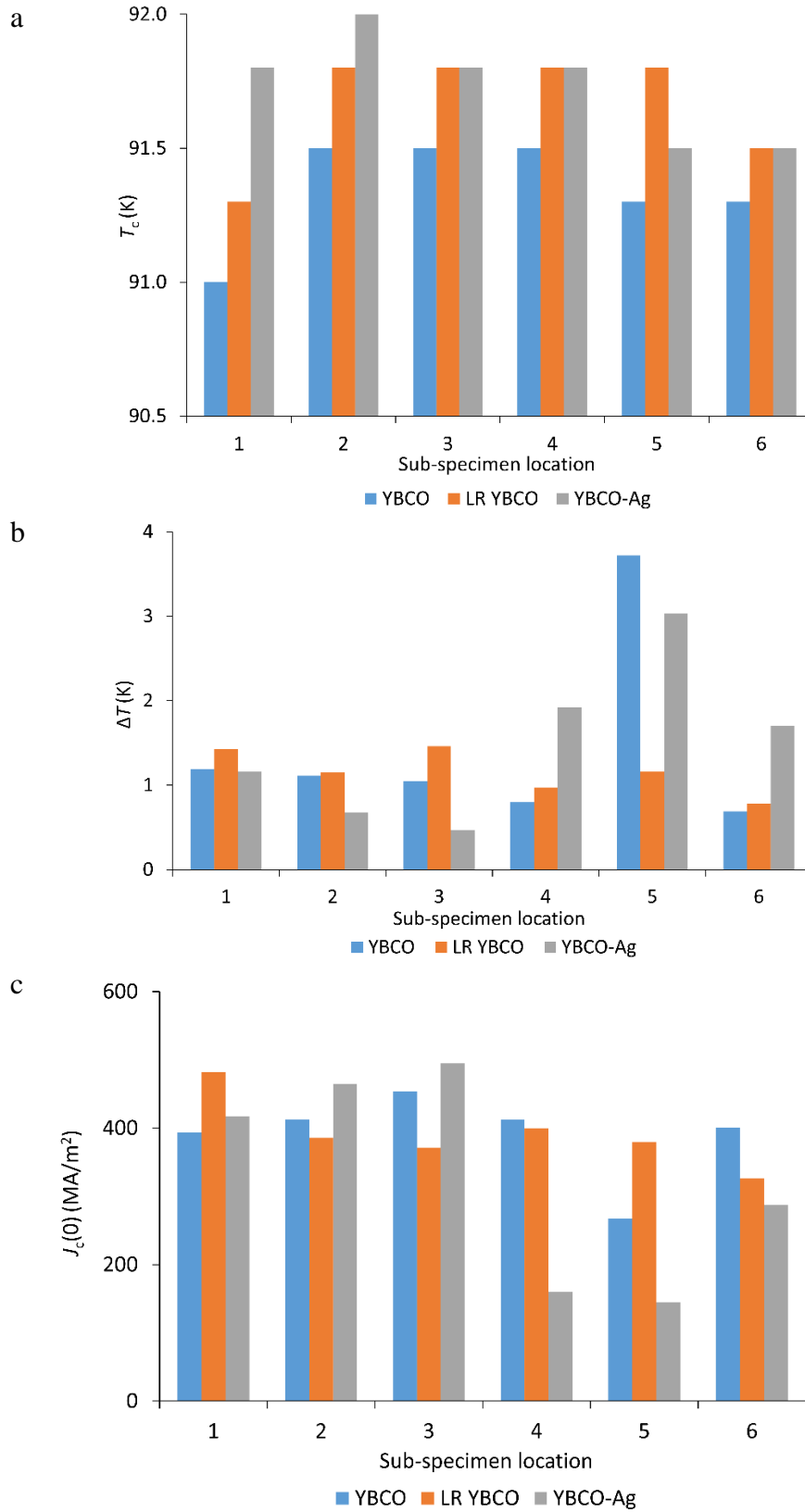


Figure 6.6: Histograms to enable comparison between corresponding sub-specimens for: a) T_c , b) ΔT_{90} , and c) J_c values.

6.3 Microstructure

The remaining half of each of the three samples used to analyse the T_c and J_c values were prepared for microstructure analysis using the optical microscope. A magnification of 50x was used to observe the pore, crack, and, where relevant, the silver distribution, while a magnification of 500x was used to observe the distribution of Y-211 agglomerates in the single grain microstructure. Images were taken centrally at 1 mm intervals in the c -axis direction and in the a/b -axis direction at approximately 1.5 mm vertically from the top of the sample. These images are shown in the appendix. In addition, the c -axis was imaged at 50x magnification at intervals corresponding to the centre of each of the sub-specimens used for physical characterisation, these images are shown in Fig. 6.7.

The microstructures of YBCO and LR YBCO are very similar, although the microstructure of YBCO-Ag is significantly different. The pores in YBCO-Ag are significantly smaller. There are also a large number of very small silver agglomerates accompanying some larger silver agglomerates which appear to have filled regions that would otherwise have been pores. In addition, the cracks present within the YBCO-Ag sample are significantly smaller than those present in both the YBCO and LR YBCO samples.

Throughout the c -axis direction the YBCO and LR YBCO samples show a very similar microstructure, although the microstructure of YBCO-Ag is significantly different. The pore size in the YBCO and LR YBCO samples is large and there are large horizontal cracks present in the sample microstructure. The pores present in these two samples range between approximately 40 μm and 270 μm , with a large number of the pores of a size closer to the largest pore present. However, in the YBCO-Ag sample, the pore size ranges between 30 μm and 140 μm , with many of these pores closer in size to the smallest pores present. In addition, the cracks in the YBCO-Ag sample are significantly smaller. There are also fewer vertical cracks present within the YBCO-Ag sample than in the other two types of sample.

Figs. 6.8 to 6.10 show images of the samples along the c -axis from directly below the seed at 500x magnification. This magnification is sufficiently high to enable the Y-211 agglomerates to be observed. These figures show there is a large variation in the size of the Y-211 inclusions. There

are many different sizes of these inclusions within each image. The LR YBCO shows a much greater uniformity in both the size of the Y-211 inclusions and in the distribution than the YBCO samples. There are fewer but larger Y-211 inclusions closer to the seed and more and smaller inclusions with distance from the seed in the YBCO samples. This was not observed in either the LR YBCO or the YBCO-Ag; the YBCO-Ag had a very uniform distribution of Y-211 inclusions both within each image and along the c -axis of the bulk single grain. These images enable some of the silver to be observed too; some of these pores are partially filled by silver, as is shown in the image taken at 5 mm.

The microstructure of the samples imaged at 50x magnification along the a/b -axis approximately 1.5 mm from the top surface show a number of small horizontal and vertical cracks present in the sample microstructure. However, these cracks are thinner in the YBCO-Ag sample than in the other two types of sample, as also observed in Fig 6.7. In addition, there are fewer cracks present and the cracks are thinner near the top of the sample than observed further along the c -axis. The pores present in the images taken near the top of the sample are much smaller than those observed further down the c -axis, and there are also fewer pores in all three samples near the top of the sample. There are a number of silver agglomerates present and there are both small and large silver agglomerates present. In many cases silver agglomerates have partially filled the pores present in the YBCO-Ag samples. In addition, the addition of silver has reduced the extent and number of vertical cracks present.

The microstructure imaged at 50x magnification at 1.5 mm from the base of the samples show some small cracks present in both the YBCO and LR YBCO images, and a larger crack present in the YBCO-Ag sample. There is a limited number of relatively small pores in the YBCO and LR YBCO images, and there are fewer and, on-average, smaller pores than at the centre of the c -axis of the sample. There is a very limited amount of silver present in the YBCO-Ag sample in comparison to that observed at the top and mid-way along the c -axis. This reduction in silver may be due to the additional liquid-phase provided at the base filling most of the pores, which could otherwise have been filled by silver. Although there is less silver present in the YBCO-Ag samples at this location, there are still fewer vertical cracks present than in the other two types of samples.

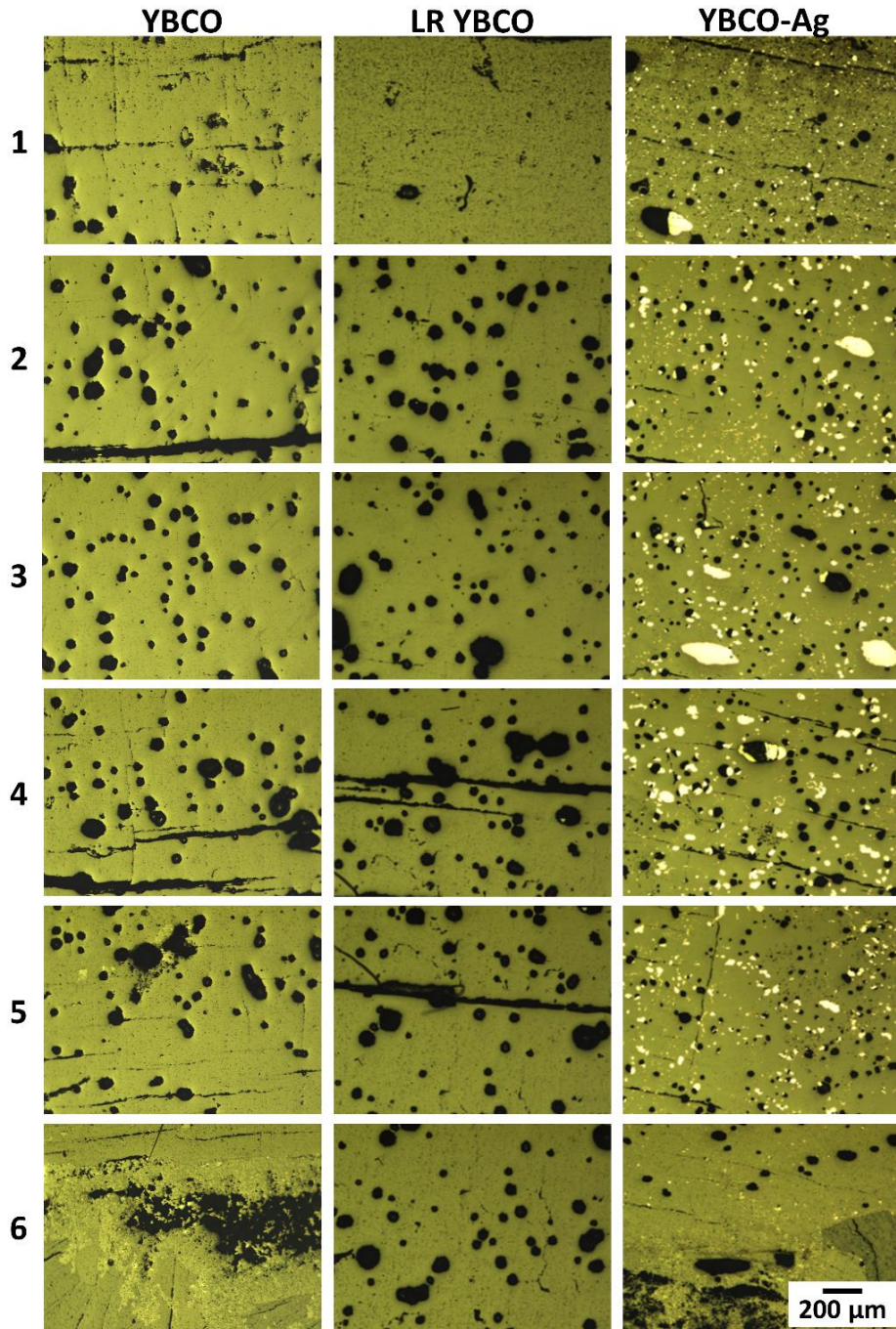


Figure 6.7: Optical microscope images taken at 50x magnification corresponding to approximately the centre of each of the sub-specimens.

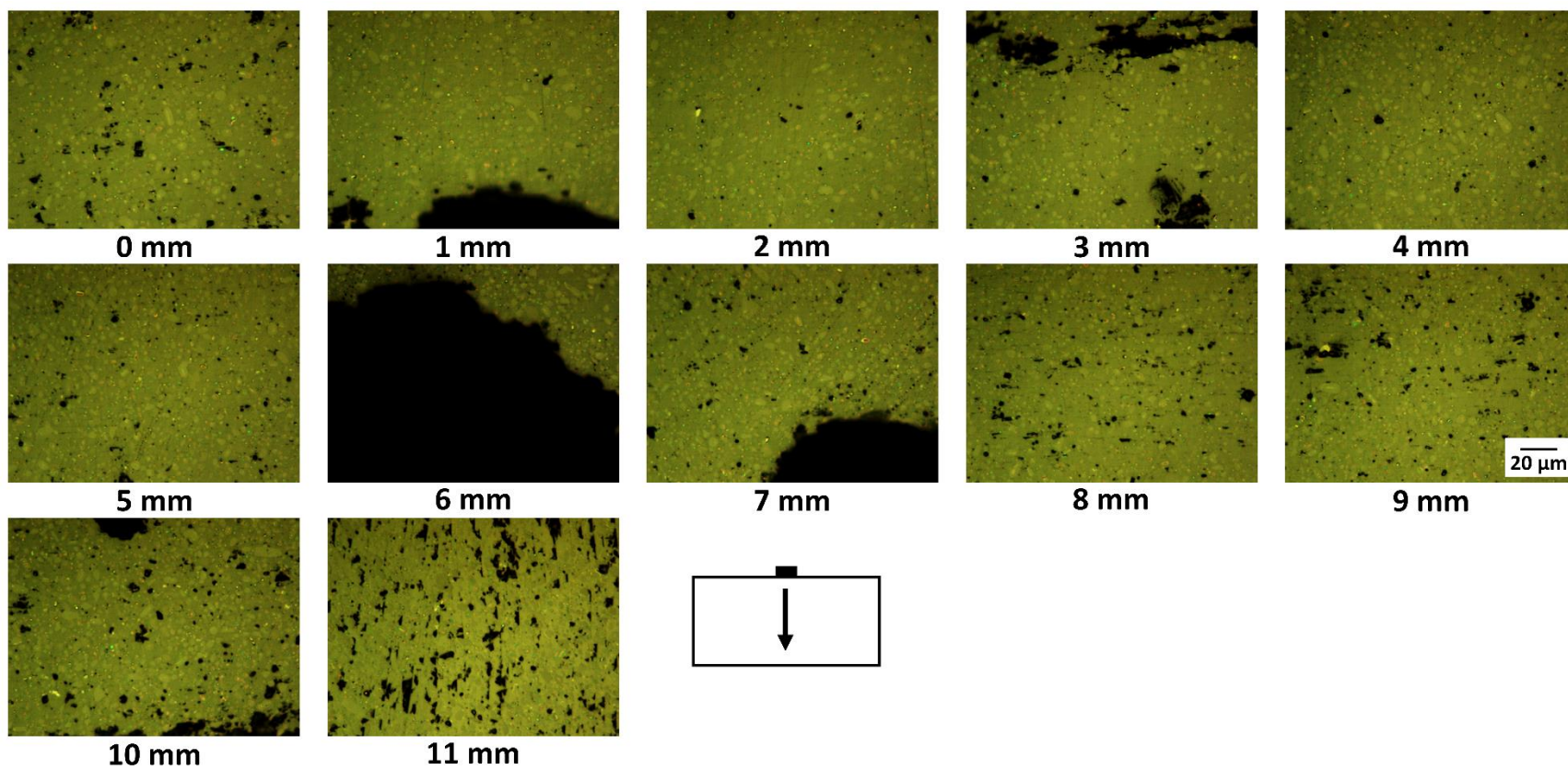


Figure 6.8: Optical microscope images along the central c-axis of a YBCO sample at 500x magnification.

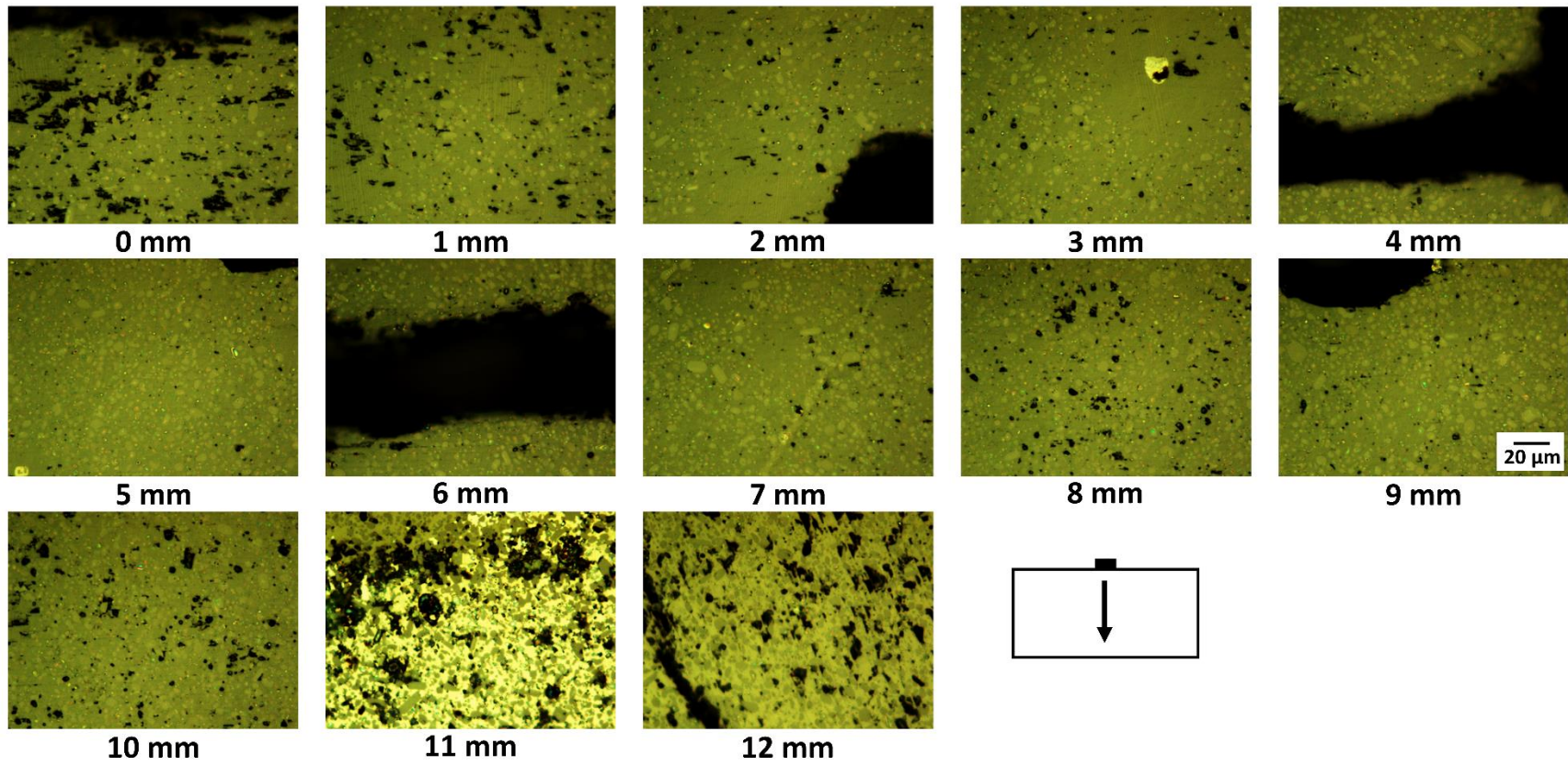


Figure 6.9: Optical microscope images along the central c-axis of a LR YBCO sample at 500x magnification.

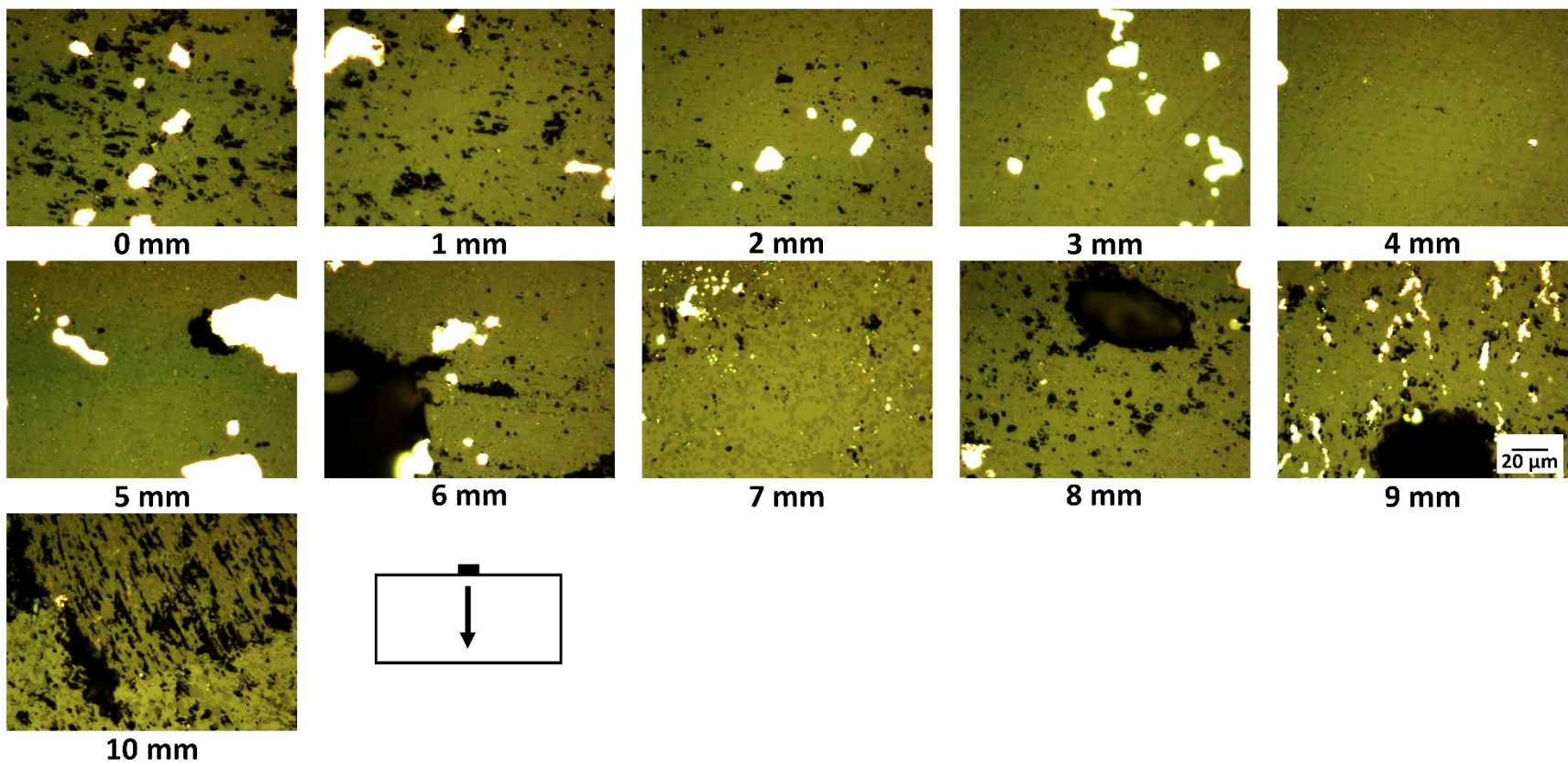


Figure 6.10: Optical microscope images along the central c -axis of a YBCO-Ag sample at 500x magnification.

6.4 Porosity and Silver distribution

The area occupied by pores and, where relevant, silver, of each image shown in Fig. 6.7 was as determined using threshold analysis, this data has been plotted in Fig. 6.11. The area occupied by pores is much lower in the YBCO-Ag samples than in either the YBCO or LR YBCO samples at all locations except locations 1 and 6. At the locations where the area occupied by silver is highest, the area occupied by pores in the YBCO-Ag sample is lowest and significantly lower than the area occupied by pores in the other types of sample. This suggests that some of the pore area must have been filled by silver agglomerates in the YBCO-Ag samples. The area occupied by pores increases with increasing distance from the seed and then begins to decrease mid-way down the sample. This is as expected from both the images taken and from observation presented in Chapter 5. The average area occupied by pores in the LR YBCO sample is similar to that of the standard YBCO sample.

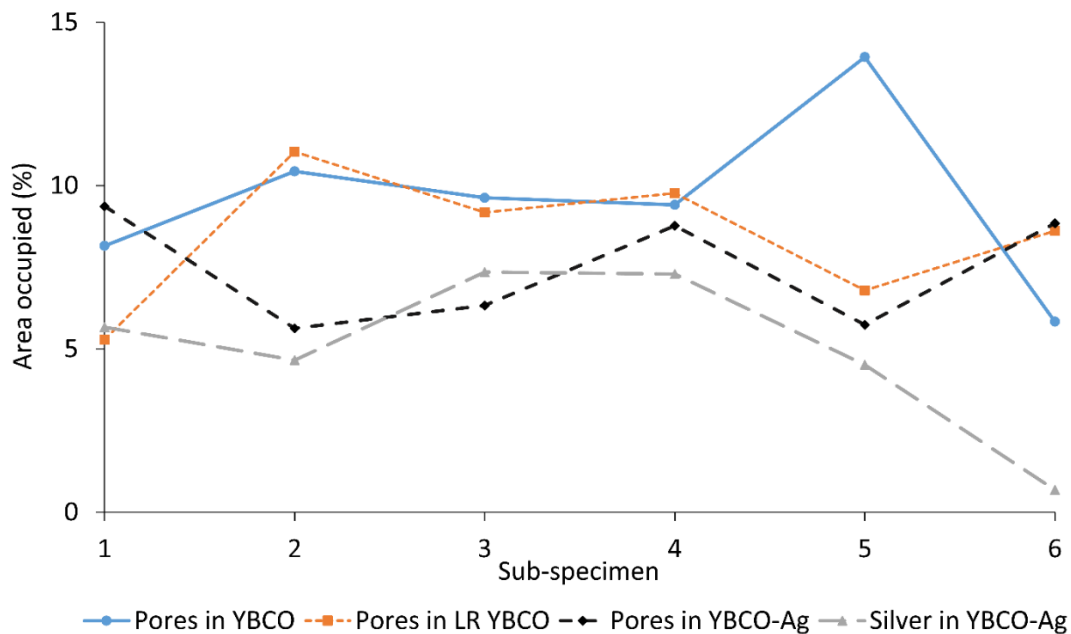


Figure 6.11: A plot of the area occupied by pores in each image of the sub-specimen, as derived using threshold analysis.

6.5 Relation between microstructure, composition and superconducting properties

The average maximum trapped field is comparable for all three types of sample. The addition of silver does not have a detrimental effect on the maximum trapped field achievable or the

uniformity of the trapped field profile. The 26 mm diameter YBCO-Ag samples show a greater variation in the maximum trapped field. This suggests that it is possible to produce YBCO-Ag samples with higher maximum trapped fields than is achievable in YBCO or LR YBCO samples of the same size.

The onset T_c value of the sub-specimens of YBCO-Ag was higher than that of the sub-specimens of YBCO and LR YBCO in almost all sub-specimens. This is both desirable, and, shows the addition of silver does not have a detrimental effect on the T_c values. The sub-specimens of YBCO-Ag have a sharper transition to superconducting (given by the value of ΔT_{90}) than the YBCO sub-specimens. This indicates that the quality, in terms of the superconducting properties, of the YBCO-Ag sample is higher than that of the YBCO sample. Conversely, although sub-specimens from the top of the YBCO-Ag sample have a sharper transition to the superconducting state than those from the top of the LR YBCO sample, the LR YBCO sub-specimens exhibit a sharper transition at the base. This suggests that the provision of additional liquid alone improves the quality of the sample towards the base, although this becomes more complex and less effective when silver is added.

The highest value of $J_c(0)$ for all sub-specimens investigated was recorded for one of the YBCO-Ag sub-specimens. The value of $J_c(0)$ in YBCO-Ag is higher than that of the corresponding sub-specimens of YBCO for the top three sub-specimens and sub-specimens two and three of LR YBCO. However, closer to the base, the corresponding YBCO and LR YBCO sub-specimens yielded higher $J_c(0)$ values. Fig. 6.12 shows plots of the area occupied by pores at the centre of each sub-specimen with the trend in $J_c(0)$ values superimposed for each sample. The porosity of the YBCO sample is relatively consistent, as is the $J_c(0)$ value, with the exception of sub-specimen five. The porosity of sub-specimen five is much higher than that of the rest of the sub-specimens from the sample and this sub-specimen has a much lower $J_c(0)$ value. This suggests that the value of $J_c(0)$ is inversely affected by the porosity. This is as expected, since a higher porosity will reduce the area of Y-123 superconducting matrix available within which the superconducting current can flow. However, as there is only a large change for one sub-specimen, more samples must be investigated in detail to check if this hypothesis is supported.

The porosity in the LR YBCO sample is lower on average. The highest porosity is 11 %, compared with 13.9 % exhibited in sub-specimen five of the YBCO sample. The value of $J_c(0)$ in the LR YBCO sample is much higher in sub-specimen one than in any of the other sub-specimens and the porosity at this location is much lower, at only 5.3 %. The $J_c(0)$ values and area occupied by pores is consistent throughout the other sub-specimens. This relationship supports the hypothesis described above that there is an inverse relationship between porosity and the $J_c(0)$ value.

In the YBCO-Ag sample, there was a large difference in the $J_c(0)$ values in sub-specimens one to three compared to sub-specimens four to six. This is unexpected since the porosity is lower in sub-specimens two to five than in the corresponding sub-specimens of the other two types. The area occupied by pores is very consistent between sub-specimens, which suggests that the sub-specimens from this sample do not support the hypothesis that the value of $J_c(0)$ is inversely related to the porosity. One reason for this could be the addition of silver. The silver is not superconducting so may behave in a similar way to a pore within the Y-123 superconducting matrix, and hence both the area occupied by pores and the area occupied by both pores and silver are plotted in Fig. 6.12. Neither the distribution of silver nor the distribution of combined silver and pores show the same or similar trend as the $J_c(0)$ values in the YBCO-Ag sub-specimens. This suggests that there are further possibilities to consider for this sample. One possible explanation is the presence of a large number of small cracks observed in Fig. 6.7 in sub-specimen locations three to five. Another possibility is that there is a combined effect of silver and porosity, but this is affected by other factors. One possible factor is the size of the silver agglomerates or pores. The relative size of the pores and, where relevant, silver agglomerates are shown in Fig. 6.13. The size of the pores or silver agglomerates do not appear to correlate in any way with the $J_c(0)$ value measured in each sub-specimen.

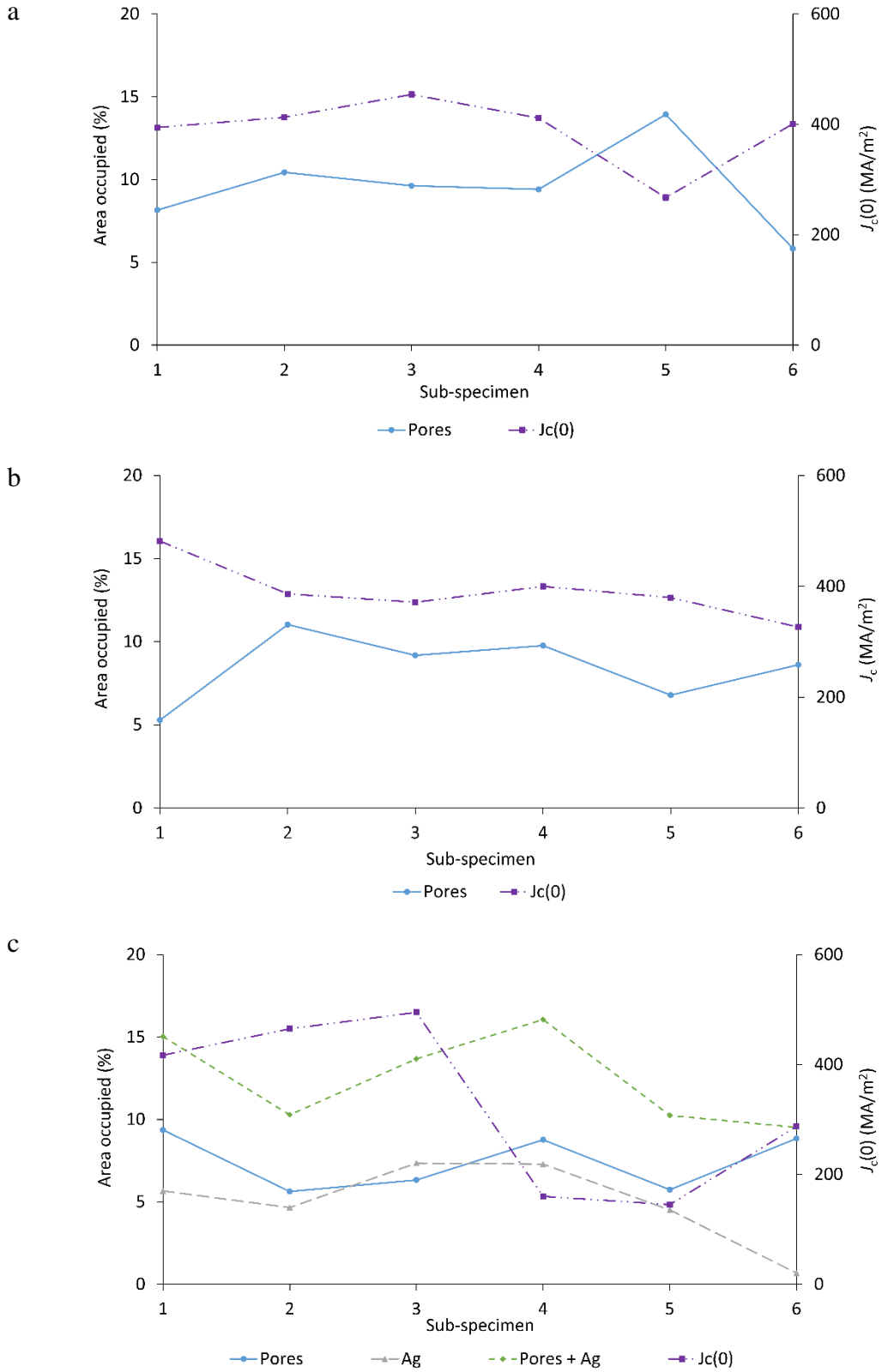


Figure 6.12: Plots of the area occupied by pores, and where relevant, silver in each image with the J_c value for the sub-specimen superimposed for: a) a YBCO sample, b) a LR YBCO sample, and c) a YBCO-Ag sample.

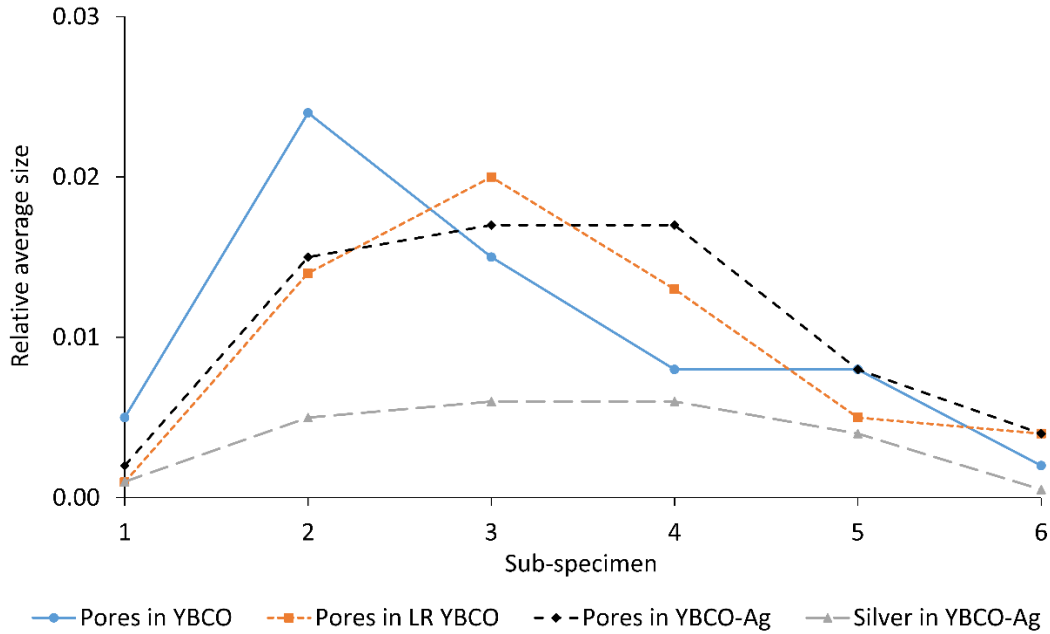


Figure 6.13: The relative average pore size, and where relevant, silver agglomerate size in each image taken from the centre of each of the sub-specimens.

6.6 Conclusions

The addition of silver to bulk YBCO single grains has had no net detrimental effect on their superconducting properties. Single grains of YBCO-Ag are able to trap a comparable field to YBCO and LR YBCO single grains of the same size. An individual single grain of YBCO-Ag was able to trap a higher maximum field than the equivalent samples of YBCO and LR YBCO, perhaps suggesting that with further optimisation of the growth process these YBCO-Ag samples may be able to achieve higher trapped fields than comparable YBCO samples. The onset T_c value was not detrimentally affected by the addition of silver, and nor was the sharpness of transition to superconducting. The sharpness of transition to the superconducting state was only better than the YBCO-Ag sub-specimens for the sub-specimens taken from the base of the LR YBCO sample. This suggests that the provision of additional liquid alone is able to improve the quality at the base of the sample. The value of J_c at the top of the YBCO-Ag sample was comparable to that of LR YBCO and much higher than achieved at the top of the YBCO sample. However, the value of J_c at the base of the LR YBCO sample was significantly higher than that at the base of the YBCO-Ag sample, whereas that at the base of the YBCO sample was slightly higher than that of the base of the YBCO-Ag sample. On studying the microstructure of the samples in both the YBCO and LR YBCO samples, the value of J_c is inversely related to the area occupied by pores. This is

expected since an increase in porosity reduces the area of Y-123 matrix available for the flow of superconducting current. However, in the YBCO-Ag sample, the relationship between the value of J_c and porosity is much more complex; there is no obvious trend between either the area occupied by pores, the area occupied by silver, the area occupied by both pores and silver or the average pore or silver agglomerate size and the trend in J_c values. There are, however, fewer vertical cracks present in these samples, which may increase the uninterrupted area over which the superconducting current can flow. This suggests that a complex mix of these variables affect the value of J_c . In order to draw more valid conclusions regarding this relationship, more samples should be investigated in detail.

The provision of silver to YBCO did not have a significant detrimental effect upon the superconducting properties of this material. Although the YBCO-Ag sample reported the best individual values of each of T_c , ΔT_{90} , J_c and trapped field, it was, however, not consistently the best in all of the sub-specimens or samples. The absence of degradation in the superconducting properties of the YBCO system when silver is added to the precursor powder suggests that use of this alloying element improves significantly the potential of YBCO-Ag for use in practical applications.

7 Small scale tests of the mechanical strength of YBCO-Ag

The widespread use of ceramic (RE)BCO superconductors is generally limited by their poor mechanical properties. Although a large number of techniques can be used to improve the mechanical properties of conventional ceramic materials, many of these are incompatible with the growth of single grain bulk YBCO by the TSMG process. Complications arise due to the need to minimize the degradation caused to the superconducting properties and the requirement to produce a large single grain. The addition of silver has been shown to improve the mechanical properties of (RE)BCO single grains without detrimental effect upon the growth process and superconducting properties. The growth of YBCO-Ag is particularly challenging, however, Chapter 5 describes the development of a process to enable growth of large YBCO-Ag single grains reliably and reproducibly.

In this chapter, the growth process developed in Chapter 5 has been used to grow large single grains of YBCO-Ag. The flexural strength at a number of locations in these YBCO-Ag single grains has been measured. In addition, the flexural strength at a number of locations in YBCO samples grown both with, and without, liquid-phase enrichment have been tested and compared. Finally, the distribution of the failure stress has been compared with the pore and silver distribution in each of the single grains.

7.1 The growth process

Three samples of each of standard YBCO, liquid-phase-enriched (LR) YBCO and YBCO-Ag were pressed in a 30 mm die, as described in Chapter 2. Images of the samples are shown in Fig. 7.1. In addition, a representative example of the whole cross sections built from individual 50x magnification images of YBCO, LR YBCO and YBCO-Ag are shown in Fig. 7.2. The pore size is noticeably smaller throughout the YBCO-Ag sample compared with the YBCO and LR YBCO samples.

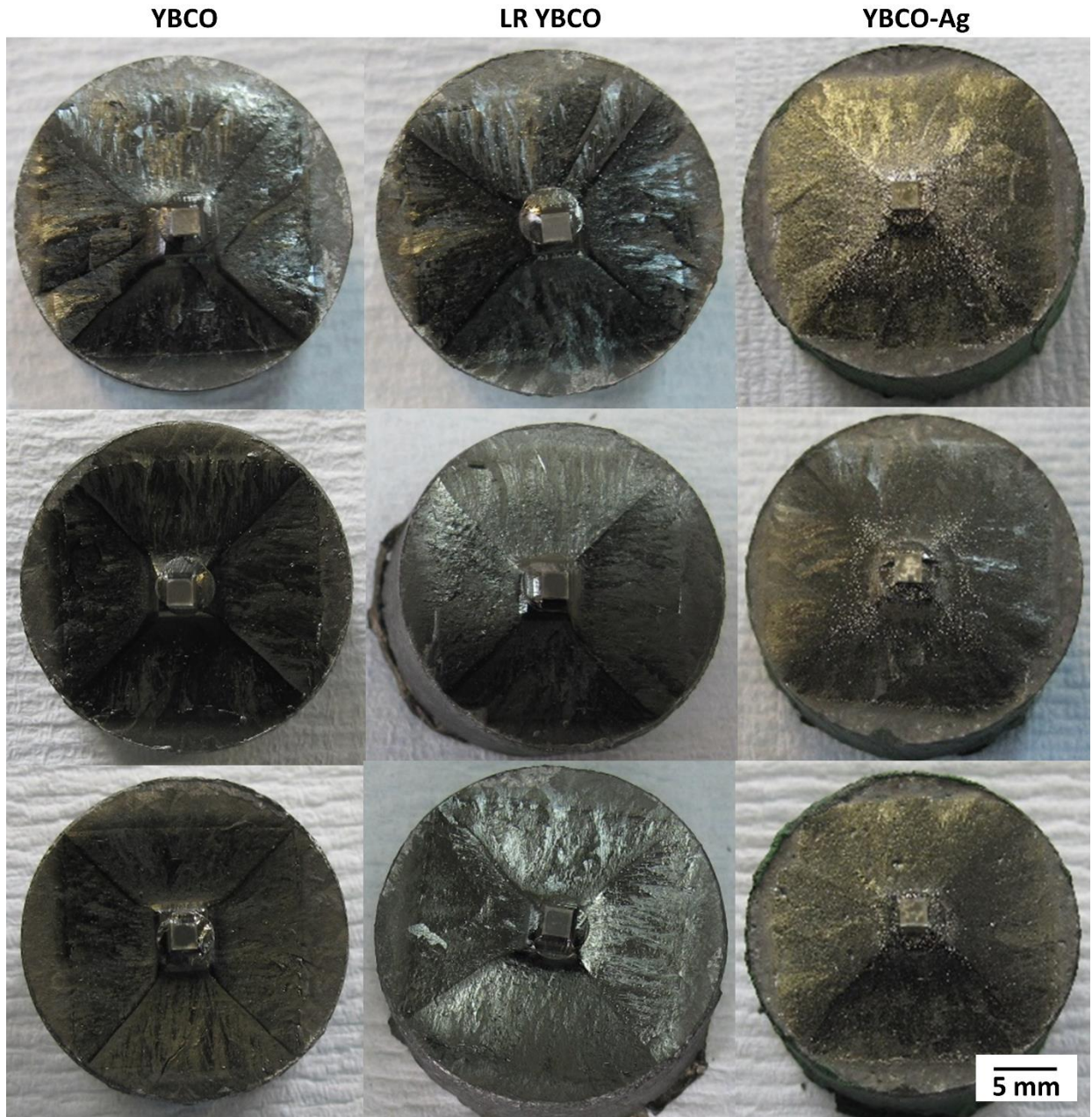
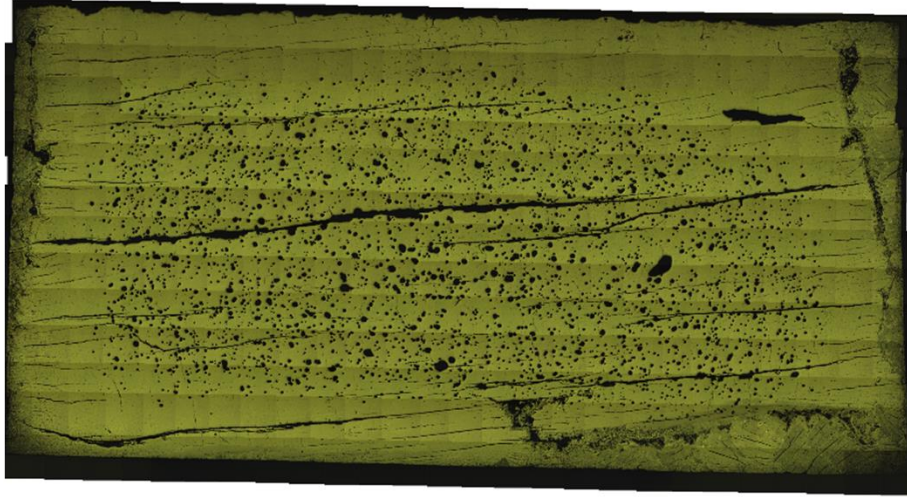
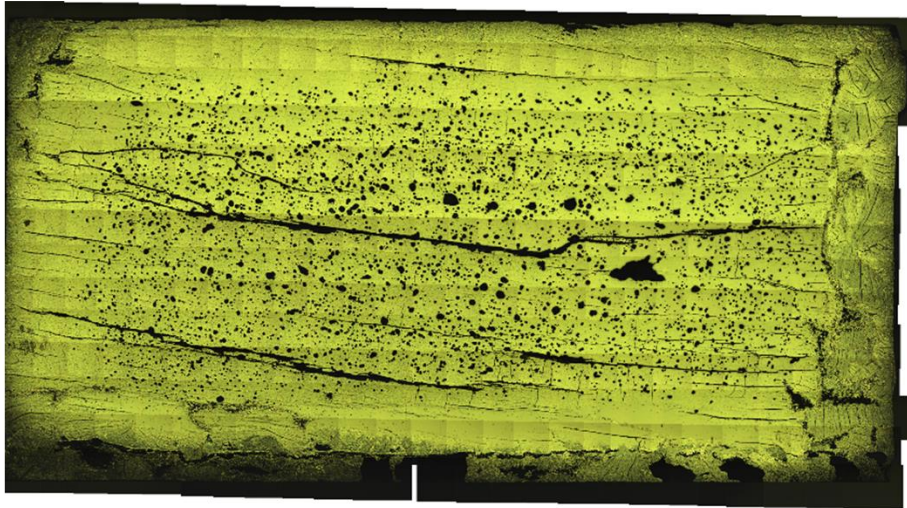


Figure 7.1: The fully grown single grains of YBCO, LR YBCO and YBCO-Ag.

a



b



c

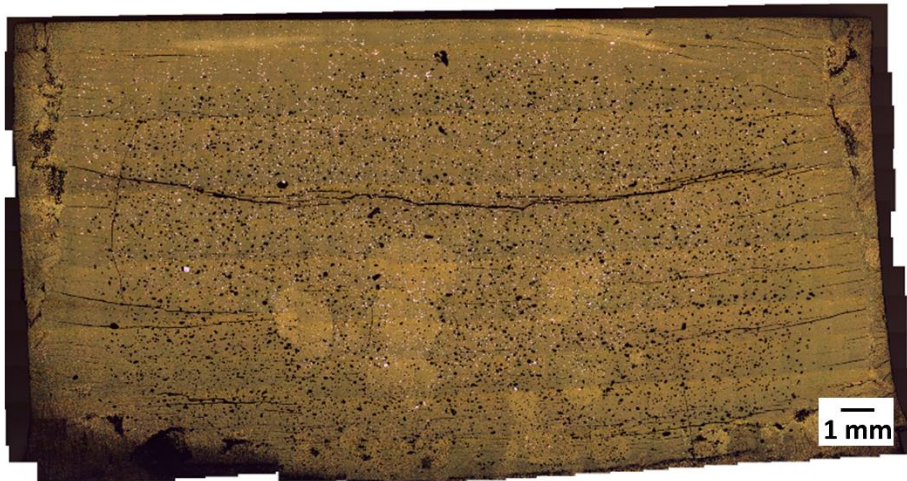


Figure 7.2: Whole cross-sections of single grains of: a) YBCO, b) LR YBCO, and c) YBCO-Ag.

7.2 Mechanical properties

A three point bend test is a simple test which can be used to measure the flexural strength of a beam in bending. In the three-point bend test loading is applied to a central point while the beam is supported on point supports at each end. One side of the beam is always in compression, the side in which the load is being applied, while the other is always in tension. This test is also useful for observing the load-displacement (or stress-strain) characteristics of a material and so the trace from this test can be used to find the Young's modulus, yield stress and ultimate tensile stress. The trace can also provide an indication of the mode of failure experienced by the sample.

Samples were prepared for the three point bend test by removing the buffer pellet from the sample and then the top and base were ground flat and parallel. Each sample was cut in half using a diamond-coated cutting wheel. One half of each sample was further cut into flexural beams of dimensions approximately 2.0 mm x 1.5 mm x 20.0 mm. Each beam was cleaned in warm acetone to remove any wax remnants from the cutting process and then lightly polished using grade 2400 silicon carbide paper. This ensured each edge was smooth. The removal of wax and ensuring the smoothness of the edges ensures that the wax remnants or any defects previously present at the edge do not have an impact on the results of the test.

A three-point bend test was used to measure the flexural strength of each beam at room temperature. A load was applied at a 0.15 mm/minute in the c -axis direction using an Instron electromechanical tensile testing machine. The loading was such that the lower surface of the beam was always in tension whereas the upper surface was always in compression. A schematic illustration of the experimental setup is shown in Fig. 7.3. The set-up enabled the flexural strength in the ab -plane to be determined.

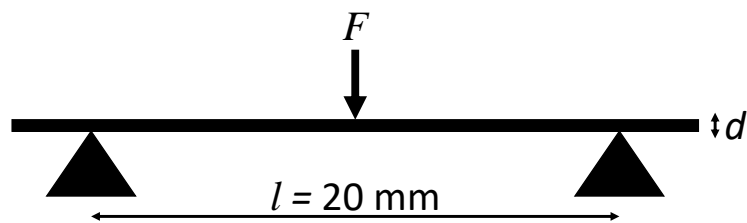


Figure 7.3: A schematic of the three-point bend test setup.

The beams were tested to failure in the tensile testing procedure. The following equation was used to calculate the flexural strength at failure:

$$\sigma_f = \frac{3Fl}{2bd^2} \quad (7.1)$$

where F is the load at failure, l is the support span (20 mm), b is the width of the test beam (1.5 mm) and d is the depth (2 mm) of the test beam.

Three-point bend tests were undertaken, on 41 beams from YBCO and LR YBCO samples and from 47 beams from YBCO-Ag samples out of a possible 54 beams of each type. The beams that were not tested contained large cracks or pores, and were broken during the cutting process or during movement following the cutting. The majority of these beams were from close to the centre of the sample, which is expected since there are generally more pores present at the centre of the sample than at the edge. The location and numbering of the flexural beams is shown schematically in Fig. 7.4.

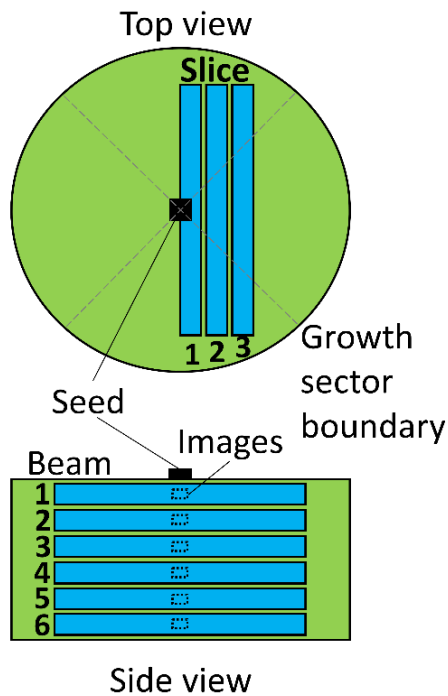


Figure 7.4: A schematic of the locations of the beams used for mechanical testing.

A typical load-displacement curve is shown in Fig. 7.5. The shape of this curve suggests the beams fail in brittle failure with very limited plastic deformation. However, this shape of graph could also suggest that the failure is shear dominated, this would mean that it would not be valid to calculate the flexural strength. The failure surfaces of the beams were studied to identify in which mode the beams failed. Each of the beams failed at approximately the centre and did not show longitudinal cracking or splitting, this suggests that failure was by brittle failure from the tensile loading rather than due to shear loading.

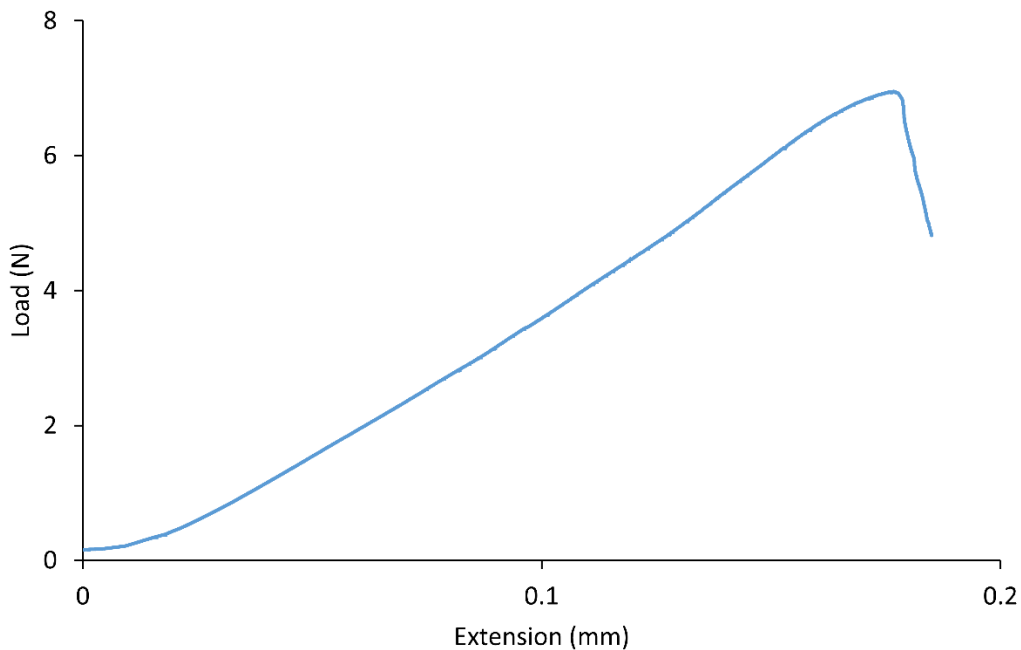


Figure 7.5: A typical load-displacement curve exhibited by the YBCO, LR YBCO and YBCO-Ag beams during the three-point bend test.

The average flexural stress at failure is plotted in Fig. 7.6 for each location from each slice and the flexural strength of each individual beam is given in Table 7.1. The beams that were unable to be tested have been excluded from the average values, but have been recorded as having zero strength for the purpose of representation in the error bars.

YBCO-Ag beams exhibited the highest average mechanical strength for the vast majority of the flexural tests. Only three corresponding beams had noticeably higher strength than the YBCO-Ag beams. In addition, the highest overall maximum mechanical strength for each corresponding beam was recorded in YBCO-Ag for every location measured except for four, as indicated by the

error bars in the figure. A maximum mechanical strength of 171 MPa was observed in the YBCO-Ag beams. However, there was significant fluctuation in the mechanical strength for corresponding beams from different samples of the same type. This fluctuation in mechanical strength is typical behaviour of brittle ceramic materials.

The provision of additional liquid improved the mechanical strength, although much less so than Ag. The effect of the additional liquid was particularly beneficial in the flexural beams tested from slice 3. In this slice, the average flexural strength was significantly higher for all flexural beams of LR YBCO than those of standard YBCO. However, there were more significant fluctuations than observed in the other two slices.

Location	Flexural strength (MPa)								
	YBCO-Ag			LR YBCO			YBCO		
	1	2	3	1	2	3	1	2	3
Slice 1									
1	75.4	64.2	-	4.9	46.3	44.0	61.7	45.0	69.3
2	53.3	58.2	41.3	51.0	49.9	55.7	22.2	34.4	-
3	55.4	40.4	61.3	-	12.2	-	-	-	10.1
4	40.6	33.6	-	51.9	49.2	0.4	49.1	-	-
5	29.3	38.7	46.3	-	-	35.4	56.0	-	19.0
6	49.4	104.9	10.2	56.7	48.0	-	-	-	-
Slice 2									
1	54.4	-	141.3	41.5	72.2	49.8	95.6	50.6	12.5
2	105.3	56.9	170.8	54.0	51.5	49.2	69.6	-	10.5
3	74.7	143.5	37.4	-	20.5	-	37.0	-	-
4	33.2	31.3	-	72.3	60.8	-	28.6	46.8	3.9
5	36.8	67.5	-	-	-	23.2	48.7	15.9	21.2
6	26.0	28.0	100.1	39.0	41.2	42.4	34.6	12.2	33.3
Slice 3									
1	68.9	82.1	65.7	103.5	79.7	64.2	51.9	17.7	40.6
2	75.7	45.4	55.0	26.0	61.5	72.8	51.3	20.1	-
3	71.6	145.3	24.5	46.1	45.2	-	11.1	37.5	-
4	24.5	123.6	-	65.0	50.9	8.9	31.1	2.2	48.0
5	56.7	89.7	75.8	-	59.3	20.6	60.9	5.9	29.2
6	79.2	89.9	-	47.8	-	75.1	33.7	-	-

Table 7.1: The flexural strength of each beam from each of the three types of sample.

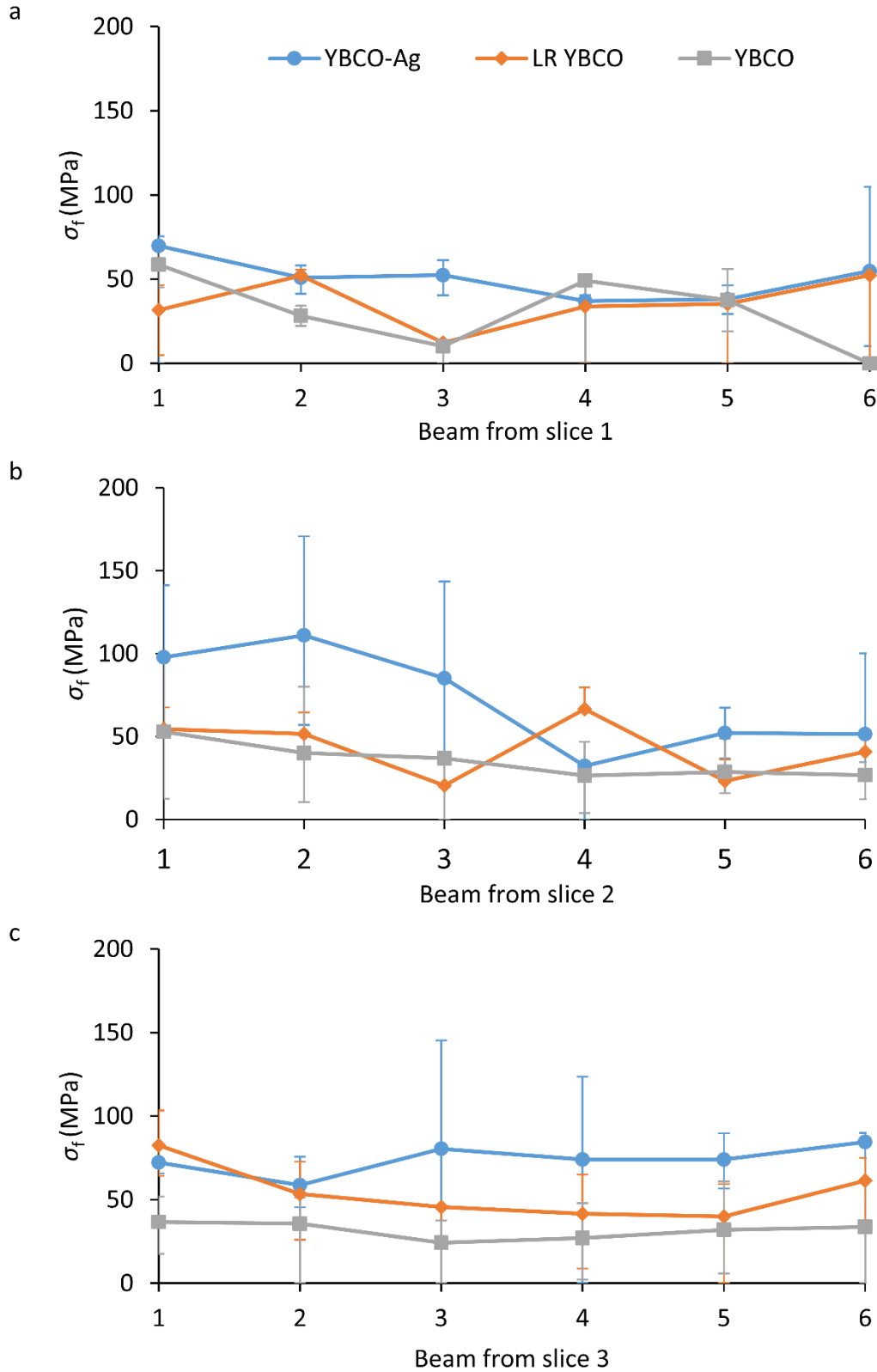


Figure 7.6: The average flexural strength of each beam in (a) slice 1, (b) slice 2 and (c) slice 3. The error bars correspond to the maximum and minimum recorded failure stress at each location.

7.3 Microstructure

The microstructure was imaged at 50x magnification at locations corresponding to the centre of each beam from slice 1, a representative example from one sample of each type is shown in Fig. 7.7. The microstructure in the corresponding beams in the other samples of the same type (either YBCO, LR YBCO or YBCO-Ag) show very similar trends in the images. The microstructures of YBCO and LR YBCO are very similar, but the microstructure of YBCO-Ag is significantly different. The pores in YBCO-Ag are significantly smaller. There are also a large number of very small silver agglomerates accompanying some larger silver agglomerates that appear to have filled areas that would otherwise have been pores.

In addition, images were taken at 1 mm intervals in the c -axis direction and along the a/b -axis direction at approximately 1.5 mm vertically from the top of the sample at both 50x magnification and 500x magnification. These are shown in the appendix.

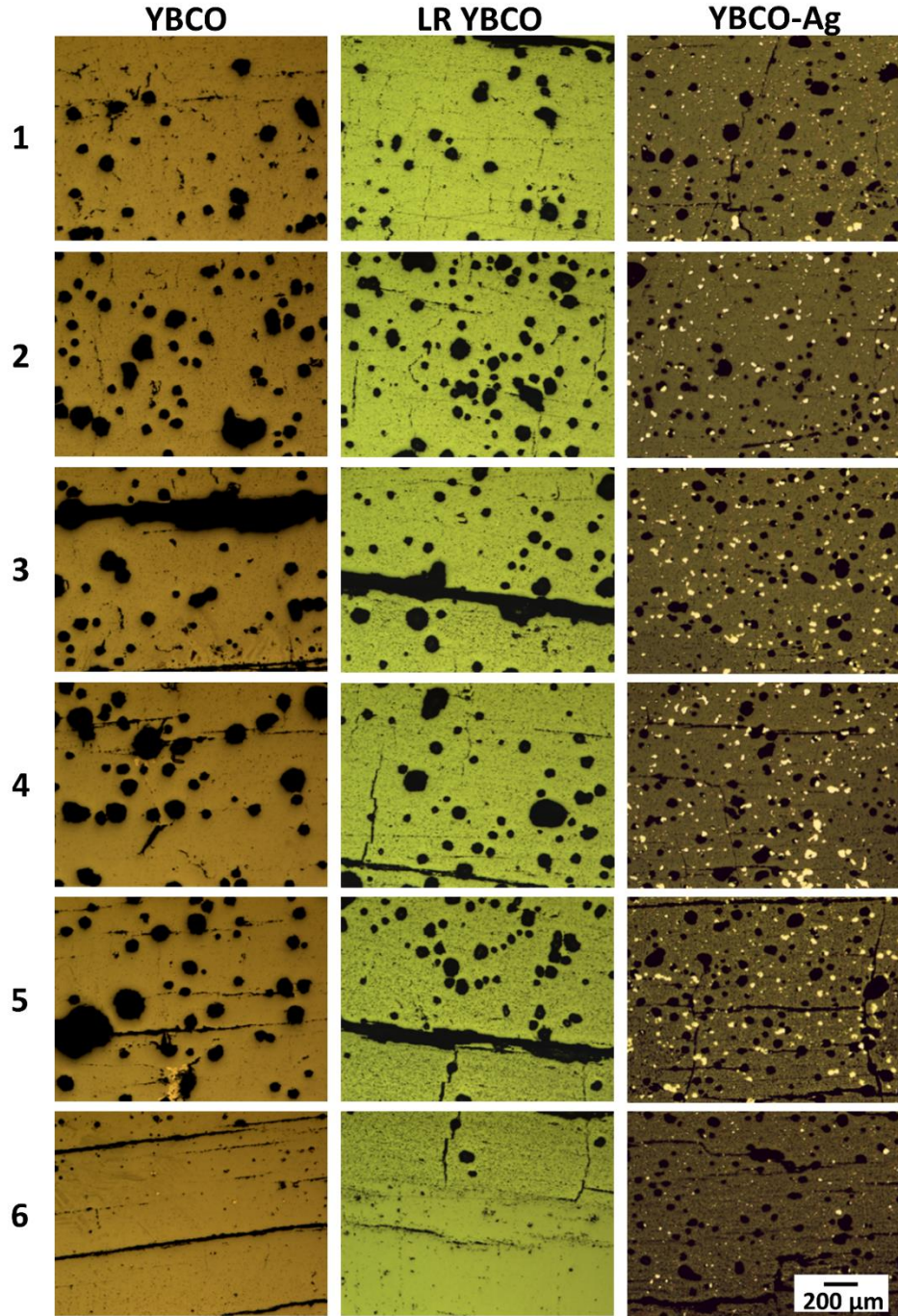


Figure 7.7: Optical microscope images taken at 50x magnification corresponding to approximately the centre of each of the beams.

Throughout the c -axis direction there are many large pores present in the YBCO and LR YBCO microstructure; the smallest pores are approximately $50\ \mu\text{m}$ in diameter and the larger pores are over $150\ \mu\text{m}$ in diameter. There are larger pores present at the centre. There are cracks present in all three samples, however, the cracks are thinner in the LR YBCO and YBCO-Ag samples than

in the YBCO sample microstructure. In the YBCO-Ag sample, the pore size is significantly smaller overall and there are few pores with a diameter greater than 150 μm , unlike in the other two samples. In addition, there is no change in the average pore size throughout the sample as occurs in the YBCO and LR YBCO samples. In the YBCO-Ag samples, there is a wide variation in the size of the silver agglomerates; there are predominantly large and small agglomerates with only a few of mid-range sizes.

At the top, in both the YBCO and LR YBCO samples, there are a number of small cracks present, however, there are fewer and these are thinner than those imaged further down the c -axis. In addition, the pores are smaller at the top than mid-way along the c -axis in all these samples, with all pores smaller than 150 μm . In comparison to the images of YBCO and LR YBCO, the pore size in the YBCO-Ag samples is on average much smaller. There are a number of silver agglomerates present that are both small and large in size. In many cases silver agglomerates have partially filled the pores present in the YBCO-Ag samples.

At the base of the samples there are some small cracks present; a large proportion of these are close to the edge of the sample. There are fewer and smaller cracks in the YBCO-Ag samples than in the YBCO or LR YBCO samples. The pores are smaller at the base of the samples in relation to the pores present at the centre of the c -axis in the YBCO and LR YBCO samples. At the base of the YBCO-Ag sample, there is a very limited amount of silver present in comparison to that observed at the top and mid-way along the c -axis. This reduction in silver may be due to the additional liquid-phase provided filling most of the pores that could have been filled by silver.

The samples were also imaged at 500x magnification to view the distribution of Y-211 inclusions. These images are included in the appendix and show there is a large variation in the size of the Y-211 inclusions. There are many different sizes of these inclusions within each image. LR YBCO shows a much greater uniformity in both the size of the Y-211 inclusions and in the distribution than the YBCO samples. In the YBCO samples there are fewer but larger Y-211 inclusions closer to the seed and more and smaller inclusions with distance from the seed. This was not observed in either the LR YBCO or YBCO-Ag; YBCO-Ag had a very uniform distribution of Y-211 inclusions

both within each image and throughout the *c*-axis of the bulk material. These images enable some of the silver to be observed too; some of these pores are partially filled by silver.

7.4 Composition

The area of each image occupied by pores and, where relevant, silver, as determined by ImageJ software, averaged over all three samples is shown in Fig. 7.8, alongside a plot of the average size of the pores and silver in each sample. The extremes of the error bars indicate the highest and lowest values recorded from all three samples at the specific location. The average porosity is much lower in the YBCO-Ag samples than in either the YBCO or LR YBCO samples at all locations except locations 3 and 6. This suggests that some of the pores must have been filled by silver agglomerates in the YBCO-Ag samples. The average area occupied by pores in the LR YBCO sample is slightly lower than that of the standard YBCO sample, but not significantly lower. The average size of the pores is significantly different in each of the samples. The average pore size in each image of the standard YBCO samples is much larger than that of all of the other samples, and shows a much greater variation between subsequent beam locations. In addition, the error bars show a significant variation in the average pore size at each location between the three samples of standard YBCO. The average pore size is significantly lower in the YBCO-Ag samples than in the LR YBCO samples. The average pore size in the YBCO-Ag sample is also very consistent between beam locations and between the three samples of YBCO-Ag. These results are as expected from the microscope images. Both the area of the image occupied by silver and the relative average size of the silver agglomerates are very consistent throughout the sample with the exception of location 6. In general, it is desirable to have a highly uniform microstructure and the uniformity in the silver distribution will enable the beneficial effects of the contribution of silver to contribute broadly to all parts of the sample.

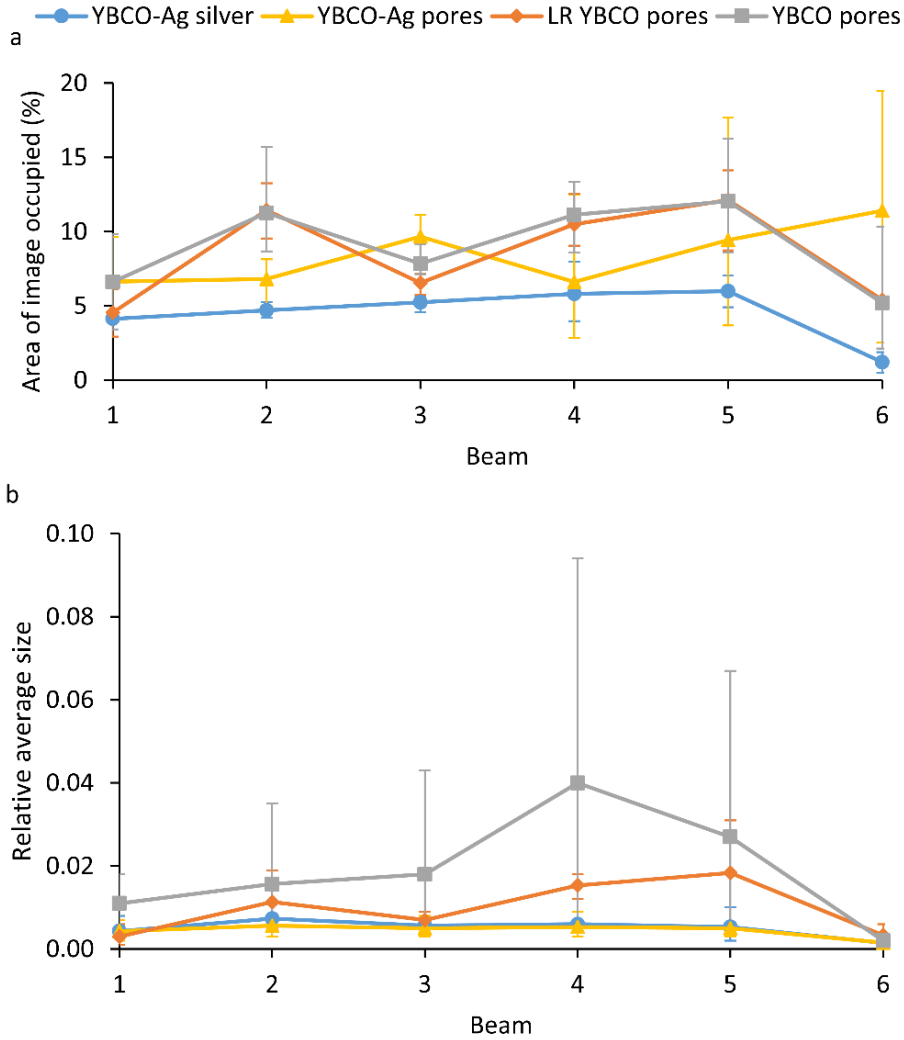


Figure 7.8: The average variation in porosity between the beams considered in terms of a) the average area occupied by pores and b) the average size of the pores present at each location.

7.5 Relation between microstructure, composition and mechanical properties

It is widely accepted that porosity in the microstructure of YBCO bulk superconductors has a negative impact on the mechanical properties of the sample, both in terms of the total area occupied by pores and the size of the pores present [30]. The addition of silver reduces both the area occupied by pores and the average size of the pores, as shown in Fig. 7.8. Both the area fraction occupied by pores and silver, and the average pore and silver agglomerate size have been plotted against the flexural strength for beams from slice 1, as shown in Figs. 7.9 and 7.10.

There is a negative correlation in the standard YBCO samples between both the average pore size within an image taken from the centre of each beam or the area occupied by pores in each of these images and the flexural strength. This indicates that as the area occupied by pores increases the failure strength of the beam decreases. In addition, as the average size of the pores increases, the strength of the beams from the YBCO samples decreases.

There is no obvious correlation between the average pore size and the flexural strength in the LR YBCO samples. There is, however, a very slight negative correlation with some outliers between the area occupied by pores and the flexural strength. This limited correlation is because the additional liquid provided affects the final microstructure. It primarily fills, or partially fills, a number of the pores at the base of the sample and some of the cracks. Therefore, the sample will behave differently. In the LR YBCO samples, the reduction in area occupied by pores and the reduction in the average pore size is, at least in part, responsible for the higher local flexural strength observed at the majority of locations compared to standard YBCO. Alongside filling some of the pores, the provision of additional liquid-phase during processing may also enable small, sharp cracks to be filled or blunted, hence providing additional mechanisms to improve the mechanical strength of the material.

The average pore size and the average area occupied by pores throughout the YBCO-Ag samples is significantly lower than in the other two types of sample. The average pore size is very low and does not show an obvious correlation with the failure stress. The area occupied by pores does, however, show a slight negative correlation if the outliers are ignored. This suggests that porosity is an important factor in the strength of YBCO and YBCO-Ag single grains. The reduction in both the area occupied by pores and the size of the pores caused by their partial filling with silver would appear to be, at least in part, responsible for the increase in local strength associated with the addition of silver. Due to the nature of failure of ceramic-like materials, there is a large variation in the mechanical strength of the same material, even for sub-specimens taken from the same original specimen, and this is likely to be responsible for the large variation in flexural stress and may be why only a slight negative correlation was observed in some cases. The addition of Ag to the samples may have a similar effect to that of the provision of additional liquid-phase, albeit more prominent. The silver fills the sharp micro-cracks, and hence blunts the sites at which crack

initiation and propagation is most and first likely to occur, hence providing additional mechanisms to improve the mechanical strength of the material.

One concern with the addition of silver was that it would fill the pores but still cause similar problems to the pores in terms of the mechanical properties. The silver agglomerates may act as flaws and provide sites at which fracture can occur. For this reason the area occupied by silver in each image and the average silver agglomerate size was plotted against the flexural strength of each bar. The plots show that there is no correlation between either the area occupied by pores or the average pore size and the flexural strength of the bar.

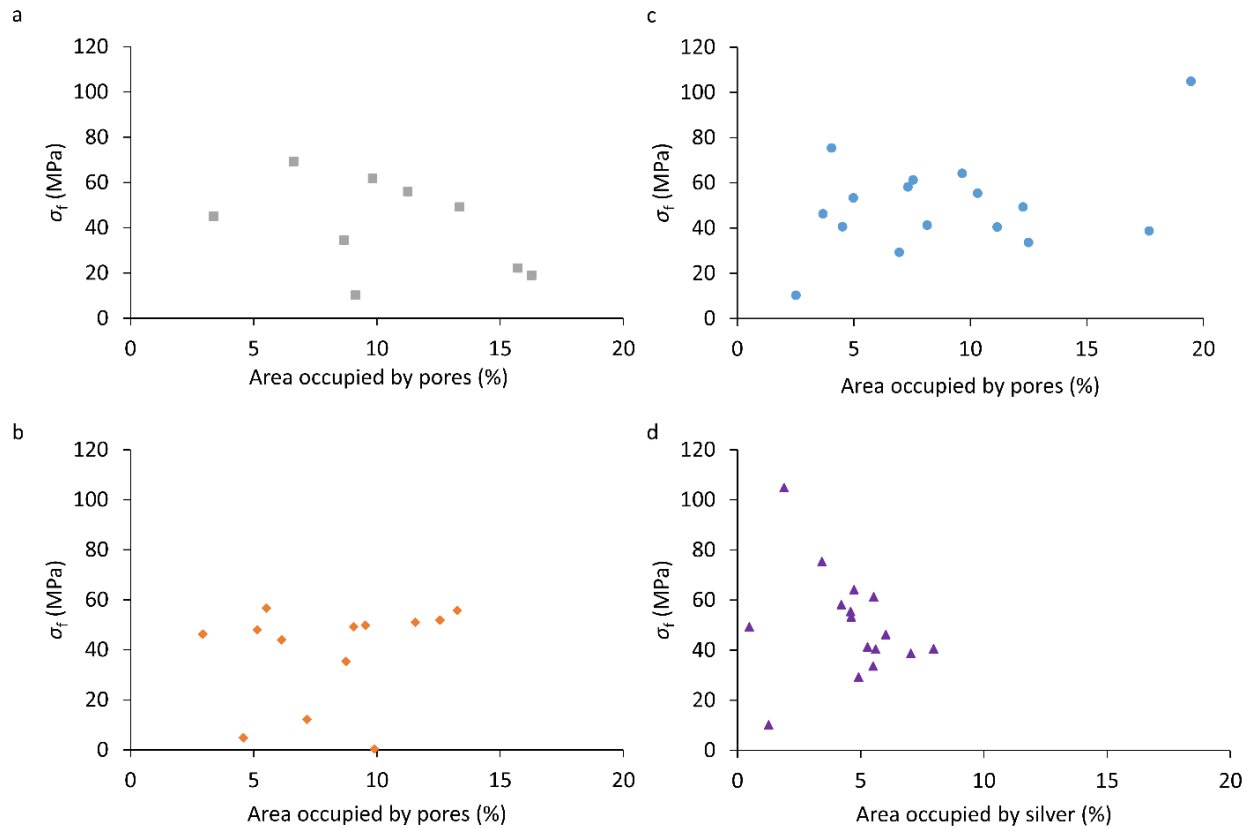


Figure 7.9: The relationship between flexural strength and area occupied by pores in slice 1 of: a) YBCO, b) LR YBCO, c) YBCO-Ag and d) the area occupied by silver in YBCO-Ag.

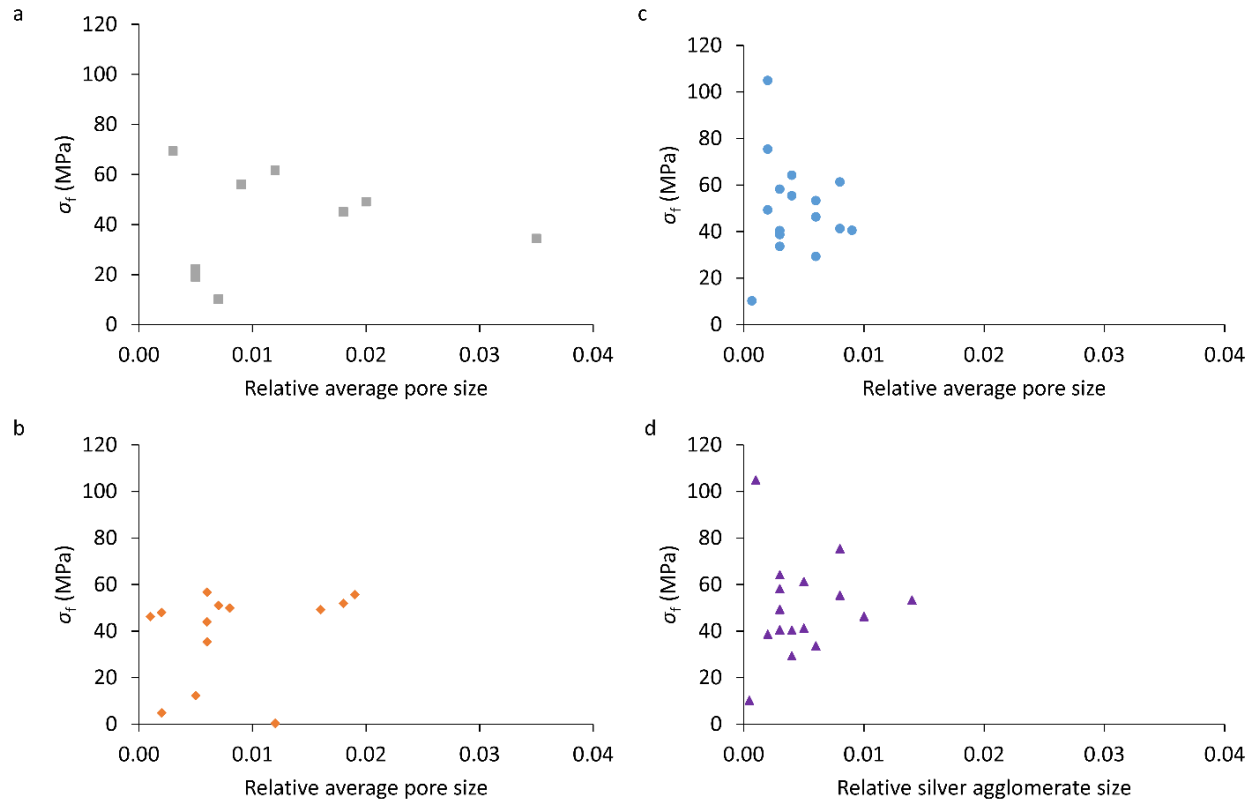


Figure 7.10: The relationship between flexural strength and relative average pore size in slice 1 of: a) YBCO, b) LR YBCO, c) YBCO-Ag and d) the area occupied by silver in YBCO-Ag.

7.6 Conclusions

The provision of additional liquid to TSMG samples of YBCO has improved significantly the mechanical strength of YBCO bulk superconductors. However, the addition of silver in addition to additional liquid has also improved the mechanical strength significantly. Small beams of YBCO-Ag were able to withstand stresses of over 170 MPa before failure. The increase observed in the flexural strength of YBCO-Ag is, in the most part, due to a significant reduction in both the average pore size and the area occupied by pores in the silver-added samples compared to both YBCO and liquid-phase-enriched YBCO. The added silver fully and partially filled a large number of pores, and hence the area occupied by and the average size of the pores were significantly reduced. The negative correlation between the pore size or area occupied by pores and the flexural strength of each beam was limited due to the ceramic-like nature of these materials.

The HTS bulk materials investigated as part of this study have a high inherent inhomogeneity. The complex growth process produces a wide range of pore sizes and shapes and cracks. In addition,

the inclusions, such as the Y-211 and the silver, are not uniformly distributed. The failure of ceramic-like materials relies upon a probability distribution with larger sized pieces of material more likely to contain a large flaw that will significantly reduce the strength of the material. Hence, in order to gain a more meaningful understanding of the relationships between failure and porosity and the inclusions present, many more samples must be tested both using the three-point bend test, and via the use of further characterisation techniques.

This initial research suggests that the addition of silver produces a significant increase in the flexural strength of YBCO. Therefore, this process modification will significantly enhance the viability of the use of YBCO in practical applications. As a result, this material will be able to withstand greater Lorentz forces, and so the limitations placed on the superconducting properties by the mechanical properties have now been significantly reduced.

8 Conclusions

This work has developed a successful and reliable growth process to produce large single grains of YBCO-Ag with good mechanical and superconducting properties via a number of incremental stages.

The provision of additional liquid to a novel recycling process for YBCO, GdBCO-Ag and SmBCO-Ag enabled the replenishment of liquid lost during the initial failed primary growth process. This additional liquid provided a sufficient concentration of (RE) species at the growth front to enable the samples to grow easily and reliably. In addition, the increased concentration of (RE) species at the growth front supported single grain growth in the presence of agglomerates of Ag and Ce-rich phases.

The provision of additional liquid in the recycling process increased the uniformity in the composition in comparison to the primary TSMG growth process. Hence, these samples have more uniform superconducting properties, albeit 15 % lower in magnitude. The resulting samples from the recycling process with added liquid-phase have shown that the ability to adapt the provision of additional liquid-phase to primary processing by TSMG, or to reduce the liquid loss during primary processing, will enable reliable fabrication of good quality single grains.

The provision of additional liquid to the primary growth of YBCO by the TSMG process provided a significant increase in the reliability of full through-thickness single grain growth in comparison to the conventional TSMG process. In order to ensure these single grains grown by the conventional TSMG process were optimised, a number of parameters were investigated prior to the provision of additional liquid-phase. These investigations showed that the optimum conditions for the growth of a single grain of YBCO by TSMG entail: the use of a buffer pellet, no prior sintering of the precursor powder pellet, additional liquid-phase and a stabilising layer of Yb_2O_3 mixed with ethanol painted onto the base of the precursor sample. In addition to deriving the optimum conditions for growth, the composition of the additional liquid-phase-rich powder used was optimised. Alongside more reliable growth, these single grains of YBCO exhibited a greater uniformity in the distribution of Y-211 particles and in the Y-123 superconducting matrix. Hence,

the single grains exhibit high levels of uniformity of the superconducting properties, as exhibited in the recycled samples, whilst retaining the same or higher magnitude of superconducting properties exhibited in YBCO single grains grown by the primary TSMG process.

The simple provision of additional liquid-phase to the conventional TSMG growth process has led to improved reliability of growth and, in turn, improved sample performance. The result of primary processing by TSMG with additional liquid, alongside the ability to support single grain growth in the presence of Ag-rich agglomerates (observed in the recycling of GdBCO-Ag and SmBCO-Ag multi-grains) has demonstrated convincingly that this adaptation may help to enable the reliable single grain growth of YBCO-Ag.

The provision of additional liquid to the primary TSMG of YBCO-Ag enabled the growth rate of YBCO-Ag to be studied systematically. The lack of growth of YBCO-Ag during simple isothermal holding, as is widely used to investigate the growth rate of these (RE)BCO bulk single grains, led to the development of a new processing technique. The so-called CCIH technique introduced a slow cooling period prior to the isothermal hold period. The slow cooling period was required to enable nucleation and growth initiation. The requirement of this period is evident within the microstructure of the bulk single grain. The distribution of silver is not uniform throughout the cross-section of the single grain. There is a 'silver-deficient' looking region directly below the seed, followed by a sudden transition to a 'silver-rich' region at a greater distance from the seed. This distribution of silver is likely a result of the difficulty of incorporating silver into the YBCO lattice during the initial stages of growth. In consequence, silver is pushed by the growth front, generating a silver deficient region below the seed that contains only a limited concentration of small silver agglomerates. Once the level of silver at the growth front reaches a threshold, however, silver is incorporated into the bulk microstructure and yields a discontinuity in the silver distribution. Many more and much larger silver agglomerates are present further away from the seed, and typically fill regions that were initially pores.

This investigation has, for the first time, enabled a model of the single grain growth rate of YBCO-Ag to be developed. The growth rate model is an essential tool for deriving optimised heating

profiles, which are essential for the successful growth of various sizes of single grains of YBCO-Ag by TSMG.

The provision of additional liquid-phase to the primary TSMG process, and the derivation of suitable optimised heating profiles, has enabled the reliable growth of single grains of YBCO-Ag. The ability to grow these YBCO-Ag single grains reliably has enabled detailed investigation of both the superconducting and mechanical properties of YBCO-Ag, and subsequent comparison with single grains of YBCO fabricated by the conventional TSMG process and the liquid-phase-enriched TSMG process.

The addition of silver has been observed to have no detrimental effect on the superconducting properties of YBCO. Single grains of YBCO-Ag trapped a magnetic field comparable to that trapped by the same size single grain of YBCO grown by both conventional TSMG and liquid-phase-enriched TSMG. This suggests that, with further optimisation, the trapped field achievable in YBCO-Ag single grains may be higher than for the same size of single grain of YBCO. In addition, the values of T_c and ΔT_{90} were comparable across all three types of single grain. The values of J_c for sub-specimens cut from the top half of the samples were comparable, with the highest values of J_c achieved in YBCO-Ag. In contrast, towards the base of the sample, the values of J_c achieved in the YBCO-Ag sub-specimens were significantly lower than those exhibited in the YBCO single grains grown by liquid-phase-enriched TSMG.

The value of J_c was inversely related to the area occupied by pores in the YBCO single grains grown by TSMG and by liquid-phase enriched TSMG. This is as expected; increasing the area occupied by pores will reduce the area of Y-123 superconducting matrix available for the flow of superconducting current. The addition of silver has increased the complexity of this relationship in the YBCO-Ag single grains. There was no obvious relationship between the values of J_c , the area occupied by pores, the area occupied by silver or the combined area occupied by pores and silver. In addition, the values of J_c showed no obvious trend with pore size or silver agglomerate size. In the YBCO-Ag samples there are, however, fewer vertical cracks present than in the other two types of samples, and hence the YBCO-Ag single grain has a larger uninterrupted area available within which the superconducting current can flow. This suggests that there is a complex

mix of variables that affect the J_c value achieved in YBCO-Ag single grains. In order to draw more detailed and valid conclusions about the factors affecting the superconducting properties in YBCO-Ag single grains, many more samples should be investigated in detail.

The provision of silver to YBCO did not have a significant detrimental effect on the superconducting properties of this material. The YBCO-Ag sample exhibited the best individual values for each of T_c , ΔT_{90} , J_c and trapped field, although it was not consistently the best in all of the sub-specimens or samples. The absence of degradation in the superconducting properties of this system when silver is added to the precursor powder suggested that the mechanical properties should be studied to identify whether this material provided greater practical potential than YBCO single grains grown by conventional TSMG.

Three-point bend tests were carried out on a minimum of 41 flexural beams from three samples of each of YBCO, liquid-phase-enriched YBCO and YBCO-Ag. This test enabled the flexural strength of each beam to be measured. The samples grown by TSMG with additional liquid-phase exhibited higher flexural strength than the single grains of YBCO grown by conventional TSMG. However, the addition of silver and the provision of additional liquid-phase significantly improved the mechanical strength of the samples compared to single grains grown by conventional TSMG, these beams exhibited strengths of over 170 MPa. The improvement in the flexural strength exhibited in the liquid-phase-enriched YBCO single grains was due to the reduction in pore and crack size at the base of the sample due to the ability of the liquid-phase to infiltrate the sample at the base. The silver provided to the YBCO-Ag samples enabled a substantial reduction in the average pore size and the area occupied by pores as the silver filled, and partially filled, the pores and a number of the cracks present, in addition to the effect of the additional liquid-phase.

Despite the obvious reductions in pore size and area occupied by pores in the YBCO-Ag samples, there is only a slight negative correlation between the size of the pores or area occupied by pores and the flexural strength. The strength of the correlation is limited due to the inherent variability in the size of the pores, shapes of the pores and cracking. In addition, the failure of ceramic-like materials is determined by a probabilistic distribution and so is inherently variable. In order to gain a more meaningful understanding of the relationships between failure and porosity and the

inclusions present, many more samples must be tested both using the three-point bend test and further characterisation techniques.

This initial research suggests that the addition of silver produces a significant increase in the flexural strength of YBCO. Therefore, the addition of silver will significantly enhance the viability of the use of YBCO in practical applications. As a result, this material will be able to withstand greater Lorentz forces and so the limitations placed upon the superconducting properties by the mechanical properties have, in consequence, now been significantly reduced.

9 Future work

Throughout this work the mass of Ag_2O added to the precursor powder has been kept constant at 10 wt%. This may not be the optimum quantity of silver to add to provide the best superconducting or mechanical properties. A focus of future work, therefore, should be to analyse the effect of the quantity of added silver on the reliability of the single grain growth process, the superconducting properties and the mechanical properties of the resulting single grain samples. The addition of significantly different quantities of silver will require the use of DTA in order to determine the peritectic temperature of each specific composition, alongside further investigation of the growth rate to enable a suitable heating profile to be derived.

In addition, although this work has investigated systematically the growth rate of YBCO with 10 wt% of added Ag_2O and derived a suitable heating profile, this heating profile is not necessarily fully optimised. Further incremental optimisation of the heating profile may be beneficial in order to control the distribution of silver and pores further.

As discussed in the conclusions section, there is a large degree of inherent variability in these samples, both due to the growth process and to the nature of mechanical failure of ceramic materials. Hence, in order to provide more valid and conclusive conclusions on both the superconducting properties and mechanical properties and how they relate to specific microstructural features, many more samples should be tested. In terms of the mechanical properties, there should be both more 3-point bend tests carried out on more samples but also a wider range of tests should be used on a large number of samples. Although the 3-point bend test can give an indication and a good comparable measure of the relative mechanical properties between the three types of samples, it may not actually be the best measure to use to enable direct comparison of the overall mechanical properties. The 3-point bend test only uses relatively small samples and does not replicate the stresses to which whole single grains will be subject during magnetisation. The results of the 3-point bend test are likely to correlate with the strength of these materials during magnetisation, although it is not a direct measure of how well they will cope with the specific directions of stress in a magnetisation situation. In order to draw more valid

conclusions, the mechanical properties of whole single grains should be tested in detail when the whole single grains is subjected specifically to radial forces.

The highly reliable growth process with a high tolerance to agglomerates of a variety of different compositions developed in this work could be further exploited to enable the growth of large single grains of (RE)BCO with a range of different alloying materials. Investigation of new compositions would enable these materials to be directly tailored to the requirements of each specific application. For example, the addition of an alloying material on properties such as the fracture toughness could be investigated to identify the best alloying material for optimisation of this specific property.

References

- [1] J. H. Durrell, A. R. Dennis, J. Jaroszynski, M. D. Ainslie, K. G. B. Palmer, Y. H. Shi, *et al.*, "A trapped field of 17.6T in melt-processed, bulk Gd-Ba-Cu-O reinforced with shrink-fit steel," *Superconductor Science & Technology*, vol. 27, 2014.
- [2] A. M. Campbell and D. A. Cardwell, "Bulk high temperature superconductors for magnet applications," *Cryogenics*, vol. 37, pp. 567-575, 1997.
- [3] F. N. Werfel, U. Floegel-Delor, R. Rothfeld, T. Riedel, B. Goebel, D. Wippich, *et al.*, "Superconductor bearings, flywheels and transportation," *Superconductor Science & Technology*, vol. 25, 2012.
- [4] B. Z. Li, D. F. Zhou, K. Xu, S. Hara, K. Tsuzuki, M. Miki, *et al.*, "Materials process and applications of single grain (RE)-Ba-Cu-O bulk high-temperature superconductors," *Physica C-Superconductivity and Its Applications*, vol. 482, pp. 50-57, 2012.
- [5] D. A. Cardwell, "Processing and properties of large grain (RE)BCO," *Materials Science and Engineering B-Solid State Materials for Advanced Technology*, vol. 53, pp. 1-10, 1998.
- [6] D. Dimos, P. Chaudhari, J. Mannhart, and F. K. Legoues, "Orientation dependence of grain-boundary critical currents in $\text{YBa}_2\text{Cu}_3\text{O}_{7-\delta}$ bicrystals," *Physical Review Letters*, vol. 61, pp. 219-222, 1988.
- [7] D. K. Namburi, Y. H. Shi, K. G. Palmer, A. R. Dennis, J. H. Durrell, and D. A. Cardwell, "An improved top seeded infiltration growth method for the fabrication of Y-Ba-Cu-O bulk superconductors," *Journal of the European Ceramic Society*, vol. 36, pp. 615-624, 2016.
- [8] Y. Shiohara and A. Endo, "Crystal growth of bulk high- T_c superconducting oxide materials," *Materials Science & Engineering R-Reports*, vol. 19, pp. 1-86, 1997.
- [9] V. R. Todt, X. F. Zhang, D. J. Miller, M. StLouisWeber, and V. P. Dravid, "Controlled growth of bulk bicrystals and the investigation of microstructure-property relations of $\text{YBa}_2\text{Cu}_3\text{O}_x$ grain boundaries," *Applied Physics Letters*, vol. 69, pp. 3746-3748, 1996.
- [10] J. H. Durrell, M. J. Hogg, F. Kahlmann, Z. H. Barber, M. G. Blamire, and J. E. Evetts, "Critical current of $\text{YBa}_2\text{Cu}_3\text{O}_{7-\delta}$ low-angle grain boundaries," *Physical Review Letters*, vol. 90, 2003.
- [11] Y. Shi, A. R. Dennis, F. Hengstberger, N. H. Babu, D. A. Cardwell, and M. Strasik, "A simple method for recycling GdBCO-Ag single grain bulk superconductors," *Superconductor Science & Technology*, vol. 24, 2011.
- [12] L. M. Fisher, A. V. Kalinov, S. E. Savel'ev, I. F. Voloshin, and V. A. Yampol'skii, "Critical current anisotropy in YBCO superconducting samples," *Physica C*, vol. 309, pp. 284-294, 1998.
- [13] H. Fujimoto, M. Murakami, S. Gotoh, N. Koshizuka, T. Oyama, Y. Shiohara, *et al.*, "Melt processing of YBaCuO oxide superconductors," *Advances in superconductivity II: Proceedings of the 2nd International Symposium on Superconductivity* pp. 285-288, 1990.
- [14] K. Sawano, M. Morita, M. Tanaka, T. Sasaki, K. Kimura, S. Takebayashi, *et al.*, "High magnetic-flux trapping by melt-grown YBaCuO superconductors," *Japanese Journal of Applied Physics Part 2-Letters*, vol. 30, pp. L1157-L1159, 1991.
- [15] G. Z. Li, L. Dong, and X. Y. Deng, "Comparisons of the microstructure and superconducting properties in Y-Ba-Cu-O single-grain superconductors grown with different liquid sources: The influence of element doping through liquid infiltration," *Ceramics International*, vol. 42, pp. 923-928, 2016.
- [16] T. Nishio, Y. Itoh, F. Ogasawara, M. Suganuma, Y. Yamada, and U. Mizutani, "Superconducting and mechanical-properties of YBCO-Ag composite superconductors," *Journal of Materials Science*, vol. 24, pp. 3228-3234, 1989.

- [17] T. Miyamoto, K. Nagashima, N. Sakai, and M. Murakami, "Mechanical properties of bulk superconductors," *Superconductor Science & Technology*, vol. 13, pp. 816-819, 2000.
- [18] S. Gruss, G. Fuchs, G. Krabbes, P. Verges, G. Stover, K. H. Muller, *et al.*, "Superconducting bulk magnets: Very high trapped fields and cracking," *Applied Physics Letters*, vol. 79, pp. 3131-3133, Nov 2001.
- [19] P. Diko, D. Volochova, M. Radusovska, K. Zmorayova, M. Sefcikova, V. Antal, *et al.*, "Influence of preparation conditions on 211 particle refinement in YBCO bulk superconductors with Ce addition," *Physica C-Superconductivity and Its Applications*, vol. 494, pp. 31-35, 2013.
- [20] K. Iida, N. H. Babu, Y. Shi, T. Miyazaki, and N. Sakai, "Single domain YBCO/Ag bulk superconductors fabricated by seeded infiltration and growth," *Journal of physics. Conference series*, vol. 97, p. 012105, 2008.
- [21] N. Sakai, S. J. Seo, K. Inoue, T. Miyamoto, and M. Murakami, "Mechanical properties of RE-Ba-Cu-O bulk superconductors," *Physica C: Superconductivity and its Applications*, vol. 335, pp. 107-111, 2000.
- [22] D. Lee and K. Salama, "Enhancements in Current Density and Mechanical Properties of Y-Ba-Cu-O/Ag Composites," *Japanese Journal of Applied Physics*, vol. 29, pp. L2017-L2019, 1990.
- [23] F. Yu, K. W. White, and R. Meng, "Mechanical characterization of top-seeded melt-textured YBa₂Cu₃O_{7-δ} single crystal," *Physica C: Superconductivity and its Applications*, vol. 276, pp. 295-308, 1997.
- [24] R. W. Rice, *Porosity of ceramics: Properties and applications*: CRC Press, 1998.
- [25] B.-S. Chang, C. K. Lee, K. S. Hong, H. J. Youn, H. S. Ryu, S. S. Chung, *et al.*, "Osteoconduction at porous hydroxyapatite with various pore configurations," *Biomaterials*, vol. 21, pp. 1291-1298, 2000.
- [26] R. W. Rice, "Relation of tensile strength-porosity effects in ceramics to porosity dependence of Young's modulus and fracture energy, porosity character and grain size," *Materials Science and Engineering: A*, vol. 112, pp. 215-224, 1989.
- [27] R. W. Rice, "Mechanically reliable ceramics: Needs and opportunities to understand and control fracture," *Journal of Physics and Chemistry of Solids*, vol. 45, pp. 1033-1050, 1984.
- [28] J. D. Birchall, A. J. Howard, and K. Kendall, "Flexural strength and porosity of cements," *Nature*, vol. 289, p. 388, 1981.
- [29] F. P. Knudsen, "Dependence of Mechanical Strength of Brittle Polycrystalline Specimens on Porosity and Grain Size," *Journal of the American Ceramic Society*, vol. 42, pp. 376-387, 1959.
- [30] H. W. Chandler, I. J. Merchant, R. J. Henderson, and D. E. Macphee, "Enhanced crack-bridging by unbonded inclusions in a brittle matrix," *Journal of the European Ceramic Society*, vol. 22, pp. 129-134, 2002.
- [31] P. Diko, "Cracking in melt-processed RE-Ba-Cu-O superconductors," *Superconductor Science and Technology*, vol. 11, pp. 68-72, 1998.
- [32] T. J. Richardson and L. C. De Jonghe, "Acoustic emission study of microcracking in 123-type ceramic superconductors," *Journal of Materials Research*, vol. 5, pp. 2066-2074, 1990.
- [33] P. Diko, N. Pelerin, and P. Odier, "Microstructure analysis of melt-textured YBa₂Cu₃O_{7-x} ceramics by polarized light microscopy," *Physica C: Superconductivity*, vol. 247, pp. 169-182, 1995.
- [34] R. J. Cava, A. W. Hewat, E. A. Hewat, B. Batlogg, M. Marezio, K. M. Rabe, *et al.*, "Structural anomalies, oxygen ordering and superconductivity in oxygen deficient Ba₂YCu₃O_x," *Physica C: Superconductivity and its applications*, vol. 165, pp. 419-433, 1990.
- [35] E. D. Specht, C. J. Sparks, A. G. Dhere, J. Brynestad, O. B. Cavin, D. M. Kroeger, *et al.*, "Effect of oxygen pressure on the orthorhombic-tetragonal transition in the high-temperature superconductor YBa₂Cu₃O_x," *Physical Review B*, vol. 37, pp. 7426-7434, 1988.

- [36] S. J. Rothman, J. L. Routbort, U. Welp, and J. E. Baker, "Anisotropy of oxygen tracer diffusion in single-crystal $\text{YBa}_2\text{Cu}_3\text{O}_7$," *Physical Review B*, vol. 44, pp. 2326-2333, 1991.
- [37] R. O. Ritchie, "Mechanisms of fatigue-crack propagation in ductile and brittle solids," *International Journal of Fracture*, vol. 100, pp. 55-83, 1999.
- [38] P. F. Becher, "Microstructural Design of Toughened Ceramics," *Journal of the American Ceramic Society*, vol. 74, pp. 255-269, 1991.
- [39] A. G. Evans, "Perspective on the Development of High-Toughness Ceramics," *Journal of the American Ceramic Society*, vol. 73, pp. 187-206, 1990.
- [40] P. d. Azambuja, P. Rodrigues J. Anior, A. R. Jurelo, F. C. Serbena, C. E. Foerster, R. M. Costa, *et al.*, "Effects of Ag addition on some physical properties of granular $\text{YBa}_2\text{Cu}_3\text{O}_7$ superconductor," *Brazilian Journal of Physics*, vol. 39, pp. 638-644, 2009.
- [41] F. Yeh and K. W. White, "Fracture-toughness behavior of the $\text{YBa}_2\text{Cu}_3\text{O}_{7-x}$ superconducting ceramic with silver-oxide additions," *Journal of Applied Physics*, vol. 70, pp. 4989-4994, 1991.
- [42] C. Cai, K. Tachibana, and H. Fujimoto, "Study on single-domain growth of $\text{Y}_{1.8}\text{Ba}_{2.4}\text{Cu}_{3.4}\text{O}_y/\text{Ag}$ system by using Nd123/MgO thin film as seed," *Superconductor Science and Technology*, vol. 13, p. 698, 2000.
- [43] Y. Nakamura, K. Tachibana, and H. Fujimoto, "Dispersion of silver in the melt grown $\text{YBa}_2\text{Cu}_3\text{O}_{6+x}$ crystal," *Physica C: Superconductivity*, vol. 306, pp. 259-270, 1998.
- [44] E. Mendoza, T. Puig, E. Varesi, A. E. Carrillo, J. Plain, and X. Obradors, "Critical current enhancement in YBCO-Ag melt-textured composites: influence of microcrack density," *Physica C: Superconductivity*, vol. 334, pp. 7-14, 2000.
- [45] M. Matsui, N. Sakai, and M. Murakami, "Effect of Ag_2O addition on the trapped fields and mechanical properties of Nd-Ba-Cu-O bulk superconductors," *Superconductor Science and Technology*, vol. 15, p. 1092, 2002.
- [46] A. Mahmood, B. H. Jun, Y. H. Han, and C. J. Kim, "Effective pore control and critical current density in liquid infiltration growth processed Y-123 superconductors with Ag addition," *Superconductor Science and Technology*, vol. 23, p. 065005, 2010.
- [47] J. Maeda, Y. Nakamura, T. Izumi, and Y. Shiohara, "The effect of residual stress on crack propagation in a YBCO/Ag composite," *Superconductor Science & Technology*, vol. 12, pp. 563-565, 1999.
- [48] J. Maeda and Y. Shiohara, "Microstructures and solidification behavior in Y-Ba-Cu-O/Ag superconducting leads," *Journal of Materials Research*, vol. 14, pp. 2739-2750, 1999.
- [49] A. Goyal, P. D. Funkenbusch, D. M. Kroeger, and S. J. Burns, "Fabrication of highly aligned $\text{YBa}_2\text{Cu}_3\text{O}_{7-\delta}$ -Ag melt-textured composites," *Physica C: Superconductivity*, vol. 182, pp. 203-218, 1991.
- [50] M. Junya, N. Yuichi, I. Teruo, and S. Yuh, "The effect of residual stress on crack propagation in a YBCO/Ag composite," *Superconductor Science and Technology*, vol. 12, p. 563, 1999.
- [51] Y. Shi, N. H. Babu, K. Iida, W. K. Yeoh, A. R. Dennis, S. K. Pathak, *et al.*, "Batch-processed GdBCO-Ag bulk superconductors fabricated using generic seeds with high trapped fields," *Physica C-Superconductivity and Its Applications*, vol. 470, pp. 685-688, 2010.
- [52] K. Iida, N. H. Babu, S. Pathak, Y. Shi, W. Yeoh, T. Miyazaki, *et al.*, "Optimum processing conditions for the fabrication of large, single grain Ag-doped YBCO bulk superconductors," *Materials Science and Engineering B-Advanced Functional Solid-State Materials*, vol. 151, pp. 2-6, 2008.
- [53] E. S. Reddy, E. A. Goodilin, M. Tarka, M. Zeisberger, and G. J. Schmitz, "Low temperature processing of single domain $\text{YBa}_2\text{Cu}_3\text{O}_y$ thick films from Y_2O_3 fabrics on Ag-Pd alloy substrates," *Physica C: Superconductivity*, vol. 372-376, Part 2, pp. 1200-1203, 2002.

- [54] A. Endo, H. S. Chauhan, T. Egi, and Y. Shiohara, "Macroseggregation of $Y_2Ba_1Cu_1O_5$ particles in $Y_1Ba_2Cu_3O_{7-\delta}$ crystals grown by an undercooling method," *Journal of Materials Research*, vol. 11, pp. 795-803, 1996.
- [55] R. Cloots, T. Koutzarova, J. P. Mathieu, and M. Ausloos, "From RE-211 to RE-123. How to control the final microstructure of superconducting single-domains," *Superconductor Science & Technology*, vol. 18, pp. R9-R23, 2005.
- [56] P. Diko, "Microstructural limits of TSMG REBCO bulk superconductors," *Physica C-Superconductivity and Its Applications*, vol. 445, pp. 323-329, 2006.
- [57] W. Zhai, Y. H. Shi, J. H. Durrell, A. R. Dennis, and D. A. Cardwell, "The Influence of Y-211 Content on the Growth Rate and Y-211 Distribution in Y-Ba-Cu-O Single Grains Fabricated by Top Seeded Melt Growth," *Crystal Growth & Design*, vol. 14, pp. 6367-6375, 2014.
- [58] F. G. Krabbes G, Canders W R, May H, Palka R, *High Temperature Superconductor Bulk Materials: Fundamentals-Processing-Properties Control-Application Aspects*. Weinheim: Wiley-VCH Verlag GmbH & Co. KGaA, 2006.
- [59] J. J. Roa, F. T. Dias, M. Martinez, J. A. Padilla, and M. Segarra, "Oxygenation kinetics of YBCO-TSMG samples using the nanoindentation technique," *Journal of the European Ceramic Society*, vol. 32, pp. 425-431, 2012.
- [60] J. R. Waldron, *Superconductivity of Metals and Cuprates*. London: IOP Publishing Ltd., 1996.
- [61] J. Bardeen, L. N. Cooper, and J. R. Schrieffer, "Theory of Superconductivity," *Physical Review*, vol. 108, pp. 1175-1204, 1957.
- [62] M. K. Wu, J. R. Ashburn, C. J. Torng, P. H. Hor, R. L. Meng, L. Gao, *et al.*, "Superconductivity at 93 K in a new mixed-phase Y-Ba-Cu-O compound system at ambient pressure," *Physical Review Letters*, vol. 58, pp. 908-910, 1987.
- [63] J. Nagamatsu, N. Nakagawa, T. Muranaka, Y. Zenitani, and J. Akimitsu, "Superconductivity at 39 K in magnesium diboride," *Nature*, vol. 410, pp. 63-64, 2001.
- [64] J. Yang, Z. C. Li, W. Lu, W. Yi, X. L. Shen, Z. A. Ren, *et al.*, "Superconductivity at 53.5 K in $GdFeAsO_{(1-\delta)}$," *Superconductor Science & Technology*, vol. 21, 2008.
- [65] D. X. Chen and R. B. Goldfarb, "Kim model for magnetization of type-II superconductors," *Journal of Applied Physics*, vol. 66, pp. 2489-2500, 1989.
- [66] S. Nariki, N. Sakai, M. Murakami, and I. Hirabayashi, "High critical current density in RE-Ba-Cu-O bulk superconductors with very fine RE_2BaCuO_5 particles," *Physica C-Superconductivity and Its Applications*, vol. 412, pp. 557-565, 2004.
- [67] M. Murakami, K. Yamaguchi, H. Fujimoto, N. Nakamura, T. Taguchi, N. Koshizuka, *et al.*, "Flux pinning by nonsuperconducting inclusions in melt-processed YBaCuO superconductors," *Cryogenics*, vol. 32, pp. 930-935, 1992.
- [68] W. M. Yang and M. Wang, "New method for introducing nanometer flux pinning centers into single domain YBCO bulk superconductors," *Physica C: Superconductivity*, vol. 493, pp. 128-131, 2013.
- [69] N. Hari Babu, K. Iida, and D. A. Cardwell, "Enhanced magnetic flux pinning in nano-composite Y-Ba-Cu-O superconductors," *Physica C: Superconductivity and its Applications*, vol. 445-448, pp. 353-356, 2006.
- [70] K. Winzer and G. Kumm, "Fluctuation-enhanced conductivity and magnetoconductivity of high-quality $YBa_2Cu_3O_{7-\delta}$ crystals," *Zeitschrift für Physik B Condensed Matter*, vol. 82, pp. 317-321, 1991.
- [71] Y. Matsuda, T. Hirai, S. Komiyama, T. Terashima, Y. Bando, K. Iijima, *et al.*, "Magneto-resistance of c-axis-oriented epitaxial $YBa_2Cu_3O_{7-\delta}$ films above T_c ," *Physical Review B*, vol. 40, pp. 5176-5179, 1989.

- [72] P. Diko, "Growth-related microstructure of melt-grown $\text{REBa}_2\text{Cu}_3\text{O}_y$ bulk superconductors," *Superconductor Science & Technology*, vol. 13, pp. 1202-1213, 2000.
- [73] D. F. Lee, V. Selvamanickam, and K. Salama, "Influences of Y_2BaCuO_5 particle-size and content on the transport critical current-density of $\text{YBa}_2\text{Cu}_3\text{O}_x$ superconductor," *Physica C*, vol. 202, pp. 83-96, 1992.
- [74] J. G. Bednorz and K. A. Muller, "Possible high- T_c superconductivity in the Ba-La-Cu-O system," *Zeitschrift Fur Physik B-Condensed Matter*, vol. 64, pp. 189-193, 1986.
- [75] T. K. Worthington, W. J. Gallagher, D. L. Kaiser, F. H. Holtzberg, and T. R. Dinger, "The anisotropic nature of the superconducting properties of single-crystal $\text{Y}_1\text{Ba}_2\text{Cu}_3\text{O}_{7-x}$ " *Physica C*, vol. 153, pp. 32-37, 1988.
- [76] K. Salama, V. Selvamanickam, L. Gao, and K. Sun, "High-current density in bulk $\text{YBa}_2\text{Cu}_3\text{O}_x$ superconductor," *Applied Physics Letters*, vol. 54, pp. 2352-2354, 1989.
- [77] H. Hojaji, K. A. Michael, A. Barkatt, A. N. Thorpe, M. F. Ware, I. G. Talmy, *et al.*, "A comparative-study of sintered and melt-grown recrystallized YBaCu_3O_x ," *Journal of Materials Research*, vol. 4, pp. 28-32, 1989.
- [78] S. Jin, T. H. Tiefel, R. C. Sherwood, M. E. Davis, R. B. Vandover, G. W. Kammlott, *et al.*, "High critical currents in Y-Ba-Cu-O superconductors," *Applied Physics Letters*, vol. 52, pp. 2074-2076, 1988.
- [79] T. Matsushita, B. Ni, M. Murakami, M. Morita, K. Miyamoto, M. Saga, *et al.*, "Critical current densities in superconducting Y-Ba-Cu-O prepared by the quench-and-melt growth technique," *Japanese Journal of Applied Physics Part 2-Letters & Express Letters*, vol. 28, pp. L1545-L1548, 1989.
- [80] M. Murakami, *Melt Processed High-Temperature Superconductors*. Singapore: World Scientific, 1992.
- [81] N. Ogawa, I. Hirabayashi, and S. Tanaka, "Preparation of a high- J_c YBCO bulk superconductor by the platinum doped melt growth method," *Physica C*, vol. 177, pp. 101-105, 1991.
- [82] L. Zhou, S. K. Chen, K. G. Wang, X. Z. Wu, P. X. Zhang, Y. Feng, *et al.*, "Preparation of enhanced J_c YBCO bulks by powder melting process with a combination of submicron 211 precursor and Pt addition," *Physica C-Superconductivity and Its Applications*, vol. 371, pp. 62-68, 2002.
- [83] P. Diko, C. Wende, D. Litzkendorf, T. Klupsch, and W. Gawalek, "The influence of starting $\text{YBa}_2\text{Cu}_3\text{O}_{7-x}$ particle size and Pt/Ce addition on the microstructure of $\text{YBa}_2\text{Cu}_3\text{O}_{7-x}$ - Y_2BaCuO_5 melt processed bulks," *Superconductor Science & Technology*, vol. 11, pp. 49-53, 1998.
- [84] C. Varanasi, M. A. Black, and P. J. McGinn, "A comparison of the effects of PtO_2 and BaSnO_3 additions on the refinement of Y_2BaCuO_5 and magnetization of textured $\text{YBa}_2\text{Cu}_3\text{O}_{6+x}$ " *Superconductor Science & Technology*, vol. 7, pp. 10-16, 1994.
- [85] C. J. Kim, K. B. Kim, and G. W. Hong, " Y_2BaCuO_5 morphology in melt-textured Y-Ba-Cu-O oxides with $\text{PtO}_2/\text{CeO}_2$ additions," *Physica C*, vol. 232, pp. 163-173, 1994.
- [86] N. H. Babu, M. Kambara, D. A. Cardwell, C. D. Tarrant, and K. Schneider, "Effect of the addition of depleted UO_2 on the microstructure of melt processed Y-Ba-Cu-O superconductors," *Physica C-Superconductivity and Its Applications*, vol. 372, pp. 1183-1186, 2002.
- [87] Y. Shi, N. H. Babu, and D. A. Cardwell, "Development of a generic seed crystal for the fabrication of large grain (RE)-Ba-Cu-O bulk superconductors," *Superconductor Science & Technology*, vol. 18, pp. L13-L16, 2005.
- [88] N. H. Babu, W. Lo, D. A. Cardwell, and Y. Shi, "The effect of undercooling and Nd422 phase content on the nucleation of large Nd-Ba-Cu-O grains fabricated by top-seeded melt processing," *Journal of Materials Research*, vol. 14, pp. 3859-3863, 1999.

- [89] T. Y. Li, L. Cheng, S. B. Yan, L. J. Sun, X. Yao, Y. Yoshida, *et al.*, "Growth and superconductivity of REBCO bulk processed by a seed/buffer layer/precursor construction," *Superconductor Science & Technology*, vol. 23, 2010.
- [90] C. J. Kim, J. H. Lee, S. D. Park, B. H. Jun, S. C. Han, and Y. H. Han, "Y₂BaCuO₅ buffer block as a diffusion barrier for samarium in top seeded melt growth processed YBa₂Cu₃O_{7-y} superconductors using a SmBa₂Cu₃O_{7-d} seed," *Superconductor Science & Technology*, vol. 24, 2011.
- [91] D. F. Zhou, K. Xu, S. Hara, B. Z. Li, Z. G. Deng, K. Tsuzuki, *et al.*, "MgO buffer-layer-induced texture growth of RE-Ba-Cu-O bulk," *Superconductor Science & Technology*, vol. 25, 2012.
- [92] Y. H. Shi, A. R. Dennis, and D. A. Cardwell, "A new seeding technique for the reliable fabrication of large, SmBCO single grains containing silver using top seeded melt growth," *Superconductor Science & Technology*, vol. 28, 2015.
- [93] N. D. Kumar, Y. H. Shi, W. Zhai, A. R. Dennis, J. H. Durrell, and D. A. Cardwell, "Buffer Pellets for High-Yield, Top-Seeded Melt Growth of Large Grain Y-Ba-Cu-O Superconductors," *Crystal Growth & Design*, vol. 15, pp. 1472-1480, 2015.
- [94] W. Zhao, Y. H. Shi, A. R. Dennis, and D. A. Cardwell, "Use of Sm-123+Sm-211 Mixed-Powder Buffers to Assist the Growth of SmBCO and ZrO₂-doped SmBCO Single Grain, Bulk Superconductors," *IEEE Transactions on Applied Superconductivity*, vol. 25, p. 5, 2015.
- [95] H. Fujimoto, M. Murakami, S. Gotoh, N. Koshizuha, T. Oyana, Y. Shiohara and S. Tanaka, "Melt processing of YBaCuO oxide superconductors," *Advances in Superconductivity: II. Proceedings of the 2nd International Symposium on Superconductivity*, p. 285, 1990.
- [96] S. Kracunovska, P. Diko, D. Litzkendorf, T. Habisreuther, J. Bierlich, and W. Gawalek, "Oxygenation and cracking in melt-textured YBCO bulk superconductors," *Superconductor Science & Technology*, vol. 18, pp. S142-S148, 2005.
- [97] D. X. Chen and R. B. Goldfarb, "Kim model for magnetization of type-II superconductors," *J. Appl. Phys.*, vol. 66, p. 2489, 1989.
- [98] C. A. Schneider, W. S. Rasband, and K. W. Eliceiri, "NIH Image to ImageJ: 25 years of image analysis," *Nature Methods*, vol. 9, p. 671, 2012.
- [99] Y. H. Shi, D. K. Namburi, M. Wang, J. Durrell, A. Dennis, and D. Cardwell, "A Reliable Method for Recycling (RE)-Ba-Cu-O (RE: Sm, Gd, Y) Bulk Superconductors," *Journal of the American Ceramic Society*, vol. 98, pp. 2760-2766, 2015.
- [100] G. Z. Li, D. J. Li, X. Y. Deng, J. H. Deng, and W. M. Yang, "Infiltration Growth and Crystallization Characterization of Single-Grain Y-Ba-Cu-O Bulk Superconductors," *Crystal Growth & Design*, vol. 13, pp. 1246-1251, 2013.
- [101] A. Mahmood, B. H. Jun, H. W. Park, and C. J. Kim, "Pre-sintering effects on the critical current density of YBCO bulk prepared by infiltration method," *Physica C-Superconductivity and Its Applications*, vol. 468, pp. 1350-1354, 2008.
- [102] P. Diko, G. Krabbes, and C. Wende, "Influence of Ag addition on crystallization and microstructure of melt-grown single-grain YBa₂Cu₃O₇ bulk superconductors," *Superconductor Science & Technology*, vol. 14, pp. 486-495, 2001.
- [103] K. Iida, N. H. Babu, Y. H. Shi, T. Miyazaki, N. Sakai, M. Murakami, *et al.*, "Single domain YBCO/Ag bulk superconductors fabricated by seeded infiltration and growth," in *8th European Conference on Applied Superconductivity*. vol. 97, S. Hoste and M. Ausloos, Eds., ed, 2008.
- [104] W. Lo, D. A. Cardwell, S.-L. Dung, and R. G. Barter, "Processing of bulk YBa₂Cu₃O_{7-δ} ceramics prior to peritectic solidification," *Journal of Materials Science*, vol. 30, pp. 3995-4002, 1995.
- [105] D. Volochova, P. Diko, M. Radusovska, S. Piovarci, V. Antal, K. Zmorayova, *et al.*, "Parameters of TSMG Process for Y_{1.5}Ba₂Cu₃O_x System with CeO₂ Addition," *Journal of Superconductivity and Novel Magnetism*, vol. 26, pp. 885-889, 2013.

- [106] A. Endo, H. S. Chauhan, Y. Nakamura, and Y. Shiohara, "Relationship between growth rate and undercooling in Pt-added $Y_1Ba_2Cu_3O_{7-x}$," *Journal of Materials Research*, vol. 11, pp. 1114-1119, 1996.
- [107] Y. Shi, N. H. Babu, K. Iida, and D. A. Cardwell, "Growth rate and superconducting properties of Gd-Ba-Cu-O bulk superconductors melt processed in air," *IEEE Transactions on Applied Superconductivity*, vol. 17, pp. 2984-2987, 2007.
- [108] J. V. J. Congreve, Y. H. Shi, A. R. Dennis, J. H. Durrell, and D. A. Cardwell, "Improvements in the processing of large grain, bulk Y-Ba-Cu-O superconductors via the use of additional liquid phase," *Superconductor Science & Technology*, vol. 30, p. 11, 2017.
- [109] T. K. Worthington, W. J. Gallagher, D. L. Kaiser, F. H. Holtzberg, and T. R. Dinger, "The anisotropic nature of the superconducting properties of single crystal $Y_1Ba_2Cu_3O_{7-x}$," *Physica C: Superconductivity*, vol. 153-155, pp. 32-37, 1988.

10 Appendix 1: Chapter 3



Figure 10.1: Recycled grains of a) Top view of YBCO, b) Side view of YBCO, c) Top view of GdBCO-Ag (note the 2 grains on the left and one grain on the right of the middle row are primary grown samples), d) Side view of GdBCO-Ag, e) Top view of SmBCO-Ag and f) Side view of SmBCO-Ag.

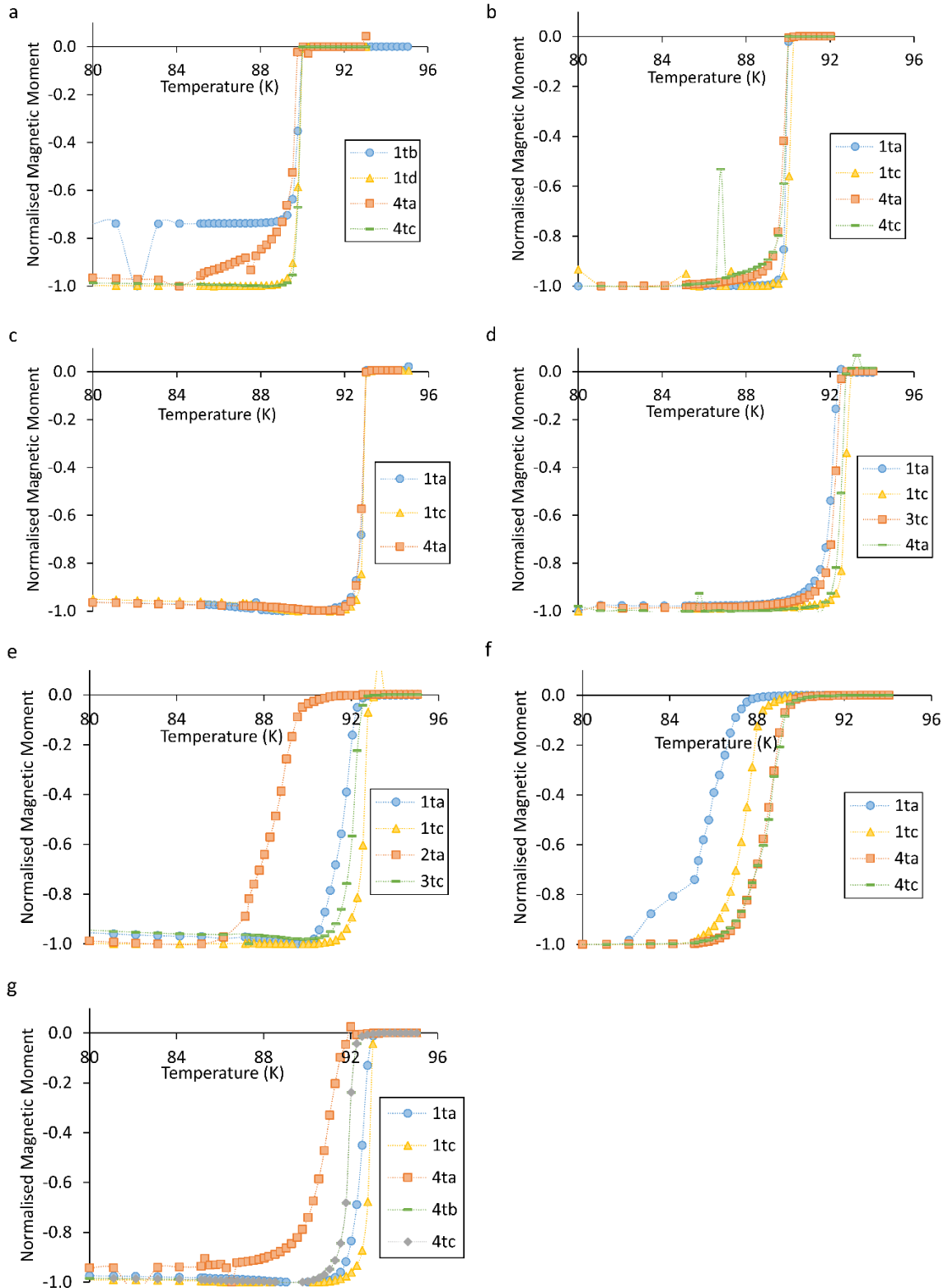


Figure 10.2: Plots of the magnetic moment evolution during a temperature sweep used to find T_c values and ΔT_{90} for sub-specimens of a) primary YBCO, b) recycled YBCO, c) primary GdBCO-Ag, d) recycled GdBCO-Ag, e) primary SmBCO-Ag, f) recycled SmBCO-Ag sample 1, and g) recycled SmBCO-Ag sample 2.

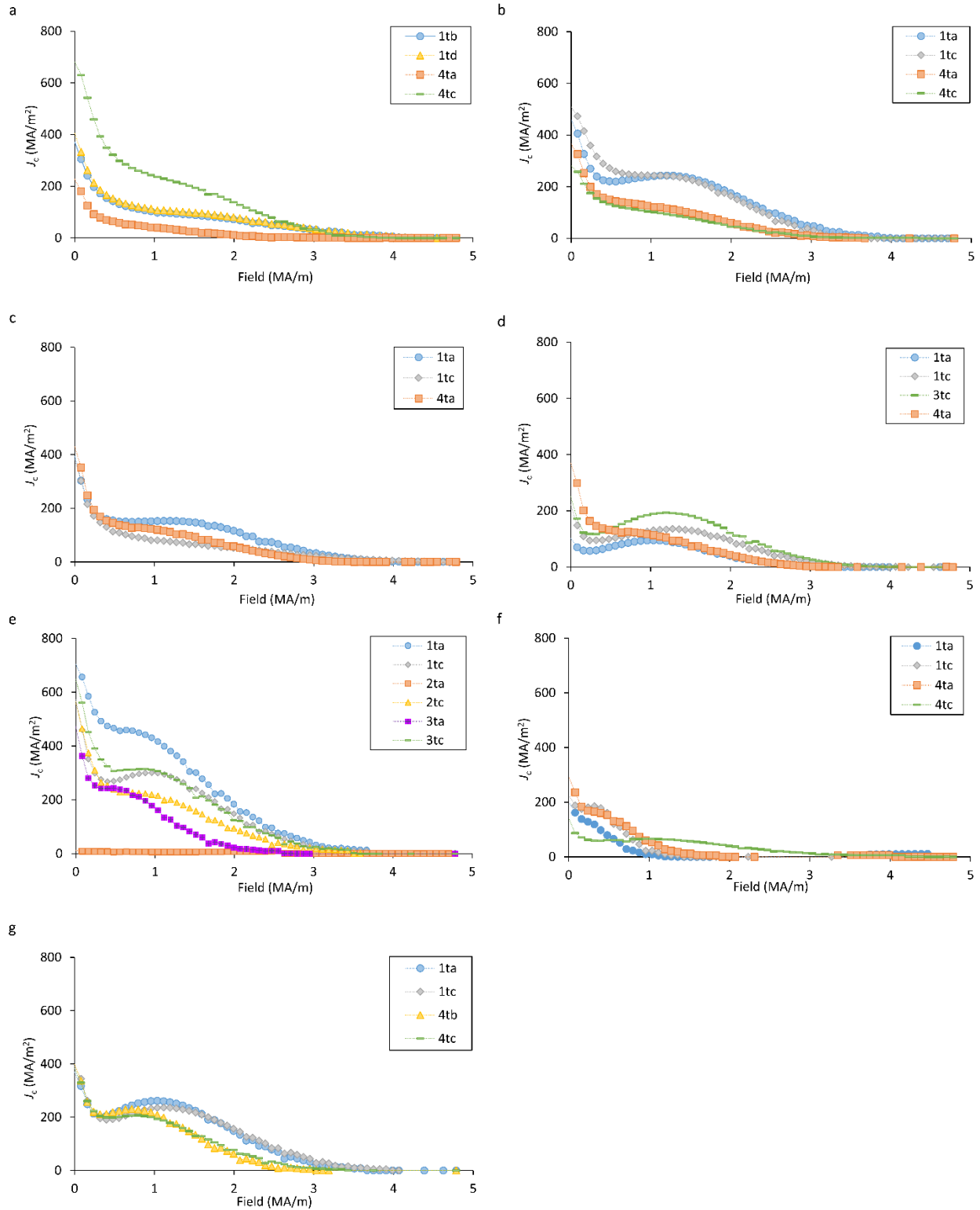


Figure 10.3: Plots of the variation in J_c values at a 77 K for: a) Primary grown YBCO, b) Recycled YBCO, c) Primary grown GdBCO-Ag, d) Recycled GdBCO-Ag, e) Primary grown SmBCO-Ag, f) Recycled SmBCO-Ag grain 1, and g) Recycled SmBCO-Ag grain 2

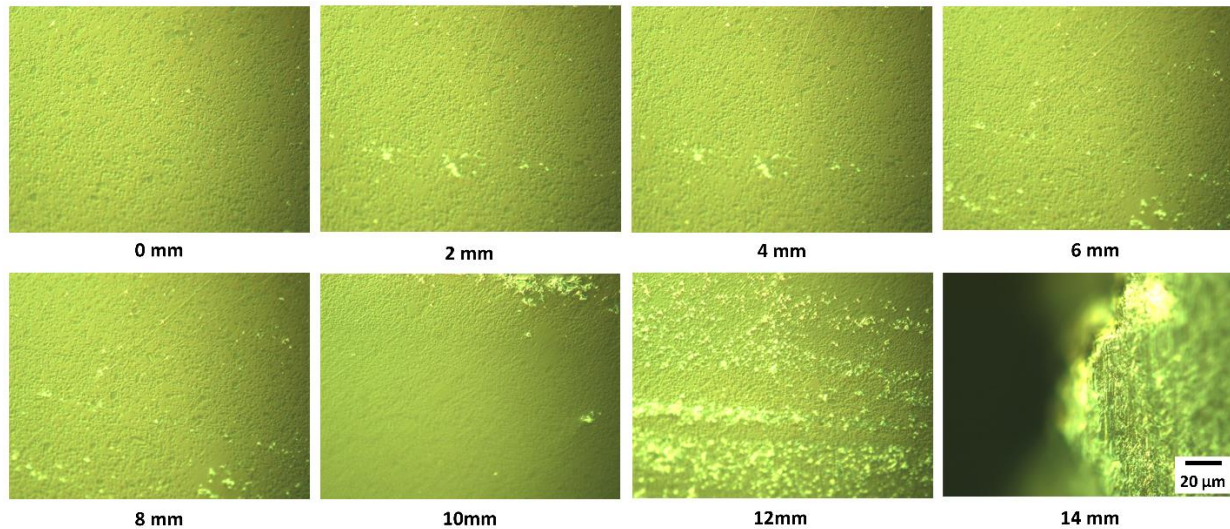


Figure 10.4: Optical microscope images along the a/b -axis of a primary grown YBCO sample approximately 1 mm below the seed at 500x magnification.

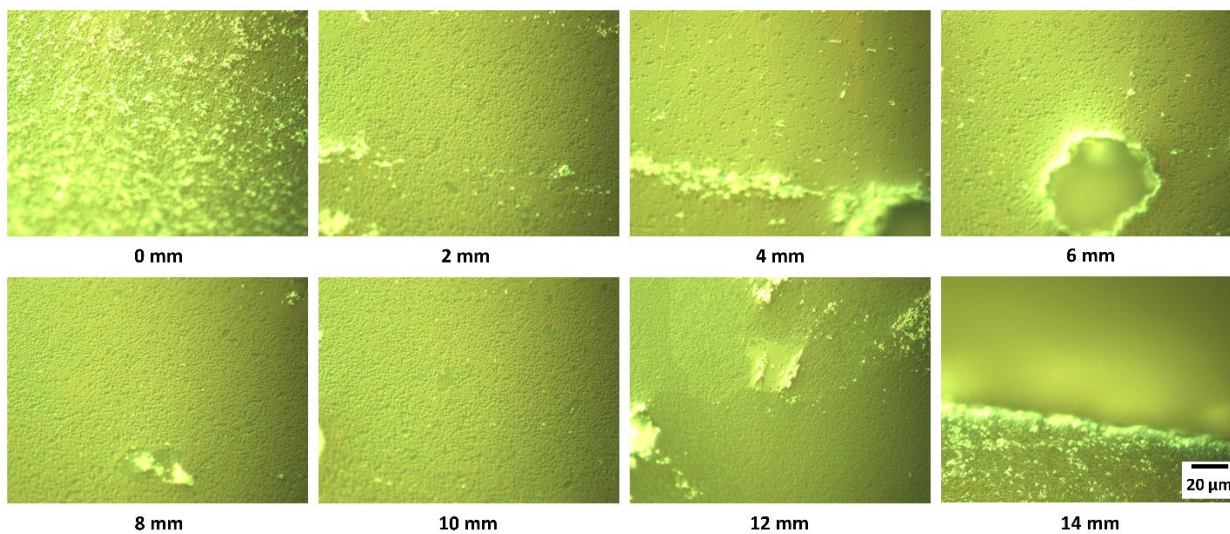


Figure 10.5: Optical microscope images along the central c -axis of a primary grown YBCO sample at 500x magnification.

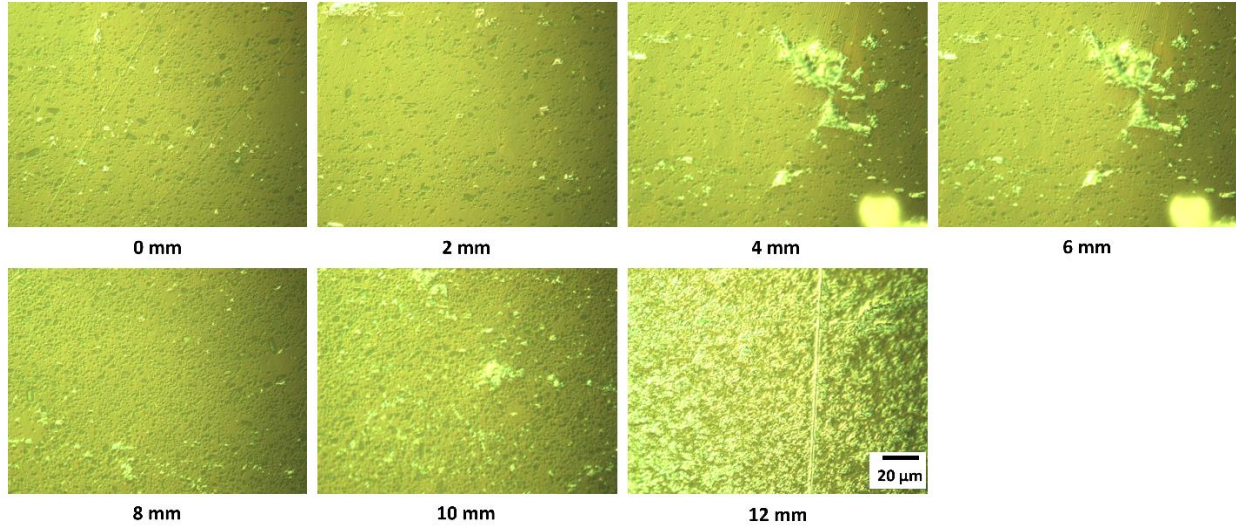


Figure 10.6: Optical microscope images along the a/b -axis of a recycled YBCO sample approximately 1 mm below the seed at 500x magnification.

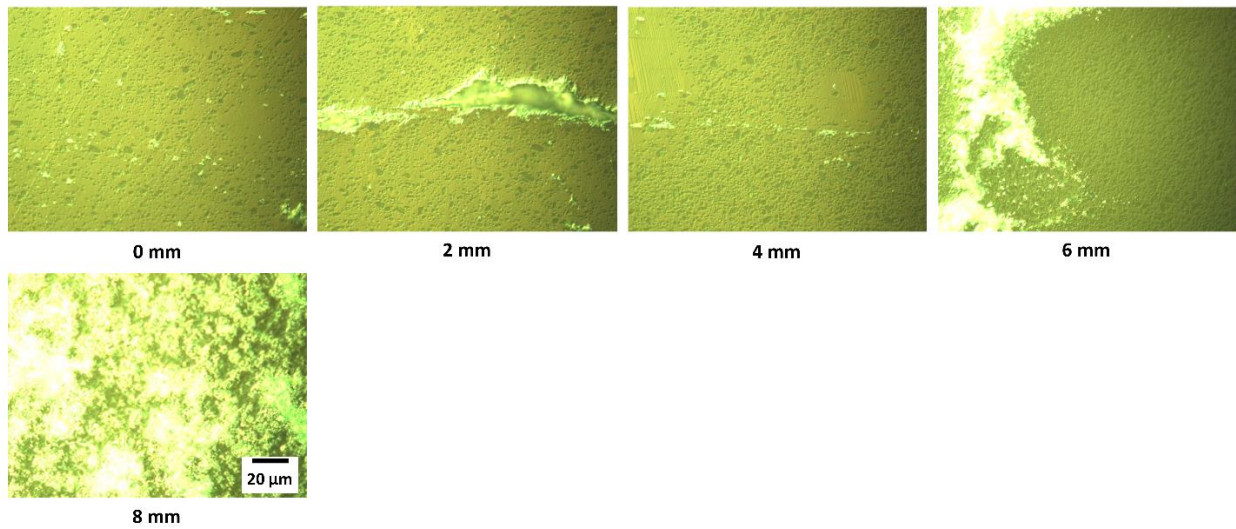


Figure 10.7: Optical microscope images along the central c -axis of a recycled YBCO sample at 500x magnification.

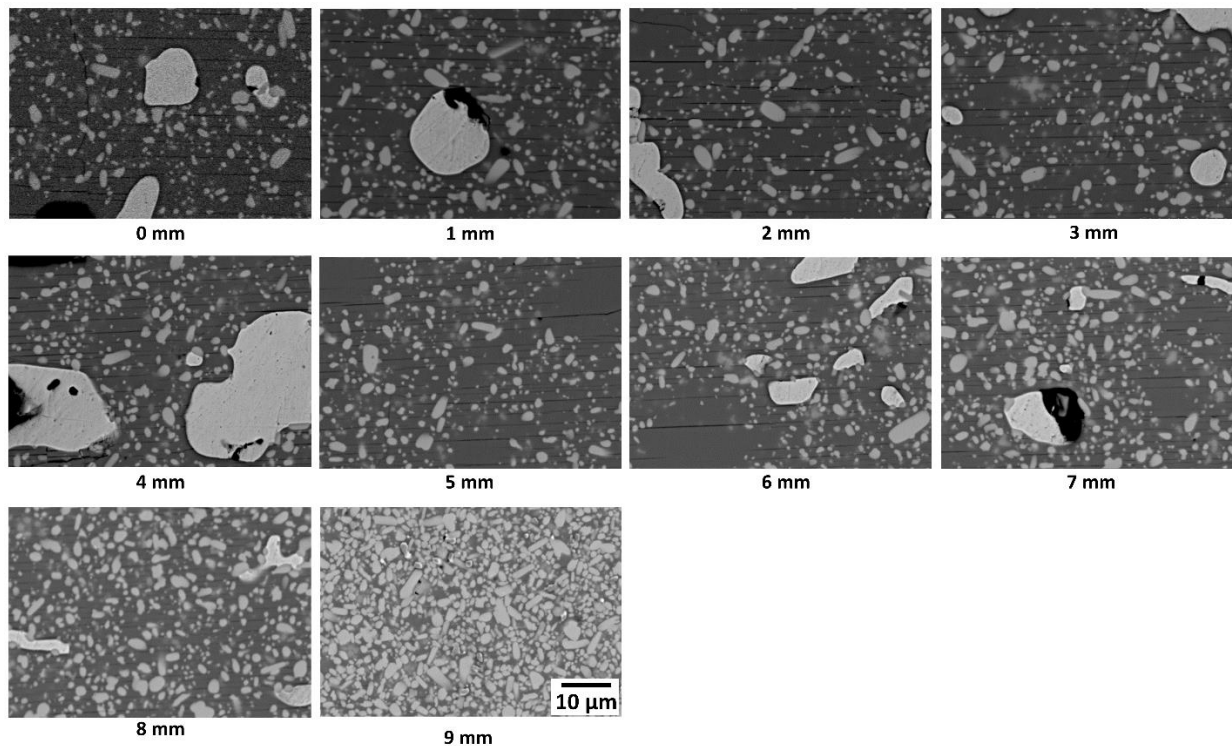


Figure 10.8: SEM images along the a/b-axis of a primary grown SmBCO-Ag sample approximately 1 mm below the seed at 2000x magnification.

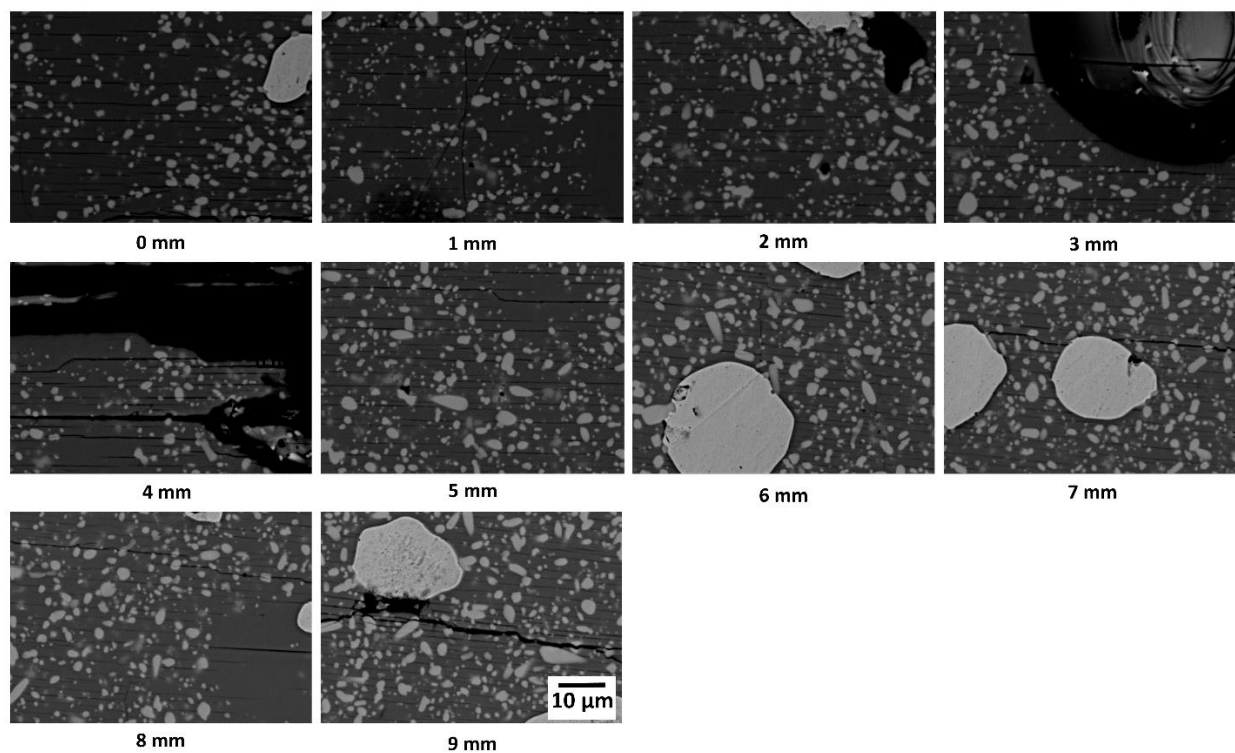


Figure 10.9: SEM images along the central c-axis of a primary grown SmBCO-Ag sample at 2000x magnification.

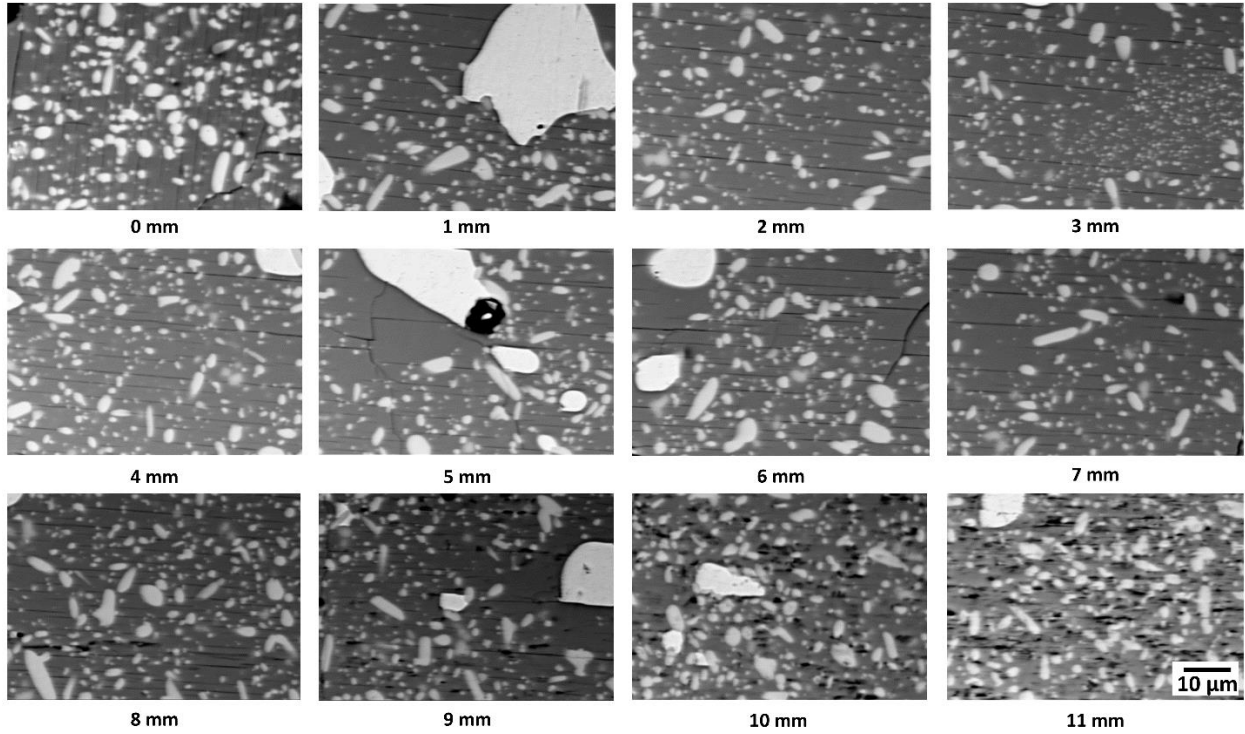


Figure 10.10: SEM images along the a/b -axis of recycled SmBCO-Ag grain 1 approximately 1 mm below the seed at 2000x magnification.

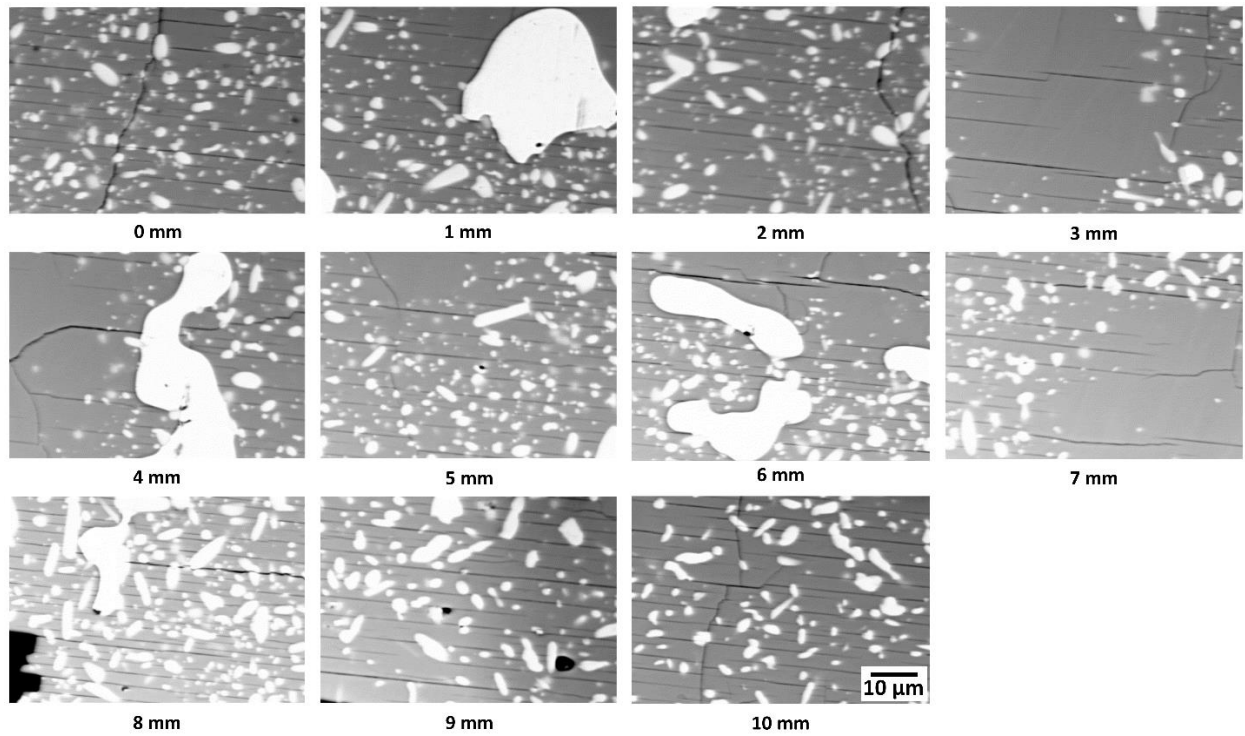


Figure 10.11: SEM images along the central c -axis of recycled SmBCO-Ag grain 1 at 2000x magnification.

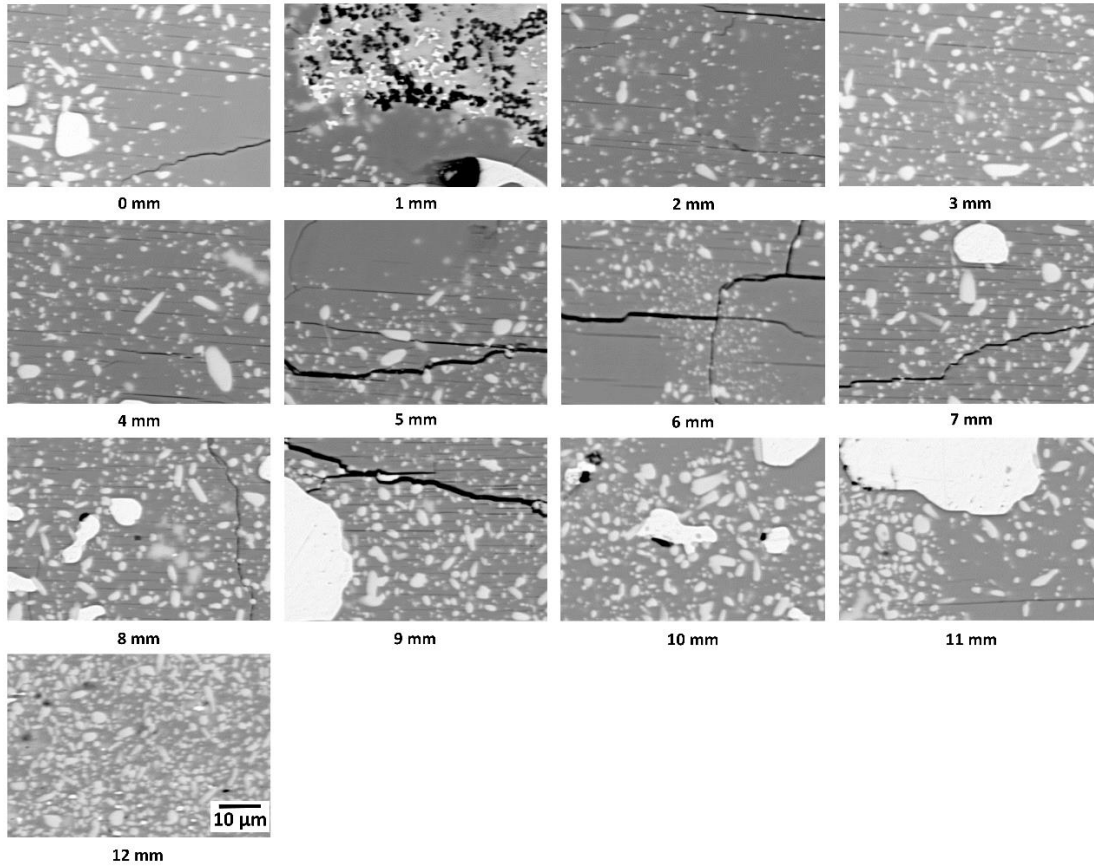


Figure 10.12: SEM images along the *a/b*-axis of recycled SmBCO-Ag grain 2 approximately 1 mm below the seed at 2000x magnification.

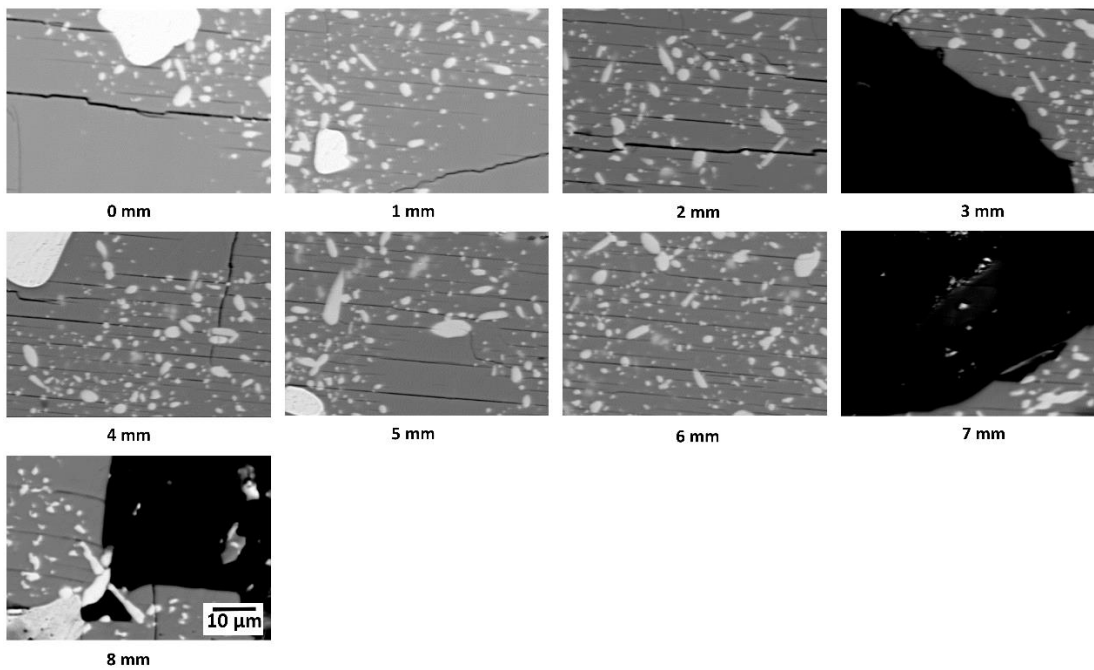


Figure 10.13: SEM images along the central *c*-axis of the recycled grain 2 at 2000x magnification.

11 Appendix 2: Chapter 4

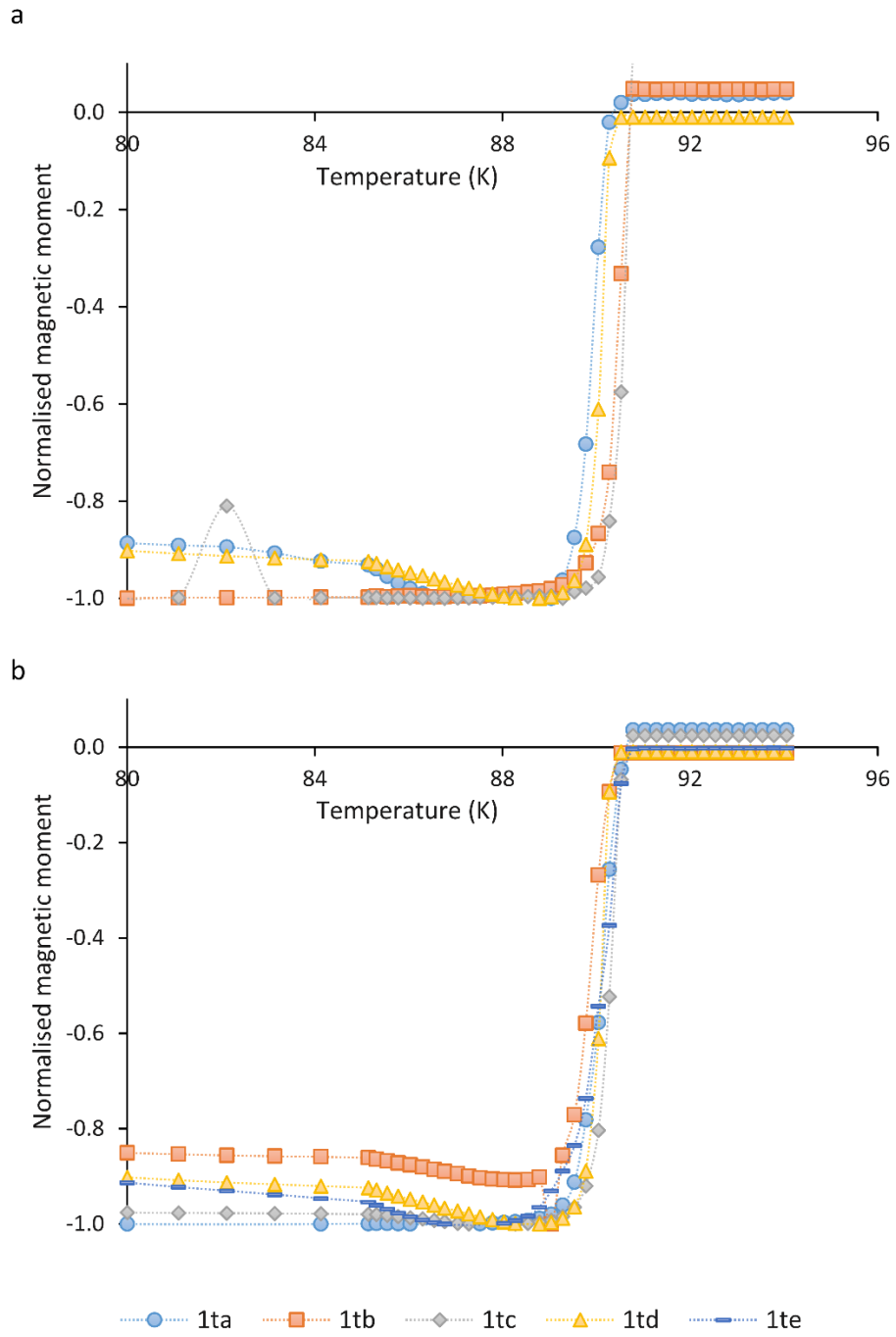


Figure 11.1: Plots of the variation in normalised magnetic moment with temperature for: a) Sample JY-02, b) Sample JY-09.

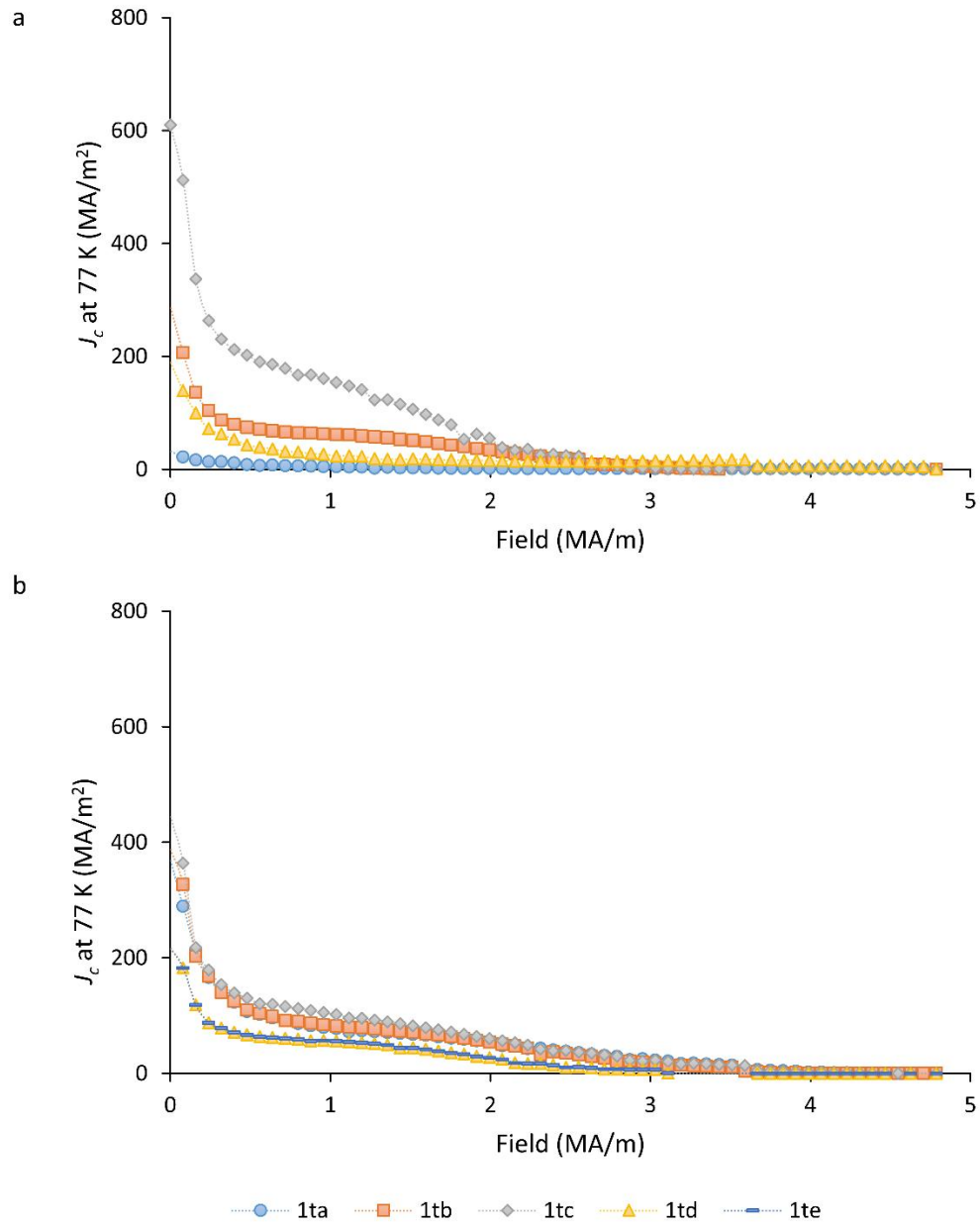


Figure 11.2: Plots of the variation in J_c value with field at a constant temperature of 77 K for a) Sample JY-02, the standard TSMG sample, b) Sample JY-09, the sample grown by TSMG with additional liquid-phase.

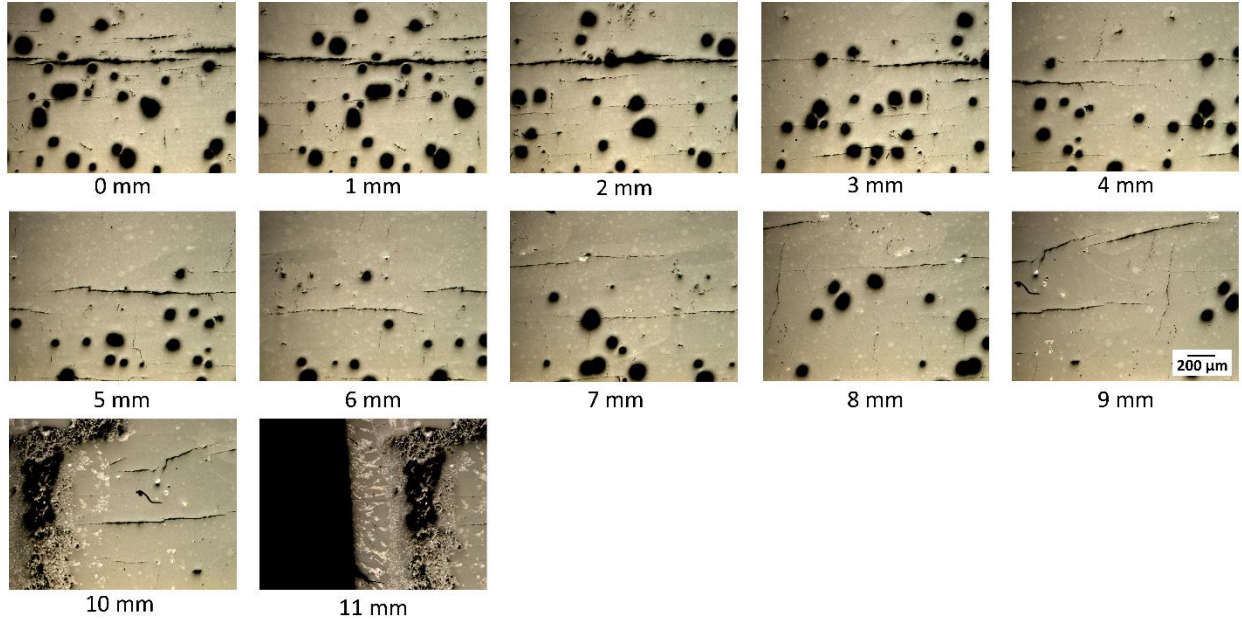


Figure 11.3: Optical microscope images along the a/b-axis of sample JY-02 approximately 1 mm below the seed at 50x magnification.

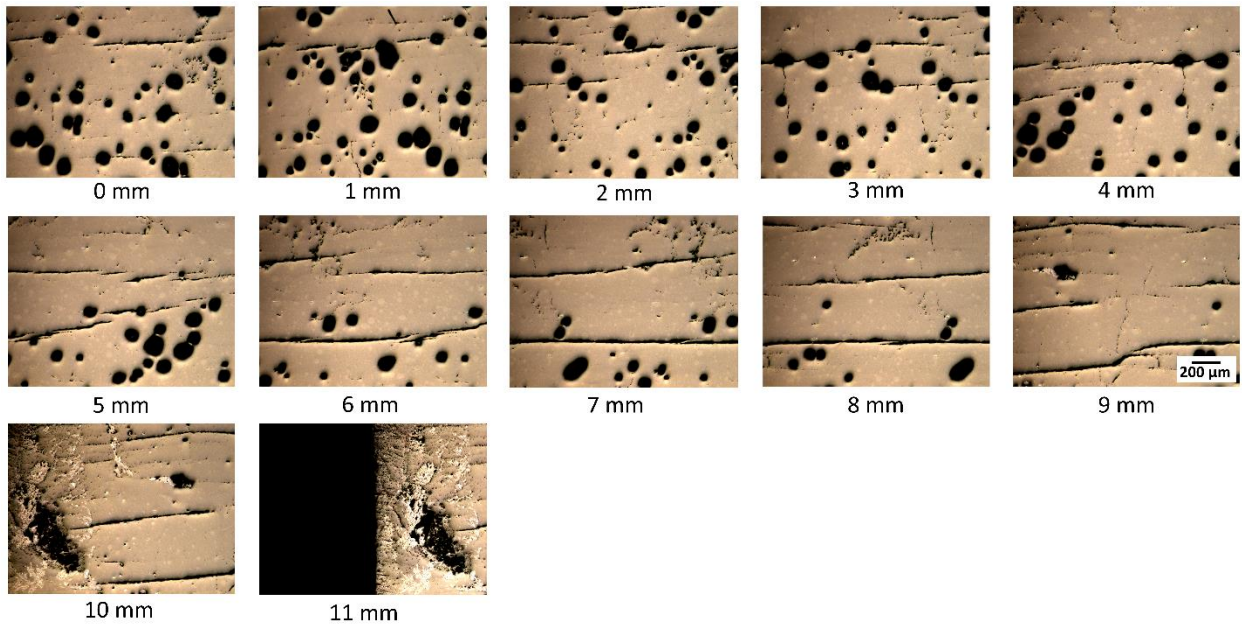


Figure 11.4: Optical microscope images along the a/b-axis of sample JY-09 approximately 1 mm below the seed at 50x magnification.

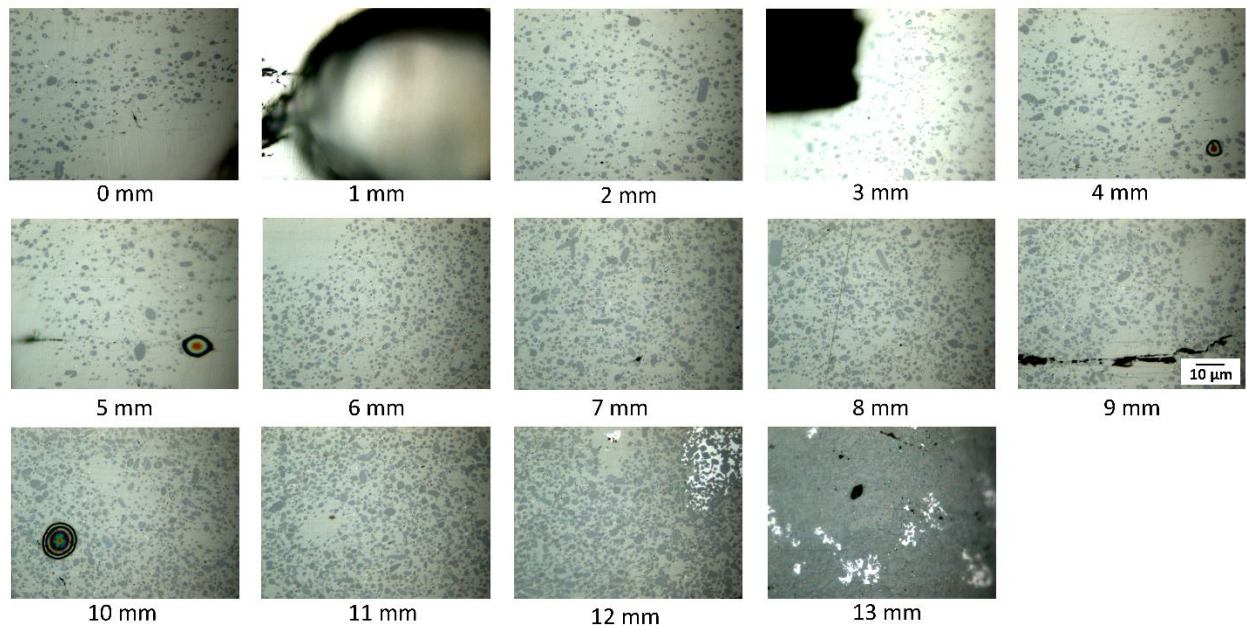


Figure 11.5: Optical microscope images along the a/b -axis of sample JY-02 approximately 1 mm below the seed at 1000x magnification.

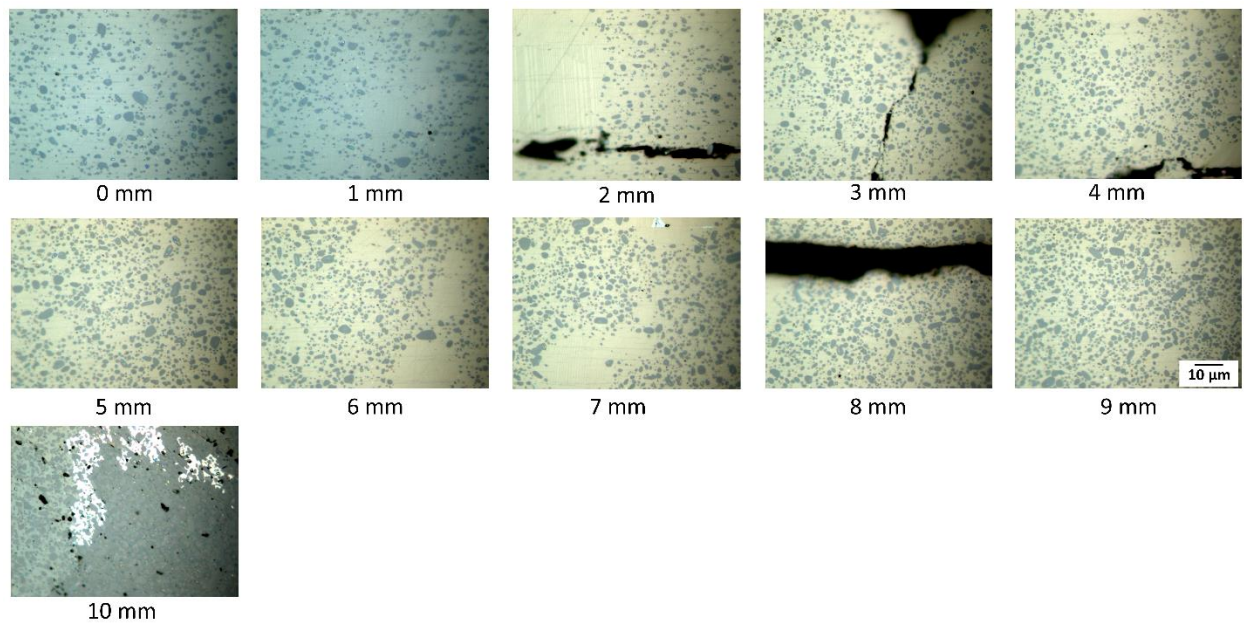


Figure 11.6: Optical microscope images along the a/b -axis of sample JY-09 approximately 1 mm below the seed at 1000x magnification.

12 Appendix 3: Chapter 6

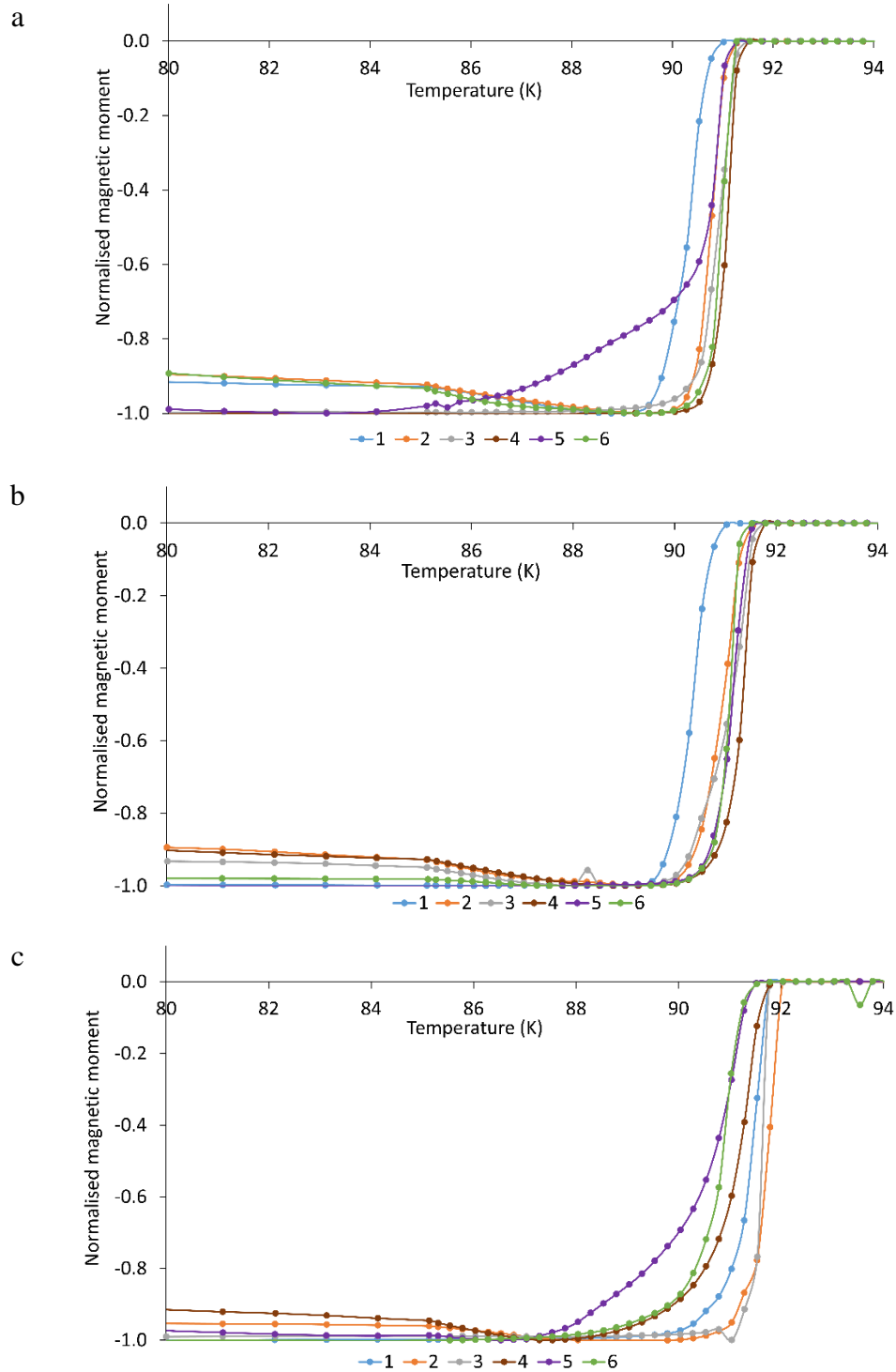


Figure 12.1: Plots of the variation in normalized magnetic moment with temperature, used to determine the transition temperature of the sub-specimens from: a) a YBCO sample, b) a LR YBCO sample, and c) a YBCO-Ag sample.

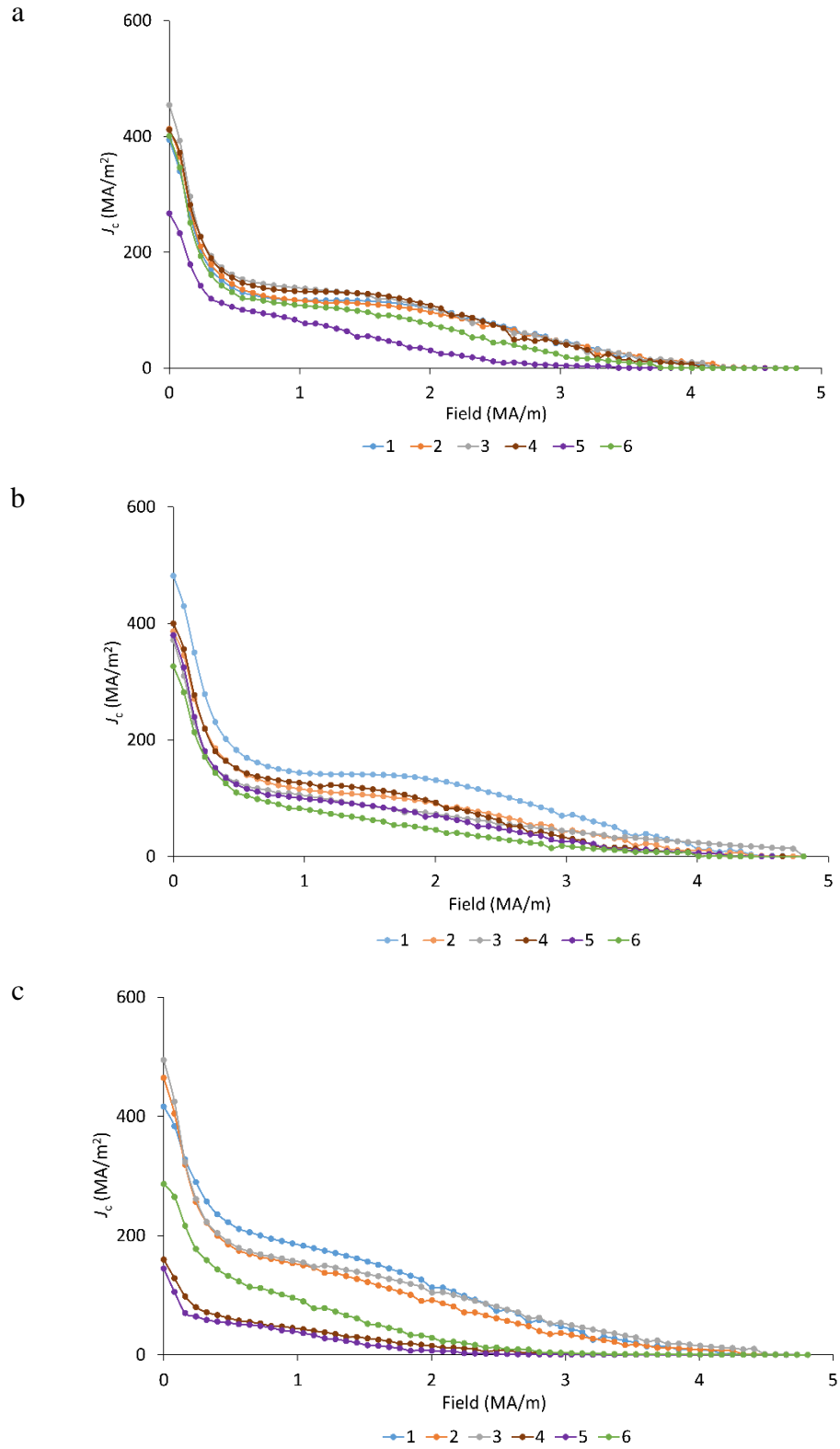


Figure 12.2: Plots of the variation in J_c values with field for the sub-specimens from: a) a YBCO sample, b) a LR YBCO sample, and c) a YBCO-Ag sample.

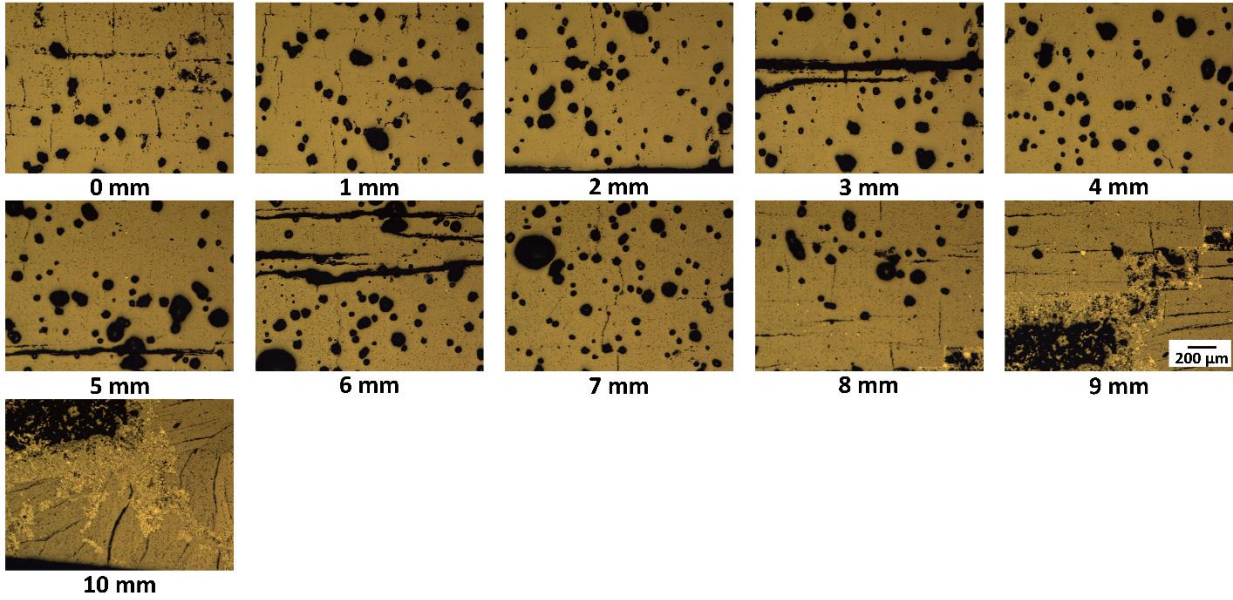


Figure 12.3: Optical microscope images along the central *c*-axis of a YBCO sample from a position just below the seed at 50x magnification.

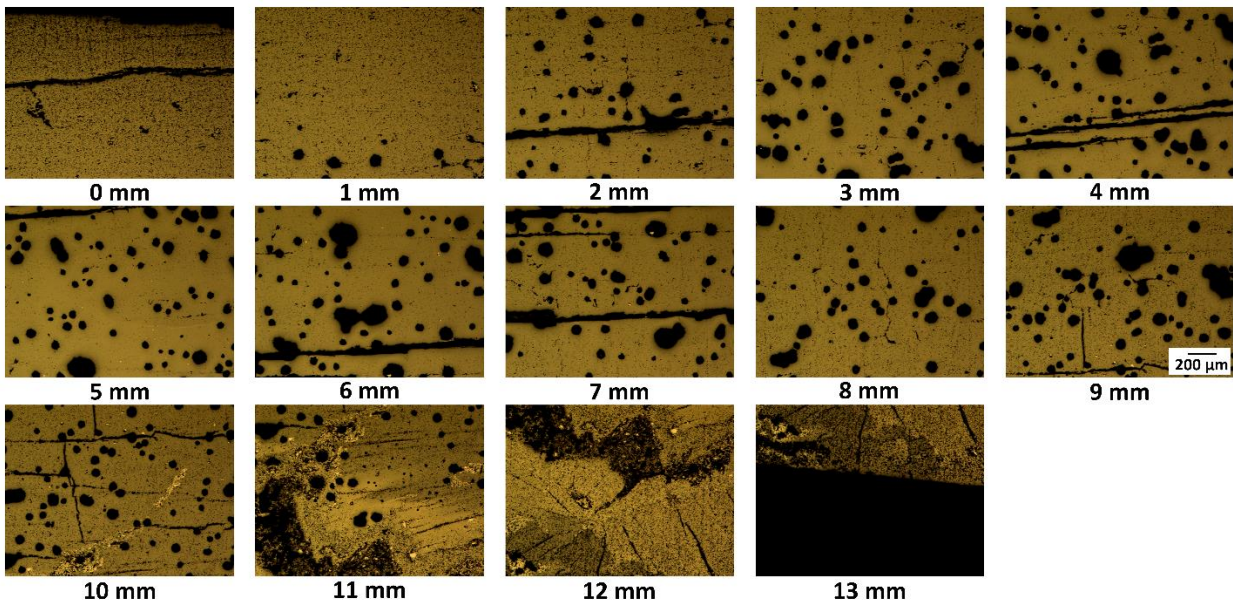


Figure 12.4: Optical microscope images along the central *c*-axis of a LR YBCO sample from a position just below the seed at 50x magnification.

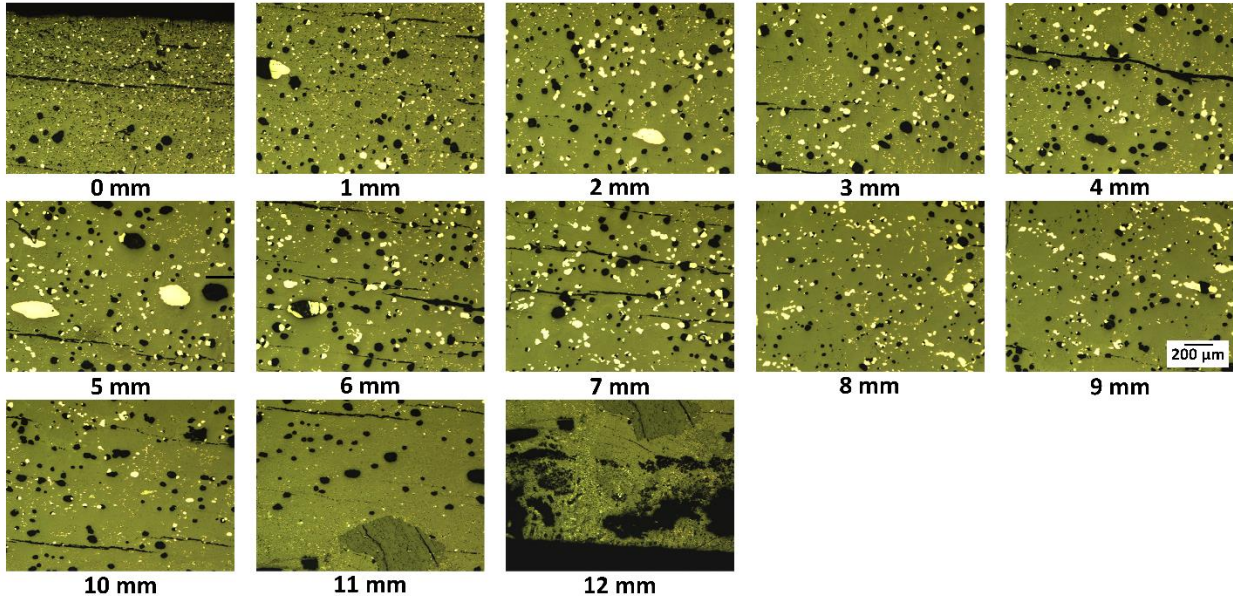


Figure 12.5: Optical microscope images along the central c -axis of a YBCO-Ag sample from a position just below the seed at 50x magnification.

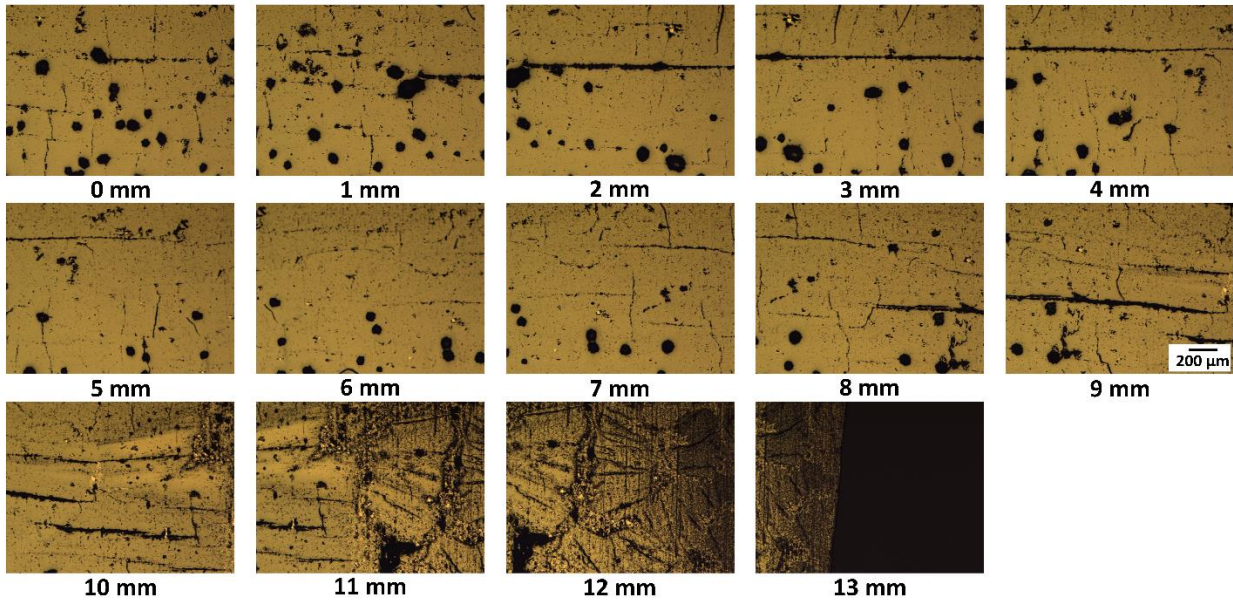


Figure 12.6: Optical microscope images along the a/b -axis of a YBCO sample approximately 1.5 mm from the top at 50x magnification.

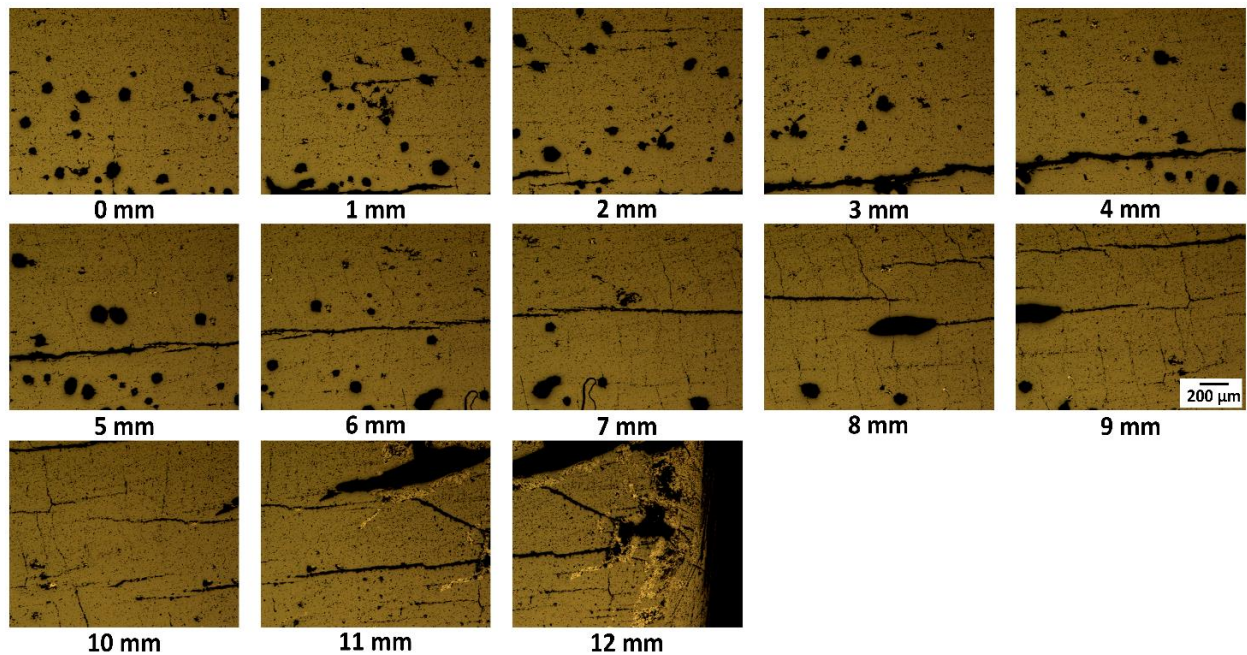


Figure 12.7: Optical microscope images along the a/b -axis of a LR YBCO sample approximately 1.5 mm from the top at 50x magnification.

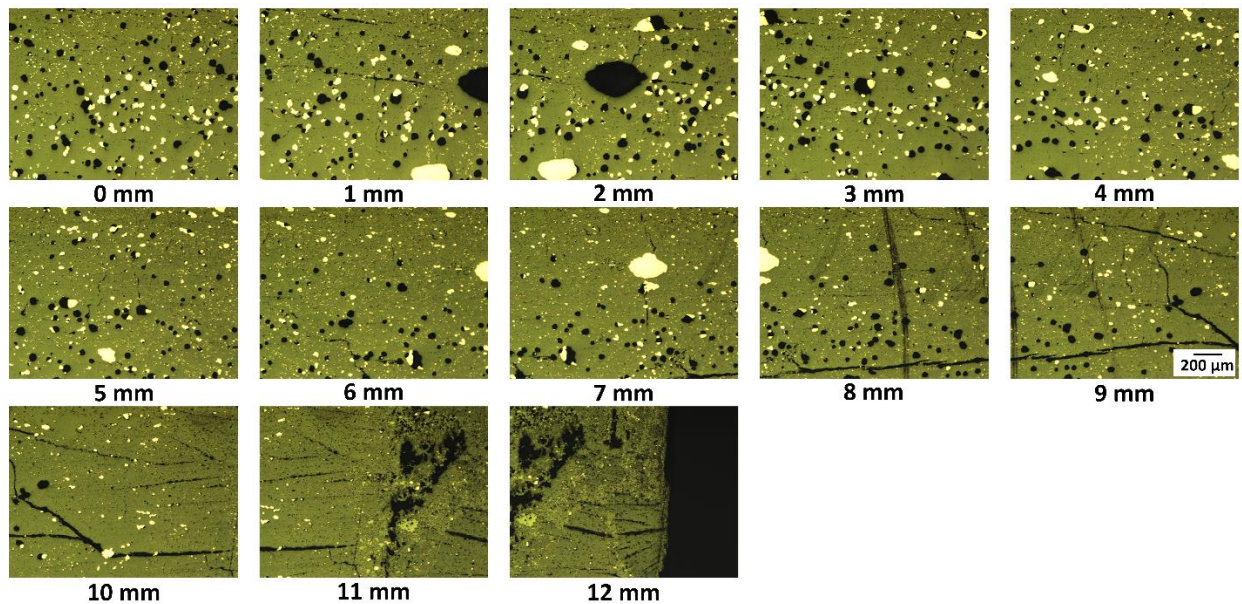


Figure 12.8: Optical microscope images along the a/b -axis of a YBCO-Ag sample approximately 1.5 mm from the top at 50x magnification.

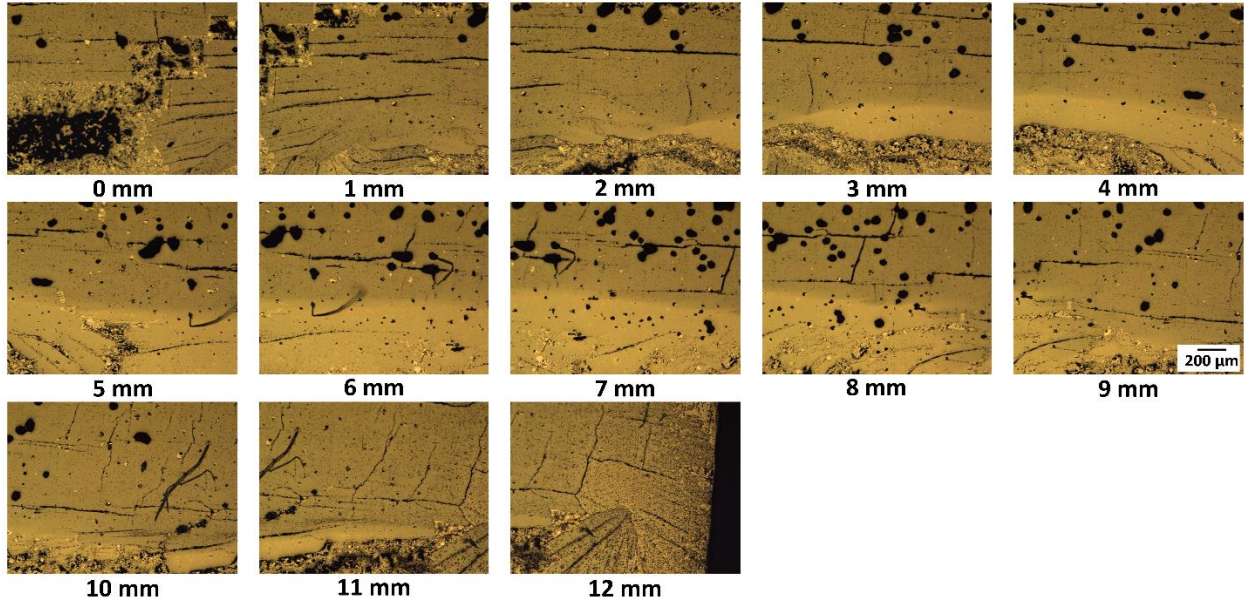


Figure 12.9: Optical microscope images along the a/b-axis of a YBCO sample approximately 1.5 mm from the base at 50x magnification.

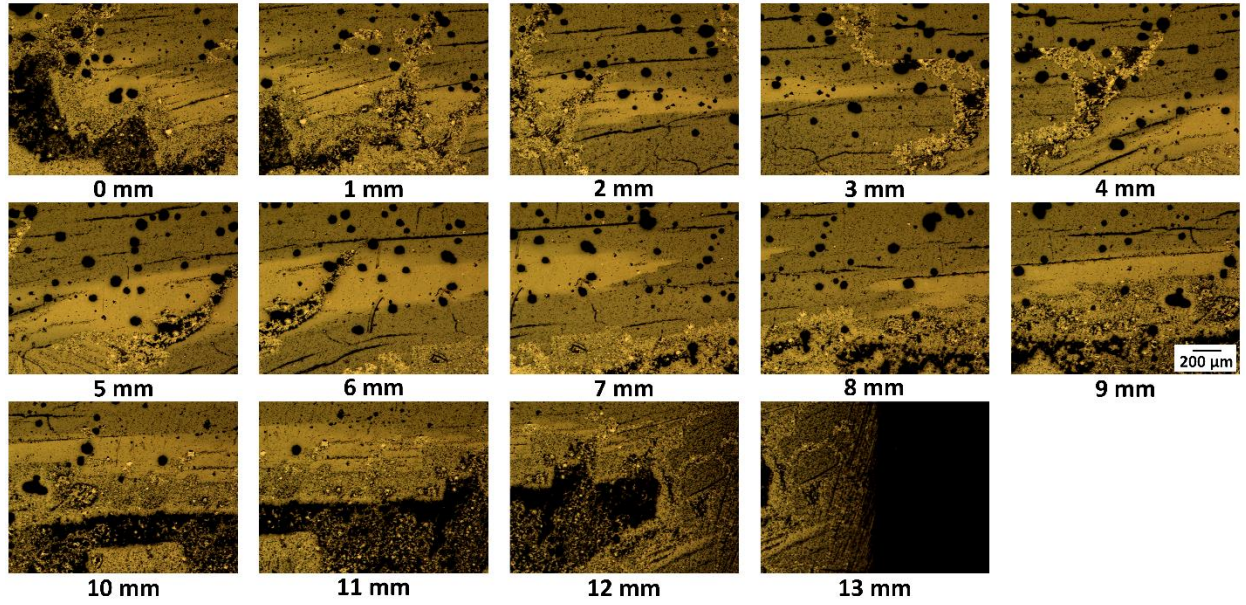


Figure 12.10: Optical microscope images along the a/b-axis of a LR YBCO sample approximately 1.5 mm from the base at 50x magnification.

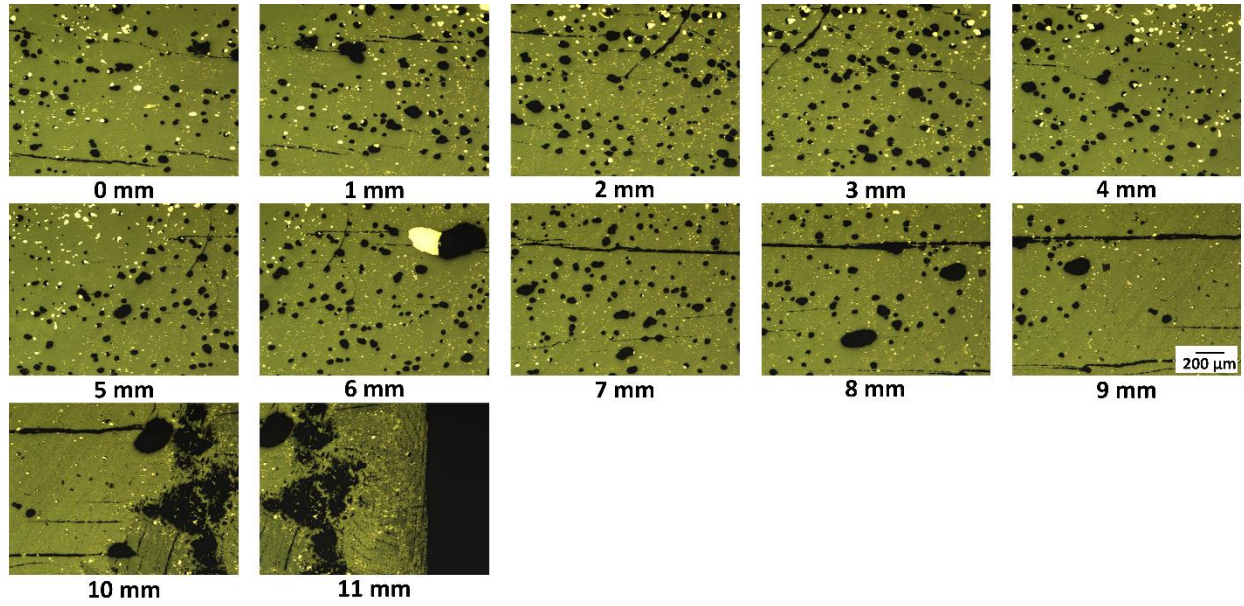


Figure 12.11: Optical microscope images along the a/b -axis of a YBCO-Ag sample approximately 1.5 mm from the base at 50x magnification.

13 Appendix 4: Chapter 7

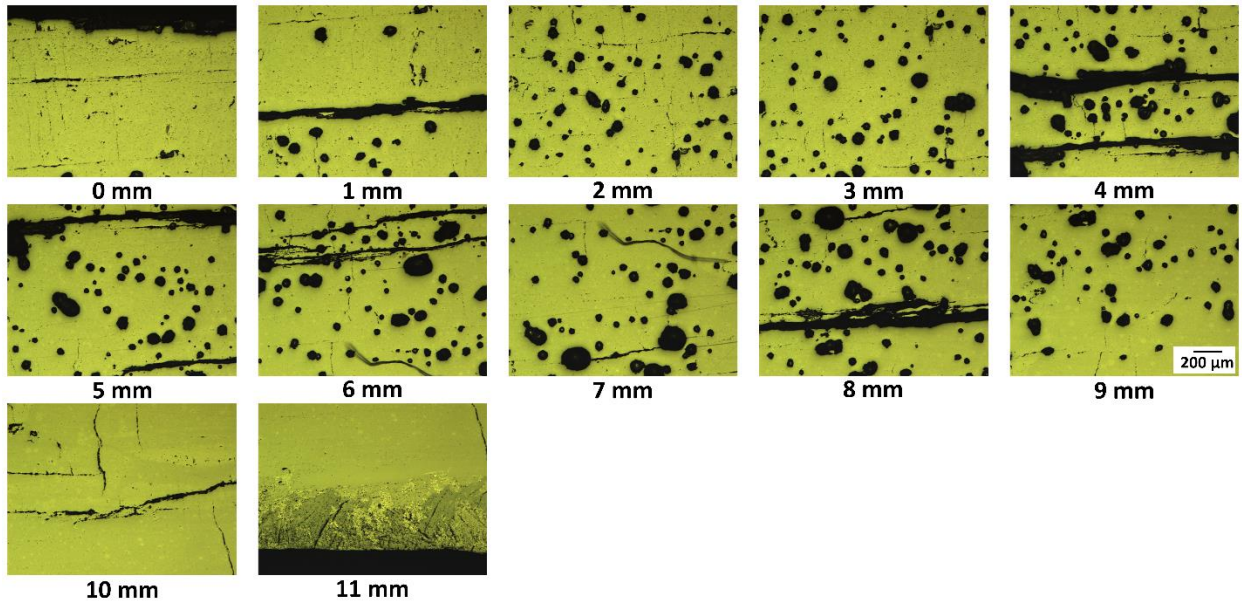


Figure 13.1: Optical microscope images along the central c-axis of a YBCO sample from a position just below the seed at 50x magnification.

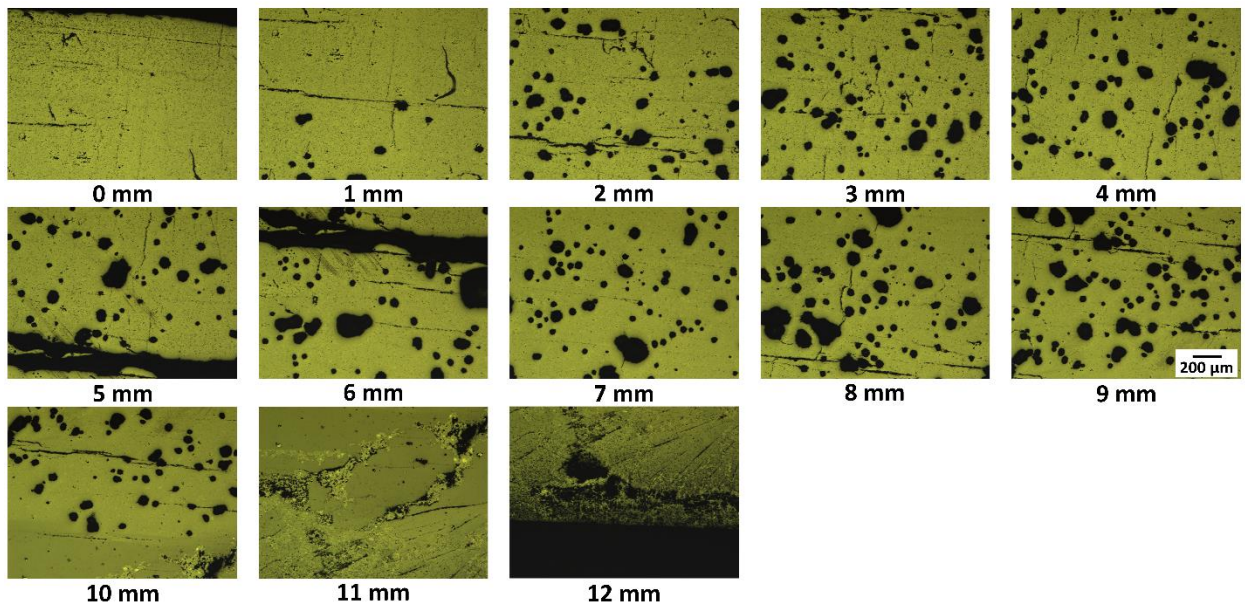


Figure 13.2: Optical microscope images along the central c-axis of a LR YBCO sample from a position just below the seed at 50x magnification.

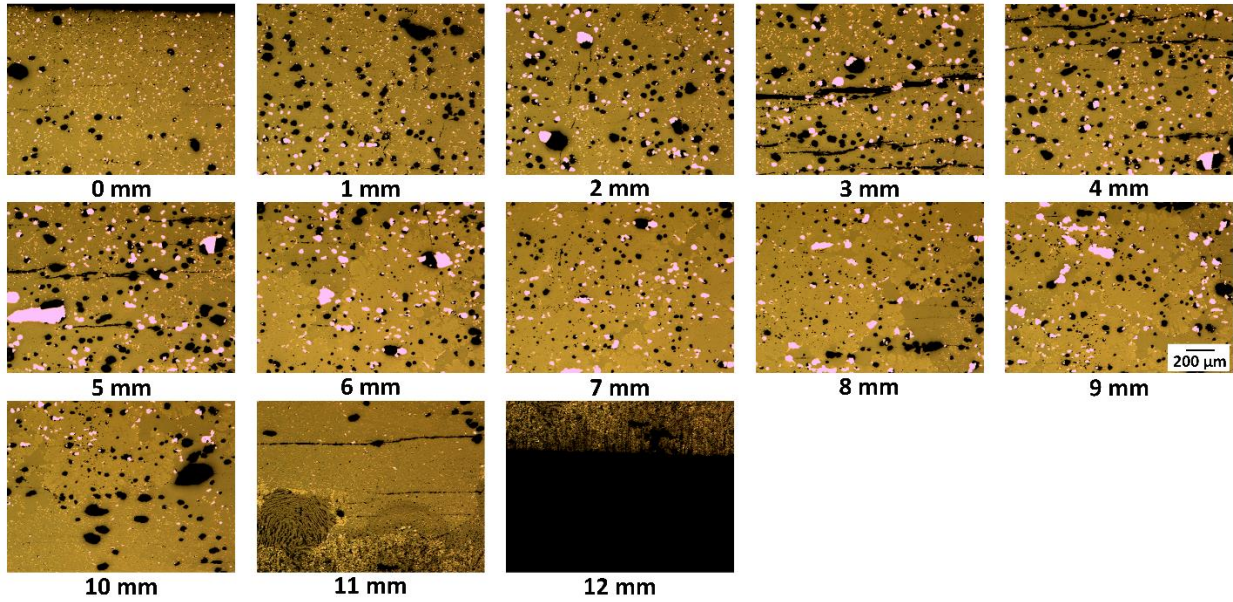


Figure 13.3: Optical microscope images along the central c -axis of a YBCO-Ag sample from a position just below the seed at 50x magnification.

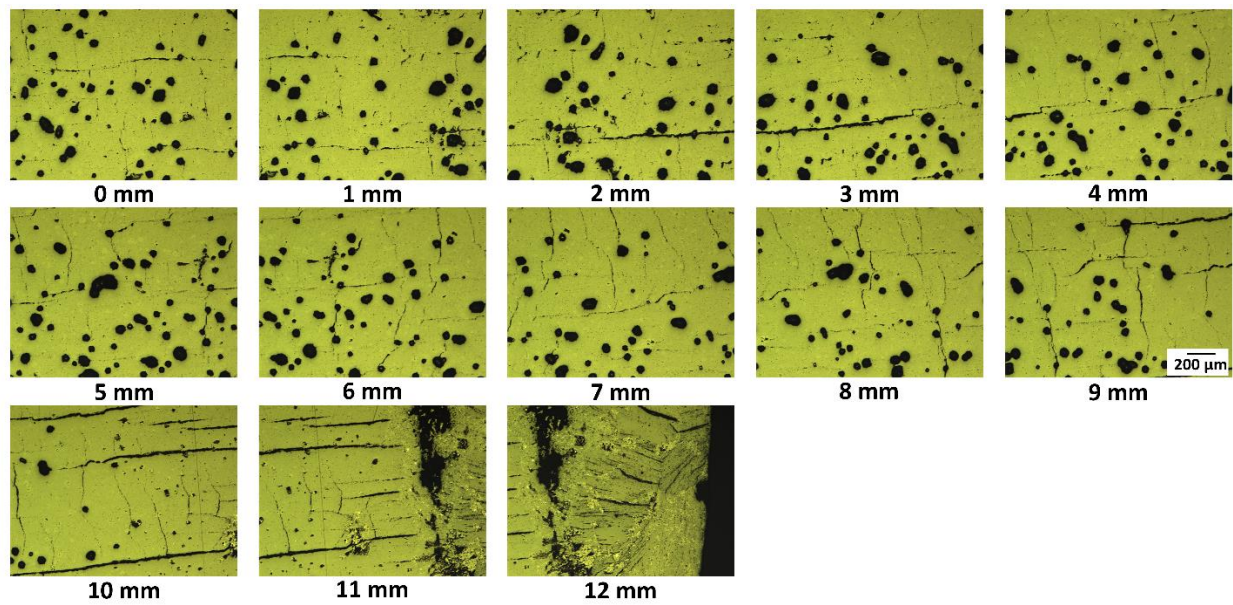


Figure 13.4: Optical microscope images along the a/b -axis of a YBCO sample approximately 1.5 mm from the top at 50x magnification.

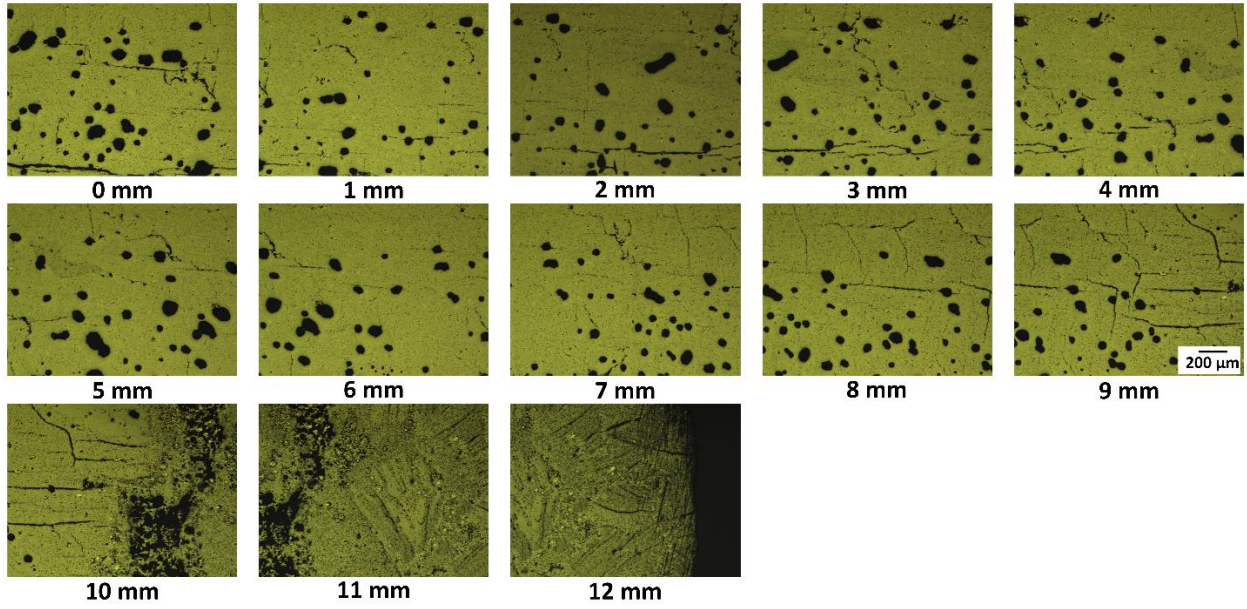


Figure 13.5: Optical microscope images along the a/b -axis of a LR YBCO sample approximately 1.5 mm from the top at 50x magnification.

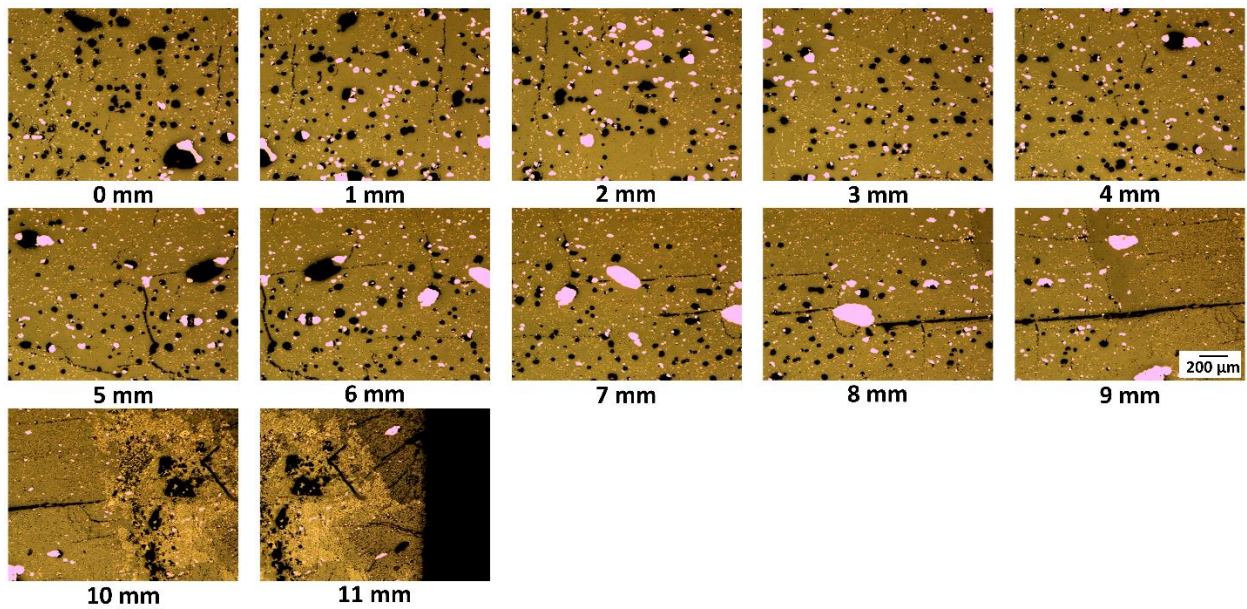


Figure 13.6: Optical microscope images along the a/b -axis of a YBCO-Ag sample approximately 1.5 mm from the top at 50x magnification.

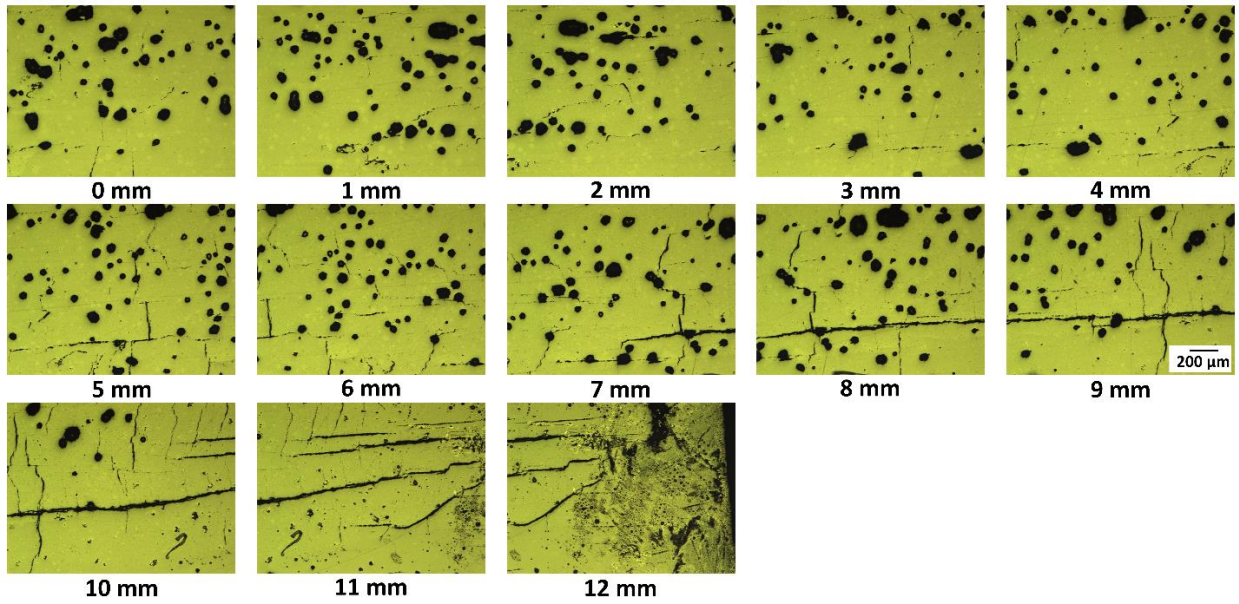


Figure 13.7: Optical microscope images along the a/b -axis of a YBCO sample approximately 1.5 mm from the base at 50x magnification.

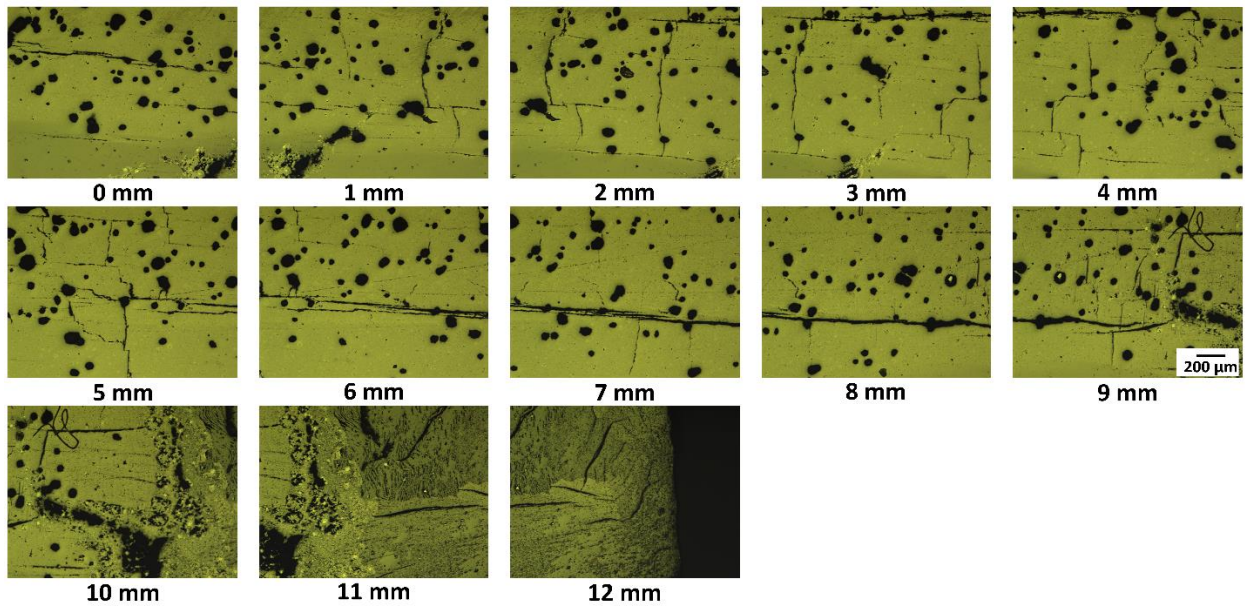


Figure 13.8: Optical microscope images along the a/b -axis of a LR YBCO sample approximately 1.5 mm from the base at 50x magnification.

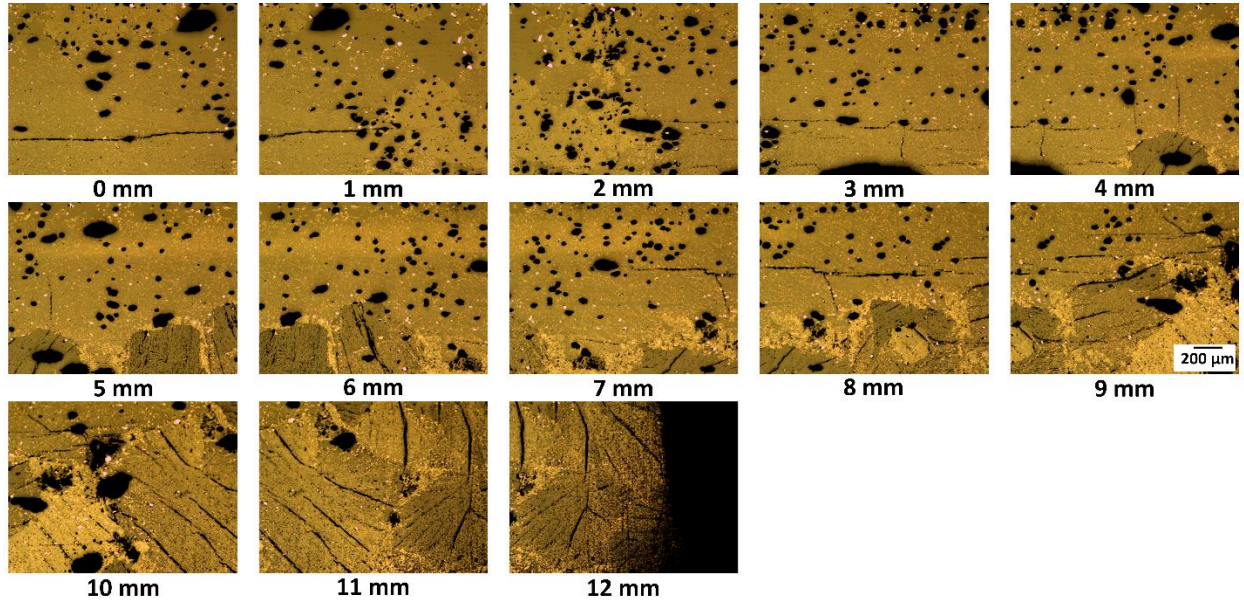


Figure 13.9: Optical microscope images along the *a/b*-axis of a YBCO-Ag sample approximately 1.5 mm from the base at 50x magnification.

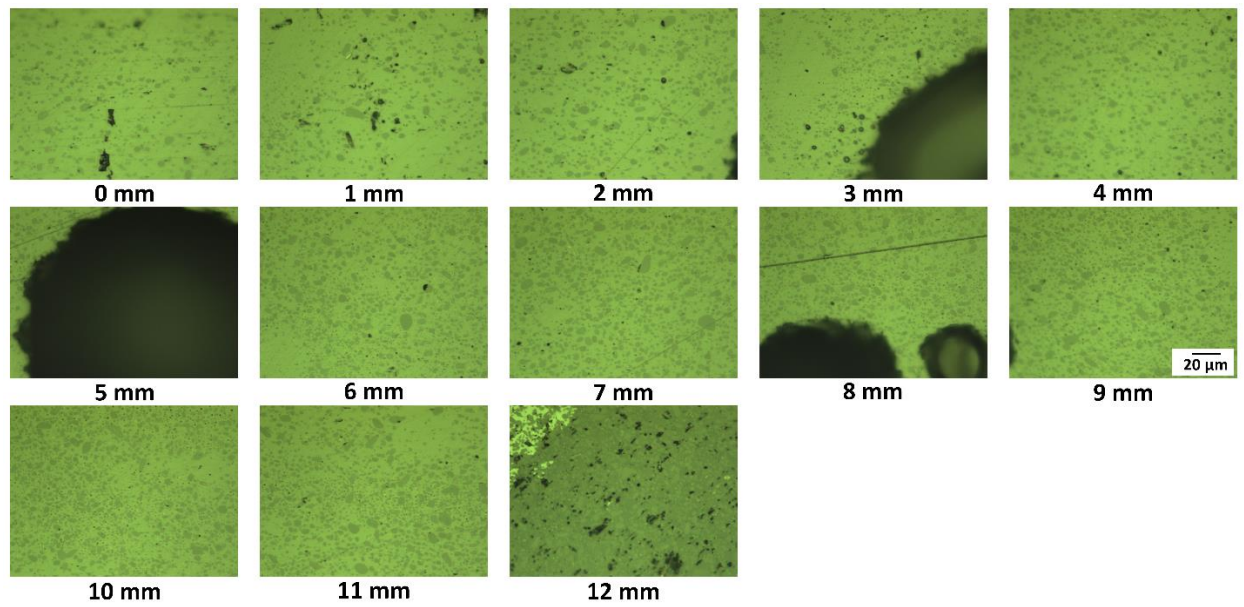


Figure 13.10: Optical microscope images along the central *c*-axis of a YBCO sample at 500x magnification.

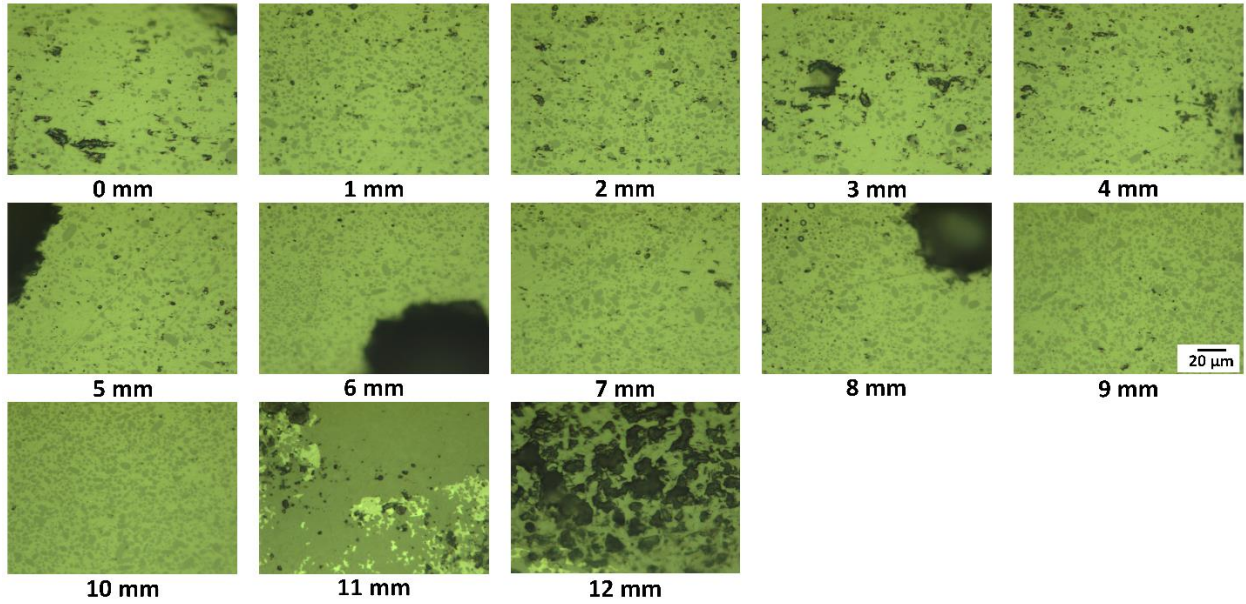


Figure 13.11: Optical microscope images along the central c-axis of a LR YBCO sample at 500x magnification.

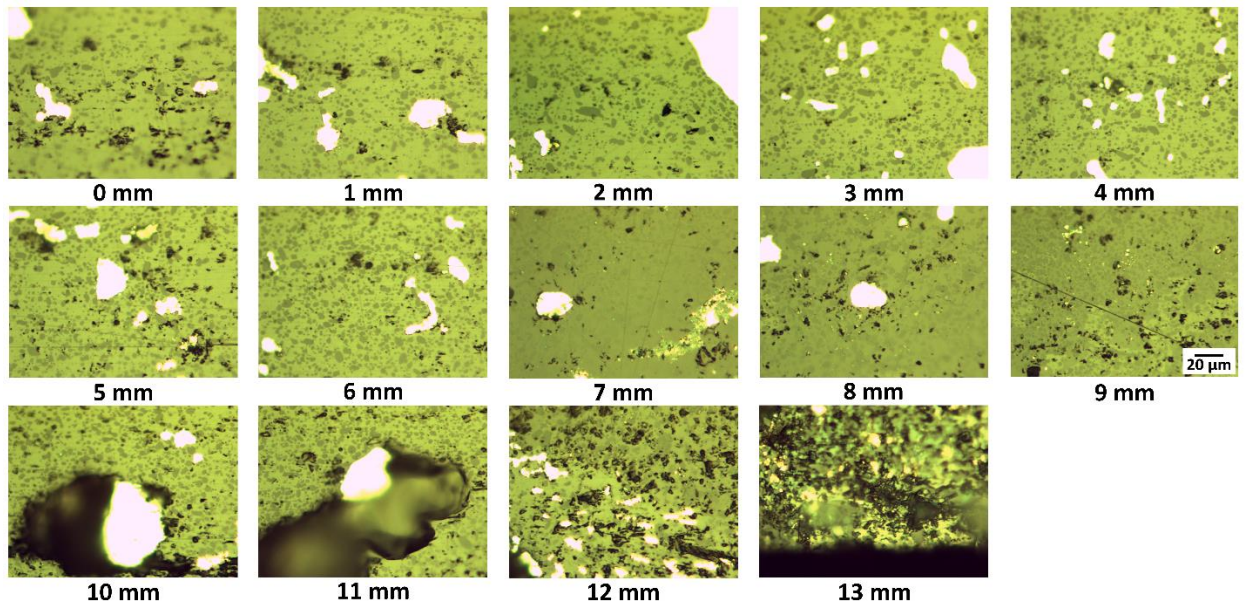


Figure 13.12: Optical microscope images along the central c-axis of a YBCO-Ag sample at 500x magnification.